

SEISMIC PROPERTIES AND PROCESSES  
ALONG THE  
SUBDUCTION PLATE INTERFACE:

THE FEBRUARY 2010  $M_w$  8.8 MAULE,  
CHILE EARTHQUAKE

Thesis submitted in accordance with the requirements of the  
University of Liverpool  
for the degree of Doctor in Philosophy (Earth Sciences) by

Stephen Paul Hicks

August 2015



# ABSTRACT

The seismogenic zone of subduction margins has the potential to generate some of the world's largest earthquakes. A detailed study of the 2010  $M_w$  8.8 Maule, Chile rupture has enabled interpretation of the controls that govern subduction zone seismic behaviour across the earthquake cycle. In this thesis, we focus on two aspects of the central Chile margin: (1) imaging physical properties in the forearc and along the plate interface; (2) assessing source complexity of megathrust ruptures.

We exploit a dataset of seismic body wave onset times from local aftershocks recorded on a temporary network to derive a 3-D seismic velocity model of the Maule rupture area. We image the main domains of the subduction zone and find a high velocity anomaly located along the plate interface, which we initially interpret as a subducted topographic high. We then develop a second, more accurate velocity model that uses an improved arrival time dataset together with observations from ocean-bottom seismometers. This refined model gives a sharper view of both the plate interface close to the trench, and the marine forearc. We show that ancient blocks of dense mantle in the lower forearc may have decelerated slip during the Maule earthquake and contributed to its nucleation. Furthermore, we infer that fluid saturated sediments inhibited significant slip close to the trench.

We study source processes of a large aftershock of the Maule sequence, the 2011  $M_w$  7.1 Araucania earthquake, by inverting local seismic waveforms for a multiple point-source faulting solution. We find this earthquake constituted rupture on the plate interface followed by almost instantaneous slip along a normal fault in the overriding plate: the first observation of its kind. The second rupture of this closely-spaced doublet was hidden from teleseismic faulting solutions, and may have been dynamically triggered by S-waves from the first event.

Overall, our work highlights the role played by the upper plate in subduction zone seismogenesis. We suggest that seismic velocities can help to characterise the behaviour of future large megathrust earthquakes. We show that the potential hazard posed by closely-spaced doublets involving the upper plate should be accounted for in real-time tsunami warning systems by using local waveform analysis.





# DECLARATION

I declare that the work presented in this thesis is the result of my own work. The material contained in the thesis has not been presented, nor is currently being presented, either wholly or in part, for any other degree or qualification.

---

Stephen Paul Hicks

21 August 2015



“Science has fallen into many errors – errors which have  
been unfortunate and useful rather than otherwise, for  
they have been the steppingstones to truth”

– *Jules Verne*

*Journey to the Center of the Earth*



# TABLE OF CONTENTS

Abstract .....	3
Declaration .....	5
Table of Contents .....	9
List of Figures .....	13
List of Tables.....	25
List of Enclosures.....	27
List of Abbreviations.....	29
Acknowledgements .....	31
Preface.....	33
<b>1. Introduction .....</b>	<b>35</b>
1.1 Megathrust earthquakes .....	35
1.2 The 2010 $M_w$ 8.8 Maule, Chile earthquake .....	40
1.3 Aims and objectives of this thesis.....	44
1.4 Thesis organisation and publication status of chapters .....	47
<b>2. Upper Plate Versus Lower Plate: Physical Controls on Megathrust Earthquake Rupture Processes .....</b>	<b>51</b>
2.1 Structural domains above and below the megathrust.....	52

## Table of Contents

2.2	Structural and compositional influences on megathrust seismogenic behaviour.....	62
2.3	Limitations and remaining questions .....	69
2.4	Summary .....	73
<b>3.</b>	<b>Seismic Imaging of Subduction Zone Structure using Local Earthquake Tomography .....</b>	<b>75</b>
3.1	Fundamentals of seismic tomography.....	75
3.2	Seismic ray tracing.....	77
3.3	The coupled hypocentre-velocity problem.....	78
3.4	Inversion for 1-D velocity structure .....	81
3.5	3-D tomographic inversion.....	83
3.6	Illuminating the subduction megathrust using local earthquake tomography: past applications.....	88
3.7	Summary .....	90
<b>4.</b>	<b>The 2010 <math>M_w</math> 8.8 Maule, Chile Earthquake: Nucleation and Rupture Propagation Controlled by a Subducted Topographic High.....</b>	<b>93</b>
	Published paper abstract .....	94
4.1	Introduction .....	94
4.2	Tomographic Inversion Scheme.....	96
4.3	Results of 3-D Tomographic Inversion.....	97
4.4	Discussion .....	100
4.5	Conclusions .....	103

<b>5. Anatomy of a Megathrust: The 2010 M8.8 Maule, Chile Earthquake Rupture Zone Imaged using Seismic Tomography .....</b>	<b>107</b>
Published paper abstract .....	108
5.1 Introduction .....	108
5.2 Characteristics of the central Chile subduction zone .....	110
5.3 The 2010 Maule earthquake .....	112
5.4 Seismic data .....	113
5.5 Velocity inversion strategy .....	115
5.6 Inversion resolution .....	119
5.7 Results and discussion .....	125
5.8 Depth-varying rupture properties and fault structure .....	139
5.9 Conclusions .....	140
<b>6. Seismic Source Imaging using Full-Waveform Analysis .....</b>	<b>143</b>
6.1 Moment tensor theory .....	144
6.2 Decomposition of the moment tensor .....	145
6.3 Moment tensor inversion .....	148
6.4 Time-domain full-waveform moment tensor inversion .....	149
6.5 3-D waveform simulations .....	159
6.6 Summary .....	162
<b>7. Seismic Slip on an Upper Plate Normal Fault During a Large Subduction Megathrust Rupture .....</b>	<b>165</b>

## Table of Contents

Manuscript abstract.....	166
7.1 Introduction .....	166
7.2 Mainshock hypocentre relocation .....	169
7.3 Synthetic tests.....	172
7.4 Multiple point-source solution .....	177
7.5 Comparison with aftershock locations and mechanisms.....	183
7.6 3-D waveform propagation effects.....	185
7.7 Discussion and conclusions.....	188
<b>8. Synthesis: Implications for the Interplay Between Megathrust Physical Heterogeneity and Seismic Source Characteristics .....</b>	<b>197</b>
8.1 Influence of localised upper plate heterogeneity on seismogenesis...	198
8.2 Physical properties of the seismogenic zone: reconciling global observations.....	206
8.3 Future outlook: Application of structural heterogeneity to 3-D seismic wave propagation simulations .....	210
<b>9. Conclusions and Future Work .....</b>	<b>215</b>
9.1 Response to project aims.....	215
9.2 Limitations of this study and ideas for future research .....	219
References .....	223
Enclosures .....	253



# LIST OF FIGURES

Figure 1.1: Map of the largest global earthquakes that have occurred since 1900, based on the USGS NEIC and ISC-GEM historic catalogues. The year and magnitude of $M_w$ 8.5+ earthquakes are labelled. The focus of this thesis is on the 2010 $M_w$ 8.8 Maule, Chile earthquake. ....	36
Figure 1.2: Simplified overview of the seismic cycle and the parameters that are used in this thesis to describe seismic sources and megathrust dynamics at each stage. ....	37
Figure 1.3: Depth segmentation of megathrust earthquake source characteristics based on Lay et al. (2012). Each domain is denoted by the letters A–D, which are discussed in the text. ....	39
Figure 1.4: Location of the Maule earthquake showing the characteristics of the coseismic rupture and postseismic stage. HF = high frequency. Inset: the location of the large map is given by the black box.....	43
Figure 2.1: Schematic view of domains that constitute the shallow part of a typical subduction zone. Labelled features are referred to in the text. Redrawn and simplified after Kopp (2013).....	53
Figure 2.2: Distribution of circum-Pacific erosional and accretionary margins based on Clift and Vannucchi (2004) and Kopp (2006) compared with earthquake characteristics. Large earthquake locations are based on Bilek (2010), but with an updated catalogue. Tsunami earthquake locations are from El Hariri et al. (2013). ....	54
Figure 2.3: Illustration of the main structural variations between erosive and accretionary margins, based on Clift and Vannucchi (2004), von Huene and Ranero (2003), and von Huene et al. (2004; 2009).....	56
Figure 2.4: Schematic view of the main structural features of the central Ecuador subduction zone showing interplay between fluid-rich sediment lenses,	

## List of Figures

seamounts, upper plate weakening, and plate coupling. Redrawn after Sage et al. (2006). .....	71
Figure 3.1: Staggered inversion workflow used in this thesis to calculate 3-D $v_p$ and $v_p/v_s$ models using local earthquake tomography. ....	82
Figure 4.1: a) Locations of past ruptures and segmentation in Chile, after Métois et al. (2012). Ellipses give the rupture area of each earthquake. The name of each segment and segment boundaries (dashed lines) are shown. The box denotes the location of the map in (b). b) Local map with bathymetry/topography (coloured scale bar). The red star is the NEIC epicentre. Blue contour lines show the coseismic slip distribution of <i>Moreno et al.</i> (2012). Red circles and white triangles are the aftershocks and stations, respectively, used in our tomographic inversion. Black crosses denote the nodes in our 3-D inversion. The grey dashed lines show the geometry of the subducting Nazca slab, based on the Slab1.0 model (Hayes and Wald, 2009). ....	95
Figure 4.2: Histograms of a) P-wave and b) S-wave onset time pick errors of the automatic algorithm, based on a subset of 20 events. ....	96
Figure 4.3: Resolution estimate of our best-fitting 3-D (left) $v_p$ and (right) $v_p/v_s$ model based on analysis of the model resolution matrix. Shading denotes spread function values and black lines show the 70% contour of the resolution kernel. The resolution limits (white lines) are based on spread function values of 2 and 4 for the $v_p$ and $v_p/v_s$ model, respectively. ....	98
Figure 4.4: a) Cross-sections through the 3-D $v_p$ model. The location and orientation of each profile is shown in Figure 4.1b. The coastline is given by black triangles. Features of the model are interpreted as follows: (a) continental crust, (b) forearc basin, (c) central basin, (d) continental mantle, and (e) subducting oceanic crust. The blue dashed line is the unperturbed thrust interface. In section C-C', (f) is a high velocity anomaly located above the plate interface, and (g) is a smaller high velocity anomaly in the Pichilemu region (section A-A'). b) Cross-section showing $v_p/v_s$ along section C-C'. Black dots are relocated aftershocks with $M_l \geq 3.0$ , with a minimum of 20 P- and 20 S-picks, respectively. The white lines	

denote the resolution limits, based on analysis of the resolution matrix (Figure 4.3). .....	99
Figure 4.5: a) Comparison of $v_p$ along the plate interface (coloured image, black contours) with the coseismic slip distribution of Moreno et al. (2012); (blue contours). The location of the high velocity anomaly beneath the coastline correlates with a region of relatively low coseismic slip. The two main slip patches correlate to lower $v_p$ along the plate interface. Locations of aftershocks (grey circles) that lie along or close to the thrust interface are shown, highlighting the sparse seismicity associated with the anomaly. The red star is the USGS-NEIC epicentre. The white line denotes the up- and down-dip resolution limits of our tomography model. b) Forearc Bouguer gravity anomaly, derived from the model of Tassara and Echaurren (2012). Black lines are the $v_p$ contours from (a) for comparison. ....	101
Figure 4.6: a) Reconstructions of the Nazca and Pacific plates at 20Ma illustrating that the central Chilean margin (green boxed area) may have formed at a similar time to an area of bathymetric heterogeneity (red boxed area) on the Pacific plate, now located at $\sim 35^\circ\text{S}$ (b). ....	103
Figure 4.7: Schematic interpretation based on our tomographic model. Our 3-D model is cut along two sections: $37.5^\circ\text{S}$ to show the velocity structure of the oceanic lithosphere, and $36^\circ\text{S}$ to show the structure of the forearc. The geometry of the rupture plane is illustrated between these two sections. The subducted topographic anomaly which lies beneath the coastal ranges at around $36^\circ\text{S}$ disrupts the regular megathrust interface; however, we cannot tell whether it is still fully coupled to the downgoing plate. The red star denotes the hypocentral location of the mainshock. White lines along the interface show the coseismic slip distribution (Moreno et al., 2012). ....	105
Figure 5.1: Geotectonic characteristics and simplified geological map of the central Chilean margin. Morphotectonic units are from Glodny et al. (2007) and the geological is map redrawn after Sernageomin (2003), Melnick and Echtler (2006a) and Vásquez et al. (2011). The red box in the inset map gives the location	

of the study area. Labels show the names of the locations referred to in this chapter. ....	111
Figure 5.2: Map of the Maule segment along the South Central Chile margin coloured by bathymetry/topography. The main rupture characteristics of the Maule earthquake are shown. The purple star shows the epicentre of the mainshock (Hayes et al., 2013) and the blue contours represent coseismic slip distribution ( $> 6$ m) in 2 m intervals (Moreno et al., 2012). Triangles correspond to seismic stations used in the velocity inversions. Black crosses indicate the horizontal grid nodes used in the 3-D inversion and red circles show the preliminary locations of 669 earthquakes used in the velocity inversions. Thick black lines show the location of cross-sections that are shown in this chapter. ....	114
Figure 5.3: Results of the 1-D velocity model inversion. a) 1-D velocity models showing the range of starting models, range of inverted models (grey shading), and the preferred velocity model (red line). b) Map of 1-D station delay terms. The reference station is indicated by the black triangle. ....	117
Figure 5.4: (left) Synthetic 3-D $v_p$ input model and (right) corresponding inversion results for the restoring resolution test. Locations of the five cross-sections are shown in Figure 5.2. Black crosses indicate inversion nodes and white dots show the locations of the 669 earthquakes used. The thick grey line gives regions of the model with good resolution. Areas with reduced resolution are faded; regions with no resolution are left blank. The location of the coastline is denoted by the white triangle. ....	121
Figure 5.5: (left) Synthetic 3-D $v_p/v_s$ input model and (right) corresponding inversion results for the restoring resolution test. Locations of the five trench-perpendicular cross-sections are shown in Figure 5.2. White dots indicate the locations of the 669 earthquakes used in the tomographic inversion. In cross-section B-B', we include a low $v_p/v_s$ anomaly in the subducting oceanic lithosphere; the inversion is not able to fully recover this anomaly. ....	122
Figure 5.6: Resolution estimate of the 2-D velocity model based on analysis of the MRM. Black crosses indicate the location of inversion nodes. The different	

colours surrounding each node represent the SF value. The black circles show diagonal elements of the resolution matrix. Green lines represent the 70% contour line of the resolution kernel. The coastline is given by the black triangle..... 123

Figure 5.7: Results of the bootstrap-resampling test showing the spatial distribution of velocity standard deviation in the 2-D model. The coastline is given by the black triangle..... 124

Figure 5.8: Resolution estimate of our 3-D velocity model based on analysis of the MRM. Features are plotted in the same way as Figure 5.6. Locations of the five cross-sections are shown in Figure 5.2. .... 125

Figure 5.9: 2-D velocity model plotted on a cross-section orientated perpendicular to the trench. Crosses indicate grid nodes and white circles give the 2-D locations of events from the tomographic inversion. Based on analysis of the MRM and the characteristic model tests, limits of well-resolved areas are given by the thick grey line. Regions with diminished resolution are faded; unresolved regions are left blank. Labels refer to the following features that are discussed in the text: mf = marine forearc; oc = oceanic crust; cf = upper forearc crust; cd = Central Depression; cm = continental mantle. The thick black line indicates the location of our calculated plate interface. The purple star denotes the hypocentral location of the Maule earthquake (Hayes et al., 2013). The location of the coastline is denoted by the white triangle. .... 126

Figure 5.10: 3-D velocity model plotted along five cross-sections, of which the locations are labelled on the far right and shown in Figure 5.2. Labels refer to the following features that are discussed in the text: PA = Pichilemu anomaly; CA = Cobquecura anomaly. Resolution limits are defined in the same way as Figure 5.9..... 128

Figure 5.11: a) 3-D  $v_p$  model plotted as depth sections. Labels refer to the following features that are discussed in the text: mf = marine forearc; oc = oceanic crust; cf = upper forearc crust; cd = Central Depression; PA = Pichilemu anomaly; CA = Cobquecura anomaly. Resolution limits are defined in the same way as Figure 5.9. (b) Forearc Bouguer gravity anomaly (Chapter Four) overlain by contours of

$v_p$  model at 25 km depth. Contours are given for  $v_p$  in the range 7.25–8.00 km/s. Inset: scatter plot showing the correlation between forearc Bouguer gravity anomaly and forearc  $v_p$  at 25 km, sampled at  $0.2^\circ$  intervals of latitude and longitude..... 129

Figure 5.12: Seismic velocities along the plate interface from the 2-D model as a function of depth for (a)  $v_p$  and (b)  $v_p/v_s$ . Grey shading shows our estimated uncertainty. (c) Histogram of plate interface aftershock earthquake depths and normalised coseismic slip distribution. Trench-perpendicular slip profiles traverse the northern slip asperity. Aftershock hypocentres are relocated from the catalogue of Rietbrock et al. (2012). (d) Depth-segmentation of the plate interface region based on interpretation of the seismic velocities and seismic character of the Maule megathrust. Letters in the left-hand column correspond to the megathrust domains of Lay et al. (2012)..... 133

Figure 5.13: Distribution of (top)  $v_p$  and (bottom)  $v_p/v_s$  along the plate interface region compared with behaviour of the Maule megathrust over the seismic cycle. Labels refer to the features discussed in the text and are defined in the caption of Figure 5.10. a) Contours of preseismic locking of the megathrust (Moreno and Rosenau, 2010) (blue lines) are for locking of greater than 0.7 and given in intervals of 0.1. (b) Mainshock epicentral location from Hayes et al. (2013). Coseismic slip distribution (Moreno et al., 2012) plotted as for Figure 5.2. White circles give the location of high frequency energy release during the Maule earthquake (Kiser and Ishii, 2011). (c) Contours of afterslip  $> 1$  m (Y. N. Lin et al., 2013), (blue lines) plotted in 0.2 m intervals. Grey circles show the distribution of relocated plate interface aftershock seismicity. .... 135

Figure 5.14: a) Scatter plot showing the relationship between coseismic slip and plate interface  $v_p$  for 20–40 km depth. The correlation coefficient,  $r$ , and a best-fitting line (black) are shown. Three groups of  $v_p$  - coseismic slip character are given by the coloured rectangles. (b) Points remapped to check whether the correlation is spatially correlated by adopting the approach of Moreno et al. (2014). This test shows that the pattern of correlation is laterally continuous, showing a spatial relationship between  $v_p$  and coseismic slip for the down-dip part of the rupture. .... 136

Figure 5.15: Comparison between manually determined hypocentral locations from our tomographic inversion (from onshore and offshore seismic stations) with those based on automatic onset time determination (from onshore seismic stations only); (Rietbrock et al., 2012).	138
Figure 5.16: Relocated and corrected aftershock locations from the full 2010 catalogue corrected for systematic mislocations. Events with a minimum of 12 P-wave and 12 S-wave observations are shown. Features are plotted in the same way as Figure 5.10.	139
Figure 6.1: Schematic workflow of time-domain moment tensor inversion using the ISOLA software package, showing the steps required and selection of parameters.	151
Figure 7.1: Location map of the Araucania earthquake. Stations used for moment tensor inversion are labelled by their corresponding station code. Other stations are used for hypocentre relocation only. Shading indicates rupture areas of great earthquakes in 1960 (Moreno et al., 2009) and 2010 (Moreno et al., 2012). Inset: Regional plate tectonic setting.	168
Figure 7.2: Signal-to-noise ratio analysis for stations used in the single and multiple point-source inversions. The dashed vertical lines denote the approximate frequency range used.	170
Figure 7.3: 1-D velocity models tested in this study based on our local tomographic model (Chapter Five). Model B (Coastline) was used for the final source solutions.	172
Figure 7.4: Synthetic source recovery tests for different source configurations (A-D). The number above each beach ball represents the input and recovered centroid time of each source. For the single-source inversion, focal mechanisms are coloured by %DC. For the multiple source inversion results, focal mechanisms are coloured by the Kagan angle (minimum rotation angle) with respect to the corresponding input beach ball.	173

## List of Figures

Figure 7.5: Single source inversion results. a) Comparison between the observed (black) and synthetic (red) waveforms. Waveforms are filtered in the frequency range 0.02–0.04 Hz. Station names are shown on the right and the components are labelled at the top. Numbers next to waveforms denote corresponding variance reduction. b) Grey beach balls show solution variability based on jackknifing tests, labelled with the station removed in each inversion. The coloured grid represents the correlation between waveforms for each trial point-source position (numbered). Solutions that lie within 90% of the maximum VR are plotted in black. The highest correlation solution is plotted in red. The red star denotes the epicentre of the Araucania earthquake. .... 178

Figure 7.6: Double-couple percentage (%DC) and variance reduction (VR) of the single point-source versus frequency. A transition occurs at 0.057 Hz, where VR suddenly decreases because the waveforms cannot be explained by a single point-source alone. This change is illustrated by representative waveforms at low and high frequencies. .... 179

Figure 7.7: Comparison between the observed (black) and synthetic (red) waveforms at high frequencies (0.02–0.08 Hz) solution using a single point-source. Station names are labelled. Numbers alongside each waveform component denote the corresponding VR. .... 180

Figure 7.8: Correlation (black line) and total moment (red dashed line) of the multiple point-source solution as a function of triangle length using iterative deconvolution. Beach balls above and below the line give the best-fitting mechanism for Events I and II, respectively. .... 181

Figure 7.9: a) Observed (black) and synthetic (red) waveforms for the best-fitting high frequency (0.02–0.08 Hz) solution using two point-sources. Station names are labelled. Numbers alongside each waveform component denote VR. Blue and green shading denotes the contribution from each event. b) Waveform correlation for each event as a function of trial point-source position (numbered). The time shifts of Events I and II are shown. Black beach balls are solutions that lie within 90% of the best-fitting solution's (red beach ball) VR. The red star denotes the



earthquake's epicentre. c) Resulting moment-rate function obtained using NNLS. .....	184
Figure 7.10: Best-fitting solutions (within the 98 <sup>th</sup> percentile) for the two-point-source, high frequency solution using the moment-constrained NNLS. The colour of each beach ball indicates the centroid time of each source. ....	188
Figure 7.11: a) Map and b) cross-section showing locations and focal mechanisms of aftershocks (Groups A and B) and mainshock events (labelled EV-I and EV-II). Faulting style is classified on principal stress orientations (Frohlich, 1992) and minimum rotation angle with respect to plate interface thrust faulting (Hayes et al., 2013), accounting for plate interface geometry (black line; Chapter Five). We plot the revised location of Event II, based on 3-D waveform modelling. Mapped faults are shown (Melnick et al., 2009; Melnick and Echtler, 2006b); MVFZ = Mocha-Villarrica fault zone. The cross-section background is from our P-wave velocity model (Chapter Five). The star denotes the hypocentre of the Araucania earthquake; the triangle shows the coastline. ....	190
Figure 7.12: 3-D view of the hexahedral mesh used for the 3-D waveform simulations. This mesh honours surface relief and bathymetry, but does not contain dipping geological discontinuities at depth. ....	191
Figure 7.13: Recovery of 3-D synthetic waveforms using the inversion based on 1-D Green's functions. In each case, input sources are based on the result from our real data inversion. On the right, the source position of Event II is placed at source position 17. In each case, the 1-D inversion results in a systematic southward shift, as shown by the arrows. ....	192
Figure 7.14: Schematic interpretation of the Araucania earthquake rupture. Plate interface thrusting (Event I) triggered a rupture along an extensional fault in the overriding plate (Event II). It is likely that two great earthquakes in 1960 and 2010 brought both faults closer to failure. As shown by ancient submarine landslide deposits in the area (Geersen et al., 2011b), a larger-scale rupture in the overriding plate has the potential to act as a tsunamigenic earthquake. Beach balls represent the focal mechanisms of both mainshock events. The inset shows the	

interpreted structure of conjugate normal faulting with the background colour representing $v_p/v_s$ (Chapter Five).....	193
Figure 7.15: Three-component velocity traces of the simulated seismic wavefield of Event I ‘seen’ by Event II. The waveform is bandpass filtered at 0.02–0.15 Hz. The 3-D simulation is generated in the same way as described in Section 7.6; a receiver is placed at the centroid location of Event II. The known centroid times of Events I and II are shown. Although we cannot pinpoint the exact nucleation time of Event II, it is clear that the arrival of high amplitude S-waves from Event I is coincident with the possible nucleation stage of Event II, based on its source duration of 18 s.....	194
Figure 7.16: Regional recordings of the $M_w$ 7.1 2011 Araucania (plate interface thrusting and upper plate normal faulting), 2012 $M_w$ 7.1 Constitución (plate interface thrusting only) and 2010 $M_w$ 7.1 Pichilemu (upper plate normal faulting only) earthquakes at the permanent GSN station, TRQA in eastern Argentina. The left-hand panel shows the normalised frequency (top) spectra and traces for each component: a) west; b) east; c) vertical. The map in the right-hand panel shows the location of the three earthquakes, corresponding CMT solutions and the location of station TRQA. ....	195
Figure 8.1: Comparison of our preliminary aftershock moment tensor catalogue (top left) with those already published for the period ending December 2010 (Agurto et al., 2012; Hayes et al., 2013). Solutions from the global CMT project (Ekström et al., 2012) are also shown (bottom right). Faulting mechanisms are classified based on the plunge angle of principal stresses (Frohlich, 1992). Reverse faulting style is chosen from the minimum rotation angle with respect to a reference solution representing pure plate interface thrusting based on slab geometry (Chapter Five). ....	205
Figure 8.2: Map and cross-sections of intraplate aftershock mechanisms combined from the different catalogues shown in Figure 8.1. Interpretations of possible upper plate fault geometries are illustrated in the cross-sections. FAP = frontal accretionary prism; PAW = palaeo-accretionary wedge; CF = crustal framework; PA = Pichilemu anomaly; OC = oceanic crust; OM = oceanic mantle.....	207

- Figure 8.3: Comparison of the relationship between plate interface structure (left:  $v_p$ , centre:  $v_p/v_s$  and megathrust slip for the Maule, Chile and Tohoku, Japan earthquakes. The Maule profiles are drawn in a similar way to Figure 5.12, using the coseismic slip model of Moreno et al. (2012). Seismic velocities for the Tohoku megathrust come from Yamamoto et al. (2014) and coseismic slip is from Gusman et al. (2012). The arrows indicate the depth offset in maximum  $v_p/v_s$  and coseismic slip between both rupture zones. .... 208
- Figure 8.4: Location and faulting mechanism of the event described in Table 8.1 that has been used to simulate seismic wave propagation the central Chile subduction zone. Red triangles denote stations with high-quality broadband recordings of this event (Figure 8.6). .... 211
- Figure 8.5: 3-D image of the mesh (as viewed from the south) that is used to generate the high frequency 3-D waveform simulations inside the entire rupture zone of the Maule earthquake. .... 212
- Figure 8.6: Representative velocity waveform fits comparing 3-D synthetics with observed waveforms for the simulated test event. Waveforms are bandpass filtered at 0.05–0.45 Hz. Locations of these stations are shown in Figure 8.4. Orange lines indicate P-wave onset times. .... 213
- Figure 8.7: Unfiltered isotropic sensitivity kernel of shear modulus (normalised), as viewed from the south, with a vertical slice through the hypocentral region of the studied event. Elevation exaggeration = 2:1. .... 214



# LIST OF TABLES

Table 1.1: Hypocentre estimates of the Maule earthquake. ....	42
Table 2.1: Estimates of the intersection depth between the continental Moho and plate interface for different subduction zones. ST = scattering tomography; RF = receiver functions; LET = local earthquake tomography; RE = reflected phases; RR = refraction seismology. ....	59
Table 2.2: Estimates of subduction channel thickness for different subduction zones. ....	62
Table 2.3: Summary of key observations for different physical properties affecting megathrust seismogenesis. ....	74
Table 5.1: Summary of inversion parameters used at each step. GAP = minimum azimuthal gap. ....	116
Table 6.1: Elementary moment tensors used in the inversion method of Kikuchi and Kanamori (1991). ....	154
Table 7.1: Hypocentral estimates for the Araucania earthquake. ....	167
Table 7.2: Single point-source CMT solutions for the Araucania earthquake. Nodal planes are described by strike/dip/rake ( $^{\circ}$ ). ....	169
Table 7.3: Results from the synthetic sensitivity tests described in Section 7.3.1 and presented in Figure 7.4. Pos. = source position; Mech. = focal mechanism; Rot. angle = rotation angle with respect to input source mechanism. ....	175
Table 7.4: Relative uncertainty estimates of different faulting styles for a single point-source offshore (source position 16). Uncertainties are calculated for both our actual station distribution (Figure 7.1) and a network of ideally distributed stations. ....	177

## List of Tables

Table 7.5: Source stability of the multiple point-source solution based on the results of removing one station at a time from the inversion (jackknifing). These jackknifing results are compared with the best-fitting solution obtained using all available stations. Source location refers to the grid position illustrated in Figure 7.9b. Stations are ordered in epicentral distance. These results show the remarkably consistent mechanisms for both sub-events, indicating independence from the exact set stations used in the inversion. ....	186
Table 7.6: Dependence of Event II solution on the position and mechanism of Event I. ....	187
Table 8.1: Source parameters of the test event used for the 3-D waveform simulation described in this section. ....	211

# LIST OF ENCLOSURES

Enclosure 1: ‘Sub-slab mantle anisotropy beneath south-central Chile’. Paper published in *Earth and Planetary Science Letters* by Stephen Hicks, Stuart Nippress and Andreas Rietbrock in December 2012.

Enclosure 2: ‘The 2010  $M_w$  8.8 Maule, Chile earthquake: nucleation and rupture controlled by a subducted topographic high. Paper published in *Geophysical Research Letters* by Stephen Hicks, Andreas Rietbrock, Christian Haberland, Isabelle Ryder, Mark Simons and Andrés Tassara in December 2012.

Enclosure 3: ‘Anatomy of a megathrust: The 2010 M8.8 Maule, Chile earthquake rupture zone imaged using seismic tomography’. Paper published in *Earth and Planetary Science Letters* by Stephen Hicks, Andreas Rietbrock, Isabelle Ryder, Chao-Shing Lee and Matthew Miller in August 2014.

Enclosure 4: ‘Seismic Speed bumps found in Chile’s earthquake zone’. News article about the main results from Chapter Five written by Becky Oskins and published by *livescience.com* / *Yahoo News* on November 4, 2014.





# LIST OF ABBREVIATIONS

%DC	Double-couple percentage
2-D	Two-dimensional
3-D	Three-dimensional
BDT	Brittle-ductile transition
CLVD	Compensated linear vector dipole
CMT	Centroid moment tensor
CSD	Closely-spaced doublet
CSN	Centro Sismológico Nacional
DC	Double-couple
DWS	Derivative weight sum
FD	Finite-difference method
$f_c$	Corner frequency
FE	Finite-element method
GAP	Minimum azimuthal gap
gCMT	Global Centroid Moment Tensor Project
GF	Green's functions
ID	Iterative deconvolution
IMAD	International Maule Aftershock Deployment
LET	Local earthquake tomography
OBS	Ocean-bottom seismometer
MFZ	Mocha Fracture Zone
MRM	Model resolution matrix
$M_l$	Local magnitude
MT	Moment tensor
$M_w$	Moment magnitude
NNLS	Non-negative least squares
$Q$	Attenuation quality factor
SEM	Spectral-element method
SF	Spread function
SNR	Signal-to-noise ratio

## List of Abbreviations

USGS	United States Geological Survey
VR	Variance reduction
$v_p$	P-wave velocity
$v_s$	S-wave velocity
$v_p/v_s$	$v_p/v_s$ ratio

# ACKNOWLEDGEMENTS

I am very grateful to my supervisors Prof. Andreas Rietbrock and Dr. Isabelle Ryder for their assistance, patience and encouragement throughout this project. I would also like to thank Stuart Nippres and Rachel Collings for useful discussions early in the project. Thanks to Dr. Xiao Wang for his invaluable IT support. I am also grateful to co-authors Christian Haberland, Mark Simons, Andrés Tassara, Matt Miller and Chao-Shing Lee for helping to improve the manuscripts. I would also like to mention the Natural Environment Research Council, who funded my PhD.

I also wish to acknowledge all field crews that took part in the development, maintenance and recovery of seismic instruments in the International Maule Aftershock Deployment. The following institutions provided seismic instruments and field crews: IRIS/PASSCAL, CNRS-INSU, GFZ and GEF/SEIS-UK. I am hugely grateful to both the Universidad de Chile and Universidad de Concepción for offering valuable support in the field. I thank the landowners of Central Chile for their cooperation during a tough period of time in the aftermath of the 2010 earthquake. I am appreciative of the National Taiwan Ocean University and UK Ocean Bottom Instrument Facility for supplying OBS instruments. Dr. Victor Ariel Gallardo, Captain Juan Vilches and Freddy Echeverria gave vital support for the offshore deployment. I am grateful to the Armada de Chile for providing vessels. I would also like to thank my field assistant in Chile, Bárbara Blanco Arrue, whose excellent English and great company were hugely valuable on the long drives. I also wish to thank Matt Miller and Klaus Bataille for giving excellent logistical help during my time in Chile.

I am indebted to my colleagues from the Earthquake Seismology research group at the University of Liverpool: Lidong Bie, Tom Garth, Amaya Fuenzalida, Christina Kelly and Hans Agurto Detzel. I would also like to thank my friends, Hal Roberts, Johnny Schofield, Sam Cooke and Tom Adams for ensuring that I was able to sufficiently switch off from PhD work now and again. I would like to thank Alice Gulliford for her unwavering support. Finally, I thank my family for their encouragement throughout my studies, even though there were some difficult times.



# PREFACE

Stephen P. Hicks graduated with a First Class Master of Earth Science Degree (MESci) in Geology and Geophysics from the University of Liverpool in 2011. In this degree, he carried out two dissertations: a geology field mapping project in South Africa and a geophysics research project on seismic anisotropy. During his undergraduate degree, Stephen undertook a three-month internship at the National Earthquake Information Center (NEIC) of the United States Geological Survey in Golden, Colorado. In October 2011, Stephen started his PhD project at the University of Liverpool, under the joint supervision of Prof. Andreas Rietbrock and Dr. Isabelle Ryder.

During his PhD, Stephen undertook fieldwork in central Chile for four weeks to decommission seismic stations and recover data from the International Maule Aftershock Deployment (IMAD). Stephen has presented work at several international conferences including the American Geophysical Union Fall Meeting (three posters and one oral presentation) and European Geosciences Union (one poster, one oral and co-convened a session). He has also presented at specialist workshops on the Maule earthquake in Chile and Germany. In September 2014, Stephen took part in a cruise to deploy ocean-bottom seismometers offshore of Washington and Oregon in the United States as part of the Cascadia Initiative project.

In addition to the papers presented as part of this thesis, Stephen first-authored an article entitled ‘Sub-slab mantle anisotropy beneath south-central Chile’ that was published in *Earth and Planetary Science Letters* in December 2012 (Enclosure 1). This work formed part of his MESci dissertation, and was written up a paper during his PhD studies.



# Chapter 1

## INTRODUCTION

Here, we establish the broad scientific background and motivation of this thesis. Once these foundations are laid, we present the main aims of the research, along with the corresponding rationale and objectives for each. Subsequently, we describe the format of the thesis and the scope of each chapter. Where appropriate, we outline the current status of manuscripts and the contribution made by co-authors.

### 1.1 Megathrust earthquakes

For earthquake seismologists, the decade commencing with the 2004 Boxing Day earthquake in Sumatra will be remembered for the sequence of large ruptures across Earth. The striking images in global media of buildings razed to the ground and massive tsunami waves have also planted earthquake hazard firmly in the minds of the public and policymakers. Several of these damaging earthquakes occurred along continental fault zones, such as the 2009  $M_w$  6.3 L'Aquila, Italy, 2010  $M_w$  7.0 Haiti, and 2015  $M_w$  7.8 Nepal earthquakes. However, the strongest earthquakes occur in subduction zones (e.g. Ruff and Kanamori, 1983); (Figure 1.1), accounting for over 95% of global seismic moment release (Pacheco and Sykes, 1992). Subduction zones occur where oceanic plates underthrust another plate (e.g. Oleskevich et al., 1999). Along the shallowest part of subduction plate boundaries (the *seismogenic zone* or *megathrust*), both plates can be locked together for hundreds of years. The accumulated strain over this time can be released within a matter of minutes during an  $M_w > 8.0$  megathrust rupture. Such megathrust earthquakes have the potential to cause

## 1.1 Megathrust earthquakes

enormous damage due to strong shaking at the surface. Even so, as shown by the 2004 Sumatra and 2011 Japan earthquakes, tsunamis can be equally, if not more, damaging. Subduction zone earthquakes caused over 300,000 deaths in the period 2004–2014 (United States Geological Survey, 2015). With these hazards, megathrust earthquakes are of enormous scientific interest.

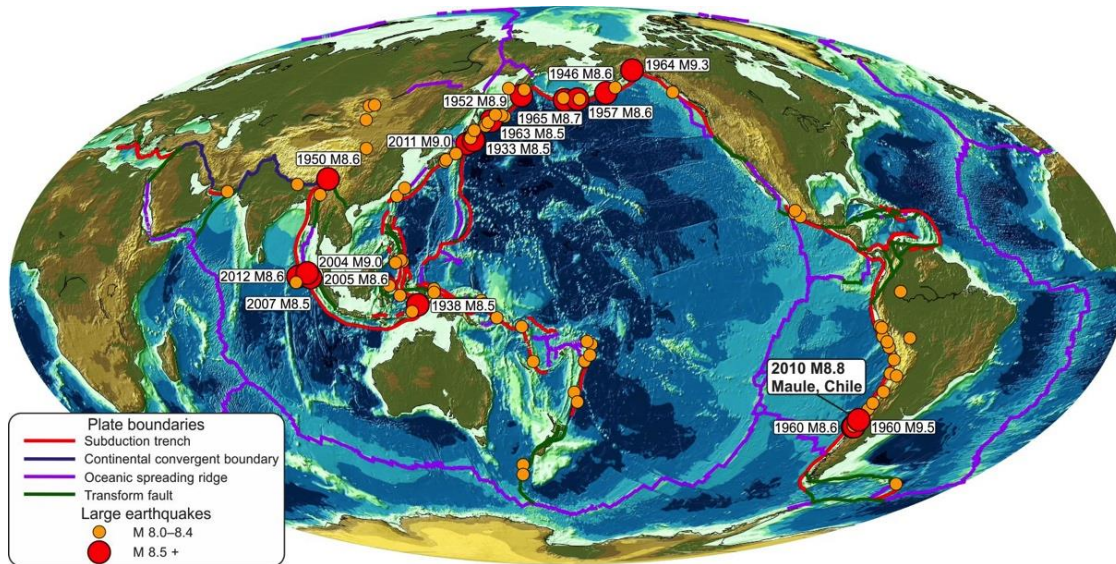


Figure 1.1: Map of the largest global earthquakes that have occurred since 1900, based on the USGS NEIC and ISC-GEM historic catalogues. The year and magnitude of  $M_w$  8.5+ earthquakes are labelled. The focus of this thesis is on the 2010  $M_w$  8.8 Maule, Chile earthquake.

Great strides have been made in rupture imaging methods, as well as observations of plate interface locking patterns before, and deformation after, large earthquakes. However, open questions still remain on the exact physical factors driving seismogenic processes throughout the earthquake cycle. Physical heterogeneity may be imaged using a wide range of seismic tools, such as passive tomography and studies of earthquake source mechanisms. A full review on the current understanding of these governing physical properties is not within the scope of this Introduction, but is discussed in Chapter Two. Yet before interpreting how different physical features may drive megathrust seismogenesis, we first need to understand how such processes are observed and parameterised across the earthquake cycle, which describes the long-term evolution of stress (or strain) along the plate interface (Figure 1.2).



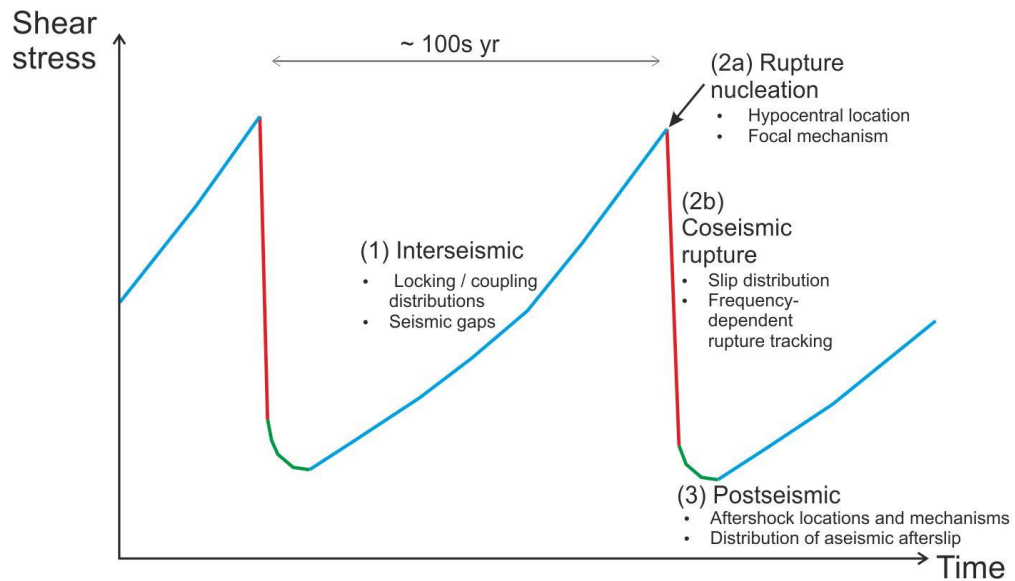


Figure 1.2: Simplified overview of the seismic cycle and the parameters that are used in this thesis to describe megathrust dynamics at each stage.

### 1.1.1 Interseismic behaviour: building up the next great earthquake

The longest phase of the seismic cycle occurs between large earthquakes and accumulating shear stress. This period is known as the *interseismic* stage (Figure 1.2). The main aim of studying interseismic deformation is to assess future hazard potential posed by large earthquakes. The *seismic gap* model, first developed by Sykes (1971), allows a basic understanding of which subduction plate boundaries are strongly locked; it is not used for probabilistic hazard assessment. A seismic gap is a region where a large earthquake occurred in the past, but has been quiet for decades; these regions are therefore considered likely sites for future large earthquakes. However, the lack of detailed knowledge on slip histories, as well as the 2004 Sumatra and 2011 Tohoku earthquakes rupturing multiple fault segments, has led to suggestions that the seismic gap model is oversimplified (Geller, 2011; Kagan and Jackson, 1995; Kagan et al., 2012; Wyss and Wiemer, 1999).

During the interseismic period, elastic strain is stored in the forearc (e.g. Wang and Hu, 2006), allowing a measureable assessment of plate coupling from observations of upper plate deformation. Datasets that are used to infer coupling distributions include GPS measurements (e.g. Moreno and Rosenau, 2010), palaeogeodetic measurements, such as corals (e.g. Simoes et al., 2004), tidal measurements (e.g. J. C.

## 1.1 Megathrust earthquakes

Savage, 1995), and satellite geodesy (e.g. Chlieh et al., 2011). Trench-parallel locking patterns are usually reliable, but locking at the up-dip end of the offshore plate interface is poorly resolved (e.g. Métois et al., 2012). To negate this problem, seafloor geodetic observations can provide better constraints on offshore coupling (Gagnon et al., 2005; Matsumoto et al., 2008).

### 1.1.2 Coseismic rupture segmentation

The conceptual subduction zone asperity model (Lay and Kanamori, 1981) was developed to describe along-strike heterogeneity in the moment release of large megathrust earthquakes. *Asperities* are regions of the plate interface that slip most strongly during a large earthquake; *barriers* inhibit ruptures. Long-lived barriers are called *segment boundaries*. Nowadays, large earthquakes are characterised by their distribution of slip on a pre-defined fault plane. Compared to interseismic locking, coseismic slip can be calculated by including more diverse datasets, such as teleseismic waveforms and tsunami data. Slip inversions assume mechanical properties of the subsurface, such as Poisson's ratio and Young's modulus. Subsurface properties can be parameterised using a range of schemes, including, homogeneous half-spaces (e.g. Tong et al., 2010), 1-D layered models (e.g. Pollitz et al., 2011), or by assigning properties to individual domains of the subduction zone (e.g. Moreno and Rosenau, 2010). The relationship between interseismic locking and coseismic slip distributions (e.g. Moreno and Rosenau, 2010; Ozawa et al., 2011; Protti et al., 2014) is often used to infer the stability of frictional properties along the plate interface.

Another source parameter often used for megathrust earthquakes is rupture duration. Slow and shallow ruptures that radiate strong long period energy (normalised to their magnitude) may be classified as tsunamigenic earthquakes (Kanamori, 1972). Rupture duration has a linear relationship with both earthquake stress drop and material rigidity of the fault (Bilek and Lay, 1999). At the high frequency end of seismic radiation spectrum, back projection methods track coherent energy on a fault plane over time (e.g. Ishii et al., 2005). Back projections of well-recorded megathrust earthquakes reveal that high frequency radiation decouples from high slip asperities inferred in coseismic slip distributions (Ishii et al., 2005; Kiser and Ishii, 2011; Koper et al., 2012; Meng et al., 2011). High frequency decoupling may result from geometrical or mechanical heterogeneities (Palo et al., 2014), although no direct

evidence has been found for physical properties exerting a control on the depth dependence of seismic radiation.

The along-strike (trench-parallel) segmentation pattern of subduction zone ruptures can be inferred from their coseismic slip distributions; less apparent is the segmentation pattern in the down-dip direction. Nevertheless, based on source characteristics of large subduction earthquakes, Lay et al. (2012) developed a unified model that describes the depth segmentation of the subducting plate interface (Figure 1.3). Domain A signifies the shallowest portion of the megathrust, from the trench to approximately 15 km depth. Although this shallow region is thought to be mostly aseismic, it can host moderately-sized tsunami ruptures ( $M_w$  6–7), such as the 1994  $M_w$  7.7 Java earthquake (Bilek and Lay, 1999). Domains B and C denote the part of the megathrust at 15–35 km depth, and 35–55 km depth, respectively; most moment release occurs in these central regions. Domain C earthquakes consistently display the depth dependence of seismic radiation discussed above. The deepest region, Domain D is characterised by slow slip, low frequency earthquakes and seismic tremor; however, these phenomena are not pervasive along all subduction zones.

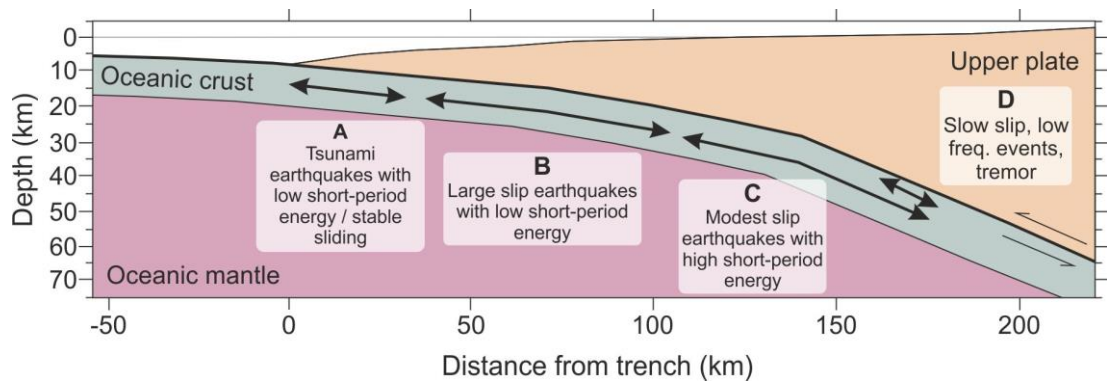


Figure 1.3: Depth segmentation of megathrust earthquake source characteristics based on Lay et al. (2012). Each domain is denoted by the letters A–D, which are discussed in the text.

Earthquake *doublets* can reveal stress transfer between faults in subduction zones. A doublet is a large earthquake following an earlier earthquake with comparable moment release, either on an adjacent patch of the fault, or on a separate fault. An example of a doublet is the interplate thrust and intraslab normal faulting events in the Kuril subduction zone in 2006 (Ammon et al., 2008). Similarly, the 2009 Samoa earthquake constituted a normal faulting event beneath the outer rise that triggered

## 1.2 The 2010 $M_w$ 8.8 Maule, Chile earthquake

thrusting on the plate interface (Lay et al., 2010b). In this instance, the initial rupture triggered seismic slip on the shallow portion of the plate interface.

### 1.1.3 Postseismic relaxation: aftershocks and afterslip

To complete the seismic cycle, large megathrust earthquakes cause intense deformation in the near field that can last for months to years (Figure 1.2). Postseismic processes are largely time dependent and decay in a similar way to rheological laws based on physical properties of the crust or mantle (Lange et al., 2014). Like coseismic slip models, aftershock distributions can reveal the seismogenic character of the megathrust, but can also reveal other active faults that lie near to the plate interface. One of the strongest postseismic deformation processes in the near field is *afterslip*, which occurs due to the frictional response of the fault plane following a large rupture (e.g. Marone, 1998). Geodetic observations can be used to determine the spatial pattern of afterslip (Bedford et al., 2013; Y. N. Lin et al., 2013; Ozawa et al., 2011). The amplitude of afterslip ranges from tens of centimetres to several metres, dependent on size of the mainshock, time, and assumptions made (Y. N. Lin et al., 2013). Strong afterslip complements coseismic slip asperities (Ozawa et al., 2011; Perfettini et al., 2010). Furthermore, spatial and temporal correlations between aftershocks and afterslip suggest that the former may be triggered by fluid-driven afterslip (Hsu et al., 2006).

## 1.2 The 2010 $M_w$ 8.8 Maule, Chile earthquake

If we can identify the physical factors that drive megathrust fault processes at different stages of the seismic cycle, we may be able to forecast future rupture potential in subduction zones. To do this, we need to gain an understanding of the relationship between physical properties and rupture behaviour for past large earthquakes, which have been recorded in great detail. A region with a large history of megathrust earthquakes is the Chile subduction zone: one of the most seismically active and strongly coupled plate boundaries on Earth (Figure 1.1). On average, a major earthquake with  $M_w > 8$  occurs every ten years in Chile (Ruegg et al., 2009). In particular, understanding seismic hazard in central Chile is vital because nearly 80% of the country's population reside here (Beck et al., 1998). Due to the excellent record of historical large earthquakes, the region is an ideal natural laboratory to study the

megathrust seismic cycle. One such event was the 1960  $M_w$  9.5 Valdivia earthquake - the largest earthquake ever recorded (e.g. Cifuentes, 1989). However, to the north of the Valdivia rupture, the Maule region had not experienced a large seismic event since the  $M$  8.5 Concepción earthquake in 1835, which was recorded by Charles Darwin during his voyage on the HMS Beagle (Darwin, 1851). This long pause led workers to identify this region as a mature seismic gap (Barrientos, 1987; Beck et al., 1998; Campos et al., 2002; Ruegg et al., 2009). These early studies led to an explosion of geophysical deployments during the 2000s, which focussed on background seismicity (e.g. Campos et al., 2002; Haberland et al., 2006), subsurface structure (e.g. Haberland et al., 2009), plate interface coupling (Ruegg et al., 2009) and morphotectonic segmentation of the margin (Melnick et al., 2009). On February 27, 2010, this segment of the subduction fault finally broke during an  $M_w$  8.8 rupture: the sixth largest earthquake ever recorded (Figure 1.1).

Initial hypocentre locations suggested that the Maule rupture nucleated within the highly-locked region offshore of the coastline between Concepción and Constitución. There is some disagreement between the hypocentre locations of reporting agencies (Table 1.1, Figure 1.4). Using high rate GPS observations, Vigny et al. (2011) relocated the low frequency nucleation point 40 km to the south-west of the of the USGS estimate, which is closer to the CSN (Centro Sismológico Nacional, Chile) estimate. Using regional seismic recordings, Hayes et al. (2013) relocated the hypocentre to 20 km north-east of the Vigny et al. (2011) estimate. Based on rupture models (e.g. Lay et al., 2010a; Y. N. Lin et al., 2013; Moreno et al., 2012; Tong et al., 2010) and aftershock distributions (Lange et al., 2012; Rietbrock et al., 2012), the earthquake went on to rupture a 500 km portion of the subduction zone. These slip models show a bilateral distribution with maximum slip of 15–27 m occurring ~120 km to the north of the hypocentre (Figure 1.4) in a region that was strongly locked before the earthquake (Moreno and Rosenau, 2010). Furthermore, there is no evidence of extensive rupture to the trench and the strongest slip was limited to the coastline. Like other well-recorded large megathrust earthquakes, the Maule rupture has a similar depth-dependence of high frequency radiation (Kiser and Ishii, 2013; Palo et al., 2014; Wang and Mori, 2011), but with an even more distinctive depth segmentation pattern across the rupture zone (Figure 1.4). From the distribution of aftershocks and afterslip, there is also a clear gap in postseismic deformation inland of the coastline (Figure 1.4).

## 1.2 The 2010 Mw 8.8 Maule, Chile earthquake

For 14 months following the Maule earthquake, GPS observations recorded around 1.2 m of cumulative afterslip, which was mainly located beneath the coastline (Bedford et al., 2013; Y. N. Lin et al., 2013). Afterslip and aftershocks have a rather patchy distribution, particularly inland of the coastline (Figure 1.4).

Reporting agency / published study		Latitude	Longitude	Depth (km)
Preliminary hypocentres	USGS NEIC	35.91°S	72.73°W	35
	Servicio Sismológico Nacional (CSN)	36.29°S	73.24°W	30
	GFZ-GEOFON	36.05°S	72.75°W	24
Relocated hypocentre	Vigny et al. (2011)	36.41°S	73.18°W	-
	Hayes et al. (2013)	36.22°S	73.11°W	35

Table 1.1: Hypocentre estimates of the Maule earthquake.

In the aftermath of the Maule earthquake, the forearc was densely instrumented with on- and offshore geophysical instruments (e.g. Beck et al., 2014; Rietbrock et al., 2012) to monitor aftershock activity. Combined together, these observations offer a unique view of megathrust behaviour at different stages of the earthquake cycle. In this thesis, we focus on using seismic observations of aftershocks to understand the detailed structure of the subsurface and seismic sources.



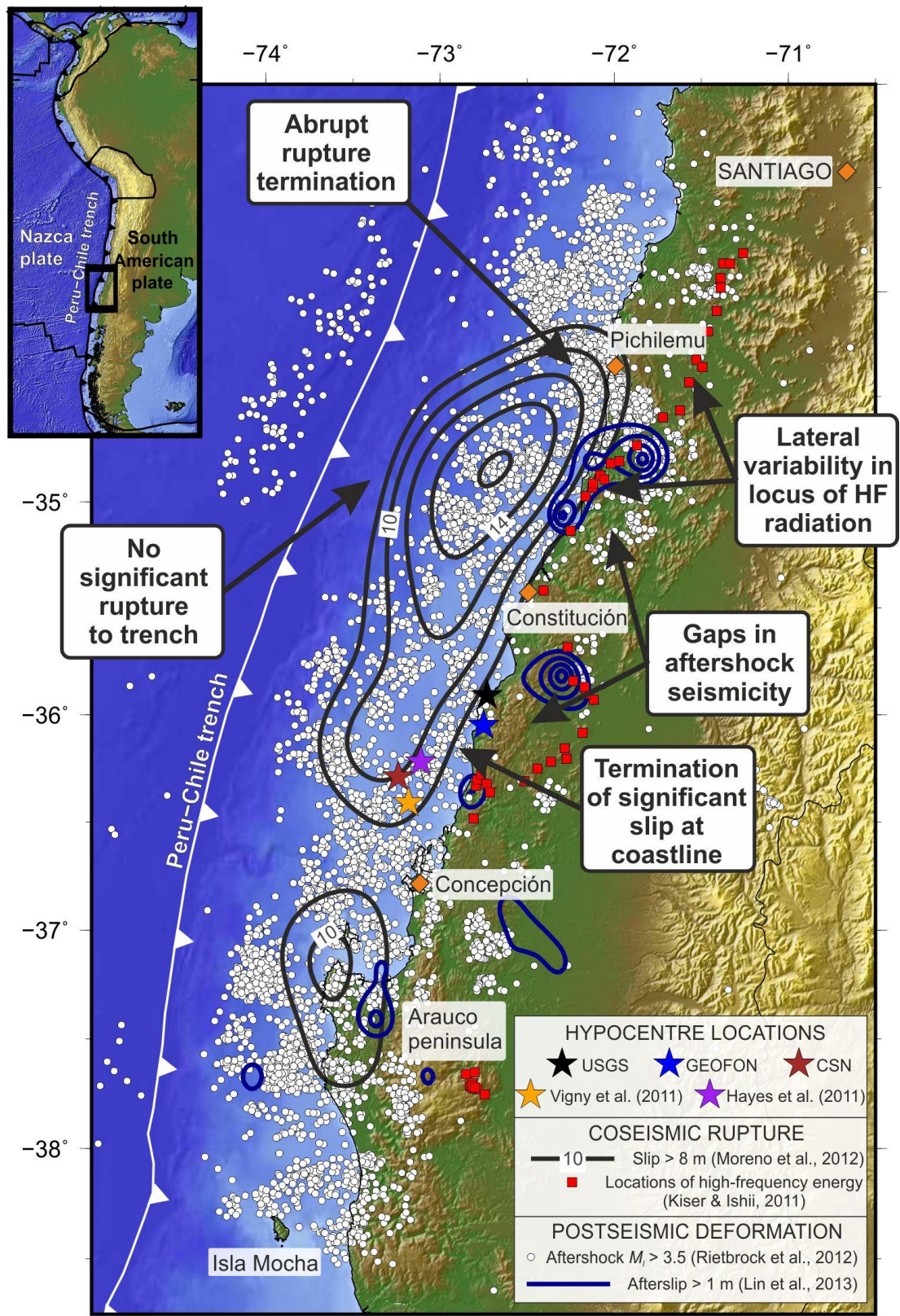


Figure 1.4: Location of the Maule earthquake showing the characteristics of the coseismic rupture and postseismic stage. HF = high frequency. Inset: the location of the large map is given by the black box.

### 1.3 Aims and objectives of this thesis

The overarching aim of this thesis is to try to identify relationships between physical heterogeneity and plate interface rupture characteristics by studying the rupture zone of the 2010 Maule, Chile earthquake. Our first aim is to identify physical heterogeneity and to relate this with recorded behaviour at different stages of the seismic cycle. We then turn our attention to the degree of slip complexity along the megathrust and how ruptures respond to structural heterogeneity in the overriding plate. Our fundamental motivation is to try to forecast future rupture characteristics along other subduction plate boundaries that are strongly coupled, yet have not experienced a large earthquake ( $M_w$  8.5+) for centuries, such as in northern Chile and Cascadia. Here, we describe the underlying scientific rational of these aims and the strategy used in this thesis to investigate them.

#### 1.3.1 Key Aim 1: Identification of physical heterogeneity

Improvements in GPS instrumentation and satellite imaging have been able to shed new light on the complex behaviour of subduction plate boundaries across the earthquake cycle, such as the distribution of asperities and barriers. However, the physical sources of asperities and barriers are disputed. It had long been proposed that subducted features on the oceanic plate play a key role in megathrust seismogenesis (e.g. Kodaira et al., 2000). The role of the upper plate, such as crustal faults (e.g. Audin et al., 2008) and forearc basins (e.g. Song and Simons, 2003), have also been proposed to exert control on megathrust behaviour. As well as the along-strike distribution of asperities and barriers of megathrust ruptures, the descriptive megathrust depth segmentation model of Lay et al. (2012) lacks understanding on the structural and compositional properties associated with each domain. The Maule earthquake provides an unprecedented opportunity to answer these fundamental scientific questions by allowing an assessment of megathrust behaviour before, during and after a large earthquake.

Each large megathrust earthquake has unique characteristics and the Maule earthquake is no exception (Figure 1.4). The complexities of this rupture raise several important questions that may advance our understanding of subduction zone earthquakes worldwide:



1. What influences the localisation of high plate interface coupling and associated large slip at depths of 15–35 km along the subduction interface?
2. What prevented the Maule earthquake from rupturing the megathrust close to the trench?
3. Similarly, is the down-dip limit of the rupture beneath the coastline signified by a change in megathrust physical properties?
4. Can we infer any changes in frictional properties along the plate interface that led to the distinctive pattern of high frequency radiation during the rupture and the ensuing gap in onshore aftershock seismicity?
5. Is the abrupt northward limit of the rupture and coincident intense upper plate faulting activity related to structural heterogeneity in the upper plate?

To answer these questions, we focus our attention on using the aftershock sequence that was recorded by a multinational temporary seismic network. The aftershock dataset is used to generate a local earthquake tomography (LET) model in order to image the 3-D velocity structure within the rupture zone. We make detailed interpretations of our seismic velocity models about petrological properties, such as bulk mineralogical compositions and fluid content. We compare these subsurface assessments with the seismogenic character of the region to assess whether any formal correlations exist between seismic properties and seismic cycle processes.

Although LET is an established method in seismology, one inherent obstacle with imaging a subduction megathrust is that most seismic sources are located offshore (Figure 1.4); yet seismic stations are typically sited on land. LET studies of shallow subduction zone structure using onshore data alone (e.g. Collings et al., 2012; Husen et al., 2003) have limited offshore imaging capability, so physical properties of the shallowest region of the plate interface are effectively hidden. This is an issue as we need to be able to understand the physical structure of the plate interface where most seismic moment release occurs and where tsunamigenic earthquakes (e.g. Bilek and Lay, 2002) typically rupture. Combined onshore and offshore datasets have been used in a handful of LET experiments (e.g. DeShon et al., 2006; Haberland et al., 2009; Husen et al., 2000). However, in these studies, a relatively small number of ocean-bottom seismometer (OBS) stations were used and few earthquakes were recorded along the shallowest portion of the plate interface, limiting imaging resolution close to

### 1.3 Aims and objectives of this thesis

the trench. Furthermore, using combined on- and offshore datasets remains a challenge due to problems in obtaining reliable earthquake locations due to local site variations (station elevations, local geology), as well as the strong trench-normal velocity heterogeneity that is to be expected in a subduction zone. To image the shallowest part of the megathrust in the Maule rupture zone, we incorporate OBS observations and develop a strategy to include these data in our LET inversion scheme.

#### 1.3.2 Key Aim 2: Assessing earthquake slip complexity and its response to structural heterogeneity

Large earthquakes involve complex redistribution of stresses to other parts of the ruptured fault and to adjacent structures (e.g. Toda et al., 2005). Consequently, seismic slip may be triggered across a wide range of distances (local, regional and global) and timescales (from seconds to years) due to static and dynamic stress transfer (e.g. Freed, 2004). Stress changes are responsible for a range of earthquake phenomena, such as foreshocks, aftershocks and doublets. Therefore, understanding the spatial and temporal evolution of stress has important implications for seismic and tsunami hazard in subduction zones. Large earthquake doublets are of enormous scientific interest due to their similar size and ability to reveal triggering mechanisms between different structures in a subduction zone (e.g. Ammon et al., 2008; Lay et al., 2010b). These prior studies of earthquake doublets have focussed on the larger ( $M_w > 7.5$ ) subduction earthquakes where two sub-events are significantly separated in distance ( $> 50$  km) and in time ( $> 30$  s). However, questions still remain over the triggering mechanism involved. How does slip on the plate interface interact with faults in the upper plate on short timescales? Can we differentiate between static and dynamic triggering of doublets?

Slip inversions yield the distribution of fault slip during a large earthquake (e.g. Moreno and Rosenau, 2010; Ozawa et al., 2011; Protti et al., 2014); such schemes tend to invert for slip on a single pre-defined fault plane. Therefore, in the case of doublets on separate faults, slip inversions may be unable to constrain the mechanism, timing and location of sub-events. A better approach is to carry out moment tensor inversion of multiple point-sources, which has been applied to teleseismic waveform in past studies of subduction doublets (e.g. Ammon et al., 2008; Lay et al., 2010b). There are uncertainties over the resolving ability of such methods. Can highly complex rupture

mechanisms be masked in teleseismic moment tensors? If so, are local seismic observations needed to resolve earthquake rupture complexity at small spatial and temporal scales? Furthermore, moment tensor inversion schemes of local and regional waveforms typically assume a 1-D velocity model. However, since a subduction zone likely comprises significant subsurface heterogeneity in the trench-normal direction, does this bias moment tensor retrieval?

In order to answer these questions relating to imaging rupture complexity and triggering mechanisms, we study the largest plate interface aftershock of the Maule sequence using multiple point-source inversion of local waveform data. We interpret source complexity with respect to structural variability that can be inferred from our obtained LET model. We exploit advances in the computation of synthetic waveforms through highly heterogeneous media to assess possible biases in source parameters (e.g. Komatitsch et al., 2004).

## 1.4 Thesis organisation and publication status of chapters

We now briefly outline the layout of this thesis, which comprises a total of nine chapters, three of which are research papers reformatted for this thesis. Therefore, where appropriate, we describe the current publication status of each chapter and the contributions made by co-authors. The formatted versions of the published papers are enclosed with this thesis.

We begin by summarising current knowledge on megathrust physical heterogeneity. We review studies of subduction zone structure and past megathrust earthquakes to describe the range of physical structures that may affect seismogenic processes along the megathrust. Beyond Chapter Two, the thesis is divided into two main parts to reflect the multiple phases of study and key aims defined in the previous section. The first of these is passive seismic imaging of the subduction zone using ray-based methods; the second focuses on probing earthquake source complexity using full-waveform approaches. These topics each begin with a chapter (Chapters Three and Six) that outlines the background theory and past application of the two methods, with a particular focus on subduction zones.

## 1.4 Thesis organisation and publication status of chapters

In Chapter Four, we describe and interpret a preliminary seismic velocity model for central Chile based on a dataset of automatically determined seismic wave onset times. One of the key observations made in this chapter is the presence of a large, high seismic velocity anomaly lying beneath the coastline in the centre of the rupture area. We interpret this structural anomaly as to its control on the nucleation and rupture process of the Maule earthquake. This chapter was accepted for publication in *Geophysical Research Letters* on 14 September 2012 and published on 16 October 2012. Full citation: *Stephen P. Hicks, Andreas Rietbrock, Christian Haberland, Isabelle M.A. Ryder, Mark Simons, and Andrés Tassara, The 2010  $M_w$  8.8 Maule, Chile earthquake: Nucleation and rupture propagation controlled by a subducted topographic high, Geophysical Research Letters 39, L19308, doi: 10.1029/2012GL053184.* Andreas Rietbrock gathered the preliminary dataset of P- and S-wave onset times and gave comments on the interpretation and discussion. Christian Haberland assisted with the analysis of the full model resolution matrix. Isabelle Ryder assisted with the comparison between seismic velocity structure and geodetic models of the Maule rupture. Mark Simons assisted with the interpretation. Andrés Tassara provided the raw Bouguer gravity model.

Based on main features of the preliminary tomographic images presented in Chapter Four, we describe an updated seismic velocity model in Chapter Five. This model is based on a higher quality seismic travel time dataset and incorporates offshore data. Compared to that of the previous chapter, our new velocity model has sharper images that allow for detailed probing of the shallow plate interface. This improvement allows for a more in-depth interpretation of absolute seismic velocities. We make direct comparisons between physical properties and megathrust behaviour at different stages of the seismic cycle. This chapter was accepted for publication in *Earth and Planetary Science Letters* on 26 August 2014 and published on 1 November 2014. Full citation: *Stephen P. Hicks, Andreas Rietbrock, Isabelle M.A. Ryder, Chao-Shing Lee, Matthew Miller, Anatomy of a megathrust: The 2010  $M_{8.8}$  Maule, Chile earthquake rupture zone imaged using seismic tomography, Earth and Planetary Science Letters, Volume 405, 1 November 2014, Pages 142-155, ISSN 0012-821X, doi: 10.1016/j.epsl.2014.08.028.* Andreas Rietbrock helped to prepare the seismic data, assisted with the tomographic inversion process and added useful comments to the interpretation. Isabelle Ryder was involved in the seismic deployment and helped to

refine the comparison between coseismic and afterslip models with seismic velocities. Chao-Shing Lee and Matthew Miller worked on the OBS deployments and assisted with the analysis of this offshore dataset.

In Chapter Seven, we apply a multiple point-source moment tensor inversion scheme to the  $M_w$  7.1 Araucania aftershock in order to explore megathrust rupture complexity and earthquake triggering mechanisms. By interpreting our results in the context of seismic velocity structure identified in the earlier chapters, we demonstrate how slip on the plate interface instantaneously triggered fault rupture in the overriding plate. This chapter was accepted for publication in *Nature Geoscience* on 13 October 2015. Citation: *Stephen P. Hicks and Andreas Rietbrock: Seismic slip on an upper plate normal fault during a large subduction megathrust rupture, Nature Geoscience, November 2015, doi: 10.1038/ngeo2585*. Andreas Rietbrock ran the 3-D full-waveform simulation on the high performance computing cluster and helped to interpret the results.

In Chapter Eight, we synthesise interpretations made in the preceding chapters to discuss the physical factors that influenced the Maule rupture and their relationship with tectonic structure along the South American subduction margin. We speculate what our findings may mean for future earthquake hazard in central Chile. We also compare our results from the Maule earthquake with similar studies from the 2011 Tohoku earthquake rupture zone. This comparison sheds light on some of the key controls on rupture size and slip localisation of large subduction earthquakes. We also demonstrate the effect of 3-D structural heterogeneity on seismic wave propagation by presenting some preliminary results from spectral element waveform simulations of moderately sized aftershocks of the Maule sequence.

Finally, in Chapter Nine, we present the main conclusions of the project, answering the research questions posed in this introduction and highlighting the significant contributions made toward understanding subduction megathrust earthquakes. We also provide recommendations for future work in this field of research.



## Chapter 2

# UPPER PLATE VERSUS LOWER PLATE: PHYSICAL CONTROLS ON MEGATHRUST EARTHQUAKE RUPTURE PROCESSES

Earth's largest earthquakes occur in subduction zones, where two plates collide and one sinks beneath the other. With 43,000 km of subduction plate boundaries (Wang, 2010), understanding the pattern of ruptures along these faults is vital for seismic and tsunami hazard assessment. However, we lack knowledge on the full history of fault locking and past slip in many subduction zones. In order to constrain future earthquake characteristics, a long-term aim in subduction zone research is to comprehend the physical controls of large earthquakes. There are critical questions that need to be answered on stress distribution and resulting strain accumulation in subduction zones. What influences the spatial pattern of coupling and eventual slip along the plate interface? Does the upper plate or subducting plate play a greater role in controlling earthquake processes? What controls the potential for shallow, tsunamigenic earthquakes?

The surge of large subduction earthquakes in the past decade, and the breadth of seismic and geodetic data have that detailed these ruptures (e.g. Lay, 2015) allow us to begin to answer these crucial questions. Therefore, a review of this subject is timely. Earlier attempts have been made to unravel the properties of the subducting plate interface and to assess the influence on large earthquake ruptures (Hyndman et

## 2.1 Structural domains above and below the megathrust

al., 1997; Ruff and Tichelaar, 1996). Kopp (2013) provides a global summary of subduction margin structural domains and their control of subduction zone earthquakes, with particular focus on the western Pacific. However, these papers do not include numerous findings from the 2010  $M_w$  8.8 Maule, Chile and 2011  $M_w$  9.0 Tohoku, Japan earthquakes. Furthermore, Kopp (2013) gives little attention to rheology and density variations in the upper plate. Wang and Bilek (2014) focussed on the role of subducted topographic relief in seismogenic processes. As described in the previous chapter, Lay et al. (2012) describe the depth distribution of rupture properties, but inferring connections with physical properties was not within the scope of this paper.

A gap still remains in integrating earthquake observations with images of physical properties to assess governing factors of the seismic cycle. Moreover, laboratory and numerical experiments are needed to directly link physical properties with fault behaviour. Here, we strictly focus on the shallowest and most strongly coupled part of the subduction zone that extends from the trench to around 50 km depth: the subduction *megathrust* (e.g. Lay et al., 2012). We begin by introducing the typical structural features along and around the plate interface, and how the characteristics of these vary between subduction zones. We then assess the role played by each of these domains at the different stages of the seismic cycle (which was outlined in Section 1.1).

## 2.1 Structural domains above and below the megathrust

We describe the main structural features that directly interact with the subducting plate interface (Figure 2.1). We start with domains of the upper plate, and gradually move from the trench through to the central forearc. The nature of the megathrust contact itself, as well as the composition and structural styles of the subducting plate, are considered. Although every subduction zone has unique physical characteristics, one unified classification divides regions of subduction into *accretionary* and *erosive* sedimentation styles (Cloos and Shreve, 1988; von Huene and Scholl, 1991; Scholl et al., 1980); (Figure 2.2).



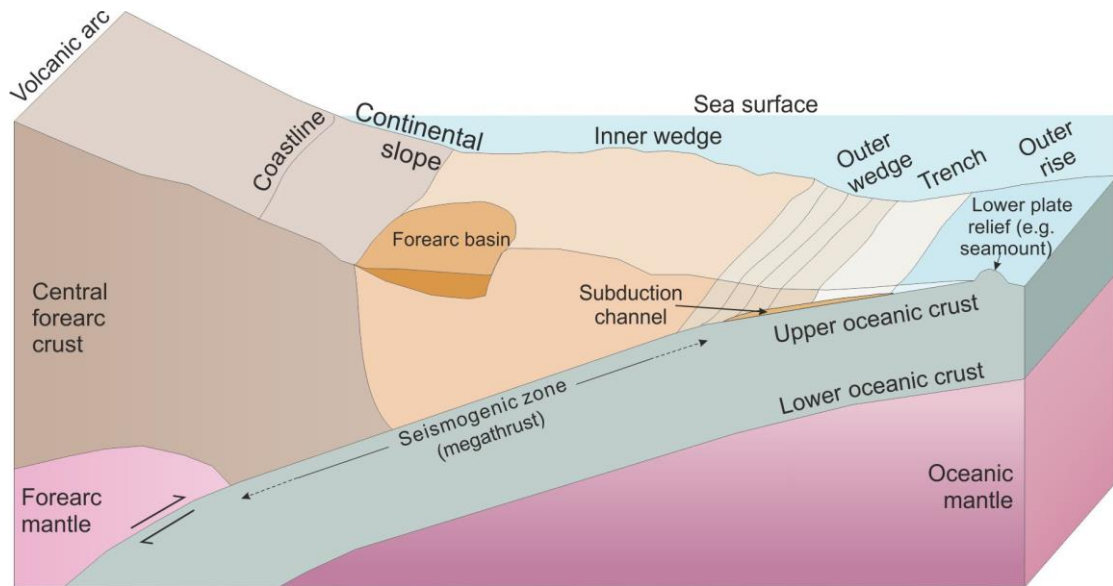


Figure 2.1: Schematic view of domains that constitute the shallow part of a typical subduction zone. Labelled features are referred to in the text. Redrawn and simplified after Kopp (2013).

Accretionary margins are dominated by growth of the prism by offscraping trench sediment and subsequently underplating this material at the base of the overriding plate (Figure 2.3). Conversely, erosive margins are characterised by the rasping or stoping of rock from the base of the upper plate, which is dragged to greater depths by the subducting plate (Cloos and Shreve, 1988). In fact, erosive margins constitute around 57% of all global subduction zones (von Huene and Scholl, 1991); (Figure 2.2). Whether a margin is accretionary or erosive depends on numerous factors, but sediment supply is likely an important factor. Subduction accretion is more likely to occur in regions of high sediment supply; erosion dominates where there is low sediment input (Cloos and Shreve, 1988) and fast plate convergence (Clift and Vannucchi, 2004). Although this classification scheme cannot accurately represent the fine-scale characteristics of all subduction zones (Kopp, 2013) it provides a framework to describe the variability in the main structural features between subduction zones (Figure 2.3).

## 2.1 Structural domains above and below the megathrust

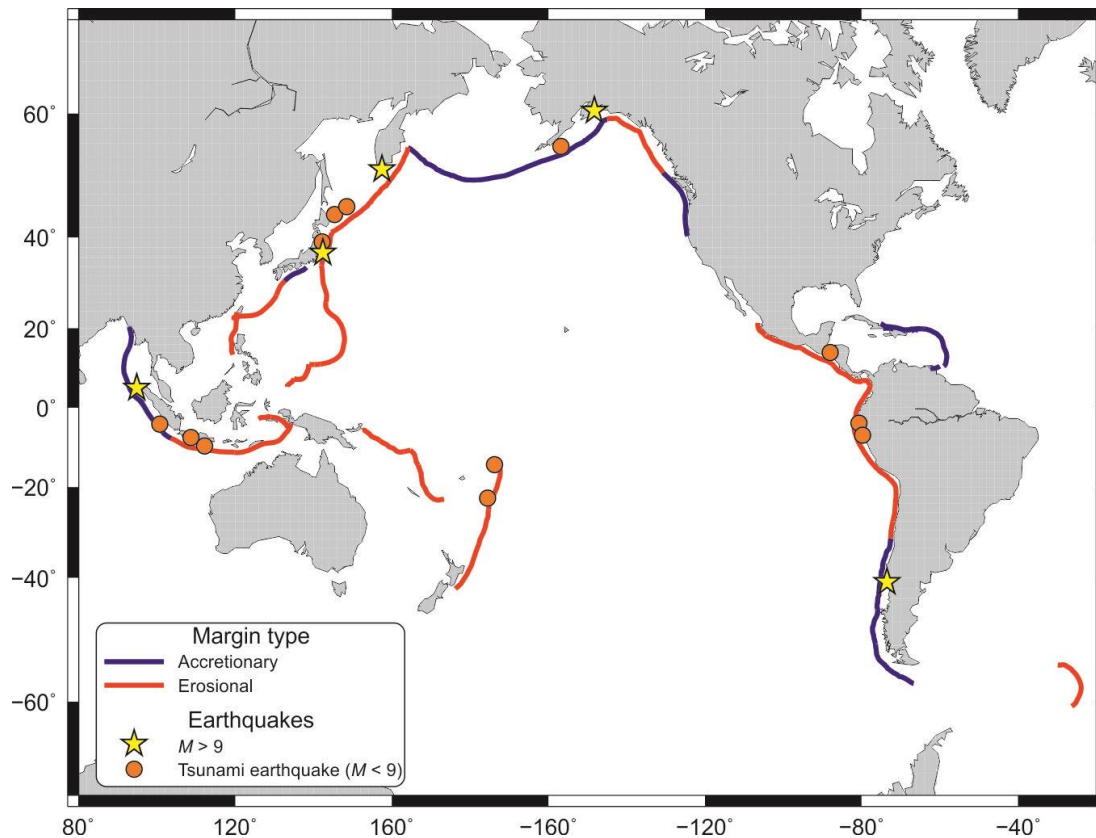


Figure 2.2: Distribution of circum-Pacific erosional and accretionary margins based on Clift and Vannucchi (2004) and Kopp (2006) compared with earthquake characteristics. Large earthquake locations are based on Bilek (2010), but with an updated catalogue. Tsunami earthquake locations are from El Hariri et al. (2013).

### 2.1.1 Marine forearc

Internal divisions of the marine forearc are typically based on slope breaks along the seafloor (Kimura et al., 2007; Wang and Hu, 2006). The most seaward domain of the upper plate is denoted by its wedge-shaped geometry that thins toward the trench (e.g. Davis et al., 1983). The *outer wedge* (frontal prism) lies adjacent to the deformation front (trench) and is up to 30–80 km wide (e.g. Contreras Reyes et al., 2008; von Huene et al., 2009); the *inner wedge* is situated further landward. Most knowledge on the structure of the forearc wedge comes from active-source seismic reflection and refraction studies (e.g. von Huene et al. 2009). These images show that the geometry and physical characteristics of the outer and inner wedges greatly depend on whether the margin is accretionary or erosive.

In accretionary margins, the outer wedge is often called the *frontal accretionary prism* (FAP), which consists of deformed sediments that accumulate at the leading edge of the overriding plate (Cloos and Shreve, 1988); (Figure 2.3). The landward inner wedge is composed of older accreted sediments and framework rocks of the central forearc. This domain is commonly defined as the *palaeo-accretionary complex* (PAC); (Contreras Reyes et al., 2008; Moscoso et al., 2011). Forearc basins overlying the outer wedge are typically bounded by backthrust faults (Singh et al., 2010). The boundary between the outer and inner wedge, where accreted sediments terminate against more consolidated sediments or the crystalline leading edge of the overriding plate, is known as the *backstop* (Cloos and Shreve, 1988); (Figure 2.3).

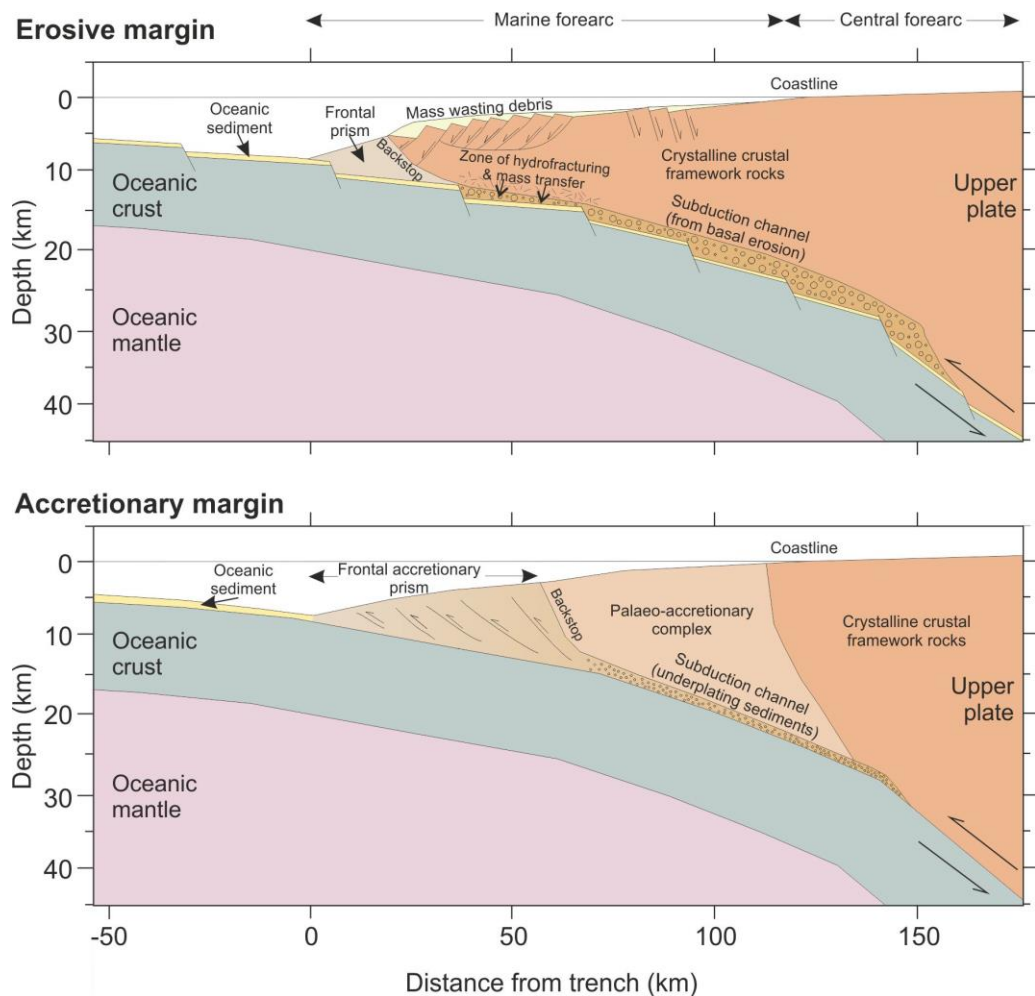


Figure 2.3: Illustration of the main structural variations between erosive and accretionary margins, based on Clift and Vannucchi (2004), von Huene and Ranero (2003), and von Huene et al. (2004; 2009).

## 2.1 Structural domains above and below the megathrust

In contrast, for erosive margins, the most seaward part of the outer wedge includes a small *frontal prism* (e.g. Wang and Hu, 2006), which consists of mass transport deposits and a small proportion of accreted sediments. The outer and inner wedges are composed of crystalline rocks belonging to the forearc crust framework that are altered and fractured (von Huene et al., 2004). This sharp compositional boundary backstop means that erosive margins typically exhibit a steeper break in slope above the outer wedge.

Active-source reflection profiles have illuminated a wide range of faulting styles within the marine forearc. Typically, in accretionary margins, the outer wedge grows and thickens along imbricate, landward-dipping thrust faults that merge at depth toward the low angle plate interface (Figure 2.3). These imbricate faults are ubiquitous features in seismic images from accretionary margins (e.g. Kopp, 2013; Wang and Hu, 2006). Large, out-of-sequence, landward-dipping thrust faults cutting through the marine forearc are known as *megasplay* faults (Strasser et al., 2009). Evidence for megasplays mainly comes from accretionary margins (Saffer and Tobin, 2011), such as Nankai (Park et al., 2002) and central Chile (Lieser et al., 2014), but also exist in erosional margins, such as Ecuador (Collot et al., 2008). Another type of reverse fault is a *backthrust*, which, in contrast to an imbricate and splay fault, has an opposite vergence to the main wedge (i.e. trenchward dipping). There is evidence of major backthrusting in the inner wedge (Chauhan et al., 2009;; Singh et al., 2010; 2011b) as well as smaller-scale backthrusts in the outer wedge (Dean et al., 2010; Henstock et al., 2006) of the Sumatran margin. Melnick et al. (2012) infer a splay fault in the south-central Chile subduction zone, although this fault is trenchward-dipping; therefore, we define this fault as a backthrust. In the Cascadia subduction zone, a series of deeply-penetrating strike-slip faults are related to oblique convergence of the subducting Juan de Fuca plate (Goldfinger et al., 1997; McCaffrey and Goldfinger, 1995).

To complete the spectrum of faulting types, studies have imaged normal faults, particularly in erosive margins (Figure 2.3). Landward-dipping normal faults are caused by sediment underplating (Okamura et al., 2008; Ranero and von Huene, 2000; Tsuji et al., 2011) and material transfer between the upper and lower plates. These normal faults are more likely to form if the wedge is extensionally critical, due to a low basal friction coefficient and an overpressured plate interface (Wang and Hu,

2006). Similarly, seaward-dipping normal faults in the inner wedge of the northern Chile margin are associated with gravitational collapse of the forearc (Contreras Reyes et al., 2014; von Huene and Ranero, 2003). However, the depth extent of upper plate faults and the nature of their contact with the plate interface are poorly resolved.

The mechanics of accretionary wedges have been investigated using two main dynamic models: the Coulomb wedge theory (Dahlen et al., 1984; Davis et al., 1983) and its modified dynamic version (Wang and Hu, 2006). For the internal composition of the marine forearc, these analyses predict that accretionary wedges and their basal décollement should have near-lithostatic pore pressures to explain slip on the underlying megathrust and the tapered geometry of the wedge (Davis et al., 1983). However, these fluid pressures likely vary throughout the seismic cycle (Wang and Hu, 2006). Overpressure conditions are inferred from strong negative-polarity seismic reflections along faults within the wedge (e.g. Bangs et al., 2009), and low P-wave velocity ( $v_p$ ) in refraction tomography images (Contreras Reyes et al., 2008; Sallarès, 2005). Nevertheless, inferring pore pressure values in the lower forearc is difficult from active source seismic profiles due to the lack of constraints on S-wave velocity ( $v_s$ ), and hence Poisson's ratio.

### 2.1.2 Central forearc crust

Moving onshore, the rock framework of the upper plate consists of igneous or metamorphic basement and lithified sedimentary rocks. Compared to the marine forearc, the central forearc is stronger and less intensely deformed (von Huene et al., 2009). The composition of the upper crust may be inferred from outcrop exposures along coastlines and coastal hill ranges; though, it is uncertain of how representative this geology is of lower crustal properties. Furthermore, active source seismic methods have limited resolution at these depths ( $> 30$  km), highlighting the value of passive geophysical methods, such as passive seismic tomography and gravity inversion.

Compositional heterogeneity of the upper plate may result from the ancient geological evolution of the forearc. For example, the upper plate in the Hikurangi subduction zone of New Zealand contains several terranes, each of which comprise metamorphosed accretionary wedges (e.g. Eberhart-Phillips and Reyners, 2012). Similarly, the lower crust in the Cascadia subduction zone is highly heterogeneous and

## 2.1 Structural domains above and below the megathrust

comprises terranes composed of metasedimentary and volcanic rocks (Ramachandran et al., 2006). Along the Chile subduction margin, the upper continental forearc is divided into several distinct trench-parallel morphotectonic units including the Coastal Cordillera, which represents the remnants of a magmatic arc formed in Jurassic-Cretaceous times, and the longitudinal valley (e.g. Husen et al., 2000).

Crustal-scale faults can also cut through the central crust (Figure 2.3), though these are more delineated and mature than faults in the offshore part of the upper plate. In many subduction zones, the central forearc comprises strike-slip faults that accommodate oblique plate convergence, the best example of which is the 1500 km Sumatra fault (Sieh and Natawidjaja, 2000) in Indonesia. Other examples include the North Island dextral belt in the Hikurangi subduction zone (Wallace, 2004) and the Lanalhue fault in south-central Chile (e.g. Glodny et al., 2008).

### 2.1.3 Forearc mantle wedge

Arcward of the coastline and beneath the central forearc crust at around 35–40 km depth, the mantle wedge is a ubiquitous feature in many subduction zones. The continental Moho delineates the boundary between the mantle wedge and central forearc crust. However, there is some variability in the depth of this intersection between different subduction zones, and the estimates depend on how it is imaged (Table 2.1).

Seismic images suggest that the mantle wedge is composed of peridotite that is serpentinised by approximately 20%. This alteration results from fluids generated by dehydration reactions in the downgoing crust and in subducted sediments (Hyndman and Peacock, 2003). The degree of serpentinisation depends on available fluid budget (Bostock, 2013). Compared to unaltered mantle, the reduced seismic velocities of serpentinised peridotite result in reduced velocity contrast across the continental Moho. The gradational nature of this boundary is one explanation for the lack of consistency in measurements of the intersection depth between the continental Moho and plate interface in individual subduction zones (Table 2.1). High degrees of mantle serpentinisation (up to 50–60%) exist in the subduction zones of Cascadia (Bostock et al., 2002), Costa Rica (DeShon and Schwartz, 2004) and northern Chile (Graeber and Asch, 1999).

<b>Subduction zone</b>	<b>Continental Moho – plate interface intersection depth</b>	<b>Method</b>	<b>Reference</b>
Cascadia	35 km	ST	Bostock et al. (2002) Fuis (1998)
Chile	50 km	RF	Yuan et al. (2000)
(north)	40–50 km	RR	Wigger et al. (1994)
Chile	32 km	RF	Dzierma et al. (2012b)
(south)	50 km	LET	Haberland et al. (2009)
Costa Rica	36 km	RF	DeShon and Schwartz (2004)
Hikurangi	40 km	RE	Stern and Davey (1990)
Japan	27–29 km	RE	Nakajima et al. (2002)
(north-east)			
Nankai	30 km	RF	Ueno et al. (2008)
Sumatra	20 km	RE	Klingelhoefer et al. (2010)

Table 2.1: Estimates of the intersection depth between the continental Moho and plate interface for different subduction zones. ST = scattering tomography; RF = receiver functions; LET = local earthquake tomography; RE = reflected phases; RR = refraction seismology.

#### 2.1.4 Subducting oceanic crust

Due to its depth in the subduction zone, most knowledge on the structure and composition of the lower plate comes from studies of the crust before it enters the subduction zone, such as ocean drilling and seismic refraction experiments. Classic studies of ophiolite sequences show that oceanic crust is composed of two main layers: pillow basalts and sheeted dykes in the upper crust, and gabbro in the lower crust. These distinct layers do not undergo major metamorphic phase changes until eclogitisation at around 45 km depth (e.g. Bostock, 2013; Hacker and Abers, 2004). Based on observations of converted teleseismic waves, Audet et al. (2009) found that pore pressures in subducted oceanic crust along the Cascadia megathrust are lithostatic. High pore pressures imply that the upper surface of the subducted crust is

## 2.1 Structural domains above and below the megathrust

impermeable; however, this study was not able to fully resolve the properties of the offshore plate interface due to a lack of ocean-bottom instrumentation.

Aside from the internal composition of the oceanic plate, a wide breadth of work has focussed on structural complexity at the top of the subducting oceanic crust. Chains of seamounts litter the ocean floor, which individually, may have relief of up to several thousands of metres. Based on mass-wasting features such as head-scars, slumps and slides at the outer wedge (e.g. Watts et al., 2010), seamounts appear to enter into the subduction zone. A crucial question to answer is: do seamounts remain intact as they begin to subduct? Due to the resulting impact on plate interface geometry, subducted seamounts have been imaged at many depths in subduction zones, from beneath the outer forearc (Bell et al., 2014) to deep beneath the forearc mantle wedge (Singh et al., 2011a). Furthermore, seamounts have a dense, mafic composition, making them identifiable from seismic, gravity and magnetic measurements (e.g. Trehu et al., 2012).

Throughout this description of subduction domains, a common theme has been the presence of faults that neighbour the megathrust interface. The lower plate is no exception. Along the Sumatra margin, subduction of elevated fracture zones in the oceanic plate is interpreted from bathymetry (Robinson et al., 2006) and seismicity patterns (Lange et al., 2010). In addition to fracture zones, extensional structures in the lower plate develop as the plate bends at the outer rise. Bending-related structures such as horsts and grabens, which can have relief up to 800 m (e.g. von Huene and Ranero, 2003), are inferred from ocean bathymetry and seismic reflection profiles (e.g. Contreras-Reyes et al., 2008). These faults may act as a conduit for fluids, hydrating the oceanic crust (e.g. Garth and Rietbrock, 2014; Peacock, 2001).

### 2.1.5 Subducted sediments

So far, we have assumed that the subducting plate interface is a sharp contact between the upper and lower plates. However, the plate boundary can be viewed as a more diffuse region that may contain a narrow (< 2 km thick) layer of sedimentary material. Deep-sea drilling projects have revealed that approximately  $2.3 \times 10^{15}$  g of sedimentary material is transported into subduction systems every year (Rea and Ruff, 1996). Pelagic sediment on top of the incoming plate can be calcareous or siliceous depending



on depositional depth. As the oceanic plate nears the trench, terrigenous material, such as clay and ash-fall tuff, is added (Cloos and Shreve, 1988). Oceanic and continental sediments combine to produce a trench thickness of around 1 km in most subduction zones (Clift and Vannucchi, 2004).

Early seafloor drilling studies show that at some subduction margins, such as the Lesser Antilles, trench sediment is accreted onto and under the leading edge of the upper plate. For other margins, such as the Marianas, sediment may be driven down to depths as great as 100 km (Cloos and Shreve, 1988). This layer of descending sediment is known as the *subduction channel*, which is defined by Cloos and Shreve (1988) as, ‘a thin layer of rapidly shearing, poorly consolidated sediment that is dragged by the descending plate beneath the overriding plate, and its accretionary prism, where present’. The subduction channel can have a bulk density of  $2200 \text{ kg/m}^3$  and a porosity of 20–25% (Cloos and Shreve, 1988). Due to these properties, sediment can act as a strong rheological anomaly and may have an important influence on dynamics of the plate interface.

Subduction channel thickness estimates may deviate from measures of trench fill because sediment may accrete onto the frontal wedge, or tectonic erosion may transfer some of this material to the subduction channel (Heuret et al., 2012). Furthermore, several different factors control the amount of sediment that is subducted (Cloos and Shreve, 1988), such as lithology of the forearc, convergence rate, topography and dip of the downgoing plate. Direct measurements estimate that the subduction channel is  $\sim 1 \pm 0.5 \text{ km}$  thick (Kopp, 2013). However, this value depends on the depth at which the channel is measured, and the imaging method used (Table 2.2). Thickness constraints can also be obtained from exhumed subduction shear zones. For example, Vannucchi et al. (2008) report a subduction channel thickness of 500 m, with significant along-strike variations, from an ancient erosive margin exposed in the Northern Apennines of Italy. Where large volumes of sediment are subducted, the edges of the channel are sharp. In contrast, the channel inlet may have a more gradational form in accretionary margins.

Subduction zone	Thickness of subducted sediment	Reference
-----------------	------------------------------------	-----------

## 2.2 Structural and compositional influences on megathrust seismogenic behaviour

Hikurangi, New Zealand	1–2 km	Eberhart-Phillips and Reyners (1999)
NE Honshu, Japan	1.0–1.5 km	von Huene et al. (1994)
Ecuador	150–600 m	Sage et al. (2006)
Nankai	2 km	Park et al. (2010)
Northern Chile	0.2 km	von Huene and Ranero (2003)
Central Chile (Maule)	0.5–1 km	Grevemeyer et al. (2003); Contreras-Reyes et al. (2008)
South-Central Chile (Valdivia)	1.2–1.8 km	Grevemeyer et al. (2003); Contreras-Reyes et al. (2010);

Table 2.2: Estimates of subduction channel thickness for different subduction zones.

## 2.2 Structural and compositional influences on megathrust seismogenic behaviour

The nature of physical properties and structures that control megathrust seismogenesis is an on-going debate in earthquake science. In the classic study of Ruff and Kanamori (1980), it was proposed that the size of earthquake asperities is related to both the age of the subducting plate and its convergence velocity. However, based on this model, the north-east Japan subduction zone would not have been able to generate a rupture that was the size of the 2011  $M_w$  9.0 Tohoku earthquake. Therefore, it is plausible that many different physical properties influence the seismogenic behaviour of subduction zones. In the early 1990s, workers began to consider upper plate rheology as a strong influence on megathrust processes (e.g. McCaffrey, 1993). At the regional scale, continental upper plates that are highly compressional, resulting in a more strongly coupled subduction plate interface, compared with oceanic and extensional upper plates (Heuret et al., 2011). Fundamentally, whether or not a large rupture can be hosted on the interface is governed by its effective shear strength, which is in turn determined by many properties, such as normal stress, pore fluid pressure,

permeability, rigidity, temperature, and coefficient of friction. These parameters may vary over much smaller scales than the lithospheric-scale variations described above. Frictional response may also be dynamic, particularly in response to large slip, with materials responding in either velocity-weakening or velocity-strengthening modes (Scholz, 1998). Therefore, megathrust seismogenic processes cannot be explained by a single property; they are more likely related to a complex interplay between the structure and composition of the main subduction zone domains, as discussed below.

### 2.2.1 The up-dip rupture limit: subducted sediments and fluids

Following the early model of Ruff and Kanamori (1980) that showed a relationship between earthquake size, plate age and convergence rate, Ruff (1989) proposed that the thickness of trench fill also influences global earthquake patterns. It was found that margins containing an excess of trench sediments, such as the southern Chile and Alaska margins, tend to produce the largest earthquakes. However, these classic studies were based on a limited earthquake record, compared to that is available today. To highlight this drawback, the trench in the rupture area of the 2011  $M_w$  9.0 Tohoku, Japan earthquake contains only 350 m of sediment fill (Kodaira et al., 2012; Nakamura et al., 2013). Nevertheless, the presence of clay at the maximum asperity of this earthquake (Chester et al., 2013) does indicate a link between subduction channel properties and rupture mechanics. Furthermore, along-strike variations in the thickness and fluid content of the subduction channel beneath Sumatra may have controlled the rupture limits of the 2004  $M_w$  9.1 and 2005  $M_w$  8.7 earthquakes (Dean et al., 2010), possibly due to the insulating effect of sediment (Geersen et al., 2013).

One feature common to many subduction margins is reduced seismicity at 5–15 km depth. The seaward extent of great earthquake ruptures coincides with a critical temperature of 100–150°C (Hyndman et al., 1995; Oleskevich et al., 1999). This isotherm typically occurs within the frontal prism, showing that sediments influence thermal properties of megathrust, which affect seismogenic character. The physical mechanism behind this thermal control remains greatly debated, with arguments focussing on the composition and the frictional properties of sediment. Early studies suggest that the dehydration of clay, and accompanied phase change from smectite to illite and chlorite, play an important role in the up-dip limit of seismogenesis (Vrolijk, 1990). However, the lack of evidence for smectite in the trench fill of some subduction

## 2.2 Structural and compositional influences on megathrust seismogenic behaviour

zones, such as Cascadia (Hyndman et al., 1997), makes this theory problematic. As for the frictional properties of clay phases, laboratory studies show that illite is frictionally stronger than smectite (e.g. Morrow et al., 1982), limiting the up-dip rupture limit. A later study by Saffer and Marone (2003) shows that illite displays velocity-strengthening behaviour under a wide range of conditions, indicating that this phase change is not the main control on the up-dip limit of seismogenesis. Even if these phase transitions do exert a control on minimum rupture depth, they still do not explain why events such as the 2011 Tohoku earthquake are able to reach the trench. Faulkner et al. (2011) suggest that clay sediments are velocity-weakening at high slip rates due to rapid thermal pressurisation. Furthermore, we have so far assumed that the up-dip limit is a sharp boundary; in reality, this boundary is likely gradational because it is controlled by a range of hydrological, thermal and compositional factors (Wang and Hu, 2006).

Whether a margin is erosional or accretionary affects sediment flux into the subduction zone. By modelling the thermal structure of convergent margins, Harris et al. (2014) found that the megathrust in accretionary margins is warmer than in erosive margins due to the insulating effect of thick deposits. If the up-dip limit of seismogenesis is thermally controlled (e.g. Saffer and Marone, 2003), accretionary margins should have a wider seismogenic plate interface, consistent with the findings of Smith et al. (2013) for the Makran subduction zone. An analysis of earthquake characteristics and margin style shows that long-duration tsunami earthquakes tend to materialise at erosive margins, whereas the largest earthquakes ( $M_w > 8.5$ ) occur at accretionary margins (Figure 2.2); (Bilek, 2010). Long source durations of shallow ruptures indicate the presence of low-rigidity material (Bilek and Lay, 1999), consistent with fluid saturated sediments beneath the outer wedge. Fluids expelled from sediment reduce effective normal stress acting on the plate interface, lowering frictional stability (Ranero et al., 2008; Scholz, 1998; Wallace et al., 2009). In many subduction zones, the up-dip limit to seismogenesis correlates with a sudden reduction in plate reflectivity, indicating diminished fluid content in the seismogenic zone (Ranero et al., 2008).

### 2.2.2 The down-dip limit of seismogenesis: the mantle wedge

The down-dip limit determines the landward extent of the seismogenic zone. Similar to the up-dip limit of seismogenesis, a thermally controlled *brittle-ductile transition* (BDT) has been proposed as the main control. Based on laboratory measurements, quartzo-feldspathic rocks become velocity-strengthening at temperatures of 350–450°C (e.g. Blanpied et al., 1995). These isotherms correspond to the down-dip limit of aftershocks following the 2004 Sumatra earthquake (Klingelhoefer et al., 2010). Oleskevich et al. (1999) suggest the conditionally-stable behaviour of serpentinite results in a zone of transitional seismogenic character at these temperatures. However, Ruff and Tichelaar (1996) found that these isotherms occur much deeper than the down-dip limit of many past ruptures (40–50 km). It is argued that a BDT based wholly on crustal lithologies may not be appropriate for depths of > 30 km because lithologies are likely heterogeneous and may include a mixture of basalt from the downgoing plate and subduction channel sediments.

With the lack of evidence supporting a thermally controlled BDT, alternative explanations were investigated. Ruff and Tichelaar (1996) found a correlation with the coastline and down-dip limit of the seismogenic zone for many circum-Pacific margins. This finding suggests that the intersection of the plate interface with the continental Moho of the overlying plate is a control on the down-dip limit of seismogenesis. Though, as described above, this boundary is not clearly defined and may vary significantly for different regions. Furthermore, the correlation is complicated by observations of megathrust ruptures extending into the forearc mantle (Heuret et al., 2011). A deep seismogenic zone exists in the Sumatra subduction zone. Here, locking was purported to be high in the mantle (Simoes et al., 2004), where the 2004  $M_w$  9.1 Sumatra earthquake nucleated and slipped (Dessa et al., 2009). Thermo-mechanical simulations indicate that rupture into the mantle occurs due to high deviatoric stresses (Dinther et al., 2013). These results indicate that the down-dip limit is thermally-governed (Dinther et al., 2013), and the velocity-strengthening behaviour of serpentinite plays a minor role. This finding could explain ruptures that do not extend into the mantle even though there is little evidence for significant serpentinitisation, such as the 1960  $M_w$  9.5 Valdivia, Chile earthquake (Haberland et al., 2009).

## 2.2 Structural and compositional influences on megathrust seismogenic behaviour

### 2.2.3 The Subducting Plate: Geometry, topography and fracture zones

Active source seismic studies reveal sharp bends in megathrust geometry at some margins that have been proposed to control the up- and down-dip limits of rupture (Contreras-Reyes et al., 2012; Ito et al., 2005). The intuitive impact of subducted seamounts on upper plate deformation combined with extensive observations of subducted topography has led many studies to correlate roughness on the downgoing plate with megathrust seismogenic character. Links between earthquake rupture zones and topographic features on the oceanic plate were originally made by Mogi (1969) and Kelleher and McCann (1976). With improved seismic imaging, there was a growth in studies during the 1990s and early 2000s providing mounting evidence for subducted topographic features strongly influencing earthquake ruptures. However, the manner in which seamounts affect seismogenesis remains strongly debated.

Originally, seamounts were thought to cause large earthquakes because they act as a point of strong resistance, thereby acting as an asperity (Cloos, 1992; Scholz and Small, 1997). There are several examples of asperity-causing seamounts in the Java, Hikurangi and Costa Rica margins; these are all associated with long duration tsunami earthquakes (Abercrombie et al., 2001; Bell et al., 2014; Husen et al., 2002). Conversely, consensus is growing that seamounts act as rupture barriers (e.g. Kodaira et al., 2000; Park et al., 2004; Singh et al., 2011a). Based on seismic reflection profiles, Kodaira et al. (2000) image a 50 km wide by 13 km thick seamount lying at 10 km depth in the Nankai subduction zone. This structure was understood to have acted as a barrier during the 1946 *M* 8.1 Nankaido earthquake, due to increased fault coupling. An alternative type of barrier behaviour has been proposed in which seamounts weaken the plate interface (Mochizuki et al., 2008; Singh et al., 2011a). Wang and Bilek (2011) show that seamounts create a favourable stress environment for small earthquakes and aseismic creep. This interpretation is plausible since there is little geological evidence in exhumed subduction complexes for wholesale seamount decapitation as proposed by Cloos (1992). Moreover, Wang and Bilek (2011) suggest that the fractured nature of subducted seamounts combines with fluid-rich sediments to weaken the plate interface.

So far, we limited our discussion to single seamounts; however, they may also occur as long, linear chains. With this in mind, it is possible that the seismogenic

character of subducted topography may depend on its morphology. Bilek et al. (2003) show that earthquakes associated with individual seamounts in the Middle America subduction zone act as asperities, whereas the subducted Cocos ridge inhibits ruptures. Similarly, in the Andean margin, the Juan Fernandez ridge correlates with segment boundaries of great earthquakes (Sparkes et al., 2010). Likewise, chains of subducted seamounts exist at the southern and northern end of the 2011 Tohoku earthquake rupture area, possibly acting as barriers to this rupture (Wang and Bilek, 2014).

Like seamounts and oceanic ridges, it is accepted that fracture zones significantly perturb mechanical coupling of the plate interface (Müller and Landgrebe, 2012). Akin to the above seamount discussion, there are conflicting opinions on the impact of fracture zones on seismogenesis. Robinson et al. (2006) showed that the 2001 Peru earthquake was stalled by the Nazca fracture zone, which has a relief of several hundred metres on the seafloor. However, fracture zones may not act as a complete barrier, as shown by the 2007 Solomon Islands earthquake in which the rupture jumped across a plate boundary fracture (Furlong et al., 2009). Conversely, from a statistical analysis of past earthquakes, Muller and Landgrebe (2012) find that most large subduction ruptures ( $M_w > 8.0$ ) occur where fracture zones intersect the trench.

#### 2.2.4 Composition, rheology and structure of forearc crust

To the first order, megathrust segment boundaries typically correlate to large morphological features of the upper plate, such as peninsulas and embayments (e.g. Ando, 1975; Kelleher, 1972). Examples of connections between coastal headlands and megathrust coupling include the Mejillones peninsula in northern Chile (Métois et al., 2013; Victor et al., 2011), the Shipunsky and Kronotsky peninsulas in the Kamchatka subduction zone (Bürgmann et al., 2005), and the Raukumara peninsula in New Zealand (e.g. Wallace et al., 2009). In contrast, the plate interface beneath the Nicoya peninsula along the Costa Rica margin was strongly locked prior to an  $M_w$  7.6 earthquake in 2012 and has a long history of large megathrust earthquakes (Protti et al., 2014). Regardless of the behaviour of individual coastal features, these observations imply that the structure of the overriding forearc exerts a strong control on plate interface seismicity.

## 2.2 Structural and compositional influences on megathrust seismogenic behaviour

The backstop tends to delineate the up-dip rupture limit of most large megathrust earthquakes (Song and Simons, 2003; Wang and Hu, 2006; Wells et al., 2003). Similarly, Wells et al. (2003) suggest that forearc basins may be an indicator of long-lived asperities in accretionary margins. As a further development of this idea, Song and Simons (2003) find that low gravity anomalies in the forearc (known as trench parallel gravity anomaly) globally correlate with regions of high slip during past large earthquakes. This relationship was explained by high shear traction eroding the base of the upper plate. Erosion subsequently causes subsidence of the overlying forearc, but the exact mechanism of basin formation remains a contentious issue (Fuller et al., 2006).

Similar to the role of low gravity anomalies in the forearc, workers have also assessed the significance of high density anomalies in the upper plate, which increase normal stress and shear strength along the megathrust (e.g. Tassara, 2010). Kodaira et al. (2006) interpret a high  $v_p$  structure in the forearc beneath the Kii peninsula in the Nankai subduction zone as an intruded igneous complex which creates strong coupling against the subducting plate. Based on numerical modelling of frictional properties, this igneous body represents a segment boundary, where earthquakes tend to nucleate. Some of the best examples of correlation between upper plate density anomalies and seismogenic characteristics come from central Chile. For example, in the region of the 1995  $M_w$  8.0 Antofagasta earthquake, dense plutonic bodies in the forearc correlate with high postseismic  $b$ -values (Sobiesiak et al., 2007). Furthermore, the 2007  $M_w$  7.7 Tocopilla earthquake ruptured an area characterised by a high gravity anomaly (Loveless et al., 2010; Tassara, 2010). These examples of dense structures acting as asperities are in contrast to the findings of Wells et al. (2003) and Song and Simons (2003). Although the asperity-barrier description is less applicable for the rupture nucleation point of large earthquakes, Tassara (2010) indicates that large earthquakes in the Chile subduction zone nucleate at the edge of high density bodies in the lower forearc, such as the Antofagasta earthquake.

Deep-rooted faults in the overriding plate can act as conduits for fluid migration and can perturb shear stress along the megathrust. One of the first documented examples of crustal faults directly influencing megathrust behaviour is the Ecuador subduction zone. Based on seismic reflection images, Collot et al. (2004)



found that transpressive faults along the margin correlate with the rupture limits of past large megathrust earthquakes. These faults are weaker than the subducting plate interface; therefore, they act as a weak mechanical barrier, allowing elastic strain release to be partitioned. Seaward-dipping backthrusts close to the backstop in the Sumatra subduction zone limit the up-dip extent of megathrust earthquakes and can act as a secondary tsunamigenic source during large earthquakes (Chauhan et al., 2009). Sediments in the outer wedge are capable of storing elastic energy, allowing rupture along weak megasplay faults during large megathrust earthquakes, depending on frictional properties along the fault (Wang and Hu, 2006). Similar to backthrusts, megasplay faults may limit the up-dip limit of megathrust seismogenesis (Park et al., 2002). A large, landward-dipping normal fault in the outer wedge offshore of north-east Japan (Tsuji et al., 2011) may have ruptured during the 2011 Tohoku earthquake, and possibly promoted the large tsunami. During the 2001  $M_w$  8.4 Peru earthquake, stress was transferred to the trench-orthogonal and extensional Chololo fault zone beneath the coast, acting as a barrier to megathrust slip (Audin et al., 2008). In the case of triggered upper plate faulting, the sense of slip on the triggered fault depends on the depth of the megathrust rupture (Li et al., 2014). Shallow megathrust earthquakes are more conducive to extensional behaviour, whereas deeper ruptures trigger splay fault or backthrust faulting.

## 2.3 Limitations and remaining questions

### 2.3.1 Complex interplay between upper and lower plates

Thus far, we have considered the roles played by each structural domain separately. In reality, the seismic response of the megathrust results from the complex intertwining and feedback between many geological structures. For example, fracture zones can dam axial turbidity flows (Cloos and Shreve, 1988), affecting the characteristics of the subduction channel at depth. Furthermore, Dean et al. (2010) and Geersen et al. (2013) show that a subducting fracture zone at the Sumatra trench causes along-strike variations in the composition and thickness of the subduction channel. These variations in sediment properties may result in segmentation of the margin due to differences in thermal structure and frictional characteristics. Like fracture zones, seamounts and horst-and-graben features on the seafloor can also strongly influence

## 2.3 Limitations and remaining questions

sediment flux into the subduction zone (Kopp, 2013). In this case, such topographic anomalies enhance erosion of the upper plate (von Huene and Ranero, 2003; Scholl et al., 1980). Therefore, subduction of seafloor topography may shallow the up-dip limit of seismogenesis, resulting in a megathrust that is more conducive to long-duration tsunami earthquakes (e.g. Bell et al., 2014). Finally, in interpretations of upper plate structures, it is generally assumed that forearc morphological features, such as peninsulas are directly related to deeper structures within the forearc. However, workers have suggested that peninsulas may result from deeper processes, causing uplift of the forearc. For example, coastal features along the Kamchatka margin may be related to ridges and fracture zones on the oceanic plate (Bürgmann et al., 2005); the Raukumara peninsula in New Zealand may be caused by underplated sediment (e.g. Bassett et al., 2010).

In a reversal of roles, the subduction channel may affect the integrity and structure of subducted seamounts. Cloos and Shreve (1996) argue that the geometry and thickness of the subduction channel determines the depth at which seamounts may truncate or fully decapitate. At erosive margins, where the subduction channel is thin at shallow depths, early truncation occurs against the strong upper plate framework. On the other hand, at accretionary margins, seamounts remain intact to greater depths, where confining pressure is higher, leading to a strong, highly-coupled plate interface. Moreover, Ruff (1989) suggests that thick subduction channels smooth out roughness along the megathrust, allowing for larger rupture areas to develop. Geometrical complexities on the plate interface can damage the base of the upper plate, generating networks of faults at the base of the overlying crust that affect the mechanical behaviour of the megathrust (Armijo and Thiele, 1990; Melnick et al., 2009). As well as seamount subduction, rupture on upper plate faults may enhance subduction erosion through mass wasting on the forearc (Tsuji et al., 2013).

The complex feedback processes between sediment, subducting topography and upper plate faulting described above is well illustrated by the central Ecuador subduction margin (Sage et al., 2006); (Figure 2.4). Here, seamount subduction enhances erosion of the outer wedge, which in turn, increases sediment flux to the trench, leading to patchy lenses of overpressured sediment. This lateral heterogeneity likely manifests itself as a complex coupling distribution. This highly variable

coupling allows the development of seaward-dipping normal faults in the overlying forearc (Figure 2.4).

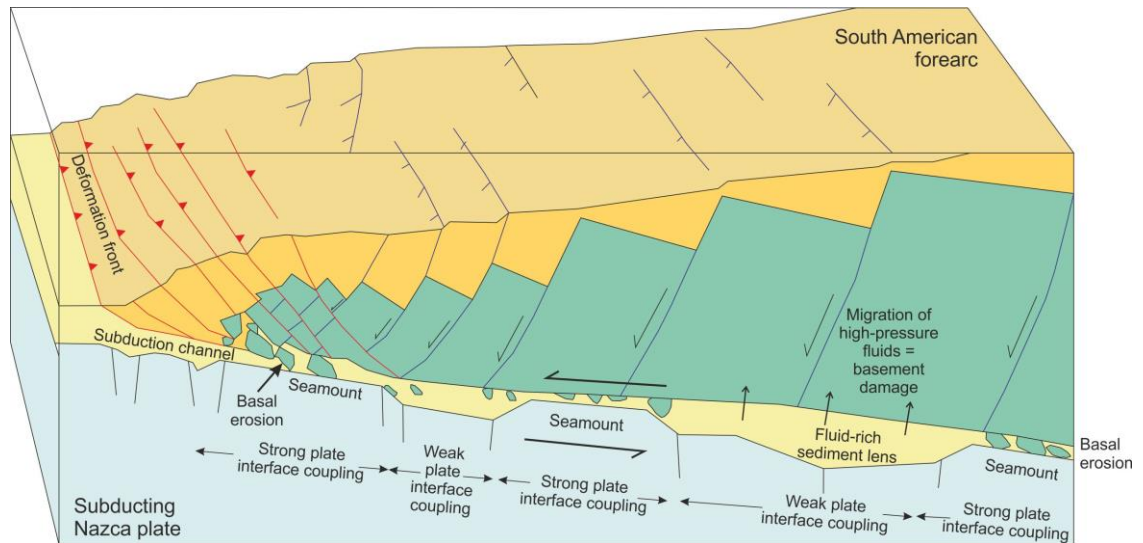


Figure 2.4: Schematic view of the main structural features of the central Ecuador subduction zone showing interplay between fluid-rich sediment lenses, seamounts, upper plate weakening, and plate coupling. Redrawn after Sage et al. (2006).

### 2.3.2 Time-dependence of the seismic cycle

As we have shown, the seismogenic behaviour of the megathrust depends on the complex interplay between many geological structures. Moreover, we have assumed the seismogenic response of these structures remains constant over time. Compared with the characteristic timescale of the seismic cycle (~100s of years), interseismic locking distributions provide a time-limited snapshot of plate interface coupling. It is often assumed that the degree of locking is long-lived; however, studies have shown that locking can rapidly change with time. For example, interseismic strain in the north-east Japan subduction zone rapidly increases (Avouac, 2011) and decays (Nishimura et al., 2004) because of nearby moderate–large earthquake ruptures. Furthermore, palaeogeodetic observations from the Sumatra subduction zone suggest that strong locking builds up within a matter of decades before a large megathrust earthquake (Meltzner et al., 2015). This time-dependent coupling may result from transient phenomena such as slow slip and seismic tremor. We do not discuss such transient processes in this thesis, but other detailed reviews exist on this topic (e.g. Beroza and Ide, 2011; Schwartz and Rokosky, 2007).

## 2.3 Limitations and remaining questions

Although plate interface coupling distributions are related to physical properties of the megathrust region, time-dependence of these properties should not be overlooked. The seismogenic character of a geological structure depends on the magnitude of dynamic shear stress at the time and elastic energy carried by the tip of the propagating rupture (Müller and Landgrebe, 2012). Consequently, the seismogenic response of structural anomalies not only depends on static frictional properties, but also on time-dependent stochastic variations in friction and shear stress (dynamic heterogeneity). These factors depend on past coupling and rupture history of a portion of the plate interface; this may explain why some structures may exhibit dual behaviour, changing their seismogenic character from one seismic cycle to another (Kodaira et al., 2006).

### 2.3.3 Moving toward finer scale structures in the upper plate

As described above, there have been many studies focussing on the seismogenic character of subducted seamounts. We believe that such large attention to seamounts has arisen as a result of two main factors. First, based on ocean bathymetry, seamounts clearly enter subduction zones, playing a vital role in large earthquake ruptures. Second, the large size of seamounts allows for their well-defined identification in subsurface images. Examples of seamounts acting as asperities tend to be historic earthquakes, such as the 1946 Nankaido (Kodaira et al., 2000), the 1947 Poverty Bay, New Zealand (Bell et al., 2014) and 1990 Nicoya, Costa Rica earthquakes. Due to the time when these earthquakes occurred, they have weakly constrained slip distributions; therefore, in our view of these examples, it is not easy to pinpoint an asperity to a comparatively small seamount. Higher-resolution rupture models are required to test the seamount asperity theory. Furthermore, for recent, well-recorded megathrust earthquakes, there has been little evidence to support the presence of subducted topographic heterogeneity within high slip regions. For instance, in the maximum slip area of the 2011 Tohoku, Japan earthquake, there is little evidence to suggest that the presence of seamounts (Wang and Bilek, 2014).

There appears to be a growing trend that as the resolving capability of seismic source inversions and subsurface imaging improves, attention is shifting toward finer-scale structures in the overriding plate and the subduction channel. However, whilst triggering between the plate interface and deep-seated faults in the subducting plate

has been documented on several occasions, there is no evidence for rapid stress transfer between upper plate faults and the megathrust. This may arise because faulting networks in the overriding plate are likely more complex than those in the oceanic plate, which has relatively uniform characteristics between different subduction zones. The structure of the upper plate is dependent on unique geological histories, so it is difficult to find systematic behaviour of overriding plate structures between subduction zones. Looking ahead, greater geophysical datasets and finer resolution images will help to resolve the detailed structure of the overriding plate.

## 2.4 Summary

Extensive work has been undertaken to understand the distribution of slip and seismic radiation during large earthquakes. Large earthquakes in the past decade have highlighted the complexity of megathrust ruptures and their varied response to geological structures (Table 2.3). Studies of individual earthquakes have revealed large structures that influence earthquakes; however, there is no unifying relationship that governs the mechanical behaviour of all subduction zones. Furthermore, the lack of accurate earthquake parameters, coupling and coseismic slip distributions may blur the correlation with certain structures. Although a wealth of seismic reflection images provide valuable information on offshore structural geometries, resolution of the seismogenic plate interface remains poor, particularly in determination of physical parameters such as Poisson's ratio.

Looking ahead, there is a need to examine smaller-scale physical properties in megathrust rupture zones, particularly in the offshore area, where most moment release occurs. Furthermore, methods such as local earthquake tomography using dense on- and offshore networks, as well as full-waveform inversion, offer improved imaging quality. There is a need to monitor time-dependent changes in the megathrust region over an entire seismic cycle. Mechanical models that simulate the time evolution of seismogenic character across a full seismic cycle (Dinther et al., 2013) will prove vital in understanding the governing physics of megathrust ruptures. However, such simulations require detailed models that contain realistic 3-D distributions of subduction zone physical structure; the next chapter describes one method of achieving this goal.

	Seismogenic character	Theory / examples
<b>Upper plate features</b>		
Trench-normal faults	High plate interface coupling, segment barrier	Peru: 2001 $M_w$ 8.4 Peru earthquake (Audin et al., 2008)
Plutons / batholiths	High slip asperity	N. Chile: 1995 $M_w$ 8.0 Antofagasta earthquake (Sobiesiak et al., 2007); (from aftershock b-value)
	Strong plate interface, rupture barrier; inhibit large ruptures	Kii peninsula, Nankai (Kodaira et al., 2006); high shear strength constraints (Tassara, 2010)
	Rupture nucleation point for large megathrust ruptures	Andean margin, S. America (Tassara, 2010)
	Long-lived segment barriers, weak plate interface coupling	Mejillones peninsula, N. Chile (Métrois et al., 2013; Victor et al., 2011)
<b>Lower plate features</b>		
Individual seamounds	Rupture asperity	Seamount decapitation (Cloos, 1992); 1994 $M$ 7.2 Java earthquake (Abercrombie et al., 2001); 1990 Mw 7.0 Costa Rica earthquake (Husen et al., 2002); 1947 Hikurangi earthquake (Bell et al., 2014)
	Rupture barrier	Subducted seamounds are fractured (Wang and Bilek, 2011); 1946 Nankaido earthquake (Kodaira et al., 2000)
Oceanic ridges	Rupture/segment barrier	Cocos ridge: 1983 Costa Rica earthquake (Bilek et al., 2003); Juan Fernandez ridge: Chilean earthquakes (Sparkes et al., 2010); 2011 $M_w$ 9.0 Tohoku, Japan earthquake (Wang and Bilek, 2014)
Fracture zones	Segment barrier	2001 $M_w$ 8.4 Peru earthquake (Robinson et al., 2006)
	Partial segment barrier (rupture jump)	2007 Mw 8.1 Solomon islands earthquake (Furlong et al., 2009)
<b>Subduction channel</b>		
Thick sediments	Allows large areas to rupture at once	Sediment smoothens plate interface contact (Ruff, 1989)
Thin sediments	Promotes stronger coupling	Ecuador subduction zone (Sage et al., 2006)
<b>Other</b>		
Gravity anomaly lows	High slip asperities	Global compilation (Llenos and McGuire, 2007; Song and Simons, 2003; Wells et al., 2003)
Gravity anomaly highs	Barriers to rupture	Global compilation (Llenos and McGuire, 2007; Song and Simons, 2003; Wells et al., 2003)

Table 2.3: Summary of key observations for different physical properties affecting megathrust seismogenesis.

## Chapter 3

# SEISMIC IMAGING OF SUBDUCTION ZONE STRUCTURE USING LOCAL EARTHQUAKE TOMOGRAPHY

As demonstrated in the previous chapter, the acquisition of detailed structural models along subduction plate boundaries is vital if we are to understand the physical factors that govern large earthquake ruptures. In this chapter, we describe seismic travel time inversion to calculate three-dimensional structural models of the Earth's interior, known as *seismic tomography*. Passive tomographic imaging is used to explore some of the research questions within Key Aim 1, as posed in Chapter One; the investigation of these questions forms a significant part of this thesis (Chapters Four and Five). Here, we provide details on the method of seismic tomography, including fundamental theory, typical workflows, and past applications in the subduction zone environment.

### 3.1 Fundamentals of seismic tomography

Seismic tomography is defined by Zhao (2015) as ‘a seismological method to determine 3-D images of the Earth's interior by combining information from a large number of crisscrossing seismic waves triggered by earthquakes or artificial seismic sources’. The method was pioneered by the early studies of Aki and Lee (1976), Aki et al. (1977), and Dziewonski (1977); its principle is similar to that of medical computerised tomography (CT) scans. In a CT scan, the location of sources and receivers is controlled; in passive seismic applications, receivers are fixed at the surface and earthquake sources are unevenly distributed. Furthermore, seismic ray

### 3.1 Fundamentals of seismic tomography

paths are dependent on velocity structure, resulting in a non-linear problem. The location, geometry and seismic properties of heterogeneous structures are inferred by calculating ray path geometries and seismic travel times using forward modelling and matrix inversion.

Seismic tomography is a well-established geophysical tool that has been used in many studies over the past 30 years for all types of seismic wave (body waves and surface waves); it can be carried out over all scale lengths (local, regional and global tomography). Seismic tomography inverts for different seismic wave parameters, such as velocity, attenuation, and anisotropy, all of which can be interpreted as physical subsurface properties. This thesis focuses on the method of earthquake body waves at a local to regional scale in order to probe seismic velocities, commonly called *local earthquake tomography* (hereafter, LET). The landmark work of Aki and Lee (1976) can be credited with a surge of LET studies in many active tectonic settings. Since then, there have been numerous developments in 3-D ray tracing and iterative non-linear inversion. Due to dense ray coverage, LET offers high-resolution imaging of seismically active subduction zones.

This project focuses on seismic velocity LET using P- and S-wave arrival times, which are in high abundance and can be measured accurately. Acquiring knowledge on the 3-D distribution of P- and S-wave velocities ( $v_p$  and  $v_s$ , respectively) allows interpretation of subsurface structure as lithological, mineralogical and fluid properties. Knowledge gained on petrological characteristics can then be used to infer factors that govern certain tectonic processes, such as large earthquake ruptures. In addition to determining physical properties, accurate seismic velocities are vital for obtaining reliable earthquake locations and source mechanisms.

In this chapter, we describe and explain the inherent disadvantage of LET that arises from its dependence on accurate starting models and earthquake locations. We then discuss strategies commonly used in 1-D and 3-D velocity inversion. Finally, we outline applications of LET in several subduction zones, as well as some of the resulting findings and limitations. This chapter is not intended to be a complete review of all aspects of seismic tomography. For a full discussion on the subject, the reader is referred to the work of Rawlinson et al. (2010) and Zhao (2015), as well as the more LET-focussed papers of Eberhart-Phillips (1993) and Thurber (1993).



### 3.2 Seismic ray tracing

The forward problem in seismic tomography involves 3-D ray tracing. Most ray tracing methods are based on the high frequency approximation in geometric optics, and can be classified as either *ray shooting* or *ray bending* (Rawlinson et al., 2010). In ray shooting, Snell's law is solved at each discontinuity, but this approach can be highly non-linear since the initial source trajectory is unknown. Most commonly, iterative schemes are used in which the initial source trajectory is perturbed until the required end point is hit, as first implemented by Julian and Gubbins (1977). An alternative routine is to iteratively adjust the ray geometry along a two-point path until it satisfies Fermat's principle (i.e. the ray path of least travel time) within a specified error margin. Many early ray bending algorithms solve the ray equation directly (e.g. Pereyra et al., 1980), a computationally expensive process.

An advancement of ray bending is *pseudo-bending*, which avoids direct solution of the ray equation, reducing computational time. In pseudo-bending, the ray equation is written as:

$$-\frac{\partial^2 \mathbf{r}}{\partial s^2} = \frac{\nabla V - \frac{dV}{ds} \cdot \frac{d\mathbf{r}}{ds}}{V} \quad ( 3.1 )$$

(Cerveny et al., 1977), where  $\mathbf{r}$  is the position vector along the ray,  $s$  is ray length, and  $V$  is seismic velocity. This equation states that the ray-normal component of the velocity gradient is antiparallel to the curvature of the ray path. Pseudo-bending incorporates a three-point perturbation scheme, based on a Taylor expansion, in which the ray path is iteratively calculated until its travel time converges within a specified limit. This algorithm was developed in a Cartesian coordinate system, making it more applicable to LET. In this thesis, we use the two-stage Um and Thurber (1987) pseudo-bending algorithm to calculate 3-D velocity models. In this method, approximate ray tracing (Thurber, 1983) is initially used, whereby travel times are computed along source-receiver arcs. Then, the dip of the plane containing the arcs is varied in the area of interest. The earliest arriving ray path is then perturbed using pseudo-bending, which systematically shifts points along the ray path to minimise the travel time along each segment. The advantage of this approach is that it can account for variable station

### 3.3 The coupled hypocentre-velocity problem

elevations, important in regions of considerable topographic relief (G. Lin et al., 2014), such as a subduction zone.

### 3.3 The coupled hypocentre-velocity problem

The absolute arrival time of a seismic body wave,  $t_{ij}$  is given by:

$$t_{ij} = \tau_i + T_{ij} \quad ( 3.2 )$$

where  $\tau_i$  is the earthquake origin time, and  $T_{ij}$  is the travel time of the wave from an earthquake source to a receiver. Using ray theory, the travel time is given by a path integral through a seismic velocity model (Thurber, 1992):

$$T_{ij} = \int_{source}^{receiver} u \, ds \quad ( 3.3 )$$

where  $u$  is the slowness field and  $ds$  is the path element (Thurber, 1983). These equations show that travel time is a function of station location, source origin and slowness field. Receiver locations and observed travel times are known; source origin (time and hypocentral coordinates) and slowness field are undetermined. Given a set of observed travel times,  $t_{ij}^{obs}$ , and assuming an initial estimation of the hypocentral location and slowness field, predicted travel times can be calculated using Eqns. 3.2 and 3.3.

The misfit between observed and predicted travel times,  $r_{ij}$  is given by:

$$r_{ij} = t_{ij}^{obs} - t_{ij}^{cal} \quad ( 3.4 )$$

Using a Taylor series expansion, travel time residuals can be expressed as a linear approximation between hypocentre and velocity parameters (Thurber, 1992):

$$r_{ij} = \sum_{k=1}^3 \frac{\partial T_{ij}}{\partial x_k} \Delta x_k + \Delta \tau_i + \int_{source}^{receiver} \delta u \, ds \quad ( 3.5 )$$

where  $\frac{\partial T_{ij}}{\partial x_k}$  is the hypocentre partial derivative, and  $x$  represents the hypocentre location. If we parameterise velocity structure into  $N$  parameters of  $m_n$ , then Eqn. 3.5 can be rewritten as:

$$r_{ij} = \sum_{k=1}^3 \frac{\partial T_{ij}}{\partial x_k} \Delta x_k + \Delta \tau_i + \sum_{n=1}^N \frac{\partial T_{ij}}{\partial m_n} \Delta m_n \quad ( 3.6 )$$

where the hypocentre derivative is related to ray vector components multiplied by slowness (Thurber, 1986):

$$\frac{\partial T_{ij}}{\partial x_k} = -\frac{1}{v} \left( \frac{dx_k}{ds} \right)_{source} \quad ( 3.7 )$$

and where  $\frac{\partial T_{ij}}{\partial m_n}$  is a partial derivative of the velocity model parameters. These partial derivatives are line integrals representing the relative weighting of each model parameter on a given arrival time. The objective of LET is to perturb and improve the model (seismic velocities and hypocentres) to minimise  $r_{ij}$ . Eqn. 3.5 shows that travel time residuals are related to both hypocentral location and the velocity structure; however, the non-linear relationship between these two variables is an inherent issue in seismic travel time inversion. To demonstrate this coupling, Thurber (1992) showed that keeping hypocentral parameters constant throughout an inversion for seismic velocity can produce significant artefacts in the final model.

### 3.3 The coupled hypocentre-velocity problem

As a result of this coupled hypocentre-velocity problem, an iterative inversion scheme is required that simultaneously solves for both parameters:

$$\mathbf{r} = \mathbf{H}\Delta\mathbf{h} + \mathbf{M}\Delta\mathbf{m} \quad ( 3.8 )$$

in which  $\mathbf{r}$  is a vector of travel time residuals.  $\mathbf{H}$  and  $\Delta\mathbf{h}$  are the matrix and vector of hypocentre partial derivatives and perturbations, respectively. Similarly,  $\mathbf{M}$  and  $\Delta\mathbf{m}$  correspond to partial derivatives and perturbations of velocity, respectively. Such an equation can be solved using matrix inversion.

The equation representing the above coupled hypocentre-velocity problem (Eqn. 3.8) can be solved using a least squares approach. In reality, LET is a mixed-determined problem due to the irregular distribution of ray paths in the Earth's subsurface, meaning that some velocity parameters are over-determined, whereas others are under-determined. Therefore, *damped* least squares inversion is required:

$$\mathbf{m} = (\mathbf{G}^T\mathbf{G} + \epsilon^2 \mathbf{I})^{-1}\mathbf{G}^T\mathbf{d} \quad ( 3.9 )$$

where  $\mathbf{m}$  is a vector containing model (hypocentre and velocity) perturbations,  $\mathbf{G}$  is a matrix of partial travel time partial derivatives with respect to model parameters (Jacobi matrix),  $\epsilon$  is the damping parameter,  $\mathbf{I}$  is the identity matrix, and  $\mathbf{d}$  is the vector containing travel time residuals. In one strategy, Eberhart-Phillips (1986) suggests the use of trade-off curves that show data variance (a measure of overall travel time residual) versus model variance (a measure of model perturbation) to select the damping parameter which minimises both. To generate trade-off curves, several one-step inversions are performed, each with a varying damping parameter.

In the coupled hypocentre-velocity problem, model perturbations must be calculated iteratively to ensure linearisation. After each inversion step,  $\mathbf{d}$  and  $\mathbf{G}$  are recalculated and Eqn. 3.9 is re-solved. In this thesis, 1-D and 3-D velocity models are calculated using iterative damped least squares inversion. To overcome the non-linearity of the problem, Kissling (1988) propose a staggered inversion, whereby a minimum 1-D model is created, which is then used as a starting point for a subsequent 2-D and 3-D tomographic inversion. Source-receiver configurations are kept relatively consistent at each step (Kissling et al., 1994). This staggered approach is now used in

many LET studies (e.g. Collings et al., 2012; Haberland et al., 2009; Kissling et al., 1994); the scheme used in this thesis is illustrated in Figure 3.1.

### 3.4 Inversion for 1-D velocity structure

As described in the previous section, LET is highly non-linear, so a staggered approach is required to improve the reliability of the final velocity structure and hypocentres. The first step is the generation of minimum 1-D velocity model (Figure 3.1). The parameters at this stage are hypocentral locations, layer velocities and station corrections (Kissling et al., 1994). Although 1-D velocity models provide minimal information on crustal structure, particularly in a subduction zone, where dipping structures are likely present (Eberhart-Phillips, 1993), they are a crucial stage before obtaining a 3-D tomographic model (Eberhart-Phillips, 1990). Errors in the 1-D reference model can result in significant artefacts in the final 3-D tomographic model, due to the tendency of the inversion to converge at local misfit minima (Kissling et al., 1994).

Station corrections are a vital part of the minimum 1-D velocity model. For stations in the middle of the network, which have an even azimuthal ray distribution, station delays represent lateral variations in the shallow subsurface.) In contrast, stations at the periphery of large networks are limited to long ray paths with limited azimuthal coverage; therefore, station corrections are a function of velocity structure in both the shallow and deep subsurface (Husen et al., 1999). Station terms are also important for subduction zone studies, where strong lateral variations in subsurface structure are expected. The combination of a 1-D velocity model with station corrections has been shown to produce accurate hypocentral locations even where the subsurface is highly heterogeneous, such as dipping structures (Kissling, 1988).

### 3.4 Inversion for 1-D velocity structure

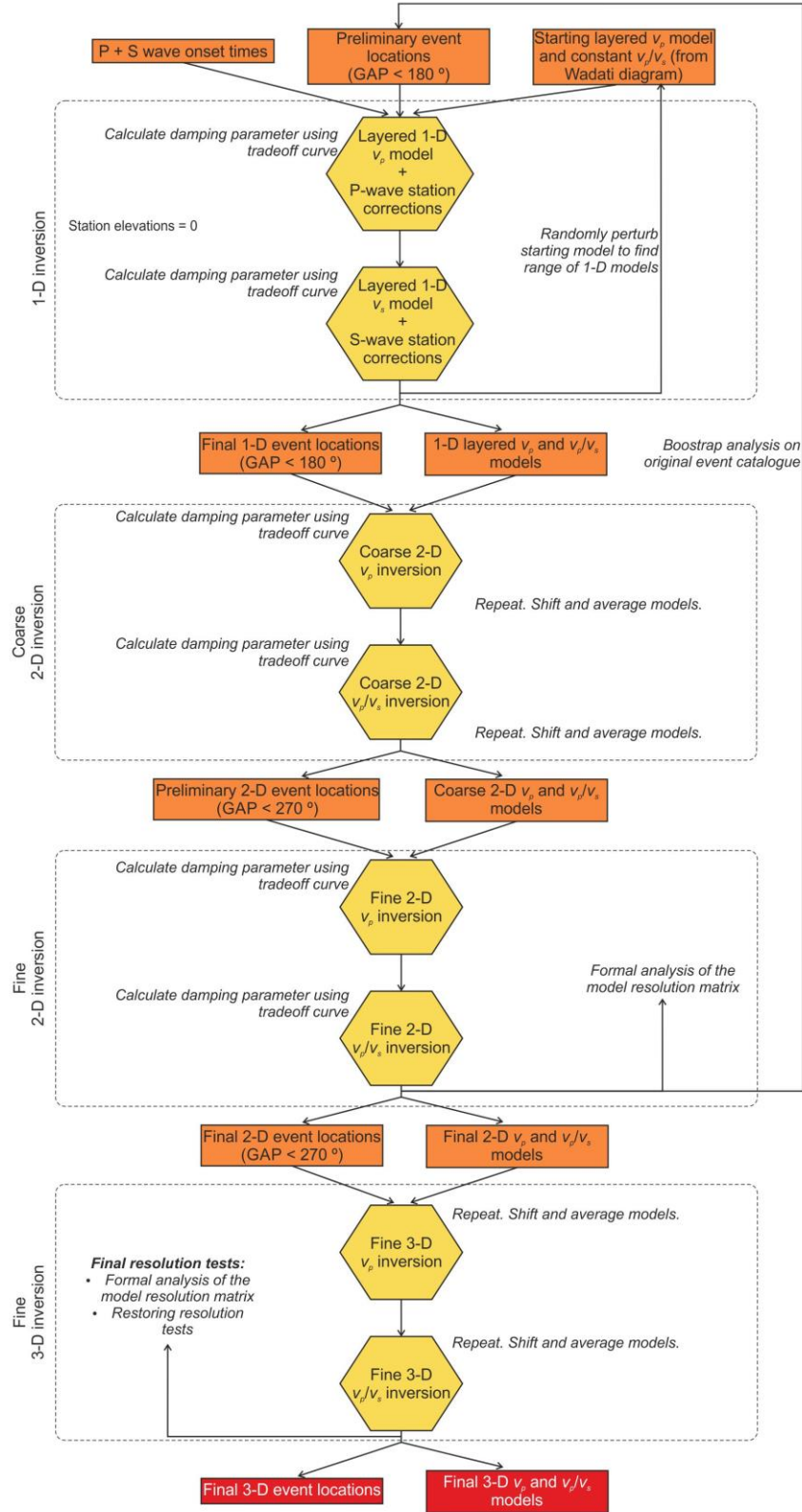


Figure 3.1: Staggered inversion workflow used in this thesis to calculate 3-D  $v_p$  and  $v_p/v_s$  models using local earthquake tomography.

Kissling et al. (1994) describe one strategy to obtain accurate 1-D velocity models. Determining the preliminary model from *a priori* information is a trial and error process. A reference station should be selected that has the most onset time observations and is located close to the centre of the network. An appropriate number of discrete layers should be chosen, such that strong velocity gradients can be represented. In 1-D velocity models, layer velocities equal the average lateral velocity, weighted by the total ray length in each element. Low velocity layers should be avoided, since these can distort ray paths, which increases the non-linearity of the problem and introduces hypocentral instabilities (Kissling et al., 1995).

In Chapters Four and Five of this thesis, we generate minimum 1-D velocity models and perform 1-D earthquake relocations using the VELEST software (Kissling et al., 1995). VELEST was first developed by Ellsworth (1977) and Roecker (1981). Since then, the algorithm has been improved and adapted following the principle of minimum 1-D models, as described by Kissling et al. (1994).

### 3.5 3-D tomographic inversion

In general, seismic velocity tomography involves three main steps: (1) model parameterisation; (2) solving the forward problem by calculating ray paths of seismic waves; (3) inversion (i.e. solving the system of equations given in Eqns. 3.8 and 3.9); and (4) assessing the resolution and errors associated with the final tomographic image (Figure 3.1). We discuss each of these four stages, with particular focus on the inversion algorithm used in this thesis, *SIMUL2000* (Thurber and Eberhart-Phillips, 1999). The SIMUL set of tomographic inversion codes, originally developed by Thurber (1983), is a well-established LET algorithm. The inversion algorithm follows that of Aki and Lee (1976), but includes developments in model parameterisation and ray tracing.

#### 3.5.1 Model parameterisation

Within the Earth's interior, structural and compositional heterogeneity exists at all length scales. Furthermore, the subsurface likely contains sharp velocity discontinuities that will be inherently smoothed out by tomographic inversion. Therefore, the choice of model parameterisation depends on the characteristic length

### 3.5 3-D tomographic inversion

scale of heterogeneity that we wish to resolve and the imaging capability of the inversion. The choice of parameterisation also affects the algorithms that are available for forward and inverse calculations (Rawlinson et al., 2010).

Since the advent of seismic tomography, different methods have been proposed for expressing subsurface structure in a 3-D model. Regular parameterisation schemes, which assign constant velocities to each node, are frequently used as they are easy to formulate. Uniform grids make initial ray tracing computationally inexpensive, since path segments in each block are straight lines (Rawlinson et al., 2010). Conversely, gridding can create artificial velocity discontinuities, requiring the use of smoothing constraints. Other more sophisticated schemes, such as triangular and tetrahedral cells, have also been developed (White, 1989). An alternative parameterisation is to define seismic velocities at the vertices on a regular grid of nodes (Thurber, 1983). This grid scheme is implemented in SIMUL2000. Linear B-spline interpolation ensures a smooth and continuously varying velocity field. The latest development of SIMUL2000 (Thurber and Eberhart-Phillips, 1999) also incorporates a flexible gridding scheme, in which blocks of grid nodes can be assigned a single velocity parameter. This flexibility helps to prevent velocity artefacts from appearing in areas of poor ray coverage.

Sometimes, structural interfaces can be explicitly parameterised to ensure that ray paths are accurately modelled at strong velocity discontinuities. This approach is warranted if sufficient *a priori* information is available. For example, Zhao et al. (1992) advanced the Thurber (1983) gridding method by incorporating boundary-grids that accurately express velocity structure along sharp discontinuities. This study found that parameterising these discontinuities can improve the accuracy of travel time calculations by providing a better starting model, further linearising the tomographic problem (Zhao, 2015). In the boundary-grid method, Zhao et al. (1992) set grid-node meshes for each distinct layer, independently; the geometries of the discontinuities remain fixed throughout the entire inversion. In this thesis, however, we do not parameterise structural interfaces due to the lack of accurate *a priori* information on plate interface geometry and other discontinuities in the study area of central Chile.



### 3.5.2 Velocity inversion

Damped least squares inversion (Eqn. 3.9) combined with parameter estimation (G. L. Pavlis and Booker, 1980; Spencer and Gubbins, 1980) is used by SIMUL2000. The damping parameter is selected from a trade-off curve of data versus model variance. An  $F$  test criterion is used to stop iterating when statistically significant convergence is reached. It is important to be able to solve for  $v_p/v_s$  because of its direct relationship with Poisson's ratio,  $\nu$ :

$$\nu = \frac{1}{2} \frac{(v_p/v_s)^2 - 2}{(v_p/v_s)^2 - 1} \quad (3.10)$$

and it is therefore an important indicator of lithology and fluid content. S-wave onsets and a  $v_s$  model can also provide more accurate hypocentral depths (Thurber, 1993), further linearising the tomographic problem. One simple way of calculating  $v_p/v_s$  is to simply take the ratio after inverting  $v_p$  and  $v_s$  individually. However, significant artefacts may occur where  $v_p$  is well resolved and  $v_s$  is less-well imaged (Zhang et al., 2009). To avoid this problem, SIMUL2000 uses S minus P times to invert for  $v_p/v_s$  (Eberhart-Phillips, 1990; 1989). This approach allows for the reduced number of S-wave onset times, as well as their greater onset time uncertainty, due to P-wave coda and possible S-wave anisotropy. S-P times are related to perturbations in  $v_p/v_s$  along the S-wave ray path by the following relationship (Thurber, 1993):

$$T_s - T_p = \int_{path} \left( \frac{v_p}{v_s} - 1 \right) \frac{ds}{v_p} \quad (3.11)$$

Tomographic inversion must not be regarded as a simple black box technique (Eberhart-Phillips, 1993). As with many tomographic inversion codes, SIMUL2000 includes many 'switches' that may affect the final result, so require careful consideration. To remove any potential artefacts caused by the grid spacing used, multiple inversions with horizontally shifted grids are carried out, which are then averaged (Figure 3.1). This averaging also results in improved imaging of dipping structures, such as subducting slabs (Collings et al., 2012; Haberland et al., 2009). Moreover, at each inversion stage, we do not invert for station corrections and keep

### 3.5 3-D tomographic inversion

hypocentres fixed for the first three iterations due to the assumption of reliable 1-D locations. Initially fixing hypocentres also ensures that resulting travel time residuals generate the overall 2-D subsurface structure inside the model.

#### 3.5.3 Assessment of model resolution and errors

The process of setting-up an inversion workflow and interpreting a tomographic model requires careful evaluation of formal resolution and covariance matrices, as well as understanding the source of potential artefacts. In early work, Backus and Gilbert (1968) recognised that solutions of geophysical inversion problems must be treated carefully and stringently examined using resolution tests. The non-uniform distribution of sources and receivers in LET results causes non-uniqueness in the interpretation of tomographic images. Therefore, it is important to analyse the resolving capability of the tomographic inversion to evaluate whether a feature in the velocity model can be trusted (Figure 3.1). There are three main methods used to assess the resolving power of tomographic inversions: (1) restoring resolution tests; (2) evaluation of data errors by jackknifing and bootstrapping; (3) formal analysis of the resolution and covariance matrices at each grid node. Each of these tests is described below.

In simple terms, a restoring resolution test involves designing a synthetic input model, calculating a corresponding set of synthetic travel times, and adding random noise. Synthetics are inverted in the same way as the real data. A comparison between the input and recovered model can thus measure the ability of the inversion to recover predefined velocity anomalies. In this thesis, we carry out restoring resolution tests by designing synthetic models that contain the main features of the subduction zone. We also estimate the standard error of velocity parameters by carrying out bootstrapping analysis of travel times (e.g. Lees and Crosson, 1989). Bootstrapping is advantageous because it is nonparametric; it assesses real errors in the data without making assumptions about their distribution.

Compared to more simple measures of resolution, such as hit count and derivative weight sum (Toomey and Foulger, 1989), formal analysis of the model resolution matrix,  $\mathbf{R}$  and covariance matrix,  $\mathbf{C}$  provides a more reliable method of assessing resolution at each grid node.  $\mathbf{R}$  and  $\mathbf{C}$  indicate the extent to which grid points

are dependent on neighbouring nodes due to poor ray coverage. Dependency on neighbouring nodes is known as *smearing* (Thurber, 1993).  $\mathbf{R}$  is the interdependence of the predicted model parameters and a filter through which the estimate is obtained from the true model. In inverse theory,  $\mathbf{R}$  and  $\mathbf{C}$  are related to  $\mathbf{G}$  by:

$$\mathbf{R} = \mathbf{G}^{-1}\mathbf{G} \quad ( 3.12 )$$

$$\mathbf{C}_m = (\mathbf{G}^{-1})^T \mathbf{C}_d \mathbf{G}^{-1} \quad ( 3.13 )$$

where  $\mathbf{C}_d$  is the data covariance matrix.  $\mathbf{C}$  contains the estimate of variance for each model parameter (diagonal elements) and the covariance between pairs of parameters (off-diagonal elements). Each row of  $\mathbf{R}$  defines an averaging vector for each model parameter. The simplest way of visualising  $\mathbf{R}$  is to plot the diagonal element of the resolution matrix at each grid point. For example, well-resolved nodes have large diagonal elements. However, diagonal elements should only be compared with other nodes in a strictly relative sense; absolute values depend on the exact grid parameterisation and damping value used. The relative size and pattern of off-diagonal elements in  $\mathbf{R}$  indicates smearing between nodes. Smearing is visualised by contouring the averaging vector row for each grid node at a certain percentage of the maximum (e.g. 70%). A well-resolved node has a symmetric contour, showing independence of adjacent nodes. SIMUL2000 directly calculates  $\mathbf{R}$  and  $\mathbf{C}$  using QR decomposition (Lawson and Hanson, 1995).

Another way to estimate smearing is by calculating the spread function ( $SF$ ) (Toomey and Foulger, 1989), which summaries each averaging vector as a single value.  $SF$  is given by:

$$SF(r_p) = \|\mathbf{r}_p\|^{-1} \sum_{q=1}^m \Omega(p, q) \mathbf{R}_{pq}^2 \quad ( 3.14 )$$

where  $\mathbf{r}_p$  is the averaging vector of the  $p$ th parameter,  $\mathbf{R}_{pq}$  is an element of the resolution matrix,  $\Omega(p, q)$  is a weighting function given by the distance between the  $p$ th and  $q$ th nodes, and  $m$  is the total number of parameters.  $SF$  is small when the averaging vector is compact and smearing is low. In a similar way to diagonal elements

### 3.6 Illuminating the subduction megathrust using local earthquake tomography: past applications

of resolution matrix, the absolute value of  $SF$  is dependent on the grid node spacing and value of the damping parameter. Therefore, acceptable thresholds of  $SF$  must be determined for each individual inversion and by comparing  $SF$  with other resolution tests.

In order to make an assessment of the resolving quality of an obtained tomographic image, one must consider all of the analyses discussed previously. All of the above tests are carried out for the tomographic inversions presented in Chapters Four and Five.

## 3.6 Illuminating the subduction megathrust using local earthquake tomography: past applications

Three-dimensional models of seismic velocities in a subduction zone can reveal details of physical properties along the subducting plate interface. Seismic velocity anomalies can be interpreted as variations in temperature, composition, volatiles, cracks or anisotropy (e.g. Zhao, 2015). Therefore, as stated earlier, the analysis of tomographic images is often non-unique, but can be made more reliable by using constraints from additional geophysical and geological evidence. Another inherent problem with LET studies in subduction zones arises from their offshore location, where few permanent seismometers are installed. The lack of instrumentation in oceans can lead to poorly determined hypocentral locations of offshore earthquakes and limited imaging capability. Ocean-bottom seismometer networks improve hypocentral determination and increase ray coverage in the offshore area, allowing the shallowest part of the subduction zone to be imaged.

Several LET algorithms are available and images generated depend on the exact dataset used. These factors make comparing tomographic results from different studies difficult. Here, we describe some key studies that have carried out LET along the subduction margins of northern Chile, New Zealand and north-east Japan. We describe the range of approaches used and summarise the main conclusions arising from the resulting images within the context of our knowledge of subduction zone structural heterogeneities detailed in the preceding chapter.

The staggered inversion scheme described in Section 3.5 is well illustrated by LET studies from the northern Chile subduction zone. The data come from aftershocks of the 1995  $M_w$  8.0 Antofagasta earthquake that were recorded on a temporary on- and offshore seismic network. Husen et al. (1999) used the VELEST algorithm to derive a minimum 1-D model, hypocentral locations and station corrections to account for elevation differences and regional velocity structure. Blasts from known local mining activities were relocated to assess the reliability of the velocity model. The minimum 1-D velocity model described above was subsequently used as a starting point for 2-D and 3-D inversions using SIMUL (Husen et al., 2002). At depths 20–50 km, the subducting slab is imaged as dipping  $v_p$  contours of 7–8 km/s and slightly elevated  $v_p/v_s$  ( $\sim 1.8$ ) oriented parallel to a narrow band of seismicity. The study also found high  $v_p$  ( $> 7$  km/s) in the lower forearc, which was interpreted as a residual magmatic intrusion. An along-strike increase in lower forearc  $v_p/v_s$  is observed, with the maximum  $v_p/v_s$  ( $> 1.8$ ) corresponding to the region of greatest moment release during the Antofagasta earthquake. One challenge in LET is the imaging of time-dependent velocity variations, which may illuminate dynamic processes along the subduction megathrust. Dataset uniqueness, as well as the somewhat arbitrary choices of smoothing and damping parameters makes imaging 4-D variations difficult. Using the same data from the Antofagasta earthquake, Husen and Kissling (2001) divided the travel time dataset into two periods, inverting for two separate velocity models. The results indicate higher  $v_p/v_s$  in the overriding plate at later stages of the postseismic phase, which was attributed to fluid flow released from the plate interface following the 1995 mainshock rupture.

Another subduction zone that has been studied in great detail using LET is the Hikurangi margin of New Zealand. This region is of scientific interest due to the subduction of a large oceanic plateau, the presence of slow slip events (e.g. Wallace and Beavan, 2010), and along-strike variations in plate interface coupling (Wallace, 2004). Extensive exposure of the forearc close to the trench ( $< 90$  km in places), allows for excellent station coverage, making the region suitable for LET imaging of the subducting plate interface. One of the most comprehensive LET studies in the region is that of Eberhart-Phillips et al. (2005), who used a similar inversion strategy to Husen et al. (2002), but using only onshore data. The flexible gridding scheme of Thurber and Eberhart-Phillips (1999) allows linking of offshore nodes where ray coverage is

### 3.7 Summary

reduced. Averaging of horizontally shifted grids improves the imaging of sharp velocity gradients. Active-source shots were incorporated into the dataset to improve imaging of the shallow subsurface in the coastal region. The resulting 3-D velocity model shows high  $v_p/v_s$  ( $> 1.8$ ) along the plate interface where there is a greater flux of subducted sediment in the more erosive northern part of the study area. This region of elevated  $v_p/v_s$  correlates to weaker plate coupling. In contrast, strong coupling relates to high  $v_p$  ( $> 6.5$  km/s) in the lower forearc crust, where there is a thinner subduction channel. These findings led Eberhart-Phillips et al. (2005) to speculate that plate coupling may be governed by subduction channel thickness.

North-east Japan has been a focus for many passive seismic imaging studies, particularly in the aftermath of the damaging 2011  $M_w$  9.0 Tohoku earthquake. Therefore, there has been much investment to install dense onshore and offshore seismic networks in order to improve understanding of plate interface seismogenic processes. Although numerous seismic observations were acquired before the Tohoku earthquake, further data from densified permanent networks and temporary deployments were available in the aftermath. Yamamoto et al. (2014) integrated all available datasets, including those from ocean-bottom seismometer (OBS) networks, to derive a detailed image of the plate interface region, from the trench to beneath the coastline. Nearly 190,000 P-wave and 170,000 S-wave travel times were inverted using the double-difference tomography code, tomoDD (Zhang and Thurber, 2006). One of the main findings from this study is the presence of two high  $v_p/v_s$  regions located up- and down-dip of the 2011  $M_w$  9.0 hypocentre. High  $v_p/v_s$  ( $> 2.0$ ) close to the trench is interpreted as fluid-rich sediments. Elevated  $v_p/v_s$  ( $\sim 1.84$ ) at greater depths of  $\sim 30$  km is understood to be caused by localised fracturing of oceanic crust.

### 3.7 Summary

In the last two decades, many advances have been made in the passive seismic imaging of subduction zones. In particular, large seismic datasets have allowed new understanding of the factors controlling megathrust ruptures. However, as shown by the case studies described above, imaging of the shallowest part of subduction zones, where most seismic moment is typically released, remains a challenge. Accounting for rough bathymetry and topography, as well as lateral velocity variations, is an inherent

obstacle when incorporating OBS data. Furthermore, imaging  $v_s$  offshore can prove difficult, as shown by the Husen et al. (2000) LET study of northern Chile, in which only single-component hydrophones were used. Therefore, developments are required in LET imaging by combining large onshore and offshore datasets. There are also avenues for progress in interpreting seismic velocity structure across a full earthquake cycle: from preseismic locking, to coseismic slip and postseismic deformation. However, diminished background seismicity in megathrust seismic gaps can also make LET imaging difficult. Also, whilst tomographic inversion is able to provide detailed imaging of subsurface velocity structure, interpreting velocities remains inherently non-unique.

To overcome these problems, one option is to study the velocity structure in a region that has already experienced a large earthquake, and where there is a large database of onset times from the ensuing aftershock sequence. In particular, ocean-bottom seismometers are required to ensure accurate earthquake locations and to improve offshore imaging. As shown by the Husen et al. (2000) study, obtaining offshore  $v_s$  models is difficult, particularly when only ocean-bottom hydrophones are used without horizontal components, thus limiting accurate determination of S-wave onsets. Furthermore, to make interpretations of subsurface geology from LET images, additional geophysical datasets should be considered (Eberhart-Phillips, 1993).

A study of the 2010  $M_w$  8.8 Maule, Chile earthquake rupture zone can allow an improved LET study of the subduction megathrust. Several studies exist that describe dynamics of the central Chile subduction zone at different stages of the seismic cycle (e.g. Bedford et al., 2014; Moreno et al., 2012). Furthermore, dense recordings of the aftershock sequence from both on- and offshore networks allow chances to image the megathrust close to the trench. In addition, the long-term segmentation and structure of the central Chile forearc is well understood from a range of geological and geophysical studies.





## Chapter 4

# THE 2010 $M_w$ 8.8 MAULE, CHILE EARTHQUAKE: NUCLEATION AND RUPTURE PROPAGATION CONTROLLED BY A SUBDUCTED TOPOGRAPHIC HIGH

This chapter is from a paper published in *Geophysical Research Letters* (Enclosure 2). The paper was accepted for publication on September 14, 2012 and published on October 16, 2012. Authors of the manuscript are Stephen Hicks (main author), Andreas Rietbrock (University of Liverpool), Christian Haberland (GFZ, Potsdam), Isabelle Ryder (University of Liverpool), Mark Simons (California Institute of Technology) and Andrés Tassara (Universidad de Concepción). The Supplementary Information of the paper is incorporated into the main body of this chapter. This research was the primary focus of my thesis from October 2011 – July 2012. The aim of this study was to image the first-order structure of the megathrust region by producing a preliminary 3-D seismic velocity model for the Maule rupture zone using an automatically determined dataset (Key Aim 1). Using this preliminary model, we made interpretations about the physical structure of the subducted oceanic crust. At this stage of the project, data from only the first two months of aftershocks recorded by onshore seismic stations were available.

### Published paper abstract

Knowledge of seismic properties in an earthquake rupture zone is essential for understanding the factors controlling rupture dynamics. We use data from aftershocks of the Maule earthquake to derive a 3-D seismic velocity model of the central Chile forearc. At 36°S, we find a high  $v_p$  ( $> 7.0$  km/s) and high  $v_p/v_s$  ( $\sim 1.89$ ) anomaly lying along the megathrust at 25 km depth, which coincides with a strong forearc Bouguer gravity signal. We interpret this as a subducted topographic high, possibly a former seamount on the Nazca slab. The Maule earthquake nucleated at the up-dip boundary of the anomaly; yet high coseismic slip occurred where lower seismic velocities overlie the megathrust. Sparse aftershock seismicity occurs within this structure, suggesting that it disrupts normal interface seismogenesis. These findings imply that subducted structures can be conducive to the nucleation of large megathrust earthquakes, even if they subsequently hinder coseismic slip and aftershock activity.

## 4.1 Introduction

The rupture dynamics of great subduction zone earthquakes are complex. Due to the vast increase in instrumentation, geophysicists can now map high order spatial variations in energy release and seismic slip along the megathrust. However, our understanding of the factors that influence these spatial variations remains limited. The February 2010  $M_w$  8.8 Maule earthquake, which ruptured an 81,500 km<sup>2</sup> area (Lay et al., 2010a) of the subduction interface between the downgoing Nazca and overriding South American plate, is no exception. This segment had not experienced a large rupture since the great 1835 Concepción earthquake (Figure 4.1a). The ‘Darwin gap’ (Lorito et al., 2011) was recognised as a mature seismic gap and geodetic measurements acquired before the 2010 event indicated strong locking of the megathrust within the gap (Métois et al., 2012; Moreno and Rosenau, 2010; Ruegg et al., 2009). The earthquake nucleated in the Darwin gap, and published coseismic slip models imply bilateral rupture propagation (Lay et al., 2010a; Lorito et al., 2011; Moreno et al., 2012; Vigny et al., 2011), with up to 20 m of slip  $\sim 100$  km north of the hypocentre, and up to 10 m of slip to the south.

The subduction zone asperity model (Lay and Kanamori, 1981) provides a conceptual framework to explain the slip distribution of large earthquakes. According to this model, areas of large coseismic slip are caused by asperities that are interseismically locked. Studies of strike-slip earthquakes (Michael and Eberhart-Phillips, 1991; T. Okada et al., 2007) suggest that asperities are associated with high seismic velocities, and therefore competent material. For subduction earthquakes, however, topographic highs (e.g. ridges, fracture zones, seamounts) on the subducting plate can act as rupture barriers (Kodaira et al., 2000; Park et al., 2004; Robinson et al., 2006).

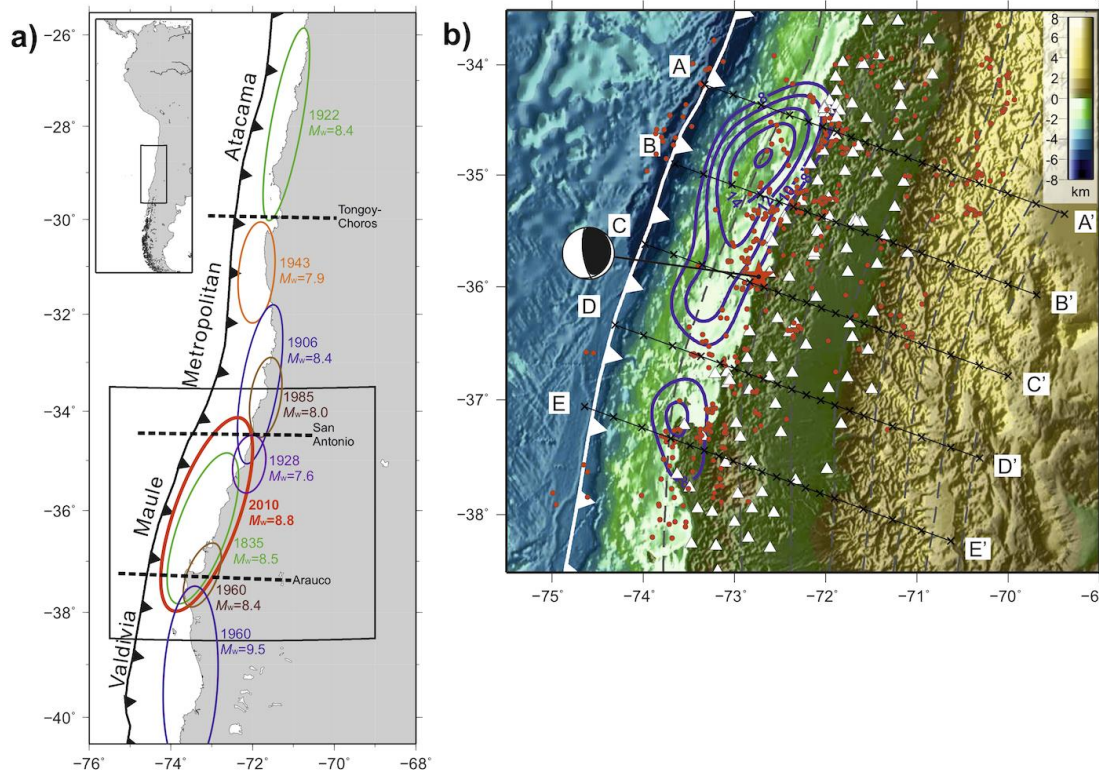


Figure 4.1: a) Locations of past ruptures and segmentation in Chile, after Métois et al. (2012). Ellipses give the rupture area of each earthquake. The name of each segment and segment boundaries (dashed lines) are shown. The box denotes the location of the map in (b). b) Local map with bathymetry/topography (coloured scale bar). The red star is the NEIC epicentre. Blue contour lines show the coseismic slip distribution of *Moreno et al.* (2012). Red circles and white triangles are the aftershocks and stations, respectively, used in our tomographic inversion. Black crosses denote the nodes in our 3-D inversion. The grey dashed lines show the geometry of the subducting Nazca slab, based on the Slab1.0 model (Hayes and Wald, 2009).

## 4.2 Tomographic Inversion Scheme

Published aftershock distributions for the Maule earthquake (Lange et al., 2012; Rietbrock et al., 2012) show a prominent gap in interface seismicity at 30–40 km depth, near 36°S. Slip models and the aftershock distribution demonstrates that physical heterogeneity may exist along the fault. It is therefore important to assess if any heterogeneity in the rupture zone is expressed in its seismic properties, and whether we can identify any correlation with coseismic slip. Here, we use travel time data from aftershocks to reveal a high velocity anomaly along the megathrust interface in the Darwin gap.

## 4.2 Tomographic Inversion Scheme

Following the Maule earthquake, a concerted multinational seismic deployment took place to record aftershock activity. The network consisted of ~160 stations covering the entire rupture area (Figure 4.1b). We determine the seismic structure in the rupture area using data from the International Maule Aftershock Dataset (IMAD). We automatically detect seismic P- and S-wave arrival times from aftershocks using an optimised STA/LTA triggering algorithm (Nippres et al., 2010) with an iterative location algorithm (Rietbrock et al., 2012), ensuring data consistency. Picking errors for the automatic analysis are shown in Figure 4.2.

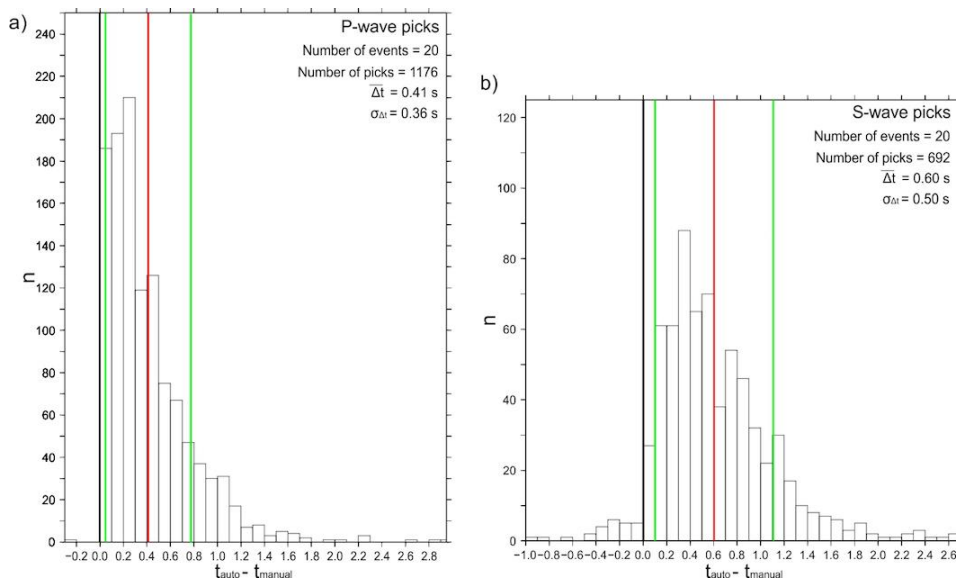


Figure 4.2: Histograms of a) P-wave and b) S-wave onset time pick errors of the automatic algorithm, based on a subset of 20 events.

We use a staggered inversion scheme (e.g. Haberland et al., 2009) to generate the velocity model. We estimate a best-fitting minimum 1-D model using the VELEST algorithm (Kissling et al., 1994). For the tomographic inversion, we choose 397 events (Figure 4.1b) from the first two months of aftershocks based on a maximum azimuthal gap criterion (onshore events  $< 175^\circ$ ; offshore events  $< 270^\circ$ ) and the number of S-wave picks ( $> 40$ ). We require a well-distributed aftershock catalogue to ensure good ray coverage in the model. This catalogue yields  $\sim 30,000$  P-wave and  $\sim 19,000$  S-wave onset times. We use the SIMUL2000 code (Thurber, 1983) to invert for both  $v_p$  and  $v_p/v_s$ . We incorporate a non-uniform nodal spacing (Figure 4.1b) in the x-direction (minimum of 15 km) to ensure high resolution where ray coverage is good, and uniform spacing in both the y-direction (80 km) and z-direction (10 km). To test reliability of the tomographic images, we analyse the model resolution matrix (Figure 4.3) to investigate the resolving capability of our data and model set-up. We find that the all nodes in the forearc are well resolved, particularly those in the onshore forearc. Smearing becomes apparent in the outer-rise and beneath the magmatic arc. The shallow areas of the marine forearc are also poorly resolved since we use land-based stations only in the inversion. The  $v_p/v_s$  model is inherently less well resolved due to fewer S-wave picks compared to P-wave picks, and the greater error associated with onset times of S-wave picks (Figure 4.2).

### 4.3 Results of 3-D Tomographic Inversion

Figure 4.4a shows the 3-D  $v_p$  structure and relocated aftershock seismicity on four cross-sections orientated perpendicular to the regional trench axis. We observe all the primary structures identified in the 3-D velocity model obtained for south-central Chile prior to the Maule earthquake (Haberland et al., 2009).

We now describe prominent features in the model (letters refer to labelled in Figure 4.4a). The continental crust of the South American plate (a) ( $v_p$  of 6.0–6.8 km/s), the top of which has two low velocity areas ( $v_p < 6.0$  km/s) constituting the marine forearc (b) and the Central valley basin (c). The continental mantle (d) is characterised by a prominent upwelling with  $v_p > 7.0$  km/s, lying  $\sim 200$  km from the trench. The top of the downgoing oceanic crust (e), a dipping structure with  $v_p \sim 6.8$  km/s is well defined by aftershocks. P-wave velocity along the plate interface is similar

### 4.3 Results of 3-D Tomographic Inversion

to that inferred from other regional seismic studies (Haberland et al., 2009; Krawczyk et al., 2006).

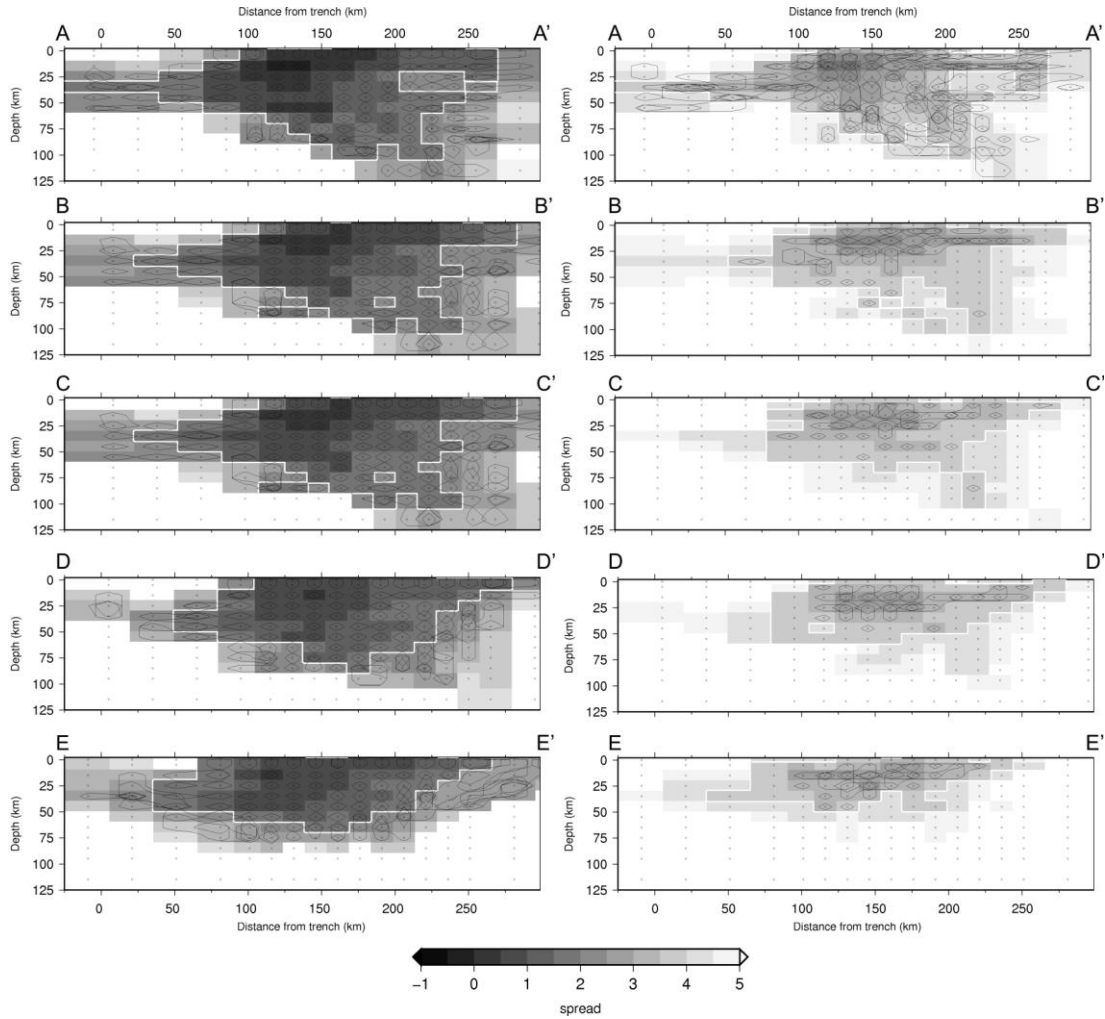


Figure 4.3: Resolution estimate of our best-fitting 3-D (left)  $v_p$  and (right)  $v_p/v_s$  model based on analysis of the model resolution matrix. Shading denotes spread function values and black lines show the 70% contour of the resolution kernel. The resolution limits (white lines) are based on spread function values of 2 and 4 for the  $v_p$  and  $v_p/v_s$  model, respectively.

Section C-C' traverses the mainshock nucleation region. Beneath the coastline, we observe a prominent, 40 km wide, high  $v_p$  ( $> 7$  km/s) anomaly (f) with significant relief (up to 10 km). From a seismic refraction profile, Krawczyk et al. (2006) also infer a high  $v_p$  anomaly in this area, interpreting it as serpentinised mantle wedge material or mafic lower crustal rocks associated with late Palaeozoic granitoid intrusions. We infer an elevated  $v_p/v_s$  of 1.89 within the anomaly (Figure 4.4b). Accounting for our relocated seismicity distribution and earlier estimates of slab interface geometry (Haberland et al., 2009; Hayes and Wald, 2009), we define a

# Chapter 4: The 2010 Mw 8.8 Maule, Chile Earthquake: Nucleation and Rupture Propagation Controlled by a Subducted Topographic High

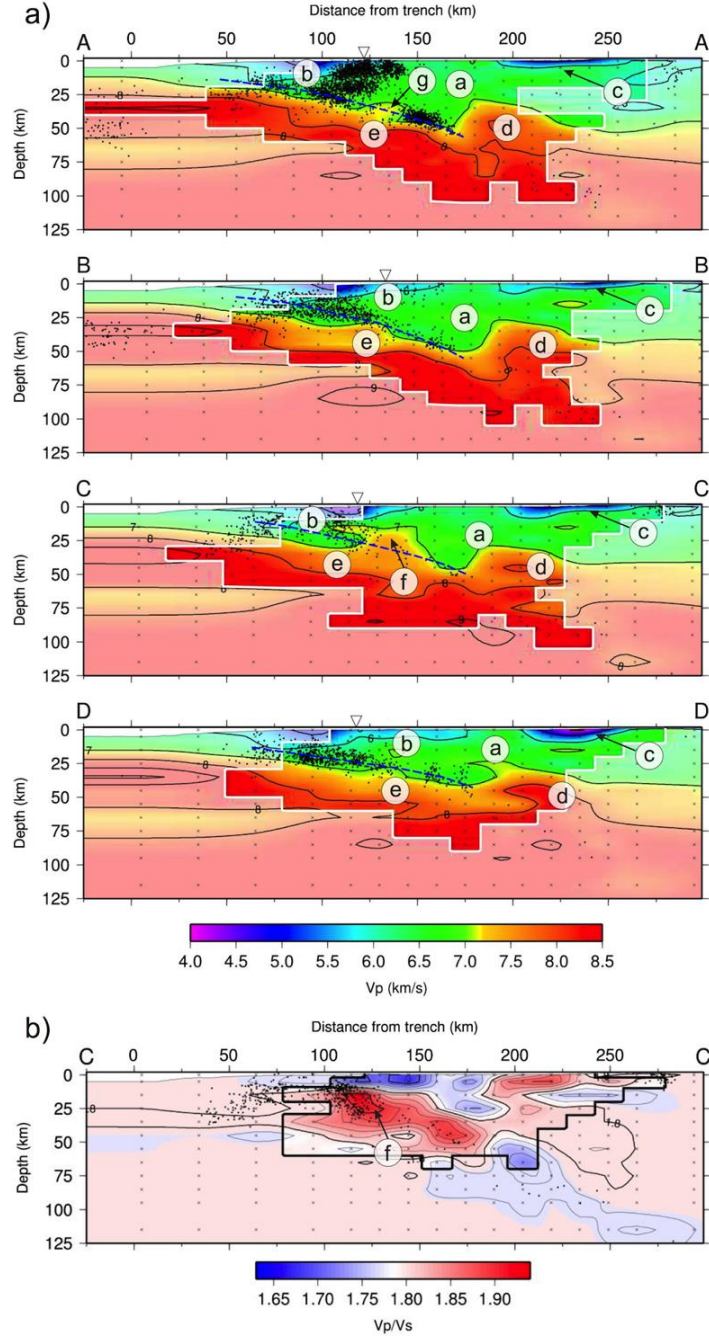


Figure 4.4: a) Cross-sections through the 3-D  $v_p$  model. The location and orientation of each profile is shown in Figure 4.1b. The coastline is given by black triangles. Features of the model are interpreted as follows: (a) continental crust, (b) forearc basin, (c) central basin, (d) continental mantle, and (e) subducting oceanic crust. The blue dashed line is the unperturbed thrust interface. In section C-C', (f) is a high velocity anomaly located above the plate interface, and (g) is a smaller high velocity anomaly in the Pichilemu region (section A-A'). b) Cross-section showing  $v_p/v_s$  along section C-C'. Black dots are relocated aftershocks with  $M_l \geq 3.0$ , with a minimum of 20 P- and 20 S-picks, respectively. The white lines denote the resolution limits, based on analysis of the resolution matrix (Figure 4.3).



## 4.4 Discussion

regional thrust interface excluding the anomaly. The anomaly protrudes above the interface by around 5–10 km (Figure 4.4). By interpolating our  $v_p$  model along the thrust interface (Figure 4.5), we find that the maximum along-strike extent of the anomaly is 60 km. The nodal spacing used in the inversion may mean that the a height and along-strike extent of the anomaly may be exaggerated. From Section A-A' (Figure 4.4a), we infer another, albeit smaller, high velocity anomaly (g) in the Pichilemu region, ~135 km from the trench, along the thrust interface (Figure 4.5a).

## 4.4 Discussion

The high  $v_p$  and  $v_p/v_s$  anomaly described above suggests that it is compositionally similar to hydrated oceanic crust (Haberland et al., 2009) or mantle (Carlson and Miller, 2003) therefore, it is of mafic origin, and must have once been subducted as part of the Nazca plate. From our tomographic images alone, we cannot resolve whether this structure represents a single seamount, an oceanic plateau, or a group of smaller seamounts. Furthermore, we cannot determine whether it remains attached to the subducting plate or was emplaced earlier in the overriding plate. We believe that this anomaly is not a residual igneous intrusion associated with the ancient magmatic arc: there is no correlation with surface outcrops of late Palaeozoic–Triassic granitoids. Also, a high  $v_p/v_s$  would not be indicative of a highly-fractionated intrusion (Christensen, 1996; Husen et al., 2000; Reyners et al., 2006).

Seismic evidence of subducted seamounts in many subduction zones is abundant (e.g. Husen et al., 2002; Kodaira et al., 2000; Park et al., 2004). However, it is important to constrain interpretations with additional geophysical evidence, and to understand potential sources of heterogeneous topography on the subducting slab. We used the Earth Geopotential Model, EGM2008 (N. K. Pavlis et al., 2008) to compute the regional Bouguer anomaly, subtracting the gravity effect of the subducting slab as given by a regional 3-D density model (Tassara and Echaurren, 2012). The resulting forearc residual gravity anomaly,  $\Delta g_{\text{forearc}}$ , is therefore due to lateral density variations above the interplate fault.



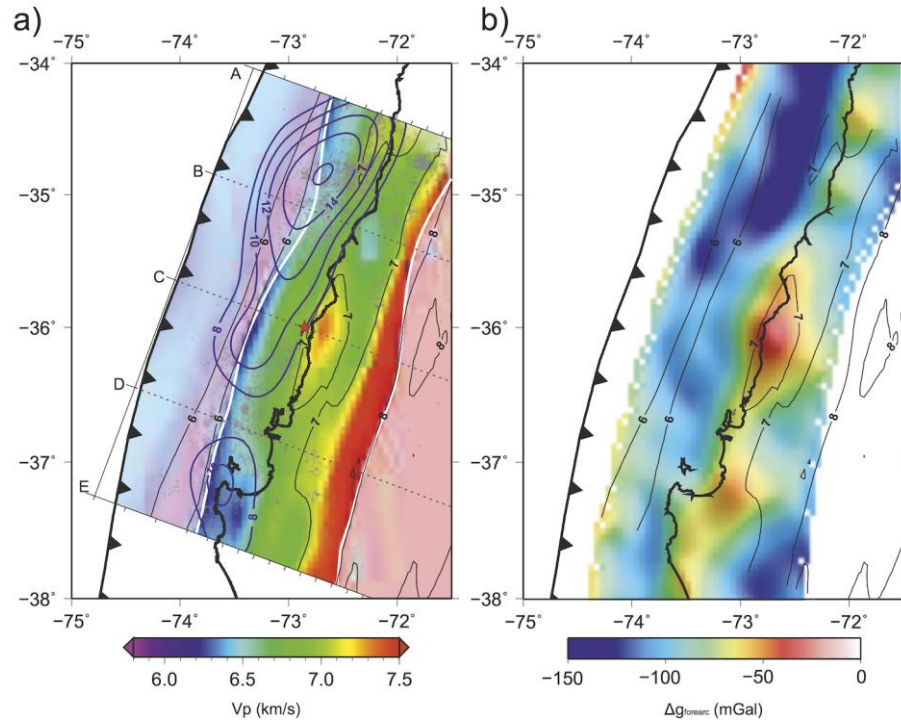


Figure 4.5: a) Comparison of  $v_p$  along the plate interface (coloured image, black contours) with the coseismic slip distribution of Moreno et al. (2012); (blue contours). The location of the high velocity anomaly beneath the coastline correlates with a region of relatively low coseismic slip. The two main slip patches correlate to lower  $v_p$  along the plate interface. Locations of aftershocks (grey circles) that lie along or close to the thrust interface are shown, highlighting the sparse seismicity associated with the anomaly. The red star is the USGS-NEIC epicentre. The white line denotes the up- and down-dip resolution limits of our tomography model. b) Forearc Bouguer gravity anomaly, derived from the model of Tassara and Echaurren (2012). Black lines are the  $v_p$  contours from (a) for comparison.

$\Delta g_{\text{forearc}}$  shows a strong spatial correlation with  $v_p$  along the megathrust (Figure 4.5b). In particular, the high  $v_p$  region eastward of the hypocentre coincides with a prominent gravity high ( $\Delta g_{\text{forearc}} > -70$  mGal). This signal reinforces our interpretation that the anomaly represents a dense mafic body located on top of the subducted slab. A smaller high  $v_p$  anomaly below the coast near 34.5°S (g) also correlates with a gravity high. We note that there is no correlation with high  $v_p$  for the positive gravity anomaly in the vicinity of the Arauco peninsula (~37.4°S), as also shown by the velocity model of Haberland et al. (2009). We therefore believe that beneath the Arauco peninsula, whilst there may be an upper crustal density anomaly, it may not have a significant seismic velocity contrast with the normal continental crust.

Westerly-dipping normal fault scarps have been identified in the marine forearc WSW of the identified anomaly (Geersen et al., 2011a). Sedimentary

#### 4.4 Discussion

underplating along the interface and subsequent gravitational collapse has been postulated to explain the presence of these faults, which are unusual along the central Chilean margin. Analogue models demonstrate that extensional faults can form in the wake of a subducting seamount due to enhanced sedimentary underplating (Dominguez et al., 2000). It is therefore feasible that a topographic high was once subducted in this region. Although no bathymetric high is observed offshore of the rupture area today, there is evidence for past subduction of a topographic anomaly related to the onset of contractional deformation along the forearc at 3.6 Ma (Folguera and Ramos, 2009). Ocean magnetic anomalies suggest that the point of intersection between the Mocha Fracture Zone (MFZ) and the Chilean trench would have been located in the Darwin gap, some 130 km north of its present position. The contemporary MFZ is associated with an abundance of seamounts.

A detailed tectonic reconstruction of the Nazca plate could reveal more about the source of the subducted structure; in particular, if it was formed at the spreading ridge, then it may have a conjugate on the Pacific plate. It is therefore worth noting that a simple tectonic reconstruction (Müller et al., 2008) reveals that the formation region of the Nazca plate, now located along the central Chilean margin, may have formed at a similar time to a zone of bathymetric heterogeneity, now located on the Pacific plate at  $\sim 35^\circ\text{S}$  (Figure 4.6). Assuming that the seamount structure is fully coupled to the downgoing plate and that the subduction rate has remained constant throughout its descent, it would have entered the trench at  $\sim 1.8$  Ma.

The topographic high in the Darwin gap is coincident with high preseismic locking (Métois et al., 2012; Moreno and Rosenau, 2010), small coseismic slip, the hypocentre of the mainshock, and reduced aftershock activity (Figure 4.5a), indicating that it influenced the rupture dynamics of the Maule earthquake. If the structure remains fully attached to the Nazca plate, then it likely influenced the rupture by acting as a geometric irregularity on the plate interface. In this case, we would expect there to be active deformation within the forearc, a signal of which may be evident at the surface.

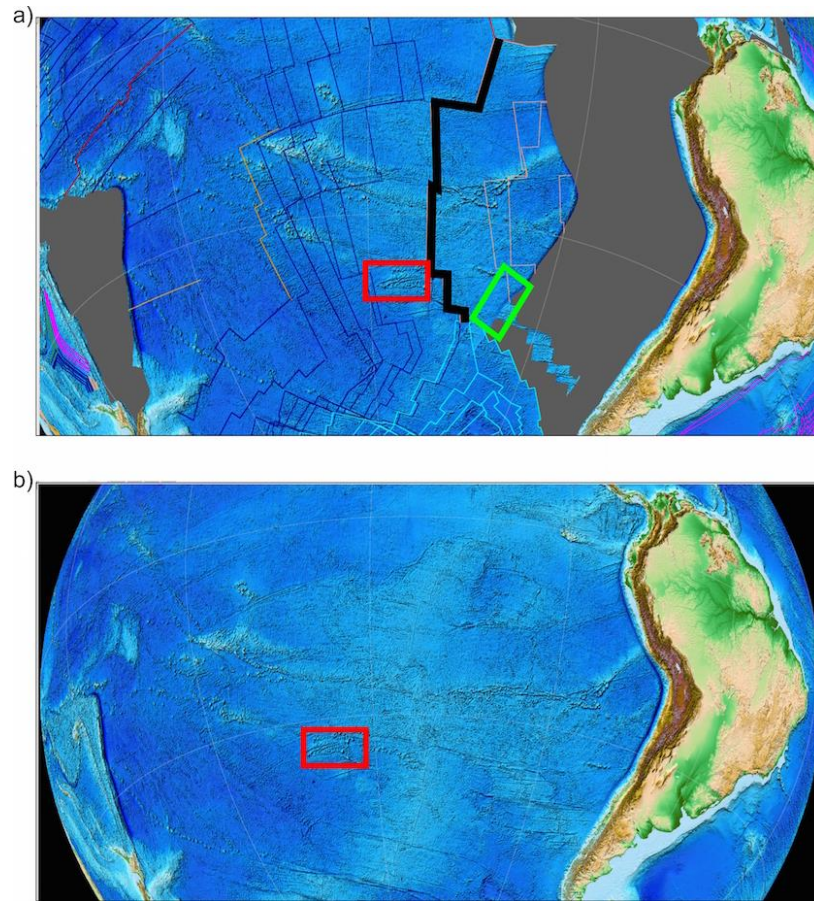


Figure 4.6: a) Reconstructions of the Nazca and Pacific plates at 20Ma illustrating that the central Chilean margin (green boxed area) may have formed at a similar time to an area of bathymetric heterogeneity (red boxed area) on the Pacific plate, now located at  $\sim 35^{\circ}\text{S}$  (b).

Such topographic features on the plate interface have been shown to act as either asperities (Husen et al., 2002) or barriers (Kodaira et al., 2000). One theory states that high relief on the downgoing plate increases coupling, thereby generating large earthquakes (Scholz and Small, 1997). Conversely, damage sustained by the overriding plate during seamount subduction may favour aseismic creep and small earthquakes, inhibiting large rupture propagation (Wang and Bilek, 2011). Due to the proximity of the subducted feature to the mainshock hypocentre, our results imply that relief on the downgoing plate increases interface coupling and initiates large ruptures. The largest slip, however, was away from the anomaly, suggesting that its heterogeneous structure and stress conditions hinder the development of large seismic slip. The complex network of fractures expected within a subducted seamount (Wang and Bilek, 2011) may contribute to the low slip in this area, despite high interseismic coupling.

## 4.5 Conclusions

Alternatively, if the topographic feature is now partially or wholly detached from the downgoing plate, or even accreted into the lower forearc crust, it could still disrupt normal seismogenesis along the interface. The sparse aftershock seismicity occurring within the region of fast material (Figures 4.1 and 4.5) would then indicate that this part of the interface is where fault slip is mainly aseismic. In this case, the up-dip boundary of the structure represents a transition between the locked and creeping zone, which is conducive to small seismic events (Lapusta and Rice, 2003). It is plausible that a small event contributed to the nucleation of the 2010 Maule earthquake. Regardless of the current state of the observed structure, it appears to have influenced the initiation of the rupture. Moreover, our model shows that in regions of large coseismic slip, the megathrust is characterised by lower seismic velocities (Figure 4.5).

## 4.5 Conclusions

Our preferred model (Figure 4.7) shows that in the Darwin gap, a subducted topographic high, possibly a former seamount, played a part in both nucleating the earthquake and modulating the coseismic slip once the rupture started. This dual behaviour of a subducted oceanic structure is a unique inference. High stress accumulation at its up-dip boundary is likely responsible for nucleating the initial rupture. Two end-member scenarios may describe the state of stress of the subducted structure. If it is sheared off from the downgoing plate, it may be continually creeping. Conversely, if it remains fully coupled to the downgoing lithosphere, it could be locked. In the latter case, the slip deficit accumulated since 1835 would be equivalent to an  $M_w$  8.0 earthquake. These scenarios could be resolved from analysis of active vertical tectonics on the surface, and subsequent models of deformation in the overriding plate.

Our model shows that variations in seismic properties along the megathrust are important in controlling rupture dynamics of large earthquakes. We stress the need for further analyses of long-term afterslip and locking models to resolve the frictional characteristics of the Darwin gap seamount. Furthermore, it is essential to locate and understand such subducted topographic features in unbroken seismic gaps around the

## Chapter 4: The 2010 Mw 8.8 Maule, Chile Earthquake: Nucleation and Rupture Propagation Controlled by a Subducted Topographic High

globe to better constrain their effect on interseismic locking and slip during large earthquakes.

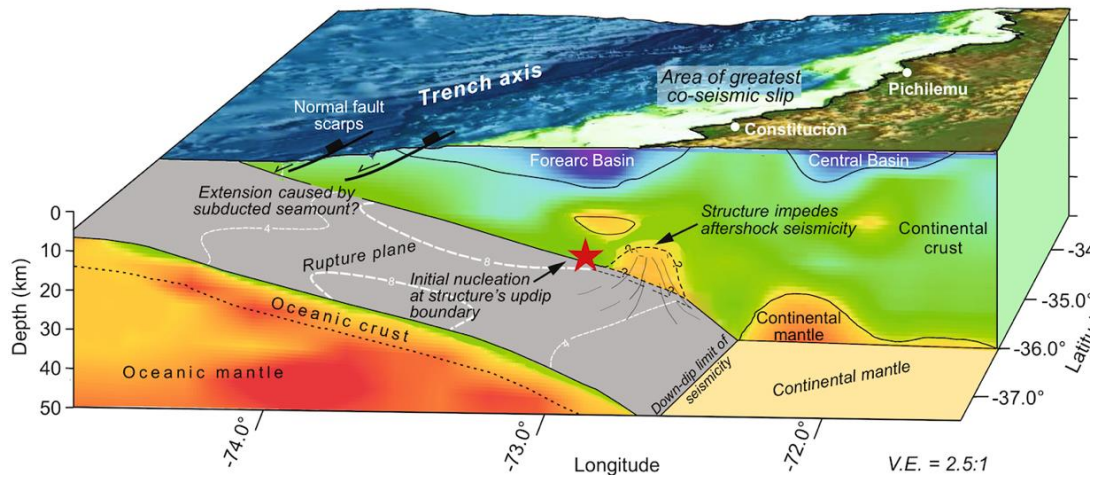


Figure 4.7: Schematic interpretation based on our tomographic model. Our 3-D model is cut along two sections: 37.5°S to show the velocity structure of the oceanic lithosphere, and 36°S to show the structure of the forearc. The geometry of the rupture plane is illustrated between these two sections. The subducted topographic anomaly which lies beneath the coastal ranges at around 36°S disrupts the regular megathrust interface; however, we cannot tell whether it is still fully coupled to the downgoing plate. The red star denotes the hypocentral location of the mainshock. White lines along the interface show the coseismic slip distribution (Moreno et al., 2012).



## Chapter 5

# ANATOMY OF A MEGATHRUST: THE 2010 M8.8 MAULE, CHILE EARTHQUAKE RUPTURE ZONE IMAGED USING SEISMIC TOMOGRAPHY

This chapter is from a paper published in *Earth and Planetary Science Letters* (Enclosure 3). The paper was accepted for publication on August 26, 2014 and published on November 1, 2014. Authors are Stephen Hicks (main author), Andreas Rietbrock (University of Liverpool), Isabelle Ryder (University of Liverpool), Chao-Shing Lee (National Taiwan Ocean University) and Matthew Miller (Universidad de Concepción). The Supplementary Information of the published paper is incorporated into the main body of this chapter. The results of this paper were disseminated through a press release and reported by several online news agencies (Enclosure 4). This research was the primary focus of my PhD project during July 2012 – April 2014. The aim of this study was to make a more detailed image of the velocity structure for the Maule rupture zone (Key Aim 1) compared to that presented in Chapter Four. Instead of using automatically determined onset times, we use a higher quality set of manually determined onset times. Furthermore, we take observations from ocean-bottom seismometer deployments to increase the imaging capability of the marine forearc. Using this more detailed model, we are able to make interpretations about the structure of the subducting plate interface and overriding forearc, providing inferences on the way they affect megathrust dynamics.

### Published paper abstract

Knowledge of seismic velocities in the seismogenic part of subduction zones can reveal how physical structures may influence large ruptures. Observations of aftershocks that followed the 2010  $M_w$  8.8 Maule, Chile earthquake allow an exceptional dataset to examine the physical properties of a megathrust rupture zone. We manually analyse aftershocks from onshore seismic stations and ocean-bottom seismometers to derive a 3-D velocity model of the rupture zone using local earthquake tomography. From the trench to the magmatic arc, our velocity model illuminates the main features within the subduction zone. We interpret an east-dipping high P-wave velocity anomaly ( $> 6.9$  km/s) as the subducting oceanic crust and a low P-wave velocity ( $< 6.25$  km/s) in the marine forearc as the accretionary complex. We find two large P-wave velocity anomalies ( $\sim 7.8$  km/s) beneath the coastline. These velocities indicate an ultramafic composition, possibly related to extension and a mantle upwelling during the Triassic.

We assess the role played by physical heterogeneity in governing megathrust behaviour. Greatest slip during the Maule earthquake occurred in areas of moderate P-wave velocity (6.5–7.5 km/s), where the interface is structurally more uniform. At shallow depths, high fluid pressure likely influenced the up-dip limit of seismic activity. The high velocity bodies lie above portions of the plate interface where there was reduced coseismic slip and minimal postseismic activity. The northern velocity anomaly may have acted as a structural discontinuity within the forearc, influencing the pronounced crustal seismicity in the Pichilemu region. Our work provides evidence for how the ancient geological structure of the forearc may influence the seismic behaviour of subduction megathrusts.

## 5.1 Introduction

Understanding the physical processes that control the behaviour of subduction zone megathrust faults remains one of the main goals in earthquake seismology. The conceptual subduction zone asperity model (Lay and Kanamori, 1981) was developed to explain the inhomogeneous moment release of large earthquakes. Asperities are regions of the plate interface that produce the strongest slip, whereas barriers inhibit rupture. Roughness on the downgoing plate, such as seamounts can act as either



asperities (e.g. Abercrombie et al., 2001) or barriers (e.g. Kodaira et al., 2004). Alternatively, features within the overriding plate, such as crustal batholiths (Sobiesiak et al., 2007), forearc basins (Fuller et al., 2006; Song and Simons, 2003) and faults (e.g. Audin et al., 2008) can also influence rupture behaviour. Based on the seismic characteristics of megathrust earthquakes, Lay et al. (2012) subdivide the plate interface fault into five distinct depth domains. Knowledge of fault properties could reveal what governs this megathrust segmentation and the physical origins of asperities and barriers.

Passive seismic imaging can shed light on fault zone structure. However, many subduction megathrusts lie offshore, where seismic instrumentation is deficient. This uneven station coverage reduces imaging capability and can cause the mislocation of offshore earthquakes. With its coastline lying  $< 100$  km to the trench in places, the central Chile margin (Figure 5.1), is an ideal natural laboratory to study the subduction interface.

In 2010, an  $M_w$  8.8 earthquake struck the Maule region of central Chile. After the earthquake, a dense seismometer network was deployed on the forearc to record aftershocks (e.g. Rietbrock et al., 2012). Fortunately, the onshore network was later supplemented by ocean-bottom seismometer (OBS) deployments, dramatically improving station coverage (Figure 5.2). Studies of preseismic locking (e.g. Moreno and Rosenau, 2010), the coseismic rupture (e.g. Moreno et al., 2012) and postseismic deformation (e.g. Y. N. Lin et al., 2013) describe the behaviour of the Maule megathrust at different stages of the seismic cycle. This behaviour suggests that spatial variations in physical properties could exist in the fault zone.

The purpose of our study is to detect physical heterogeneity along the Maule megathrust using seismic tomography. In our preliminary tomographic study of the rupture zone based on automatically determined P- and S-wave arrival times (Chapter Four), we identified a large seismic velocity anomaly lying along the plate interface. This study used observations from onshore stations only, resulting in reduced offshore imaging capability. To build on this work, we manually analyse onset times and incorporate OBS observations to derive a more detailed 3-D velocity model of the rupture zone. We examine the quality of our velocity model by analysing the resolution

## 5.2 Characteristics of the central Chile subduction zone

matrix and by testing characteristic models. We compare plate interface velocity structure with behaviour during the seismic cycle, providing valuable insights into the physical origins of asperities and barriers.

## 5.2 Characteristics of the central Chile subduction zone

Along the Central Chilean margin, earthquakes are driven by subduction of the Nazca plate beneath the South American plate at a rate of 74 mm/yr (e.g. DeMets et al., 2010). Large earthquake ruptures along the margin tend to occur within highly-coupled segments (Métois et al., 2012). We focus on the Maule segment, which is demarcated by the Mocha Block to the south and the Juan Fernández Ridge to the north (Contreras-Reyes et al., 2013). The Maule segment last fully ruptured during the great 1835 Concepción earthquake and was recognised as a mature seismic gap (e.g. Ruegg et al., 2009).

Active- and passive-source seismic studies have established the deep subsurface structure in parts of the Maule segment. The 7 km thick oceanic crust subducts at an angle of  $\sim 6^\circ$  beneath the trench (Contreras Reyes et al., 2008; Moscoso et al., 2011), steepening to  $\sim 15^\circ$  beneath the coastline (e.g. Haberland et al., 2009; Hayes et al., 2012). The marine forearc comprises two domains: the frontal accretionary prism and the palaeo-accretionary complex (outer wedge), (e.g. Contreras Reyes et al., 2008). The continental Moho intersects the subducting plate beneath the eastern coastal ranges; however, its exact position is debated. Based on our preliminary tomographic model presented in the preceding chapter, we interpreted the slab-mantle intersection to lie at  $\sim 50$  km depth, similar to that estimated south of the Maule segment (e.g. Haberland et al., 2009). Conversely, Dannowski et al. (2013) postulate that based on receiver functions, the intersection lies at  $\sim 38$  km depth in the Maule segment. Further east, the continental crust thins to  $\sim 30$  km, defining the underlying arch-shaped, high velocity continental mantle (e.g. Haberland et al., 2009). In Chapter Four, we found a high  $v_p$  anomaly on the plate interface beneath the coast at  $36^\circ\text{S}$  that was interpreted as a subducted seamount.

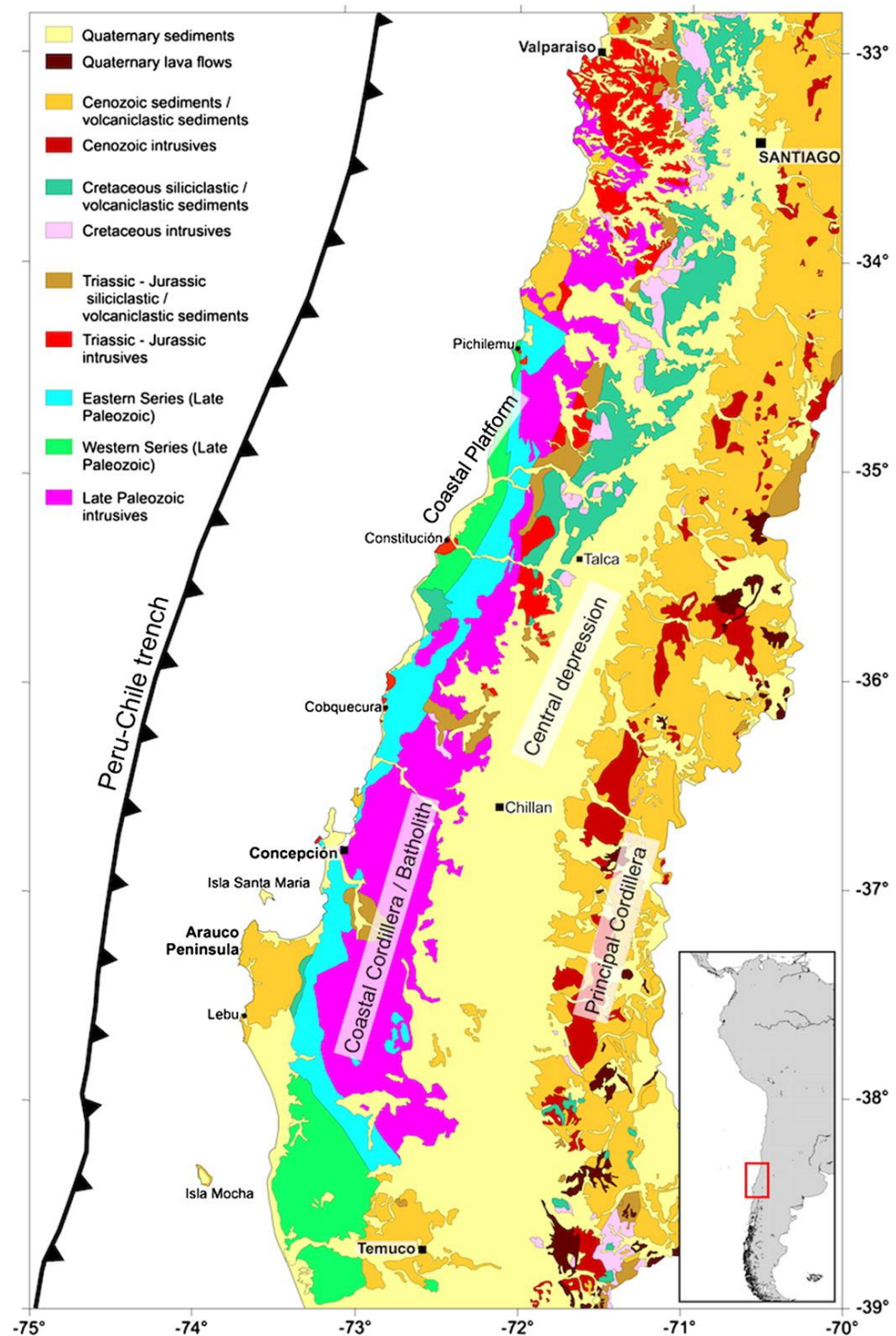


Figure 5.1: Geotectonic characteristics and simplified geological map of the central Chilean margin. Morphotectonic units are from Glodny et al. (2007) and the geological is map redrawn after Sernageomin (2003), Melnick and Echtler (2006a) and Vásquez et al. (2011). The red box in the inset map gives the location of the study area. Labels show the names of the locations referred to in this chapter.

### 5.3 The 2010 Maule earthquake

The geology of the coastal cordillera (Figure 5.1) encompasses a late-Palaeozoic paired intrusive-metamorphic belt with two series of metasediments (e.g. Martin et al., 1999). The Western Series constitutes low-grade metapsammopelitic rocks with intercalations of metabasite derived from an ancient accretionary prism. Along the eastern coastal cordillera, late Palaeozoic granite batholiths intrude the Eastern Series. The composition of these granites indicates a shallow, crustal-derived source (Lucassen et al., 2004). Although these Palaeozoic rocks dominate the surface geology, outcrops of Triassic plutons lie along the coastline. Some of these intrusions contain fayalite, indicating a mantle-derived magmatic source (Vásquez and Franz, 2008). The intrusions were emplaced when the margin was undergoing post-orogenic collapse and rifting, marking the transitional period between Gondwanan amalgamation and contemporary Andean-style subduction (Vásquez et al., 2011).

### 5.3 The 2010 Maule earthquake

On February 27, 2010, an  $M_w$  8.8 earthquake ruptured a ~500 km long portion of the Maule segment. The earthquake nucleated offshore, 25 km from the coastline (Figure 5.2), (Hayes et al., 2013). Coseismic slip models for the rupture show that most plate interface slip occurred approximately halfway between the trench and the coastline. The models further reveal that two asperities were ruptured during the earthquake: one to the north, the other to the south of the mainshock epicentre (Figure 5.2). In this chapter, we refer only to the coseismic slip models of Moreno et al. (2012) and Lin et al. (2013) since these are based on a wide range of constraints (Section 1.1.2). Back-projection of teleseismic waves reveal that high frequency radiation came from a deeper portion of the fault, of which the overall pattern suggests triggering on physically distinct portions of megathrust (Kiser and Ishii, 2011).

Following the rupture, most aftershocks occurred along the plate interface at 10–35 km depth, with a second band at 40–45 km depth (Lange et al., 2012; Rietbrock et al., 2012). In Chapter Four, we showed that the resulting gap in seismicity coincides with the location of a high P-wave velocity anomaly. Another feature of the aftershock sequence was intense shallow, normal faulting seismicity in the north, near Pichilemu (2012). Bedford et al. (2013) and Lin et al. (2013) indicate that most postseismic deformation was aseismically released, assumed to be afterslip. Bedford et al. (2013)

show that most afterslip occurred seaward of the coastline; Lin et al. (2013) suggest most afterslip occurred landward of the coastline.

## 5.4 Seismic data

### 5.4.1 Temporary seismic networks

Following the Maule earthquake, teams from Chile, the US and Europe installed seismometers in the rupture area to record aftershock seismicity. The International Maule Aftershock Deployment (IMAD) is composed of ~160 three-component broadband instruments on the continental forearc (Figure 5.2). Most stations were deployed within one month after the earthquake. Station coverage peaked between April and June 2010, with many stations active until September 2010. Onshore data alone, however, is insufficient for accurately imaging the offshore region, where most coseismic and aftershock activity occurred. Fortunately, after the Maule earthquake, UK and Taiwanese institutions deployed two separate OBS networks in the rupture area (Figure 5.2). The Taiwanese deployment is composed of 17 OBS instruments that were initially active from 15th July to 8th August 2010. The stations were then moved northward in a second stage from 14th August to 6th September. The UK deployment had 10 OBS instruments offshore of the Arauco Peninsula from August 2010 to March 2011.

### 5.4.2 Catalogue selection, onset times and initial event locations

For a well-resolved tomography model, we require a uniform source-receiver distribution across the rupture area to ensure that resolution is even throughout the model. Due to the uneven aftershock distribution, we used a set of criteria to select the event dataset. From an automatic catalogue (Rietbrock et al., 2012), we first chose events with large magnitudes ( $M_l > 4.0$ ) so that many clear onsets are recorded throughout the network. Second, we subdivided the area into smaller 2500 km<sup>2</sup> blocks and selected an equal number of events in each, ensuring an even event distribution. Third, we selected events that were located within each OBS network during their operational periods. Fortunately, both the northern and southern OBS networks were simultaneously active for 15 days (22/08/10–06/09/10); therefore, as a final step, we chose events located between these two networks during this time.



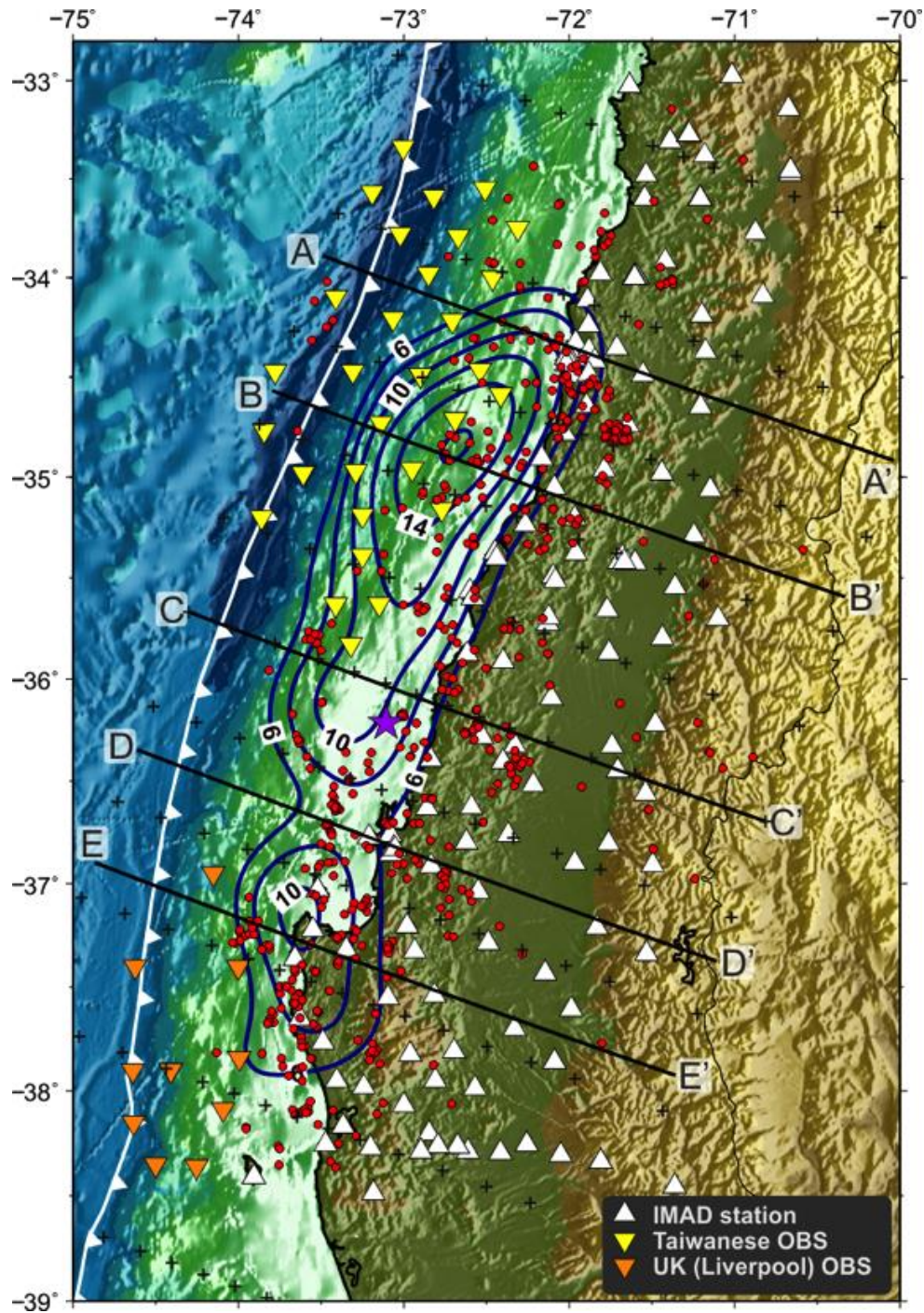


Figure 5.2: Map of the Maule segment along the South Central Chile margin coloured by bathymetry/topography. The main rupture characteristics of the Maule earthquake are shown. The purple star shows the epicentre of the mainshock (Hayes et al., 2013) and the blue contours represent coseismic slip distribution (> 6 m) in 2 m intervals (Moreno et al., 2012). Triangles correspond to seismic stations used in the velocity inversions. Black crosses indicate the horizontal grid nodes used in the 3-D inversion and red circles show the preliminary locations of 669 earthquakes used in the velocity inversions. Thick black lines show the location of cross-sections that are shown in this chapter.

These criteria resulted in an initial catalogue of 710 events. We manually determined onset times of P- and S-waves for these events using the SDX software (<http://doree.esc.liv.ac.uk:8080/sdx>). Based on onset time uncertainties, we assigned each observation a weight as follows: Weight 0 ( $< 0.04$  s); Weight 1 (0.04–0.10 s); Weight 2 (0.10–0.20 s); Weight 3 (0.20–1.00 s); Weight 4 ( $> 1.00$  s). Using these onset times, we located the events inside the one-dimensional (1-D) velocity model of Haberland et al. (2006) using HYPO71PC (W. H. K. Lee and Valdes, 1985). We rejected events with an azimuthal maximum azimuthal gap (GAP) of  $> 270^\circ$  and with fewer than 12 P-wave and 4 S-wave observations. We also rejected all observations with weights of 3 and 4. Applying these criteria reduced the initial dataset by 6%, leaving a high-quality catalogue of 669 events (Figure 5.2), comprising 38,000 P-wave and 13,000 S-wave onset times.

## 5.5 Velocity inversion strategy

We used a staggered velocity inversion scheme (e.g. Collings et al., 2012; Haberland et al., 2009) in which we inverted for 1-D model, followed by a coarse 2-D model, a fine 2-D model, and finally a 3-D model. Such a strategy ensures that a smooth regional velocity model in the trench-perpendicular direction can be established without velocity artefacts (from the 1-D model) in poorly resolved regions, which may affect event locations. Establishing a 2-D model with reliable earthquake locations is an important step before resolving any 3-D (trench-parallel) velocity variations. At each step, we chose damping values from trade-off curves of data variance versus model complexity (e.g. Eberhart-Phillips, 1986). The inversion parameters used at each stage are summarised in Table 5.1.

### 5.5.1 1-D inversion

We selected events located inside the network ( $\text{GAP} < 180^\circ$ ), leaving 627 events for the 1-D inversion. We inverted for P-wave velocity ( $v_p$ ) and S-wave velocity ( $v_s$ ) using VELEST (Kissling et al., 1994). VELEST requires that all stations are located within the uppermost layer. However, the greatest station elevation is 2.2 km and deepest OBS station lies 5.4 km below sea level; a model with an 8 km thick uppermost layer is impractical. We negated this problem by adopting the strategy of Husen et al. (1999),

## 5.5 Velocity inversion strategy

setting station elevations to zero and allowing station terms to absorb systematic onset errors. We kept station damping low in the 1-D inversion to ensure that site terms accounted for station elevations and regional 2-D velocity variations. For the 1-D inversion, we tested 2000 initial models that were generated by randomly perturbing the velocity of each layer in our starting model (Haberland et al., 2006). In each inversion, we used a  $v_p/v_s$  of 1.79, as determined from Wadati diagram analysis. From the 2000 inversions, we selected the model with the lowest root mean square residual as our best  $v_p$  model and then inverted for a 1-D  $v_s$  model.

Inversion step	Min. horiz. spacing (km)	Min. vertical spacing (km)	GAP	No. events	Damping values	P Data var.		S-P data var.	
						$\sigma^2$	%	$\sigma^2$	%
<b>Min. 1-D model</b>	-	5	180°	627	$v_p$ : 100 $v_s$ : 100	.34	100	.43	100
<b>2-D coarse model</b>	25	10	180°	589	$v_p$ : 10000 $v_p/v_s$ : 333	.10	31	.22	51
<b>2-D fine</b>	16	8	210°	669	$v_p$ : 3000 $v_p/v_s$ : 333	.10	28	.21	48
<b>3-D model</b>	16	8	210°	669	$v_p$ : 333 $v_p/v_s$ : 40	.04	12	.09	22
<b>Final 3-D model with station corr.</b>	16	8	210°	669	$v_p$ : 333 $v_p/v_s$ : 40 Station: 100	.04	11	.08	20

Table 5.1: Summary of inversion parameters used at each step. GAP = minimum azimuthal gap.

The best-fitting 1-D model (Figure 5.3a) has low  $v_p$  of 5.1 km/s at shallow depths, increasing to 6.1 km/s at 5 km depth. Velocities of greater than 7 km/s are reached at 20 km depth. The uppermost layer of the minimum 1-D model is poorly constrained due to the lack of shallow events and expected velocity structure differences between the offshore and onshore areas. Velocities in the uppermost layer are  $\sim 0.8$  km/s slower than the model of Haberland et al. (2006), a result of the greater amount of offshore observations in our study.



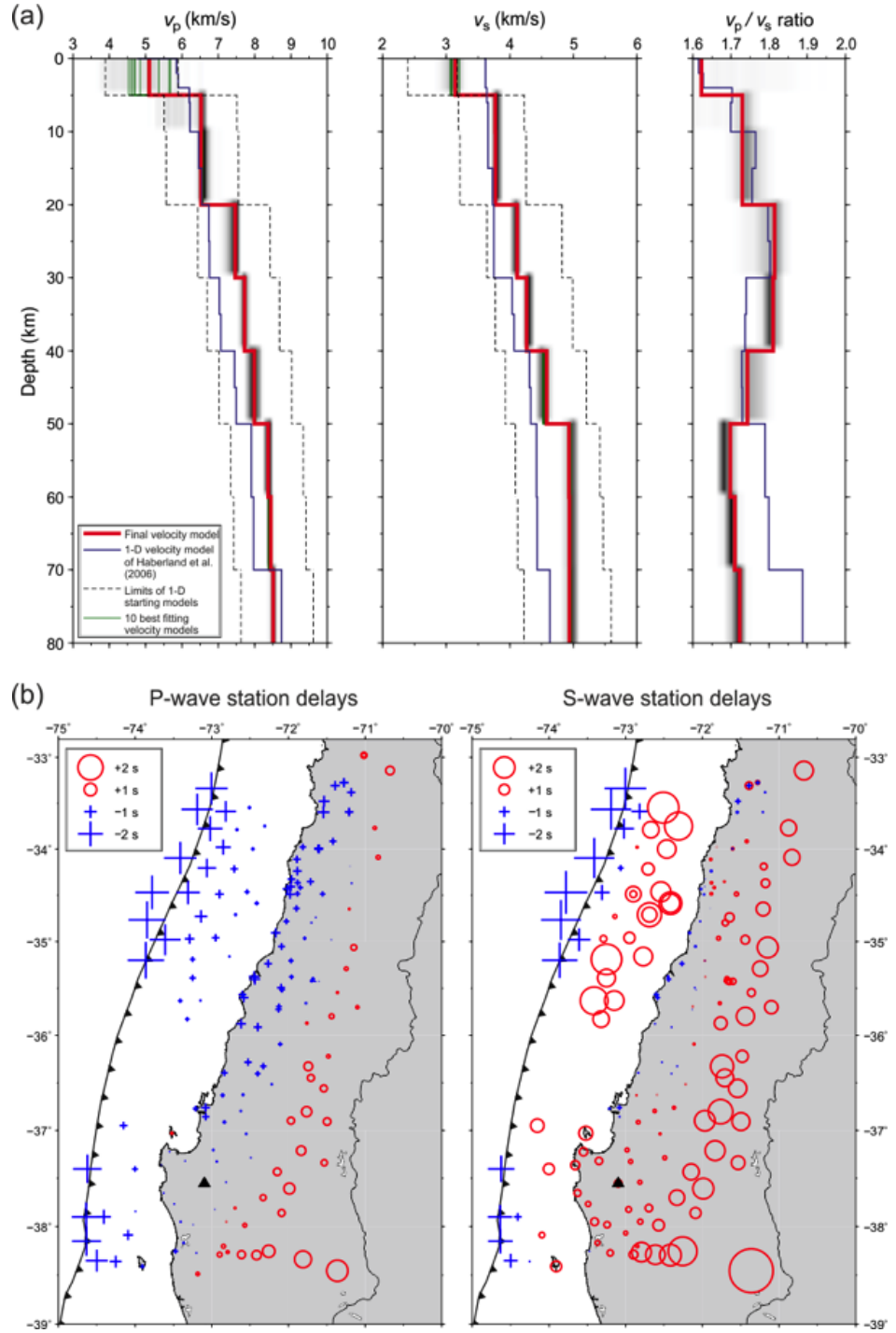


Figure 5.3: Results of the 1-D velocity model inversion. a) 1-D velocity models showing the range of starting models, range of inverted models (grey shading), and the preferred velocity model (red line). b) Map of 1-D station delay terms. The reference station is indicated by the black triangle.

Station delays are important for generating accurate 1-D event locations if the subsurface has significant 2-D velocity variations. We find large negative delays for both P-waves ( $> -3.0$  s) and S-waves ( $> -2.7$  s) at OBS stations located offshore of the

## 5.5 Velocity inversion strategy

trench axis (Figure 5.3b). The P-wave station terms increase toward the magmatic arc, with stations there having the largest P-wave delays ( $< 1.7$  s). There is also a trench-parallel variation in onshore P-wave station terms, with values more positive toward the south. In contrast, S-wave delays are large and positive at stations on the continental shelf (up to 2.9 s). The systematic trench-perpendicular variation in station delays mainly results from dipping structures in the subsurface, and to a lesser extent, station elevation differences.

### 5.5.2 2-D and 3-D tomographic inversion

For the 2-D and 3-D tomographic inversions, we used SIMUL2000 (Eberhart-Phillips and Michael, 1998; Thurber, 1983). This algorithm simultaneously inverts for seismic velocity and hypocentral parameters using an iterative damped least squares method; it uses a direct inversion for  $v_p/v_s$  to account for the reduced number of high-quality S-wave observations compared to P-wave observations. Velocities are inverted on a rectangular grid of nodes with linear B-spline interpolation. In each inversion, we did not invert for station corrections and kept hypocentres fixed for the first three iterations.

We first inverted for a coarse 2-D model, in which a 3-D grid was used, but velocity nodes in the along-strike direction were kept fixed, effectively forming a 2-D inversion. The grid for 2-D inversion had a uniform horizontal grid spacing of 25 km and 10 km spacing in depth. Beneath the outer rise and trench, we linked vertically adjacent nodes at depths of 15 km or greater due to diminished ray coverage. Linking nodes (Thurber and Eberhart-Phillips, 1999) allows for coarser node spacing in parts of the model. Without linking nodes, we found that the inversion introduced low velocity artefacts in this part of the model, biasing earthquake depths beneath the outer rise. For the fine 2-D and 3-D inversions, we used a minimum horizontal grid spacing of 16 km and a minimum vertical spacing of 8 km. For the 3-D inversion, we introduced a set of nodes in the trench-parallel direction, each 55 km apart, providing 13 nodes to image velocity variations in the trench-parallel direction (Figure 5.2). These nodal spacings allow for a finer resolution image than that of our tomographic model presented in Chapter Four.

For the coarse 2-D inversion, we used events inside the network ( $\text{GAP} < 180^\circ$ ) to establish the main velocity structure. Nonetheless, a test showed that when the closest stations were located more than 40 km from an earthquake, its depth was poorly constrained. This finding was important for events located in between the two OBS networks (Chen et al., 1982; Frohlich et al., 1982). Therefore, we only chose events that had their closest two stations at an epicentral distance of less than 40 km. These criteria resulted in a catalogue of 589 events for the coarse 2-D inversion. Once the main velocity structure was established, we subsequently relaxed the station distribution ( $\text{GAP} < 210^\circ$ ) for the fine 2-D inversion to improve ray coverage at the edges of the grid.

To improve the lateral imaging capability of our inversions, we applied an extra smoothing technique. We performed two additional inversions, each shifting the horizontal node locations by a third of the nodal spacing, and calculating the average velocity of these. For the 3-D inversion, we also carried out this averaging in the trench-parallel direction. Such an averaging technique has been used in local earthquake tomography studies (e.g. Collings et al., 2012; Haberland et al., 2009).

## 5.6 Inversion resolution

### 5.6.1 Resolution tests

Our first resolution test focussed on the full model resolution matrix (MRM). Nodes with good ray coverage have large diagonal elements of the MRM. Nodes with poor coverage have small diagonal elements of the MRM due to their dependency on neighbouring grid points. This effect is known as smearing. We estimated the magnitude of smearing by calculating the spread function (SF), which assesses the ratio between off-diagonal and diagonal terms (Toomey and Foulger, 1989). To accurately visualise the direction and size of smearing of nodes, we contoured each row of the MRM at the 70% value of its corresponding diagonal element.

As another resolution test, we analysed the sensitivity of our velocity models to the event catalogue; we achieved this by performing a bootstrap resampling. Compared to formal MRM analysis, bootstrap resampling is useful because noise is intrinsically contained within the dataset. Calvert et al. (2000) suggest that such event-

## 5.6 Inversion resolution

based resampling should produce similar results to resampling individual picks. We randomly resampled the event catalogue, forming a catalogue of 530 events (80% of our original catalogue). Once the 530 events were chosen, we randomly chose duplicate events, ensuring the catalogue was of the same size as for the actual inversion (589 events). Using the same inversion workflow, the velocity models were then stored and the process repeated 100 times.

As a final assessment of imaging capability, we carried out restoring resolution tests. By designing synthetic velocity models, we assessed the capacity of our dataset to resolve the geometry and amplitude of velocity anomalies. We calculated synthetic travel times using the true source-receiver geometry. To reflect the true quality of our observations, Gaussian noise was added to the travel times with a standard deviation depending on onset time uncertainties (0.04–0.20 s; Section 5.4.2). We then inverted the travel times using the same workflow of our real inversion. We designed the synthetic velocity model with two objectives in mind. First, we examined whether our inversion could constrain the geometry and amplitude of high velocity bodies lying along the plate interface that we identified in Chapter Four. Second, we tested whether we could resolve lateral variations of  $v_p/v_s$  in the subducting oceanic crust. Our input model also comprised the main domains of the Central Chile subduction zone identified in Chapter Four and from earlier studies (e.g. Haberland et al., 2009). The final 3-D model used as input for the restoring resolution test is shown in Figure 5.4 ( $v_p$ ) and Figure 5.5 ( $v_p/v_s$ ).

### 5.6.2 2-D model resolution

MRM analysis of the 2-D  $v_p$  model (Figure 5.6a) shows that most nodes have large diagonal elements and symmetric resolution kernels. This finding indicates that in most parts, the model is well resolved up to the trench and down to depths of 80–90 km beneath the Central Depression. Compared to our tomographic model in Chapter Four, the inclusion of OBS data dramatically improves imaging resolution of the marine forearc. Beneath the magmatic arc, at depths of 20–90 km, diagonal elements are small with large and elongate resolution contours, indicating poor resolution. Resolution is also poor west of the trench, beneath the outer rise.

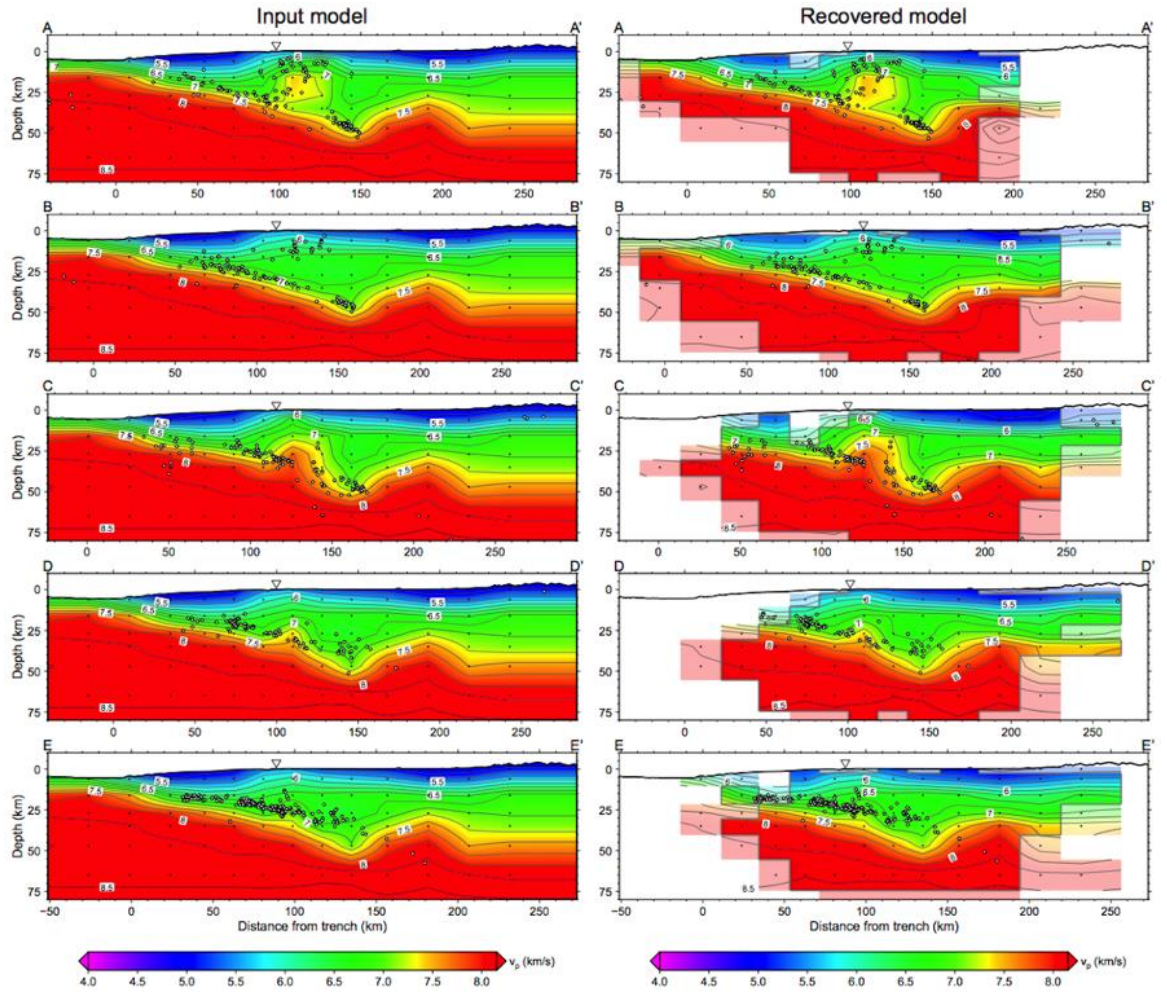


Figure 5.4: (left) Synthetic 3-D  $v_p$  input model and (right) corresponding inversion results for the restoring resolution test. Locations of the five cross-sections are shown in Figure 5.2. Black crosses indicate inversion nodes and white dots show the locations of the 669 earthquakes used. The thick grey line gives regions of the model with good resolution. Areas with reduced resolution are faded; regions with no resolution are left blank. The location of the coastline is denoted by the white triangle.



## 5.6 Inversion resolution

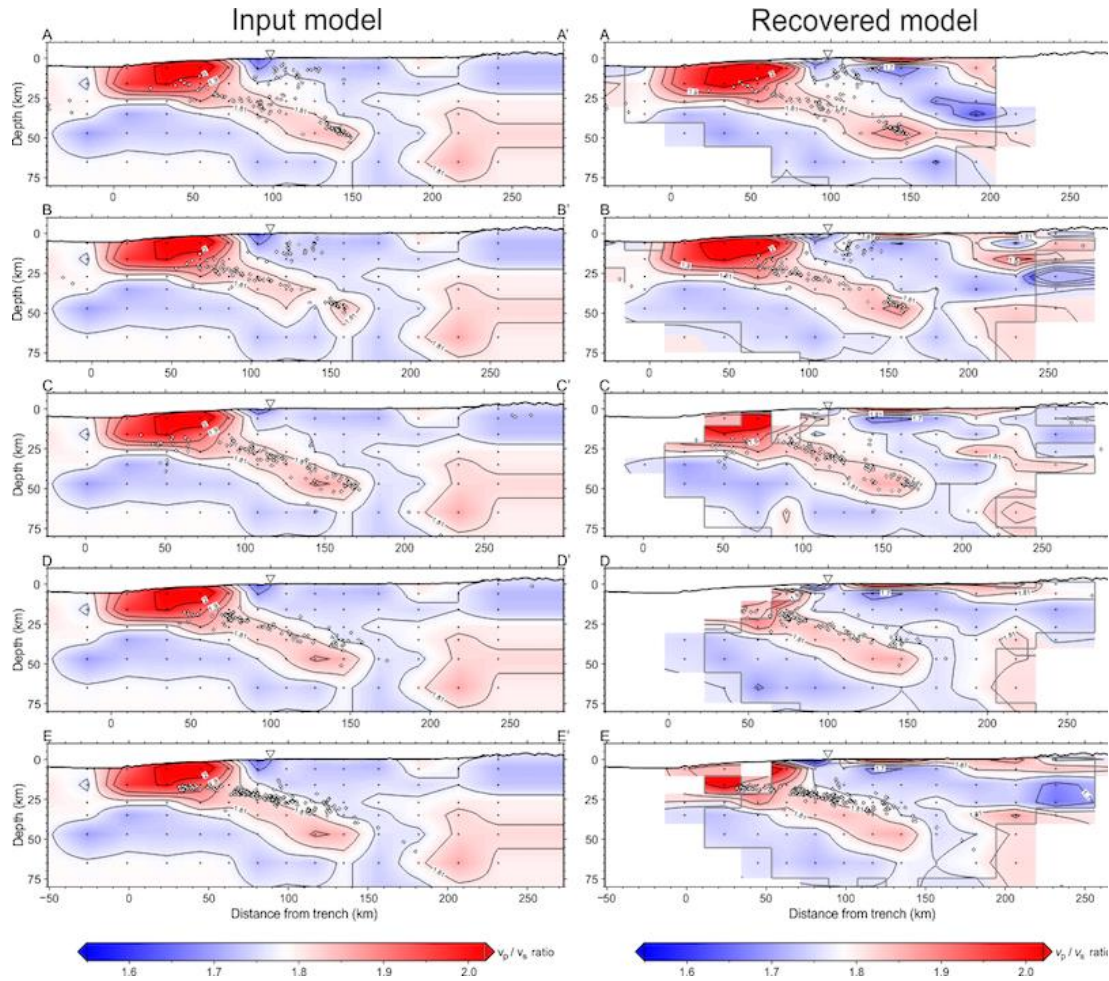


Figure 5.5: (left) Synthetic 3-D  $v_p/v_s$  input model and (right) corresponding inversion results for the restoring resolution test. Locations of the five trench-perpendicular cross-sections are shown in Figure 5.2. White dots indicate the locations of the 669 earthquakes used in the tomographic inversion. In cross-section B-B', we include a low  $v_p/v_s$  anomaly in the subducting oceanic lithosphere; the inversion is not able to fully recover this anomaly.

From the results of the bootstrapping test (Figure 5.7),  $v_p$  is well constrained throughout the model ( $\sigma_{vp} < 0.01$  km/s), indicating that the model is insensitive to the event selection criteria. Overall, the continental forearc (10–40 km depth) is the best-resolved part of the 2-D  $v_p$  model. The restoring resolution tests indicate that the size of resolved features varies with depth due to the irregular source-receiver distribution. For example, we are unable to sufficiently resolve a thin low velocity structure at 50–80 km depth, such as that imaged at the base of the continental mantle by Haberland et al. (2009). This poor resolution at greater depths is due to the lack of intermediate depth aftershocks beneath the Central Depression and magmatic arc (Figure 5.2).

For the 2-D  $v_p/v_s$  model, SF values are higher and resolution kernels are larger than in the  $v_p$  model (Figure 5.6b). This is likely due to our dataset comprising 66% fewer S-wave than P-wave observations, and fewer S-wave observations at larger epicentral distances. Some vertical smearing is present at shallow and deep nodes beneath the marine forearc, but overall, the well-resolved areas are comparable to that of the  $v_p$  model (Figure 5.6). The maximum  $\sigma_{v_p/v_s}$  is 0.04 (Figure 5.7).

Based on the combined interpretation of results from our resolution tests, SF values of less than 2.1 and 4.2 represent well-resolved areas in the 2-D  $v_p$  and  $v_p/v_s$  models, respectively. Laterally, we are able to resolve the subducting oceanic lithosphere from the trench to  $\sim 80$  km depth beneath the magmatic arc. Both the marine and continental forearcs are well resolved.

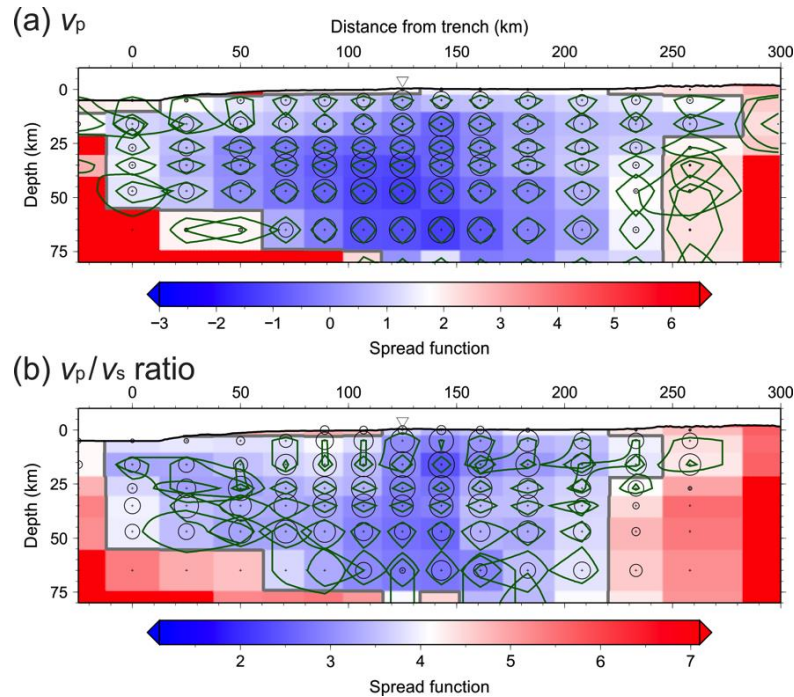


Figure 5.6: Resolution estimate of the 2-D velocity model based on analysis of the MRM. Black crosses indicate the location of inversion nodes. The different colours surrounding each node represent the SF value. The black circles show diagonal elements of the resolution matrix. Green lines represent the 70% contour line of the resolution kernel. The coastline is given by the black triangle.

## 5.6 Inversion resolution

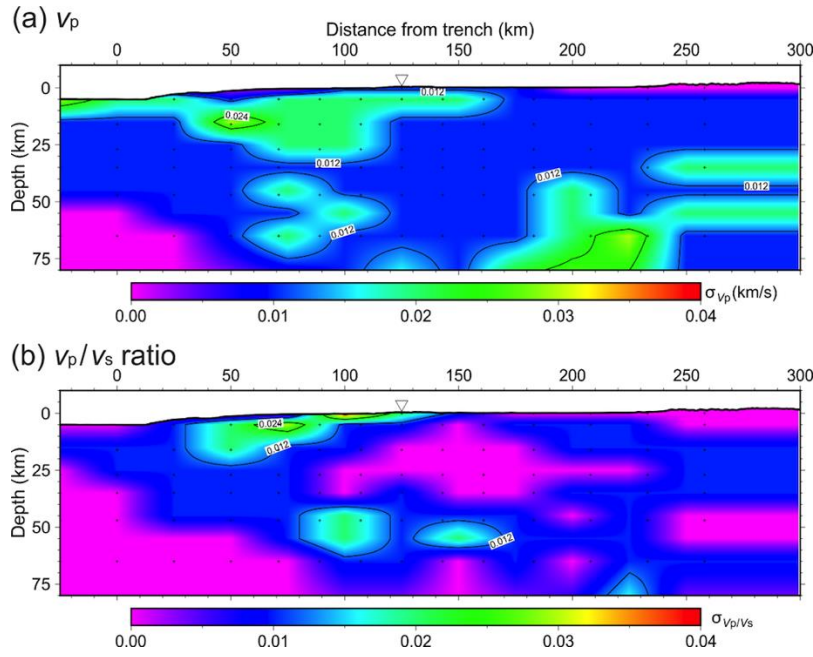


Figure 5.7: Results of the bootstrap-resampling test showing the spatial distribution of velocity standard deviation in the 2-D model. The coastline is given by the black triangle.

### 5.6.3 3-D model resolution

From the restoring resolution tests (Figure 5.4), the 3-D inversion is able to accurately recover the shape and amplitude of the input anomalies. In the continental mantle,  $v_p$  is overestimated by  $\sim 13\%$  and velocities in the shallow marine forearc are  $\sim 30\%$  too fast. Amplitudes of high velocity anomalies in the subducting crust are well recovered. Likewise, for  $v_p/v_s$ , the inversion is able to recover most features of the input model, but is not able to fully recover patches of high  $v_p/v_s$  in the subducting lithosphere (Figure 5.5). In the Central Depression, shallow marine forearc and continental mantle,  $v_p/v_s$  values are exaggerated by around 2%.

MRM analysis of the 3-D model (Figure 5.8) shows that the well-resolved area in each cross-section is similar to that of the 2-D  $v_p$  model. Nodes in the southernmost cross-section have strong smearing beneath the magmatic arc. The offshore region is poorly resolved at  $\sim 36^\circ\text{S}$  due to the lack of OBS coverage there. In the north, however, nodes are well resolved up to the trench due to denser OBS coverage. Along the onshore forearc, resolution is best in the north where there is abundant crustal seismicity. Although its resolution is lower,  $v_p/v_s$  anomalies are real (as shown by the restoring resolution test) but anomalies could be averaged over a distance greater than



the node spacing (Eberhart-Phillips et al., 2005). Overall, SF values of less than 2.1 indicate good resolution in the 3-D  $v_p$  model. The resolving capability of the 3-D  $v_p/v_s$  model is similar to that of the  $v_p$  model, with SF values of less than 4.1 indicating good resolution.

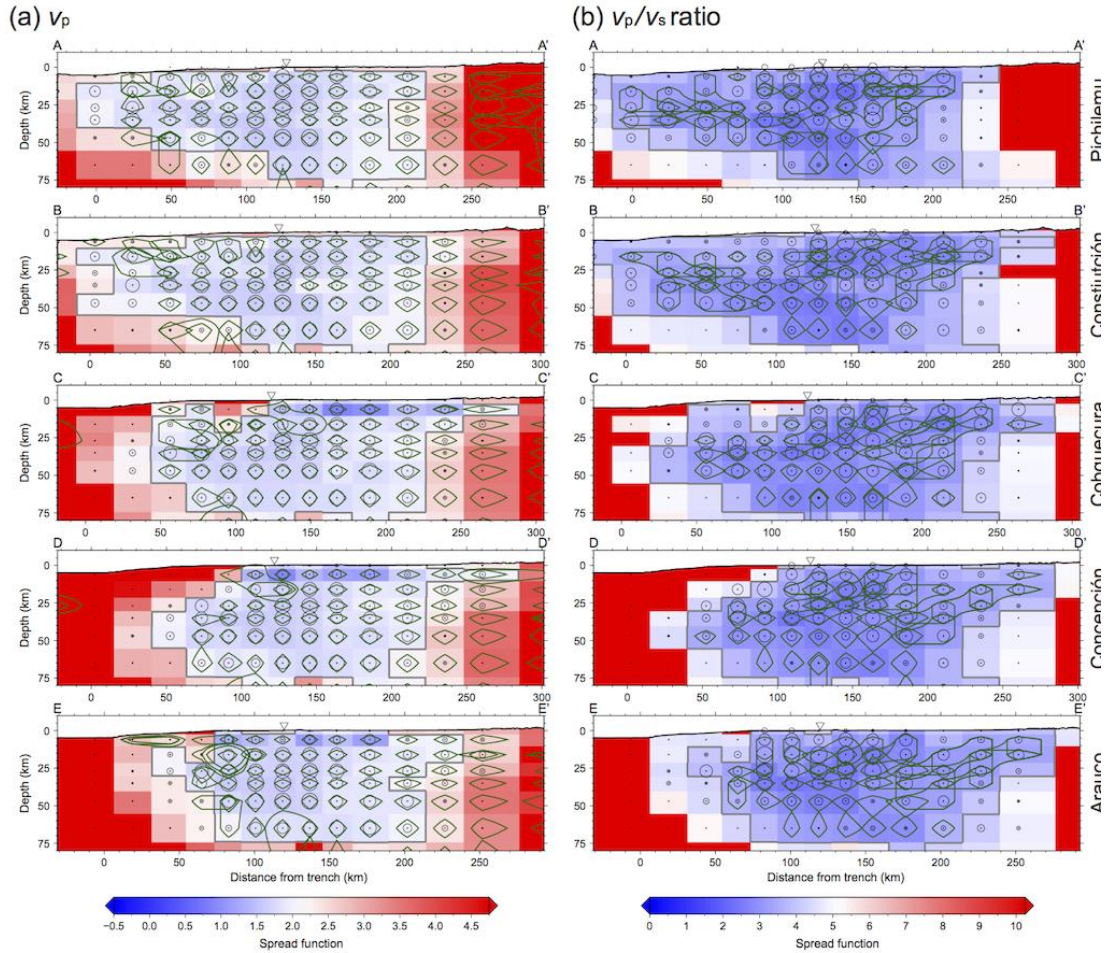


Figure 5.8: Resolution estimate of our 3-D velocity model based on analysis of the MRM. Features are plotted in the same way as Figure 5.6. Locations of the five cross-sections are shown in Figure 5.2.

## 5.7 Results and discussion

### 5.7.1 Description and interpretation of velocity models

The 2-D model is shown on a cross-section in Figure 5.9. The 3-D model is displayed on vertical and horizontal sections in Figures 5.10 and 5.11, respectively. Features described in this section correspond to labels in the figures.

## 5.7 Results and discussion

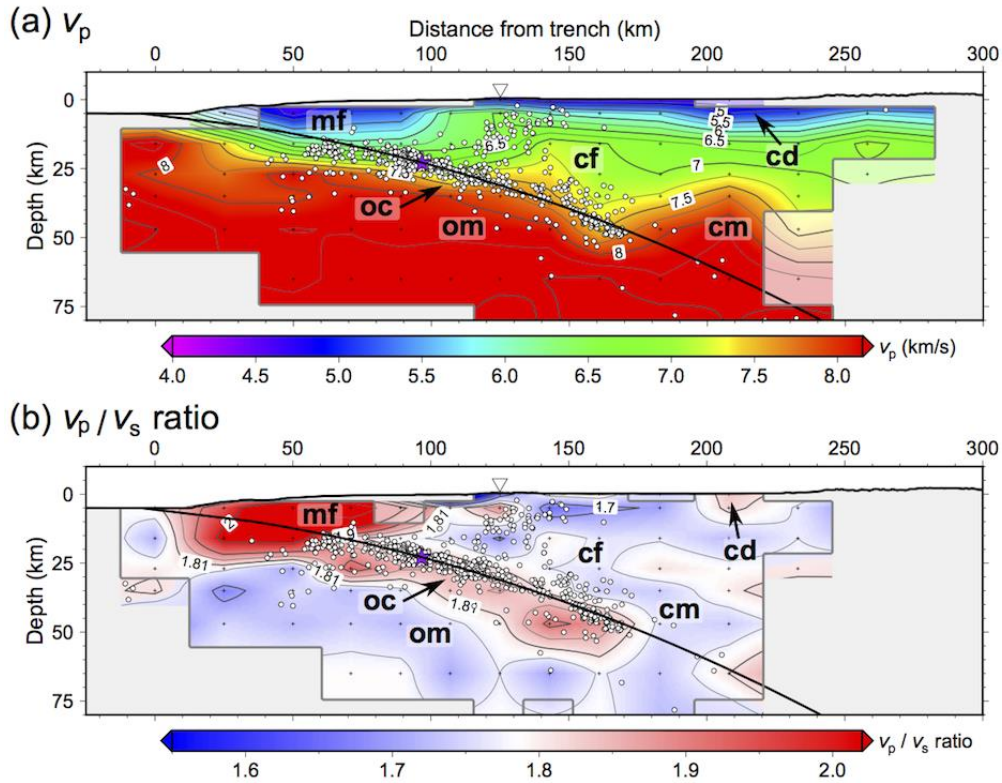


Figure 5.9: 2-D velocity model plotted on a cross-section orientated perpendicular to the trench. Crosses indicate grid nodes and white circles give the 2-D locations of events from the tomographic inversion. Based on analysis of the MRM and the characteristic model tests, limits of well-resolved areas are given by the thick grey line. Regions with diminished resolution are faded; unresolved regions are left blank. Labels refer to the following features that are discussed in the text: mf = marine forearc; oc = oceanic crust; cf = upper forearc crust; cd = Central Depression; cm = continental mantle. The thick black line indicates the location of our calculated plate interface. The purple star denotes the hypocentral location of the Maule earthquake (Hayes et al., 2013). The location of the coastline is denoted by the white triangle.

### *Subducting oceanic lithosphere*

The most prominent feature of the velocity models is an east-dipping structure with high  $v_p$  (6.9–8.0 km/s), (labelled ‘oc’). This feature also has a strong  $v_p$  gradient and elevated  $v_p/v_s$  of 1.80–1.85 (Poisson’s ratio of 0.28–0.29) along the main band of seismicity. These velocities are in agreement with previous studies in the area (e.g. Contreras Reyes et al., 2008; Haberland et al., 2009) and indicative of either hydrated oceanic crustal material (e.g. Hacker and Abers, 2004) or high pore fluid pressure. Based on velocity contours alone and the high  $v_p/v_s$  anomaly, we are unable to trace the oceanic lithosphere to depths of more than 50 km, indicating that the crust has a

lower pore pressure or is less hydrated at these depths. From our tomographic images, we are unable to determine the exact location of the oceanic Moho. Assuming a 7 km thick crust (e.g. Contreras Reyes et al., 2008), the mid-lower oceanic mantle has  $v_p$  of 7.8–8.5 km/s and a low  $v_p/v_s$  of 1.70–1.76 (Poisson's ratio of 0.24–0.26), suggesting it is not hydrated.

### *Marine forearc*

The offshore forearc region (labelled '*mf*') has low  $v_p$  (4.75–6.25 km/s) and a high  $v_p/v_s$  of 1.9–2.2. The location of such velocities is consistent with sediments and meta-sediments in the frontal prism and outer wedge, respectively. This  $v_p/v_s$  correspond to a Poisson's ratio of 0.31–0.37. Tsuji et al. (2008) relate such values to overpressured sediments in a pore pressure model for the Nankai accretionary prism. Beneath the coastline, a strong horizontal  $v_p$  gradient represents the boundary between the outer wedge and the upper continental forearc. Studies find similar velocities in the marine forearc south of the Maule segment (Contreras Reyes et al., 2008; Haberland et al., 2009) and in other subduction zones (Collings et al., 2012; Reyners et al., 2006). Overpressured fluids could result from either dehydration of the oceanic crust (e.g. Kodaira et al., 2004) or the smectite-illite transition at 100–150°C (Moore and Saffer, 2001). Based on a thermal model for South Central Chile (Völker et al., 2011), the temperature of this phase transformation coincides with the eastward limit of the frontal prism.

### *Continental forearc*

The upper continental forearc (labelled '*cf*') beneath the Coastal Cordillera has a moderate  $v_p$  of 5.5–7.0 km/s and reduced  $v_p/v_s$  of  $\sim 1.71$  (Poisson's ratio of 0.24), consistent with a granitic composition (Christensen, 1996). This interpretation is supported by the widespread outcrops of granite across the Coastal Cordillera (Figure 5.1) that likely extend through the upper crust (Groß et al., 2008). Such velocities could also correspond to metabasite and metagreywacke compositions of the Western and Eastern Series, respectively (Christensen, 1996; Krawczyk et al., 2006). In the shallow crust ( $< 10$  km depth), low  $v_p$  ( $< 6$  km/s) corresponds to sediments in the Central Depression (labelled '*cd*').



## 5.7 Results and discussion

In the lower forearc, prominent high  $v_p$  anomalies (7.6–8.0 km/s) lie beneath the coast (Figures 5.10 and 5.11). One is located at 36°S (hereafter called the Cobquecura anomaly; labelled ‘CA’); the other to the north at 34°S (hereafter referred to as the Pichilemu anomaly; labelled ‘PA’). Based on the 7.5 km/s  $v_p$  contour, the Cobquecura anomaly is up to 40 km wide and 20 km thick, intersecting the plate interface at its base. This anomaly represents a significant velocity increase of 8% relative to the input 2-D model. The smaller Pichilemu anomaly lies further above the plate interface. Crucially, both anomalies have a slightly elevated  $v_p/v_s$  of  $\sim 1.81$  (Poisson’s ratio of 0.28) and a strong positive signature in the forearc Bouguer gravity field, helping to constrain their composition. Specifically, there is a moderate positive correlation between gravity and  $v_p$  in the lower forearc (Figure 5.11).

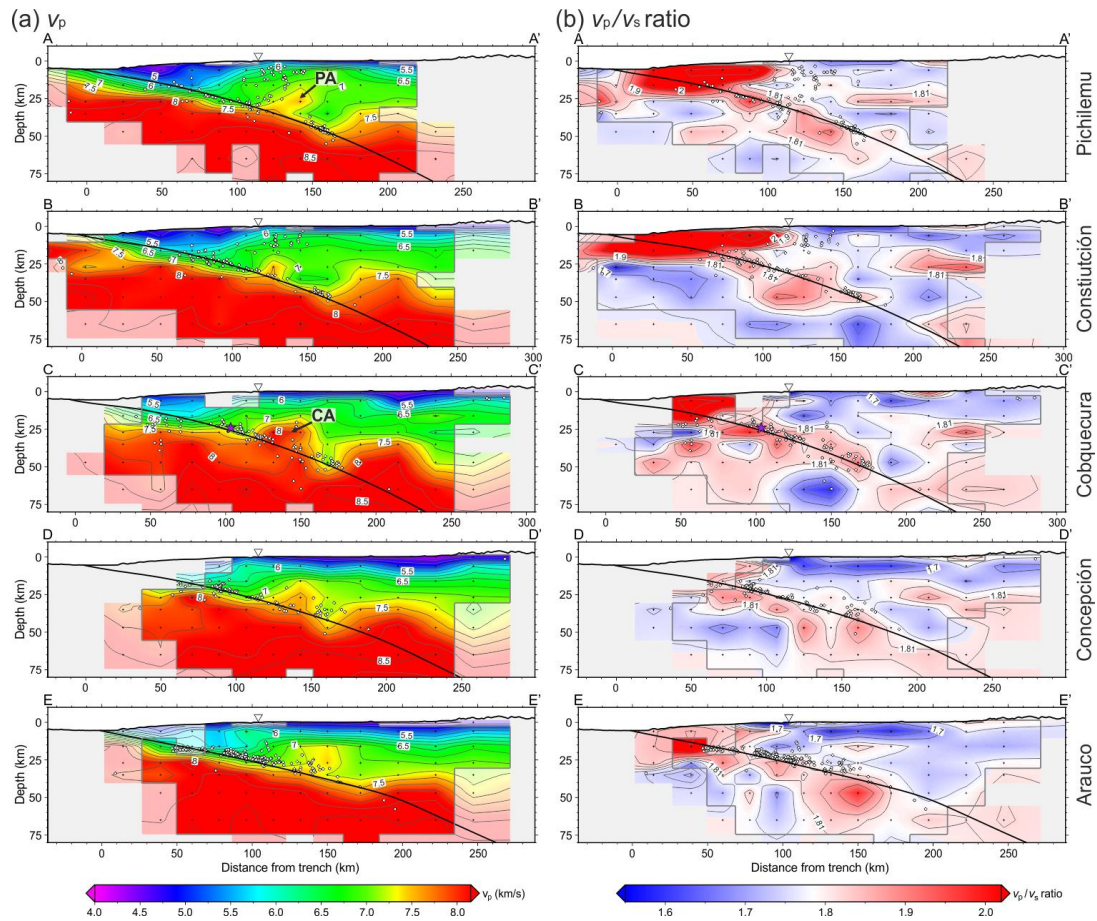


Figure 5.10: 3-D velocity model plotted along five cross-sections, of which the locations are labelled on the far right and shown in Figure 5.2. Labels refer to the following features that are discussed in the text: PA = Pichilemu anomaly; CA = Cobquecura anomaly. Resolution limits are defined in the same way as Figure 5.9.

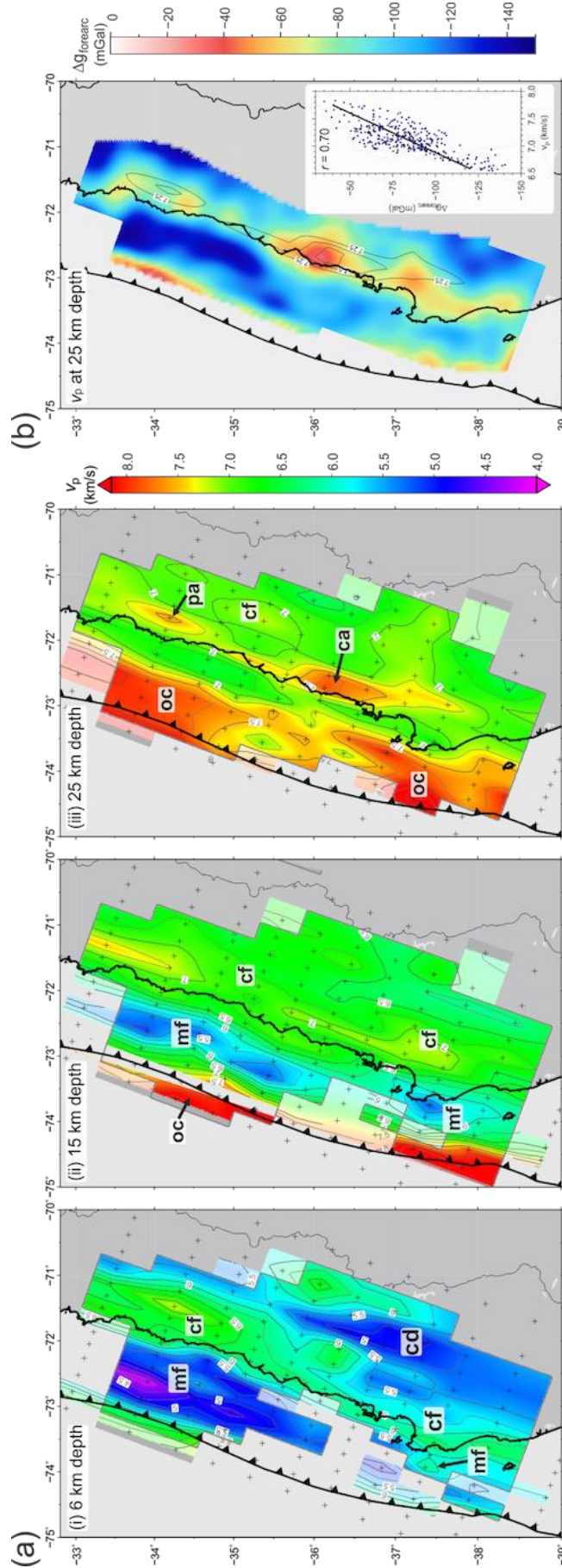


Figure 5.11: a) 3-D  $v_p$  model plotted as depth sections. Labels refer to the following features that are discussed in the text: mf = marine forearc; oc = oceanic crust; cf = upper forearc crust; cd = Central Depression; PA = Pichilemu anomaly; CA = Cobquecura anomaly. Resolution limits are defined in the same way as Figure 5.9. (b) Forearc Bouguer gravity anomaly (Chapter Four) overlain by contours of  $v_p$  model at 25 km depth. Contours are given for  $v_p$  in the range 7.25–8.00 km/s. Inset: scatter plot showing the correlation between forearc Bouguer gravity anomaly and forearc  $v_p$  at 25 km, sampled at  $0.2^\circ$  intervals of latitude and longitude.

## 5.7 Results and discussion

Interpretation of the seismic velocities and gravity signal associated with the Cobquecura and Pichilemu anomalies clearly indicates dense, ultramafic material. Weakly-serpentinised peridotite ( $< 20\%$ ) at these depths can explain the velocities (Christensen, 2004). Serpentinised peridotite at the base of the continental forearc could represent a subducted oceanic topographic high, such as a seamount. Instead, our improved velocity model indicates that the Cobquecura anomaly is larger and seismically faster than previously shown in Chapter Four. Given these findings, we find a seamount interpretation less plausible. Dense material in the lower forearc could be a deeper manifestation of the Palaeozoic granite batholith; however, the elevated  $v_p/v_s$  rules out the possibility of residual intrusive material lying at its base (Husen et al., 2000; Reyners et al., 2006).

The surface projection of the ultramafic bodies corresponds reasonably well with the location of Triassic intrusions (Figures 5.1 and 5.11). South of  $37.5^\circ\text{S}$ , a notable absence of high velocity bodies (Haberland et al., 2009) is consistent with a lack of Triassic intrusions in this region (Figure 5.1). In contrast to the Palaeozoic granites, these intrusions contain a stronger mantle source signature (Vásquez et al., 2011), possibly relating to the underlying ultramafic bodies. The Triassic intrusions were emplaced during extension (Vásquez et al., 2011) caused by either slab detachment (Parada et al., 1999), asthenospheric upwelling (Franzese and Spalletti, 2001) or slab steepening (Vásquez et al., 2011). It is plausible that any of these mechanisms could have emplaced mantle material beneath the ancient volcanic arc. Remnants of this material could now lie at the base of the present-day forearc.

Interpreting the emplacement mechanism responsible for these blocks of mantle material depends on their regional extent. Although large outcrops of Triassic intrusive rocks have been mapped north of the Maule segment (Figure 5.1), they do not extend south of the Maule segment. Given the discrete nature of these blocks, it is possible that the tectonic process responsible for their emplacement was more localised and limited to the central Chile region. Understanding the structure and petrology of such localised blocks of mantle material in the lower forearc crust could provide constraints on the genesis of arc magmas and could shed light on localised slab processes, such as slab melting.

### *Continental mantle*

Beneath the easternmost Coastal Cordillera, at depths of 25–35 km,  $v_p$  exceeds 7.25 km/s, defining a dome-shaped feature that is present along the margin (labelled ‘*cm*’). Its location, regional geometry and velocity suggest that it represents the continental mantle wedge. Low-moderate  $v_p/v_s$  of  $\sim 1.76$  (Poisson’s ratio of 0.26) in its western part are indicative of unserpentinised mantle (Carlson and Miller, 2003). Beneath the magmatic arc, we observe areas of elevated  $v_p/v_s$ , indicating hydrated asthenospheric mantle, although its extent is unresolved.

By inspection of the velocity contours that intersect the plate interface, we find that the continental Moho, represented by a  $v_p$  of  $\sim 7.75$  km/s, intersects the subducting plate interface at a depth of 45–50 km. This depth estimate is similar to that of Bohm (2004) and Haberland et al. (2009), but deeper than that of Dannowski et al. (2013) based on receiver functions. From our perspective, high  $v_p$  anomalies in the lower forearc could contaminate the lower resolution and laterally averaged receiver function image, resulting in a misplaced continental Moho.

### *Plate interface zone*

The curved region of seismicity, dipping away from the trench, delineates the plate interface. To define geometry of the fault, we selected all events that lie within  $\pm 15$  km depth of plate interface estimates (Haberland et al., 2009; Hayes et al., 2012) and fitting a second-order polynomial. Since seismicity did not reach the trench, we fixed the shallowest part of the interface to the trench at 7 km depth (e.g. Contreras Reyes et al., 2008). In 3-D, we followed a similar workflow proposed by Hayes and Wald (2009). We find that our revised interface geometry corresponds to the mean depth of thrust mechanism aftershocks (Agurto et al., 2012; Hayes et al., 2013). By projecting this interface through our 3-D velocity model, we can assess the velocity structure of the plate interface. To account for both hypocentre and velocity uncertainties, we estimate the error in plate interface velocity.

As described above, we defined the geometry of the plate interface with aftershock hypocentres. Errors in these locations could lead to a poorly defined plate interface. Furthermore, since the plate interface represents a sharp discontinuity in

## 5.7 Results and discussion

physical properties, it is a region of strong velocity gradient. Consequently, it is possible that an ill-defined plate interface may cause significant deviations from our calculated plate interface velocity. Furthermore, each node is likely to contain a small velocity error due to noise in the dataset (Figure 5.7). To account for these intrinsic velocity errors, we used our 2-D bootstrap resampling results (see Section 5.6.2). To estimate uncertainties in plate interface seismic velocity, we perturbed our 2-D interface geometry by  $\pm 3$  km depth (the maximum formal error of hypocentral depth in our tomographic inversions) in all 100 of our bootstrapped velocity models. From all 100 samples, we then found the 90<sup>th</sup> percentile in the range of velocities (90% confidence level) along the interface.

The results of this error analysis are shown by the grey shading in Figure 5.12. We find uncertainties in plate interface velocity are greatest along the shallowest portion of the plate interface (up to 0.6 km/s in  $v_p$  and 0.06 in  $v_p/v_s$ ), where the velocity gradient is strong and nodal values are poorly constrained (Figure 5.7). At 20–30 km depth, the uncertainty in  $v_p$  reduces to 0.33 km/s and in  $v_p/v_s$  to 0.03. Based on these results, our interpretation of the segmentation in seismic velocities with depth along the Maule megathrust (Figure 5.12) remains within our estimated uncertainties.

Accounting for these uncertainties, the velocity structure of the plate interface region shows a clear zonation of seismic properties with depth (Figure 5.12). Given the spacing of nodes with depth, our model represents the average plate interface velocity over a total thickness of 6–8 km. Therefore, any thin ( $< 4$  km thick) low velocity layers along the plate interface (e.g. Haberland et al., 2009) are unlikely to be imaged. Along the shallowest part of the plate interface, beneath the frontal prism,  $v_p$  is relatively low ( $\sim 6.6$  km/s) and  $v_p/v_s$  is high (1.87–2.05). Beneath the outer wedge,  $v_p$  sharply increases with depth ( $\sim 0.03$  km/s per km) and  $v_p/v_s$  decreases to  $\sim 1.84$ . Beneath the lower forearc crust,  $v_p$  stays more constant at  $\sim 7.5$  km/s, but reaches up to 8.0 km/s where the plate interface intersects the Cobquecura and Pichilemu anomalies (Figure 5.12). At depths of  $\sim 44$  km,  $v_p$  decreases to  $\sim 7.4$  km/s. Beneath the Central Depression,  $v_p$  further increases to  $\sim 8.5$  km/s and  $v_p/v_s$  decreases to  $\sim 1.78$ . Therefore, the next logical step is to consider whether this segmented velocity structure of the plate interface influences megathrust behaviour.



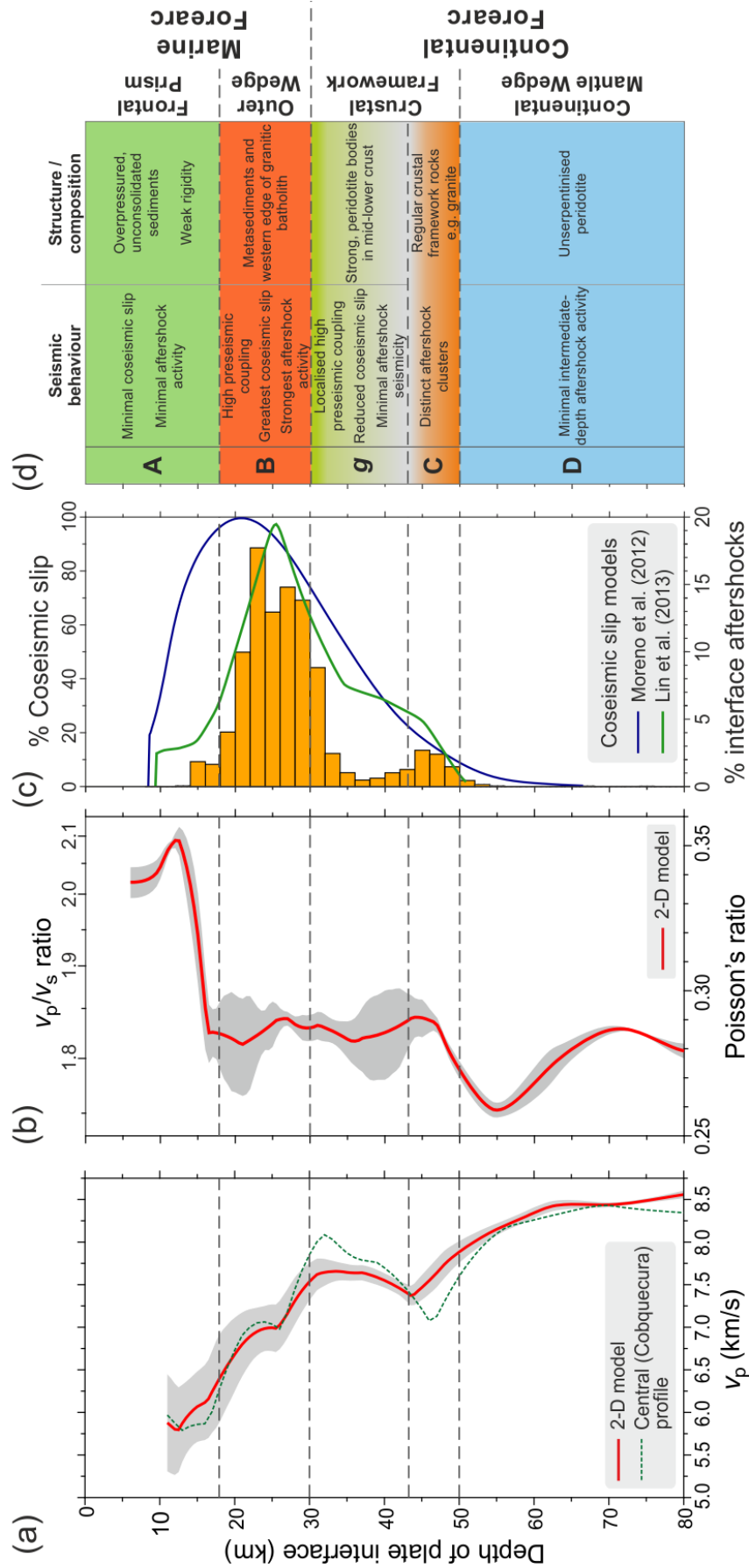


Figure 5.12: Seismic velocities along the plate interface from the 2-D model as a function of depth for (a)  $v_p$  and (b)  $v_p/v_s$ . Grey shading shows our estimated uncertainty. (c) Histogram of plate interface aftershock earthquake depths and normalised coseismic slip distribution. Trench-perpendicular slip profiles traverse the northern slip asperity. Aftershock hypocentres are relocated from the catalogue of Rietbrock et al. (2012). (d) Depth-segmentation of the plate interface region based on interpretation of the seismic velocities and seismic character of the Maule megathrust. Letters in the left-hand column correspond to the megathrust domains of Lay et al. (2012).

## 5.7 Results and discussion

### 5.7.2 Correlating megathrust behaviour with plate interface velocity structure

#### *Preseismic coupling of the megathrust*

Based on the locking model of Moreno et al. (2010), the Maule megathrust before the 2010 earthquake was strongly coupled ( $> 90\%$ ) beneath the outer wedge, where the plate interface has moderate  $v_p$  (6.25–7 km/s) and elevated  $v_p/v_s$  of 1.88 (Figure 5.13a). The interface was also strongly locked ( $> 90\%$ ) beneath the coast, at the base of the Cobquecura ultramafic body. For the Arauco peninsula region, Moreno et al. (2014) identify a correlation between weakly locked regions of the interface and elevated  $v_p/v_s$  due to high fluid pressures. We also observe a strong correlation ( $r = -0.71$ ) for the region south of  $37^\circ\text{S}$ . However, we do not find such a clear correlation for the whole rupture zone. This finding indicates that factors controlling preseismic locking may change across the Maule segment.

#### *Nucleation and rupture of the Maule earthquake*

The Maule earthquake nucleated in a region of high  $v_p$  ( $\sim 7.2$  km/s) and strong dip-parallel  $v_p$  gradient, at the periphery of the Cobquecura anomaly (Figure 5.13b). This inference is in line with Tassara (2010), who shows that ruptures along the Andean margin generally nucleate at the edge of forearc density anomalies. A local increase in stress at the edge the Cobquecura anomaly could have led to onset of the rupture.

Following nucleation, most coseismic slip occurred along the plate interface beneath the outer wedge, where we find moderate  $v_p$  ( $\sim 6.5$  km/s) and elevated  $v_p/v_s$  ( $\sim 1.86$ ), (Figures 5.12 and 5.13b). Coseismic slip was minimal beneath the frontal prism ( $v_p < 6.25$  km/s;  $v_p/v_s > 1.85$ ) and continental mantle wedge ( $v_p > 7.5$  km/s;  $v_p/v_s < 1.8$ ). Coseismic slip was reduced beneath the forearc where  $v_p > 7.25$  km/s. Both high slip asperities correspond to weaker  $v_p$  gradient with depth. This homogeneous velocity structure is partly due to the lack of high  $v_p$  anomalies beneath the coast in the Constitución and Arauco regions. Therefore, it is possible that slip localisation during the Maule earthquake was affected by the presence of long-lived mafic bodies in the lower forearc. Overall, there is strong negative correlation between  $v_p$  and coseismic slip for the down-dip portion of the rupture (Figure 5.14).

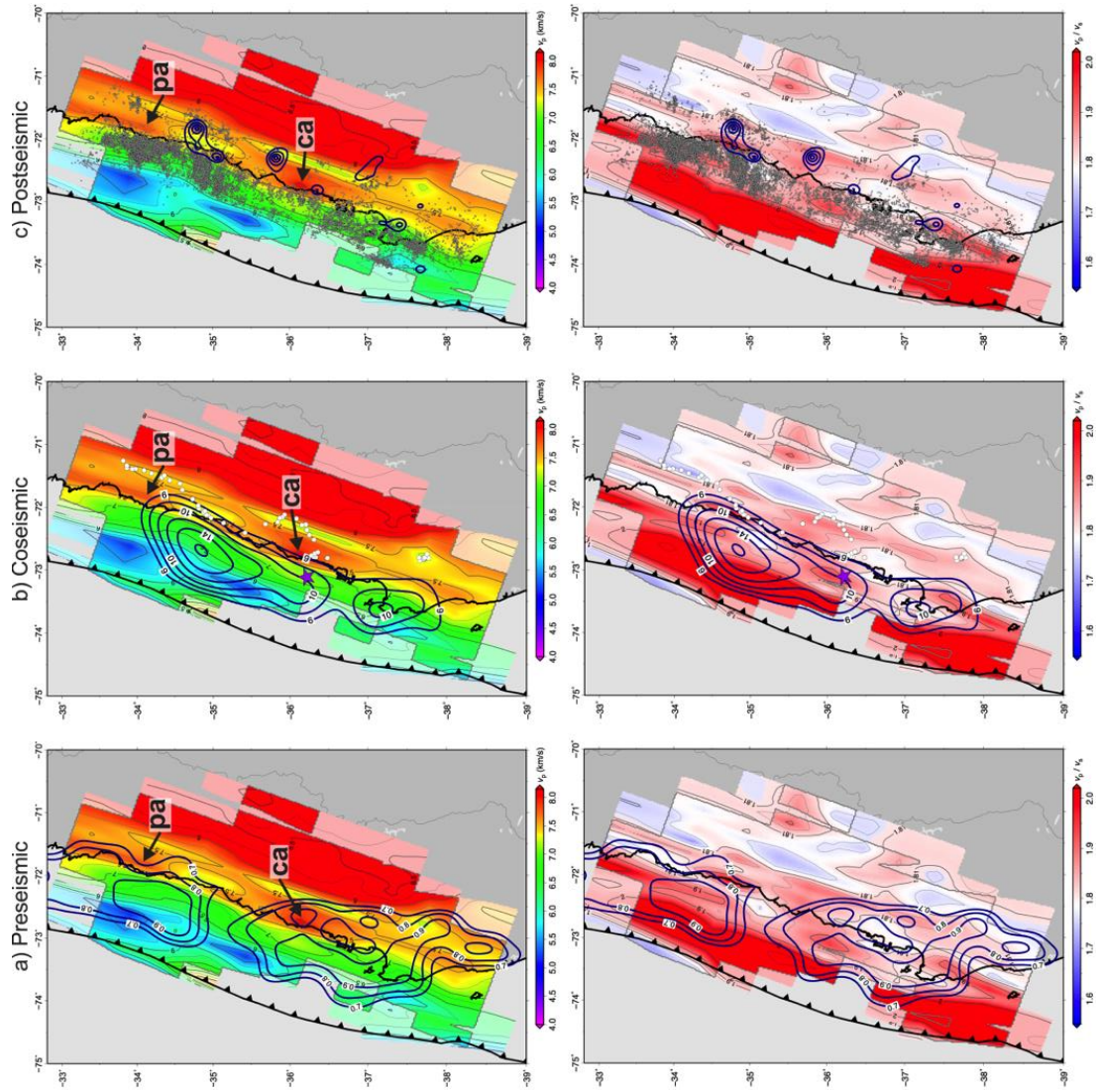


Figure 5.13: Distribution of (top)  $v_p$  and (bottom)  $v_p/v_s$  along the plate interface region compared with behaviour of the Maule megathrust over the seismic cycle. Labels refer to the features discussed in the text and are defined in the caption of Figure 5.10. a) Contours of pre-seismic locking of the megathrust (Moreno and Rosenau, 2010) (blue lines) are for locking of greater than 0.7 and given in intervals of 0.1. (b) Mainshock epicentral location from Hayes et al. (2013). Coseismic slip distribution (Moreno et al., 2012) plotted as for Figure 5.2. White circles give the location of high frequency energy release during the Maule earthquake (Kiser and Ishii, 2011). (c) Contours of afterslip  $> 1$  m (Y. N. Lin et al., 2013), (blue lines) plotted in 0.2 m intervals. Grey circles show the distribution of relocated plate interface aftershock seismicity.

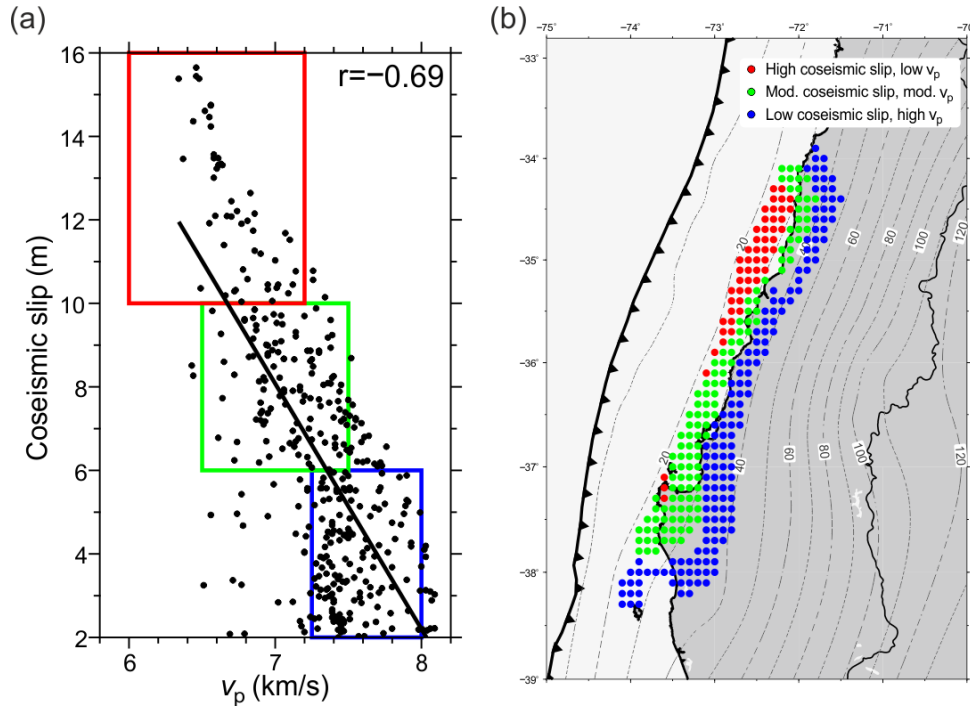


Figure 5.14: a) Scatter plot showing the relationship between coseismic slip and plate interface  $v_p$  for 20–40 km depth. The correlation coefficient,  $r$ , and a best-fitting line (black) are shown. Three groups of  $v_p$  - coseismic slip character are given by the coloured rectangles. (b) Points remapped to check whether the correlation is spatially correlated by adopting the approach of Moreno et al. (2014). This test shows that the pattern of correlation is laterally continuous, showing a spatial relationship between  $v_p$  and coseismic slip for the down-dip part of the rupture.

At shallow depths along the fault ( $< 17$  km), coseismic slip was reduced by 50% (Y. N. Lin et al., 2013). At these depths,  $v_p$  sharply decreases and  $v_p/v_s$  abruptly increases to more than 2 (Figure 5.12). Comparison of slip with seismic velocity at shallow depths suggests that overpressure conditions (Spinelli et al., 2006) and low-rigidity material at the base of the frontal prism inhibited slip. The smectite-illite transition may contribute to this overpressure (Moore and Saffer, 2001) and influence the transition between velocity-strengthening and velocity-weakening frictional behaviour (Saffer and Marone, 2003).

For the high frequency part of the rupture (Kiser and Ishii, 2011), there is a striking visual correlation with velocity structure along the plate interface (Figure 5.13b). The locations of high frequency energy release appear to step down around the high velocity anomalies, with most energy coming from deeper regions of the plate interface that have intermediate  $v_p$  and elevated  $v_p/v_s$ . High frequency energy release

during an earthquake can be caused by sudden changes in rupture speed or slip (Madariaga, 1977). Based on coseismic slip distribution (Moreno et al., 2012), we propose that the rupture was slowed by the high velocity anomalies beneath the coast, generating stopping phases at the down-dip termination of the rupture.

*Postseismic deformation following the Maule earthquake*

To investigate the relationship between velocity structure and aftershock seismicity, we relocated the 2010 aftershock catalogue of Rietbrock et al. (2012), which was based on automatic onset time picks using onshore stations only, inside our 3-D velocity model. We find systematic differences in hypocentral location between our locations and those of Rietbrock et al. (2012); (Figure 5.15). Events in the outer rise region relocate further away from the trench, whereas events located offshore between the trench and coastline relocate further onshore. We suggest that these discrepancies are due to two reasons. First, OBS stations were not used in the strategy of Rietbrock et al. (2010) leading to poorly constrained locations of offshore earthquakes. Second, automatic analysis leads to errors in onset time picking. We found these errors to be largest for S-waves from events located far offshore. To make a more reliable estimate of aftershock distribution, we corrected for these mislocations. We calculated the average epicentral mislocation vector at each point on a 20 x 80 km grid. We also found the average difference in depth at each point on a 25 km x 8 km grid for each of the five trench-perpendicular cross-sections.

After correcting for aftershock mislocations, we find that the Cobquecura and Pichilemu anomalies clearly lie within the distinct gap of plate interface aftershock seismicity (Figures 5.13 and 5.16). Intense crustal seismicity also occurred along the western edge of the Pichilemu anomaly. It is plausible that structural heterogeneity in the lower forearc influenced the distribution of plate interface and shallow crustal seismicity following the Maule earthquake. Tomographic images from Japan also show a similar relationship between crustal high velocities and aftershock seismicity (Kato et al., 2013; 2010b). Significant afterslip occurred in regions of intermediate plate interface  $v_p$  (7.2–7.5 km/s) and elevated  $v_p/v_s$  (1.82–1.84); (Figure 5.13). This finding suggests that afterslip following the Maule earthquake may have been compositionally driven.

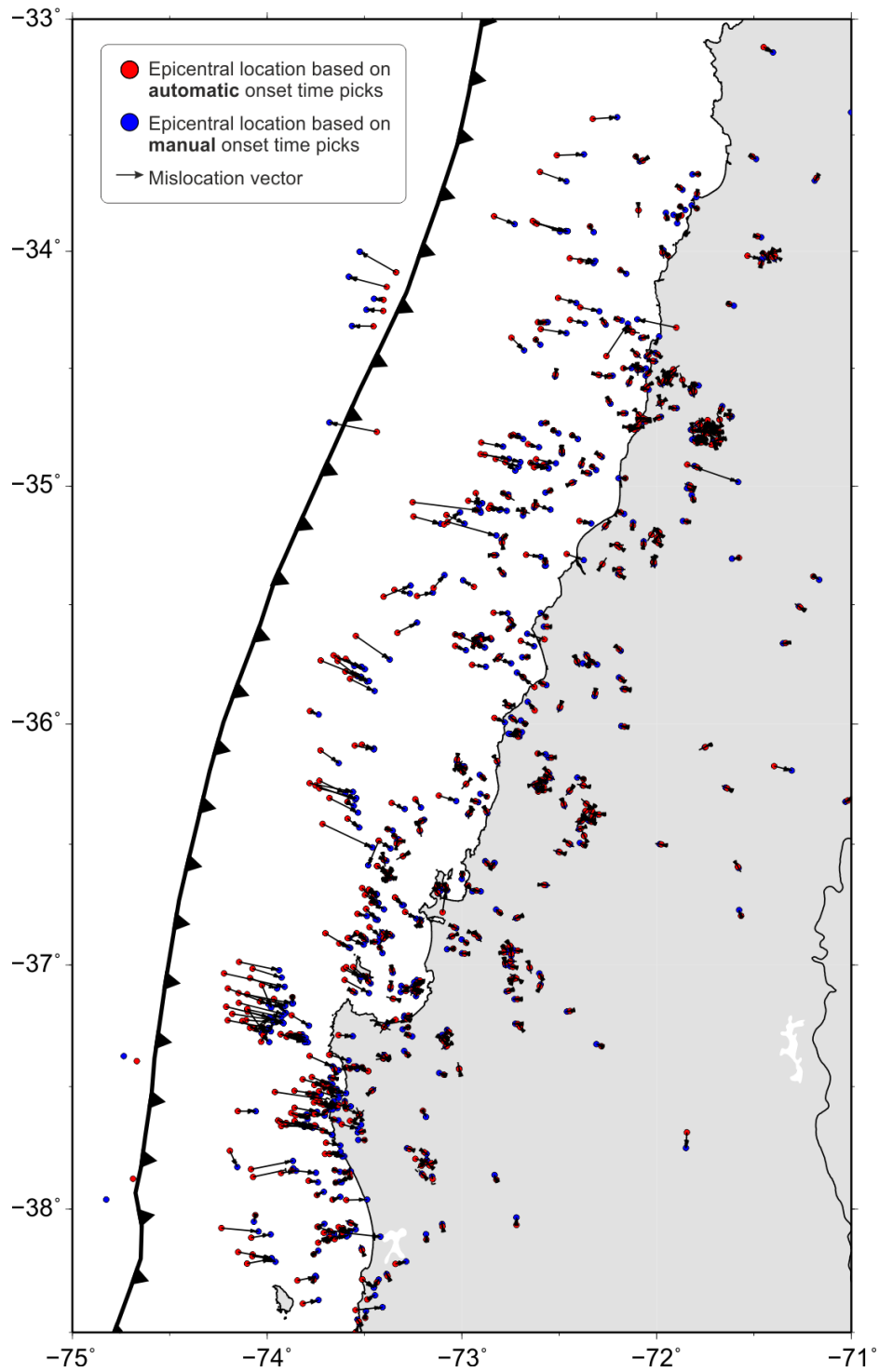


Figure 5.15: Comparison between manually determined hypocentral locations from our tomographic inversion (from onshore and offshore seismic stations) with those based on automatic onset time determination (from onshore seismic stations only); (Rietbrock et al., 2012).



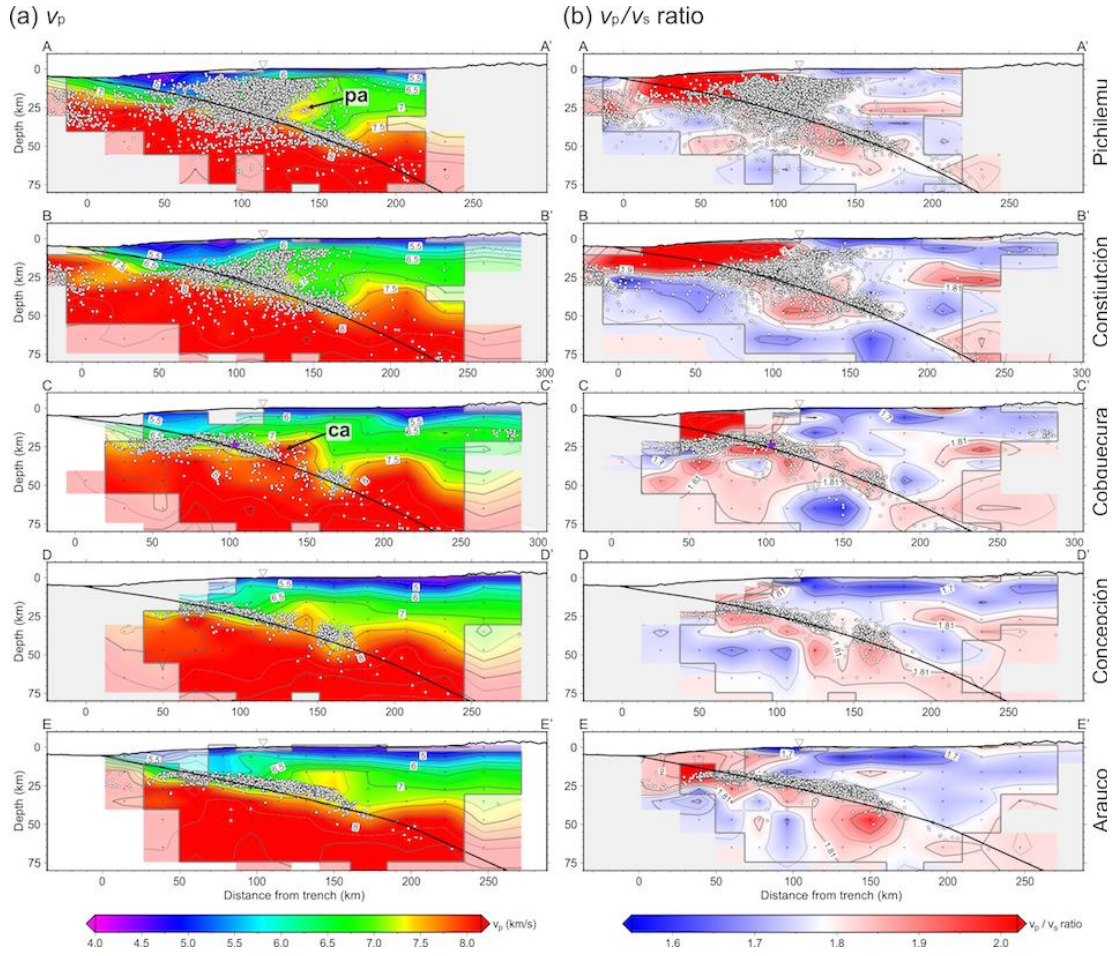


Figure 5.16: Relocated and corrected aftershock locations from the full 2010 catalogue corrected for systematic mislocations. Events with a minimum of 12 P-wave and 12 S-wave observations are shown. Features are plotted in the same way as Figure 5.10.

## 5.8 Depth-varying rupture properties and fault structure

Based on depth variation of subduction zone rupture characteristics, Lay et al. (2012) classify the megathrust into four distinct domains (A–D). Based on the physical properties and seismogenic characteristics of the Maule megathrust, we can draw parallels with this classification (Figure 5.12). The plate interface beneath the frontal prism ( $< 17$  km depth) was largely aseismic during the Maule rupture, corresponding to Domain A. The high  $v_p/v_s$  and Poisson's ratios provide direct evidence for low-rigidity material existing at shallow depths that was proposed by Bilek and Lay (1999) to influence aseismic behaviour and occasional slow, tsunami earthquakes. The depth of the plate interface beneath the outer wedge (17–30 km) corresponds to Domain B,

## 5.9 Conclusions

the most seismogenic part of the megathrust. For the Maule earthquake, the greatest coseismic slip and aftershock activity occurred in this domain, and is where the plate interface is structurally more homogeneous.

Domain C should theoretically lie at 35–55 km depth beneath the continental forearc. However, at 30–44 km depth, where the plate interface intersects ultramafic bodies in the lower forearc, coseismic slip was reduced and postseismic slip was minimal; such seismic characteristics deviate from Domain C. Therefore, we instead propose a new domain, ‘g’, for the Maule megathrust. At greater depths (44–50 km), the predominance of high frequency radiation and localised aftershock clusters agrees well with Domain C, where  $v_p$  indicates a return to normal interface structure. It has been proposed that the maximum depth of the seismogenic zone is influenced by the intersection of the 350–450°C isotherm with the plate interface (e.g. Hyndman et al., 1997). Though based on Völker et al. (2011), these temperatures are not reached until 65–90 km depth, so temperature is unlikely to play a role in the deeper segmentation of the Maule megathrust.

## 5.9 Conclusions

In this chapter, we have presented a detailed seismic velocity model ( $v_p$  and  $v_p/v_s$ ) 2010  $M_w$  8.8 Maule, Chile earthquake rupture zone. A dense aftershock dataset from onshore and offshore seismic networks has allowed an in-depth study of physical properties along the megathrust interface and in the overlying forearc.

Our velocity model shows that two high velocity anomalies with  $v_p > 7.5$  km/s lie beneath the coast in the central and northern parts of the rupture zone at the base of the continental forearc. We interpret these high velocity anomalies as large (up to 15 km thick), dense bodies of ultramafic peridotite. A comparison with the surface geology suggests that these bodies could be relic blocks of mantle.

By comparing the location of these bodies with the behaviour of the earthquake, we have shown that they may have played a role in controlling the down-dip and along-strike distribution of slip during the rupture. It also appears that these anomalies influenced the location of high frequency seismic energy. Hence, long-lived structural and compositional heterogeneities in the forearc can act as a rupture barrier



during large earthquakes and can influence the along-strike segmentation of ruptures along the central Chile margin.

These ultramafic blocks are also associated with a distinct gap in plate interface aftershock seismicity. The Pichilemu velocity anomaly acted as a structural discontinuity, influencing the focus of normal faulting aftershock seismicity in the overriding crust. At the shallow end of the seismogenic zone, overpressured, low-rigidity sediments at the base of the frontal prism likely inhibited shallow rupture during the Maule earthquake. The megathrust fault beneath the Cobquecura anomaly was strongly locked before the Maule earthquake, yet experienced little coseismic slip. This part of the fault was recognised by Moreno et al. (2012) as an area of remaining slip deficit after the Maule earthquake, and has since experienced minimal postseismic slip. This behaviour raises questions over the current state of stress and overall rheological nature of the Cobquecura anomaly, which is discussed in more detail in Chapter Eight.

Overall, plate interface  $v_p$  of  $> 7.5$  km/s inhibited seismic and aseismic slip both during and after the Maule earthquake. Therefore, an understanding of physical properties along the plate interface could help in determining the seismic hazard of a subduction zone. Seismic velocity could be used as a proxy in other subduction zones to estimate rupture size potential and the regions conducive to high frequency seismic energy release and localisation of shallow crustal aftershock seismicity.



## Chapter 6

# SEISMIC SOURCE IMAGING USING FULL-WAVEFORM ANALYSIS

So far in this thesis, we have gained insight into the physical properties of a subduction zone by considering seismic velocities along ray paths. As the preceding two chapters have shown, the results based on ray theory have furthered our knowledge of structural heterogeneity in the vicinity of the subduction plate interface. The next logical step is to assess the earthquake source process to understand how the ruptures respond to, and stress is transferred between, upper plate structures. Instead of using ray theory, modelling of full-waveforms is used as it can yield detailed constraints on earthquake source mechanisms, and by including low-frequency waves it can also be used to improve subsurface imaging.

In particular, the use of ray-based routines to calculate earthquake mechanisms is not suitable for the studies of subduction earthquakes. Traditionally, focal mechanisms are extracted from small parts of the seismogram, such as P-wave polarities and P-/S-wave amplitude ratios. However, these methods are inappropriate for offshore subduction earthquakes, where station coverage is biased to one side of the focal sphere, leading to non-linearity (Kubo et al., 2002) and unconstrained fault planes (e.g. Kisslinger, 1980). Furthermore, P-wave polarities may be small and hard to pick at stations located close to nodal planes. These focal mechanisms provide information about faulting style at the initial break; not the entire source rupture process for intermediate and strong earthquakes ( $M_w > 5.5$ ), (Kubo et al., 2002).

## 6.1 Moment tensor theory

A more advanced method of determination is to invert for the seismic moment tensor (hereafter, MT), which can yield information on source position and timing, magnitude, focal mechanism, as well as constraints on extended ruptures, if required. The MT is normally calculated using seismic waveform analysis. In this chapter, we describe the theory of MTs and their decomposition. We then outline an inversion workflow, paying particular attention to the time-domain method that is used in Chapters Seven and Eight. We show here that most full-waveform MT inversions assume 1-D structural models. As detailed in previous chapters, such models are inappropriate for subduction zones, where there are strong lateral variations in seismic velocities. Subsequently, we describe how the method of simulating full-waveforms in a 3-D structural model and the implications for understanding earthquake MTs and subsurface velocity structure.

## 6.1 Moment tensor theory

A seismic source can be described as two forces acting in opposite directions and separated by a small distance. This configuration is known as a linear dipole. Such single couples fail to represent real seismic sources and are better described by orthogonal linear dipoles in a 3-D coordinate system: a seismic MT. The condition of zero net moment means that the MT matrix is symmetric ( $m_{ij} = m_{ji}$ ), reducing the nine elements to six (as shown by the greyed-out elements of the tensor):

$$m_{ij} = \begin{bmatrix} m_{11} & m_{12} & m_{13} \\ m_{21} & m_{22} & m_{23} \\ m_{31} & m_{32} & m_{33} \end{bmatrix} \quad ( 6.1 )$$

This symmetry means that the fault-normal vector and slip vector are interchangeable, showing the ambiguity between active fault and auxiliary planes, which arises from the seismic radiation pattern of a point-source. To resolve this ambiguity, studies of aftershocks, surface faulting or rupture directivity are needed to determine the active plane (Jost and Herrmann, 1989).

The point at which the MTs are calculated is sometimes assumed to the earthquake hypocentre (i.e. the rupture nucleation point). By solving for the source position and origin time of larger earthquakes, Dziewonski et al. (1977) found

discrepancies between the location given by the MT, and that of the hypocentre. It was concluded that MTs are sensitive to the rupture *centroid*: the location and time of greatest slip. Thus, the *centroid moment tensor* (CMT) gives a weighted mean position of the source in space and time. Centroid time may be approximated as half of the source duration (Udías et al., 2014).

## 6.2 Decomposition of the moment tensor

The decomposition of the MT is non-unique; it can be carried out in multiple ways, each forming different interpretations. The eigenvalues and eigenvectors of  $\mathbf{m}$  correspond to the maximum, intermediate and minimum principal stress axes. This relationship means that  $\mathbf{m}$  can be transformed into any coordinate system, where its basis vectors are eigenvectors of the three principal stress axes. This basis system results in the diagonalised MT,  $\mathbf{M}$ :

$$\mathbf{M} = \begin{bmatrix} \sigma_1 & 0 & 0 \\ 0 & \sigma_2 & 0 \\ 0 & 0 & \sigma_3 \end{bmatrix} \quad (6.2)$$

(Jost and Herrmann, 1989), where  $\sigma_i$  corresponds to the three principal stress axes. Decompositions of the MT can thus be carried out using eigenvalue and eigenvector analysis.

The trace of  $\mathbf{M}$  describes *isotropic* components, which are caused by volume change of the source. If the trace of  $\mathbf{M}$  is positive, the source has an implosive component; if it is negative, the source is partly explosive. Calculation of these volumetric components of the MT is complex and non-linear (Zahradnik et al., 2008b); isotropy can also be difficult to interpret. Therefore, volume change is often assumed to be negligible ( $\sigma_1 + \sigma_2 + \sigma_3 = 0$ ), leaving the *deviatoric* MT, which can be explained as equivalent forces (e.g. Jost and Herrmann, 1989):

$$\mathbf{M}_{FULL} = \mathbf{M}_{ISOTROPIC} + \mathbf{M}_{DEVIATORIC} \quad (6.3)$$

In the case of the deviatoric MT, one eigenvalue is independent and the other two are equal and opposite (e.g.  $\sigma_2 = -\sigma_3 - \sigma_1$ ). It is normally assumed that MTs of tectonic

## 6.2 Decomposition of the moment tensor

earthquakes are purely deviatoric as they occur due to displacement along a fault plane (shear dislocation) that results from high compressive stress (Udías et al., 2014).

The deviatoric part can be subsequently decomposed in many different ways. One method decomposes into major- and minor-couples; however, more commonly used is decomposition into *compensated linear vector dipole* (CLVD) and *double-couple* (DC) components:

$$\mathbf{M}_{DEVIA TORIC} = \mathbf{M}_{DC} + \mathbf{M}_{CLVD} \quad ( 6.4 )$$

For some tectonic earthquakes, if no eigenvalue equals zero, yet the sum of eigenvalues vanishes (e.g.  $\sigma_2 = \sigma_3 = -\frac{\sigma_1}{2}$ ), the MT can have CLVD components (Jost and Herrmann, 1989). The use of CLVD was first proposed by Knopoff and Randall (1970) for deep earthquakes; it is defined as a sudden change in shear modulus normal to the fault plane, without volume change. As %CLVD increases, the quadrant distribution of the focal mechanism becomes more distorted.

To estimate the relative contributions of CLVD and DC, the parameter,  $\varepsilon$  is defined:

$$\varepsilon = \frac{|\sigma_{min}|}{|\sigma_{max}|} \quad ( 6.5 )$$

(Dziewoński et al., 1981), where  $\sigma_{min}$  and  $\sigma_{max}$  are the smallest and largest eigenvalues of the deviatoric part of  $\mathbf{M}$ , respectively. For a pure DC source,  $\varepsilon = 0$  because  $\sigma_{min} = 0$ . The percentage contribution of CLVD and DC components (%CLVD and %DC, respectively) is thus given by:

$$\%CLVD = 200\varepsilon \quad ( 6.6 )$$

$$\%DC = 100(1 - 2\varepsilon) \quad ( 6.7 )$$

MTs with a departure from pure DC faulting may provide insights on special rupture phenomena (Frohlich, 1994; Julian et al., 1998). Several physical explanations of low %DC have been proposed, yet many studies suggest that non-DC components may be artificial and require careful interpretation. Physical origins of non-DC

earthquakes include unsteady fluid flow, tensile- and shear-faulting on curved structures (e.g. Julian et al., 1998). Non-DC earthquakes typically occur in volcanic and geothermal areas, as well as in deep ( $> 150$  km) parts of subducted slabs (Frohlich, 2006) due to complex rupture mechanisms. Non-DC earthquakes may also result from simultaneous rupture on more than one fault (Frohlich, 2006; Zahradnik et al., 2008c), (see Section 6.4.4), although multiple sub-events with parallel fault planes, slip directions or intermediate stress axes may not always yield a low %DC for a single event (Julian et al., 1998). Moreover, Adamová and Šílený (2010) argue that non-DC components of moderate–strong earthquakes may come from the radiation directivity effects of extended ruptures. Earthquakes with low %DC can result from heterogeneity and anisotropy of the host medium close to the source (Adamova and Sileny, 2010; Julian et al., 1998).

Zahradnik et al. (2008c) demonstrate that when the timing or position used in an MT calculation is incorrect, %DC can take virtually any value. Alternatively, high CLVD components may arise due to errors or noise in the observed waveforms, an incorrect Earth model, or non-linear wave propagation effects. For multiple ruptures, %DC can be dependent on the moment ratio between sub-events. %DC may also be dependent on station coverage (Zahradnik et al., 2008c).

Finally, another decomposition that is commonly used converts the MT into fault plane geometries. Aki and Richards (1980) derived relationships between strike,  $\phi$ , dip,  $\delta$  and rake,  $\lambda$  of a shear dislocation source (fault plane) as scalar seismic moment,  $M_0$ , and individual MT components,  $m_{ij}$ :

$$M_{11} = -M_0(\sin \delta \cos \lambda \sin 2\phi + \sin 2\delta \sin \lambda \sin^2 \phi) \quad (6.8)$$

$$M_{12} = -M_0(\sin \delta \cos \lambda \cos 2\phi + 0.5 \sin 2\delta \sin \lambda \sin 2\phi) \quad (6.9)$$

$$M_{13} = -M_0(\cos \delta \cos \lambda \cos \phi + \sin 2\delta \sin \lambda \sin \phi) \quad (6.10)$$

$$M_{22} = -M_0(\sin \delta \cos \lambda \sin 2\phi - \sin 2\delta \sin \lambda \cos^2 \phi) \quad (6.11)$$

$$M_{23} = -M_0(\cos \delta \cos \lambda \sin \phi - \cos 2\delta \sin \lambda \cos \phi) \quad (6.12)$$

$$M_{33} = M_0 \sin 2\delta \sin \lambda \quad ( 6.13 )$$

## 6.3 Moment tensor inversion

One way of calculating MTs is to use seismic wave amplitudes (e.g. Šílený and Milev, 2008), which are linear functions of MT components, containing more information than polarities alone. The inherent problem with using amplitudes is their sensitivity to structural heterogeneities in the subsurface. Amplitude ratios ( $P/S_V$ ,  $P/S_H$  or  $S_H/S_V$ ) reduce these effects and can also solve for non-DC mechanisms (e.g. Hardebeck and Shearer, 2002; Jechumtálová and Šílený, 2005; Snoke, 2003). However, amplitude ratios are non-linear functions of the MT, making inversion difficult (Julian et al., 1998).

Waveform inversion is advantageous over polarity and amplitude methods because it does not require perfect azimuthal coverage (Zahradník and Custódio, 2012a) and relatively few measurements are required to generate stable solutions (Campus et al., 1996; Dreger and B. Savage, 1999). Waveforms can be used to calculate source-time functions, source position and timing, as well as solving for extended ruptures and time-dependent mechanisms (Julian et al., 1998). Full-waveform inversion can be carried out in either the time- (e.g. Herrmann et al., 2011) or frequency-domain (e.g. Romanowicz, 1982). Different types of seismic waves can be used in the inversion, including body waves, surface waves and free oscillations. However, as noted by Julian et al. (1998), the method is limited by the accuracy of *Green's functions* (GF), the impulse response of the subsurface. Few methods exist that allow GF to be calculated in complex structural models, so most waveform inversions use low frequencies (e.g.  $< 0.1$  Hz) to negate structural heterogeneity.



As first identified by Gilbert (1973), the relationship between elements of GF and the MT allows the inversion of surface deformation observations. Ground displacement,  $x_s(t)$  is linearly related to the MT components,  $m_j$  and GF,  $G_{ij}$  in the following relationship:

$$x_s(t) = \sum_{n=1}^6 G_{ij}(t)m_j \quad (6.14)$$

(e.g. Zahradnik and Custódio, 2012a), which can be written in general matrix form as:

$$\mathbf{d} = \mathbf{G}\mathbf{m} \quad (6.15)$$

In the time-domain,  $\mathbf{d}$  is a vector composed of  $n$  recordings of observed ground displacement waveforms. Conversely, in the frequency-domain, Eqn. 6.15 is given separately for each frequency and  $\mathbf{d}$  contains the real and imaginary parts of the displacement spectra. Generally,  $\mathbf{G}$  is a  $n \times 6$  matrix containing GF calculated using *a priori* structural models, and  $\mathbf{m}$  is a vector containing the six (or in the case of deviatoric inversion, five) MT elements (e.g. Jost and Herrmann, 1989). The MT problem is over-determined since observations typically exceed the number of unknown MT parameters. Thus, Eqn. 6.15 is generally solved using least squares inversion:

$$\mathbf{m} = (\mathbf{G}^T \mathbf{G})^{-1} \mathbf{G}^T \mathbf{d} \quad (6.16)$$

Inversion schemes often solve for full CMT solutions since MT components typically trade-off with location (Dziewoński and Woodhouse, 1983). In the following section, we describe the least squares CMT inversion scheme that is used in Chapters 7 and 8 of this thesis.

## 6.4 Time-domain full-waveform moment tensor inversion

CMT inversion consists of several stages, for example, the careful selection, processing and analysis of seismic records, which are important for obtaining stable solutions. An interactive graphical approach is one way to carry out these tasks. Therefore, Sokos and Zahradnik (2007) developed the ISOLA-GUI software package,

## 6.4 Time-domain full-waveform moment tensor inversion

a MATLAB graphical user interface which uses the Fortran codes of Zahradnik et al. (2005) for CMT inversion. ISOLA adapts the Kikuchi and Kanamori (1991) MT inversion method for local and regional waveform applications. In this section, we describe and explain the strategy of time-domain full-waveform inversion using ISOLA (as summarised in Figure 6.1). We first explain its usage for single point-source approximations in Section 6.4.3. ISOLA can also be used for extended ruptures and multiple point-source situations, which is subsequently discussed in Section 6.4.4.

ISOLA has been used in a wide range of tectonic settings. Examples of its use for large ruptures include the 2011  $M_w$  9.0 Tohoku-Oki, Japan (Zahradnik et al., 2011), the 2010  $M_w$  7.2 Van, Turkey (Zahradnik and Sokos, 2014) and the  $M_w$  6.3 L'Aquila, Italy (Gallovic and Zahradnik, 2012) earthquake. The algorithm has also been applied to small–intermediate sized earthquakes (e.g. Agurto et al., 2012; Sokos et al., 2012; Zahradnik et al., 2008b) and microearthquakes (Fojtíková et al., 2010).

### 6.4.1 Pre-processing, filtering and station selection

The reliability of CMT inversion mainly depends on the quality and amount of available waveforms, as well as station coverage; all inversions should begin with careful analysis of waveforms (Figure 6.1). Data are clipped or contain glitches should be removed (Dziewoński et al., 1981). Furthermore, waveforms should be checked for the near-field effects of permanent displacement, tilting and rotation (Zahradnik and Plešinger, 2010). These disturbances can be particularly strong at low frequencies (Maercklin et al., 2011). *Signal-to-noise ratio* (SNR) should also be assessed to ensure that signals are not dominated by natural or instrumental noise within the range of frequencies considered. During pre-processing, instrument response is removed and observed waveforms are converted to displacement. Linear trends and the trace mean are also removed (Figure 6.1).

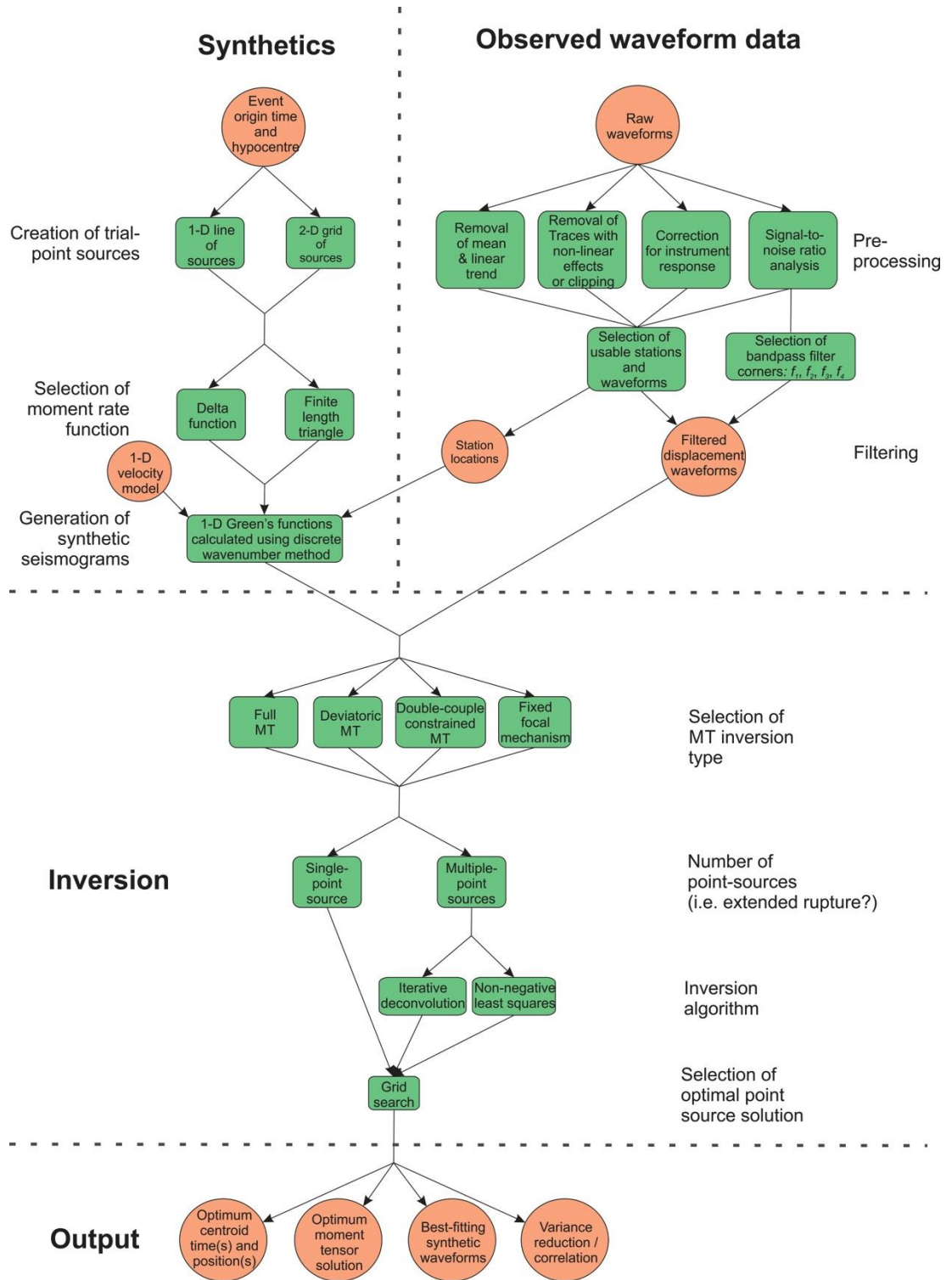


Figure 6.1: Schematic workflow of time-domain moment tensor inversion using the ISOLA software package, showing the steps required and selection of parameters.

## 6.4 Time-domain full-waveform moment tensor inversion

The next step is to bandpass filter waveforms. The amplitude response of the filter is denoted by four frequencies:  $f_1, f_2, f_3, f_4$ , defining a cosine taper at its edges, and a flat response between  $f_2$  and  $f_3$  (Zahradnik et al., 2008c). The frequency range used depends on several factors and should be carefully investigated to ensure a reliable MT solution (Figure 6.1). The noise level of the waveforms, determined through SNR analysis, limits the lowest usable frequency ( $f_1, f_2$ ). Zahradnik and Custódio (2012a) show that MT solutions are more stable when waveforms contain low frequency signals ( $< 0.05$  Hz). Similarly, the highest usable frequency ( $f_3, f_4$ ) is also noise-dependent, especially for weaker events, whose waveforms may be contaminated by the microseismic noise peak in the frequency range 0.2–0.4 Hz. The upper frequency limit also depends on epicentral distance and the accuracy of GF (e.g. Zahradnik and Sokos, 2014). In the case of a point-source approximation and a delta moment-rate function, the upper bandpass cut-off ( $f_3, f_4$ ) should be lower than the corner frequency,  $f_c$  of the earthquake (where  $f_c \sim 1/\tau$ , in which  $\tau$  is the source duration). If  $f_4 > f_c$ , a source with finite duration should be used. To complicate the matter further,  $f_c$  may be station-dependent due to directivity effects.

Traditionally, it is assumed that wide coverage of the focal sphere allows for accurate MT results (e.g. Satake, 1985). However, waveform inversion using limited stations (two to three) performs better than traditional studies, such as those based on P-wave polarities using the same number of stations (Campus et al., 1996; Dreger and B. Savage, 1999; Zahradnik et al., 2008b). Zahradnik and Custódio (2012a) investigate the effect of station coverage on MT retrieval. This study found that poor azimuthal coverage does not result in poorly constrained fault planes; however, good coverage is important for obtaining centroid position and accurate %DC. Likewise, Kumar et al. (2014) find that if station coverage is reduced, ISOLA can accurately resolve the DC mechanism, but it performs poorly when significant CLVD components are present. For sources outside the network, MT accuracy depends on event depth (Zahradnik and Custódio, 2012b). Earthquakes with shallow depth ( $< 10$  km) are better resolved than deeper sources (40–60 km). This finding favours studies of offshore megathrust earthquakes, which tend to have relatively shallow depths ( $< 30$  km). Taking the station coverage to a more extreme scenario, workers have also investigated MT inversion using three-component waveforms recorded at a single station (Dreger and Helmberger, 1993; Zahradnik and Custódio, 2012a). These studies found that single-

station MT inversion is more accurate when low frequency signals are available, but solutions may lack stability.

#### 6.4.2 Velocity model, source definition and computation of Green's functions

As explained in the previous section, knowledge of the Earth model and resulting accuracy of corresponding GF is crucial for reliable MT solutions. Jechumtálová and Bulant (2014) conclude that MTs calculated using local waveforms are more sensitive to velocity model accuracy than station coverage. To calculate GF, ISOLA uses a layered 1-D model of  $v_p$ ,  $v_s$ , density and seismic attenuation quality factor,  $Q$ . In this thesis, we use the 3-D velocity model presented in Chapter Five to calculate 1-D profiles. We keep  $Q$  fixed to 300 since it is unlikely to affect MT solutions at the low frequencies considered here ( $< 0.09$  Hz).

Hypocentre locations of earthquakes may be inaccurate, but MT solutions can provide better depth estimates, especially for shallow events (Zahradnik et al., 2008b) and those situated outside of the network (Herrmann et al., 2011). Moreover, for intermediate–large ( $M_w > 5.5$ ) earthquakes, finite rupture effects may cause a discrepancy between hypocentre and centroid locations. For both of these reasons, which are incidentally applicable for subduction megathrust earthquakes, ISOLA can generate sets of sources on a line or on a 2-D plane (Figure 6.1). Fixed-epicentre inversions that use a vertical line of trial point-sources (along the depth axis) are common in regional CMT studies of small–intermediate sized ( $M_w < 5.5$ ) earthquakes (Agurto et al., 2012; Hayes et al., 2013; Herrmann et al., 2011); 2-D planes may be chosen for large earthquakes (e.g. Quintero et al., 2014; Zahradnik and Sokos, 2014). Once the source is defined, GF are computed (Figure 6.1) using the discrete wavenumber algorithm of Bouchon (1981) in the time-domain. Green's functions must be calculated up to frequencies that are greater than or equal to  $f_4$ .

#### 6.4.3 General inversion for single point-sources

In this section, we describe the general algorithm used in ISOLA to calculate single point-source MT solutions. ISOLA can solve for either the full MT (DC + CLVD + ISOTROPIC), the deviatoric MT (DC + CLVD) or for a pure-DC constrained source (Figure 6.1). The Kikuchi and Kanamori (1991) method is adopted, in which, the MT

## 6.4 Time-domain full-waveform moment tensor inversion

$(m_{kj})$  is represented by the sum of six elementary tensors,  $M_n$  (five pure-DC sources and one explosive source; Table 6.1), each weighted by  $a_n$ :

$$m_{kj} = \sum_{n=1}^{N_e} a_n M_n \quad (6.17)$$

where  $N_e$  is the number of elementary tensors (i.e.  $N_e = 5$  for a deviatoric MT).



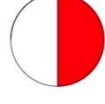
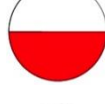
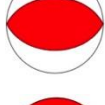

$n$	Elementary tensor	Graphical representation
1	$\begin{bmatrix} 0 & 1 & 0 \\ 1 & 0 & 0 \\ 0 & 0 & 0 \end{bmatrix}$	
2	$\begin{bmatrix} 1 & 0 & 0 \\ 0 & -1 & 0 \\ 0 & 0 & 0 \end{bmatrix}$	
3	$\begin{bmatrix} 0 & 0 & 0 \\ 0 & 0 & 1 \\ 0 & 1 & 0 \end{bmatrix}$	
4	$\begin{bmatrix} 0 & 0 & 1 \\ 0 & 0 & 0 \\ 1 & 0 & 0 \end{bmatrix}$	
5	$\begin{bmatrix} -1 & 0 & 0 \\ 0 & 0 & 0 \\ 0 & 0 & 1 \end{bmatrix}$	
6	$\begin{bmatrix} 1 & 0 & 0 \\ 0 & 1 & 0 \\ 0 & 0 & 1 \end{bmatrix}$	

Table 6.1: Elementary moment tensors used in the inversion method of Kikuchi and Kanamori (1991).

To calculate the best-fitting MT coefficients,  $a_n$ , ISOLA minimises the difference,  $\Delta$  between observed and synthetic displacement waveforms in the time-domain (Kikuchi and Kanamori, 1991):

$$\Delta = \sum_{s=1}^{N_s} \int \left[ x_s(t) - \sum_{n=1}^{N_e} a_n w_{sn}(t) \right]^2 dt \quad (6.18)$$

where  $w_{sn}(t)$  represents the synthetic seismogram (Green's functions) at each station,  $s$ , and  $N_s$  is the number of displacement records. This equation can be re-written as:

$$\Delta = R_x - 2 \sum_{n=1}^{N_e} a_n G_n(t) + \sum_{m=1}^{N_e} \sum_{n=1}^{N_s} R_{nm} a_m \quad (6.19)$$

where:

$$R_x = \sum_{s=1}^{N_s} \int [x_s(t)]^2 dt \quad (6.20)$$

$$R_{nm} = \sum_{s=1}^{N_s} \int [w_{sn}(t) w_{sm}(t)] dt \quad (6.21)$$

$$G_n = \sum_{s=1}^{N_s} \int [w_{sn}(t) x_s(t)] dt \quad (6.22)$$

By setting:

$$\frac{\partial \Delta}{\partial a_n} = 0 \quad (6.23)$$

for all values of  $n$ , the following normal equations relationship is obtained:

$$\sum_{m=1}^{N_e} R_{nm} a_m = G_n \quad (6.24)$$

Finally, solving for  $a_m$  gives:

$$a_n = \sum_{m=1}^{N_e} R_{nm}^{-1} G_m \quad (6.25)$$

This over-determined problem is solved using least squares inversion (Eqn. 6.16) and results in a final MT solution of:

## 6.4 Time-domain full-waveform moment tensor inversion

$$m = \begin{bmatrix} a_2 - a_5 + a_6 & a_1 & a_4 \\ a_1 & -a_2 + a_6 & a_3 \\ a_4 & a_3 & a_5 + a_6 \end{bmatrix} \quad ( 6.26 )$$

A measure of misfit between observed and synthetic waveforms, *variance reduction* (VR) is given by:

$$VR = 1 - \frac{\Delta}{\int x^2(t)dt} \quad ( 6.27 )$$

which is directly related to waveform correlation,  $c$ :

$$c = \sqrt{VR} \quad ( 6.28 )$$

When centroid location and time are unknown (CMT inversion), the problem becomes non-linear, so ISOLA performs a grid search over these parameters and automatically selects the solution that minimises  $VR$  (e.g. Quintero et al., 2014; Zahradnik et al., 2008a; Zahradnik and Sokos, 2014). The resulting MT solution can then be decomposed into DC and CLVD components, if required (Section 6.2).

Recorded waveforms contain errors and GF are imperfect, so when a solution is calculated, visual and quantitative checks are required to assess waveform fits and solution reliability. Sokos and Zahradník (2013) provide a detailed explanation of the error and uncertainty tools available in ISOLA. Here, we briefly describe the approaches used in this thesis. Although the overall value of  $VR$  can be used to measure solution quality, close stations that have large amplitudes can bias its value. Therefore, it is important to assess  $VR$  for individual stations and components. In this case, poorly correlated waveform fits should be evaluated and possibly eliminated from the inversion. Possible errors in waveforms highlight the need to carry out *jackknifing*, which is the process of systematically removing individual stations and components from the inversion to calculate the effect of data and modelling errors on CMT parameters (Sokos and Zahradnik, 2013). These analyses can help to remove poor waveforms that may be affected by disturbances such as station tilting or clipping, which were not recognised during initial pre-processing. First-motion polarities can be used to validate the obtained focal mechanism, as well as its centroid depth and the



velocity model assumed. MT solutions should also be crosschecked with any reported CMT solutions, such as those from the USGS-NEIC and GCMT project.

#### 6.4.4 Multiple-source moment tensor inversion

If the observed waveforms are complex, an earthquake may be composed of multiple point-sources (sub-events) with different centroids and variable focal mechanisms. Extended ruptures are often manifested as directivity effects in recorded waveforms (Zahradnik and Sokos, 2014). Therefore, the observed waveforms,  $x$  are a function of the cumulative sum of  $N$  moment-rate tensors,  $\mathbf{M}$  convolved with spatial derivatives of GF:

$$x = \sum_{i=1}^N \mathbf{M}_i * \mathbf{G}_i \quad ( 6.29 )$$

Calculating time-dependent MTs using teleseismic waveforms is an established method (e.g. Kanamori et al., 1992; Lay et al., 2010b; Tsai et al., 2005), but ISOLA represents the first application to regional/local waveforms; it has been used in several studies for this purpose (Quintero et al., 2014; Zahradnik et al., 2005; Zahradnik and Sokos, 2014). The aim of multiple point-source inversion is not to produce smooth slip distributions; it is instead more akin to imaging discrete slip patches (e.g. Vallée and Bouchon, 2004). The advantages of a multiple point-source representation over slip inversions are the former's ability to determine event timings, which can constrain rupture velocity, and to retrieve mechanisms on different faults. Further sub-events can be added until VR converges; although VR may increase, the improvement in fit must be statistically significant. Moreover, sub-events with different faulting styles should be independently verified with other seismological and geophysical observations.

To retrieve multiple sub-events, the highest usable frequency,  $f_4$  must be greater than the source corner frequency,  $f_c$  (Section 6.4.1). In this case, GF should be computed using a moment-rate function of finite length, such as a triangle (Figure 6.1). To find multiple sub-events at different locations, a 2-D grid of trial point-sources is used to find the best-fitting location of each event (Section 6.4.2). *A priori*

## 6.4 Time-domain full-waveform moment tensor inversion

information on fault geometry may be used to constrain the grid to a given plane (e.g. Quintero et al., 2014; Zahradnik and Sokos, 2014).

For multiple point-source inversion, ISOLA can take two different approaches. The first method is *iterative deconvolution* (ID). ID works by systematically grid searching over a set of point-sources on a given plane to minimise the L2 misfit between observed and synthetic waveforms (Zahradnik et al., 2005). Each point-source,  $\mathbf{M}_i$  is given by a unit tensor,  $\mathbf{a}$ , scalar moment,  $m$ , and time,  $T$ :

$$\mathbf{M}_i = \mathbf{a}_i m T(t) \quad (6.30)$$

The first step is to approximate the entire waveform using the first point-source:

$$\mathbf{x} - \mathbf{M}_1 * \mathbf{G}_1 = 0 \quad (6.31)$$

This equation is solved using least squares to find the  $\mathbf{M}_1$  and a grid search finds the position and centroid time that gives the highest correlation value. Synthetics of the first source,  $\mathbf{s}_1$  are subsequently removed from the observed waveforms and a second source is solved for, in the same way (Zahradnik and Sokos, 2014):

$$(\mathbf{x} - \mathbf{s}_1) - \mathbf{M}_2 * \mathbf{G}_2 = 0 \quad (6.32)$$

In ID, the moment-rate function is equal for both sources. Therefore, to negate potential artifacts caused by this assumption, ISOLA also adopts *non-negative least squares* (NNLS) inversion (Zahradnik and Sokos, 2014). The NNLS problem is parameterised in a different way to ID: sources have their DC MTs and positions,  $\mathbf{a}$  prescribed. The moment rate is represented by  $J$  shifted triangle functions,  $D(t)$ , each centred at time positions,  $t_j^i$ . The calculated non-negative weight of each triangle is given by  $n_j^i$ :

$$\mathbf{M}_i = \mathbf{a}_i \sum_{j=1}^J n_j^i D(t - t_j^i) \quad (6.33)$$

This relationship is formed as a linear inverse problem by inserting Eqn. 6.33 into Eqn. 6.29, and obtaining:

$$\mathbf{x} - \sum_{i=1}^N \sum_{j=1}^J n_j^i \mathbf{a}_i D(t - t_j^i) * \mathbf{G}_i = 0 \quad (6.34)$$

which is minimised using NNLS (Lawson and Hanson, 1995). In the use of NNLS in this thesis, source positions are determined using a grid search, and DC mechanisms are given by corresponding optimum ID result. The moment of each source can be constrained, which stabilises the inversion, although it has been shown that the exact value of total moment does not dramatically influence centroid times and positions (Quintero et al., 2014). Furthermore, it is found that multiple point-source inversions using NNLS tend to calculate sub-events that are more compact in space compared with ID. Zahradnik et al. (2014) show that if station distribution is poor, such as for offshore subduction zone earthquakes, the NNLS method produces more reliable results than ID.

## 6.5 3-D waveform simulations

As discussed in Section 6.4.2, MT inversions of regional/local waveforms typically assume simple 1-D Earth models and flat relief. However, the effects of topography and structural heterogeneity can lead to complex waveform phenomena that cannot be modelled with 1-D GF (e.g. Magnoni et al., 2014). Accounting for topographic effects, such as amplified ground motion and multiple reflections on hills and ridges (e.g. S. J. Lee et al., 2009) may reduce waveform misfit. Topography and bathymetry tends to be steep above a subduction forearc (e.g. forearc basins, coastal ranges and the magmatic arc); these features should be accounted for in accurate waveform modelling. In Chapters Four and Five, we inferred significant 2-D and 3-D velocity variations beneath the central Chile forearc. Therefore, the effect of inaccurate GF on MT studies in this region should be assessed. An improvement in GF accuracy is advantageous because it also allows MT inversion of small earthquakes (i.e.  $M_w < 3.0$ ), since higher frequency waveforms signals ( $> 0.1$  Hz) need to be modelled.

## 6.5 3-D waveform simulations

### 6.5.1 The spectral element method

The advent of parallel computing has allowed accurate numerical waveform simulations at a range of scales. One simulation approach uses *finite-differences* (FD), which have been widely used in past studies (e.g., Madariaga, 1976; Virieux, 1986; Olsen and Archuleta, 1996; Moczo et al., 2007). The main disadvantage of the FD method is its poor handling of sharp structural interfaces, such as topographic relief (e.g. Tarras et al., 2011). Therefore, FDs are not appropriate for a subduction zone setting, where there are strong topographic variations and complex geological interfaces such as the subduction megathrust and the continental Moho (see Chapter Two). Instead, *finite-elements* (FE) may be favoured due to their flexibility in honouring geological discontinuities although their calculation comes at a high computational cost.

In this thesis, we use the *spectral-element method* (hereafter, SEM), which is based upon the linear anelastic wave equation. The primary advantage of SEM is that it combines the accuracy of pseudo-FE methods with the flexibility of FD. SEM calculates seismic wavefields on a mesh of hexahedral finite-elements; at each element, high degree Lagrange polynomials are used to ensure spatial accuracy (Magnoni et al., 2014). The Lagrangian method provides simple time integration without the complexity of solving linear equations. Moreover, the diagonal mass matrix associated with this method means that SEM is well adapted for use on parallel, high performance computing architecture. The SEM was first used to simulate local and regional scale wave propagation (e.g. Komatitsch et al., 2010; Seriani et al., 1992; Tape et al., 2010), but has since been adapted for use on a global scale.

In this thesis, we use the SEM-based software package, *SPECFEM3D Cartesian* (e.g. Peter et al., 2011) to model waveforms from earthquakes in the central Chile subduction zone. Simulations are calculated using an accurate structural model based on the 3-D  $v_p$  and  $v_p/v_s$  models described in Chapter Five. In SPECFEM3D, seismic sources are defined by their six MT components, time shift, centroid location and half duration of the source-time function. Attenuation is calculated by an empirical relationship that is related to  $v_s$  (Olsen et al., 2006).

### 6.5.2 Mesh design

To produce wave propagation simulations, we generate a 3-D mesh that honours the topography and bathymetry of the central Chile subduction zone. A high-quality hexahedral mesh is vital for the numerical accuracy of simulations. An important parameter to consider in mesh design is the maximum order of Lagrange polynomials,  $n$ . If  $n < 4$ , numerical inaccuracies become similar to those of traditional FE methods. If  $n > 4$ , numerical accuracy improves, but computational cost becomes a limiting factor. Therefore, in the simulations presented in this thesis, we use  $n = 4$ . The minimum mesh grid spacing,  $\Delta x_{min}$ , depends on  $n$ , the minimum  $v_s$  of the model, and the shortest resolvable period,  $T_0$ :

$$\Delta x_{min} = v_{smin} T_0 \frac{n+1}{f(n)} \quad (6.35)$$

where the number of points per wavelength,  $f(n)$  should be greater than or equal to 5 (Casarotti et al., 2008). The second constraint governing mesh design is the stability of the simulation time step. For a given mesh spacing, there is an upper limit of the time step, which is dependent on Courant stability number,  $C$ , and maximum  $v_p$  inside the model:

$$\Delta t < C \frac{\Delta x_{min}}{v_{pmax}} \quad (6.36)$$

If this criterion is exceeded, numerical calculations become unstable;  $C$  values of 0.3–0.4 can be assumed for deformed and heterogeneous meshes (Casarotti et al., 2008).

Based on the grid criteria described above, local and regional waveform simulations can require a mesh that contains hundreds of thousands to tens of millions elements. This issue highlights the need to generate a mesh using a parallel computing process. We use the semiautomatic meshing code, *GEOCUBIT* (Casarotti et al., 2008), which uses a Python interface to send meshing commands in parallel. This code can generate hexahedral meshes that honour surface topography and geological discontinuities. In this thesis, we set mesh elements to triplicate above 40 km, an average depth for the Moho in central Chile (Chapters Four and Five). This finer spacing allows accurate simulations in areas of low  $v_s$ , such as the marine forearc, and

## 6.6 Summary

greater element spacing in high  $v_p$  regions at depth to reduce computational expense by allowing a larger time step. In this thesis, the upper mesh surface is based on high-resolution models of topography and bathymetry for the central Chile margin. We use the 90 m resolution Shuttle Radar Topographic Mission digital elevation model and the 30 s General Bathymetric Chart of the Oceans (GEBCO) dataset.

## 6.6 Summary

This chapter has described and explained a detailed workflow of full-waveform MT inversion that calculates either single point-source solutions or multiple point-source solutions for complex ruptures. The latter method forms the basis of the following chapter, which focuses on detailed source processes of large subduction earthquakes. Single point-source inversion of smaller earthquakes is implemented to provide independent evidence for active faulting adjacent to the subducting plate interface (Chapters Seven and Eight). Many methods are available to measure modelling and data uncertainties, which should be used to assess the stability of MT solutions. Interpreting non-DC earthquakes remains a challenge: on-going debates show how non-DC earthquakes can be attributed to both faulting complexity and artefacts due to assumptions used in waveform modelling. Therefore, the interpretation of complex MTs requires careful consideration.

Rough topography and structural heterogeneity can strongly affect waveforms of earthquakes that are recorded at the surface. To illustrate this point, waveforms based on realistic 3-D structure can improve waveform fits in MT inversion by more than 50% (Ramos-Martínez and McMechan, 2001). 3-D effects are likely to be prominent in a subduction zone, yet no published studies have investigated this topic. Advancement in this field is probably limited due to several factors, including the lack of high-quality broadband data, the shortage of well-constrained velocity models, and the high computational cost of 3-D simulations. The central Chile subduction zone provides a natural laboratory to assess 3-D wave propagation, due to the availability of a detailed structural model (as presented in Chapters Four and Five) and extensive broadband recordings of aftershocks following the Maule earthquake. In the following chapter, we demonstrate how full-waveform simulations can be used show how MT solutions of offshore subduction earthquakes may be biased. We also use 3-D

simulations to establish how stress is transferred from plate interface slip to adjacent faults in the upper plate. In Chapter Eight, we also assess how full-waveform inversion can be used to provide additional constraints on subsurface velocity structure.





## Chapter 7

# SEISMIC SLIP ON AN UPPER PLATE NORMAL FAULT DURING A LARGE SUBDUCTION MEGATHRUST RUPTURE

This chapter is from a paper that has been published in *Nature Geoscience*. The manuscript was first submitted on June 17, 2015, accepted for publication on September 23, 2015, and published online on November 16, 2015. The paper is written by Stephen Hicks (main author) and Andreas Rietbrock (University of Liverpool). This research was the primary focus of my PhD research during May 2014 – June 2015. The Methods section and Supplementary Information of the submitted manuscript are incorporated into the main body of this chapter. The aim of this chapter is to assess of a source complexity of a megathrust earthquakes by performing multiple point-source inversion of locally recorded seismic waveforms (Key Aim 2). We also use simulations of 3-D wave propagation to assess possible biases in source mechanism parameters. The results illustrate how slip on the plate interface responds to structural heterogeneity in the upper plate at short timescales.

### Manuscript abstract

Understanding the distribution of fault slip during large subduction zone earthquakes is vital for quantifying accumulation and release of tectonic stresses during the seismic cycle. Slip inversions are typically constrained to a single known fault plane. However, slip may occur on multiple faults due to stress triggering, resulting in phenomena such as earthquake doublets. While such phenomena are reported for faults within the subducting plate, there are no documented cases of rapid stress triggering from the plate interface to faults in the overriding plate. By analysing local seismic waveforms, we show that an  $M_w$  7.1 earthquake in the Chile subduction zone, assumed to have a simple mechanism of plate interface thrusting, was composed of two ruptures on separate faults. Within 12 seconds, a plate interface thrust event triggered a large rupture on an upper plate normal fault 30 km away. This configuration of a partitioned rupture is consistent with normal faulting in the ensuing aftershock sequence. Our result provides new evidence for instantaneous triggering of seismic slip in the upper plate caused by a plate interface rupture. The upper plate rupture was masked from teleseismic waveforms and not reported in global moment tensor solutions. Our findings pose new challenges for real-time tsunami warning systems in the detection of shallow upper plate ruptures.

## 7.1 Introduction

A recent succession of large ( $M_w > 8$ ) earthquakes in circum-Pacific subduction zones has focussed attention on the relationship between physical properties and stress distribution along the megathrust plate interface. Seismic ruptures along the megathrust can be viewed as smooth and spatially varying patches of slip on a single fault; in this case, the subducting plate interface (e.g. Moreno et al., 2012). The fault geometry used in early coseismic slip models is underpinned by centroid moment tensor (CMT) solutions often reported by earthquake monitoring agencies. Although more sophisticated slip inversions use curved faults based on regional subduction geometry (e.g. Hayes et al., 2012), slip is nearly always assigned to a single fault.

An alternative rupture configuration is slip occurring on separate faults due to static or dynamic triggering processes (Freed, 2004), resulting in phenomena such as doublets (e.g. Ammon et al., 2008). A doublet is the occurrence of two nearby

earthquakes with similar magnitude. The time delay between ruptures can range from months (e.g. Ammon et al., 2008) to seconds (Lay et al., 2013). Many documented cases of subduction zone doublets involve triggering between the subducting plate interface and deep-rooted faults in the downgoing plate (Ammon et al., 2008; Lay et al., 2010b). Although the implications for tsunami hazard are significant, there are no reported cases of rapid triggering from the plate interface to the upper plate, where there are complex faulting networks (Audin et al., 2008; Melnick et al., 2009). To resolve triggered faulting in such cases, dense local seismic observations are needed. A region with a suitably dense network of seismometers is the central Chile subduction zone after the  $M_w$  8.8 Maule earthquake in 2010. The ensuing aftershock sequence was captured in detail by the International Maule Aftershock Deployment (e.g. Beck et al., 2014; Rietbrock et al., 2012).

	Origin time (UTC)	Longitude (°)	Latitude (°)	Depth (km)	Ref.
<b>1-D relocated</b>	20:20:15	-73.82	-38.47	39	This study
<b>3-D relocated</b>	20:20:15	-73.73	-38.54	23	
<b>CSN (Chile)</b>	20:20:11	-73.96	-38.34	18	Centro Sismológico Nacional (2011)
<b>USGS NEIC</b>	20:20:17	-73.33	-38.36	24	USGS-NEIC (2011)
<b>GFZ- GEOFON</b>	20:20:17	-72.33	-38.23	12	GFZ-GEOFON (2011)

Table 7.1: Hypocentral estimates for the Araucania earthquake.

Here, we focus on the largest interplate aftershock of the Maule sequence: the  $M_w$  7.1 Araucania earthquake that occurred on 2 January 2011 at 20:20:18 UTC (Table 7.1). Based on CMT solutions derived from teleseismic waveforms (Figure 7.1; Table 7.2), the Araucania earthquake appears to be a ‘straightforward’ plate interface thrusting event (Ekström et al., 2012; United States Geological Survey National Earthquake Information Center, 2011). Its epicentre lies that acted as a barrier during the 1960  $M_w$  9.5 Valdivia (Moreno et al., 2009) and 2010  $M_w$  8.8. Maule (Moreno et al., 2012; Rietbrock et al., 2012) earthquakes (Figure 7.1). Moreover, the upper plate in this area is heavily faulted (Melnick et al., 2009; Moreno et al., 2012). Therefore,

## 7.1 Introduction

the Araucania earthquake is an ideal candidate to examine possible connections between the plate interface and upper plate faults.

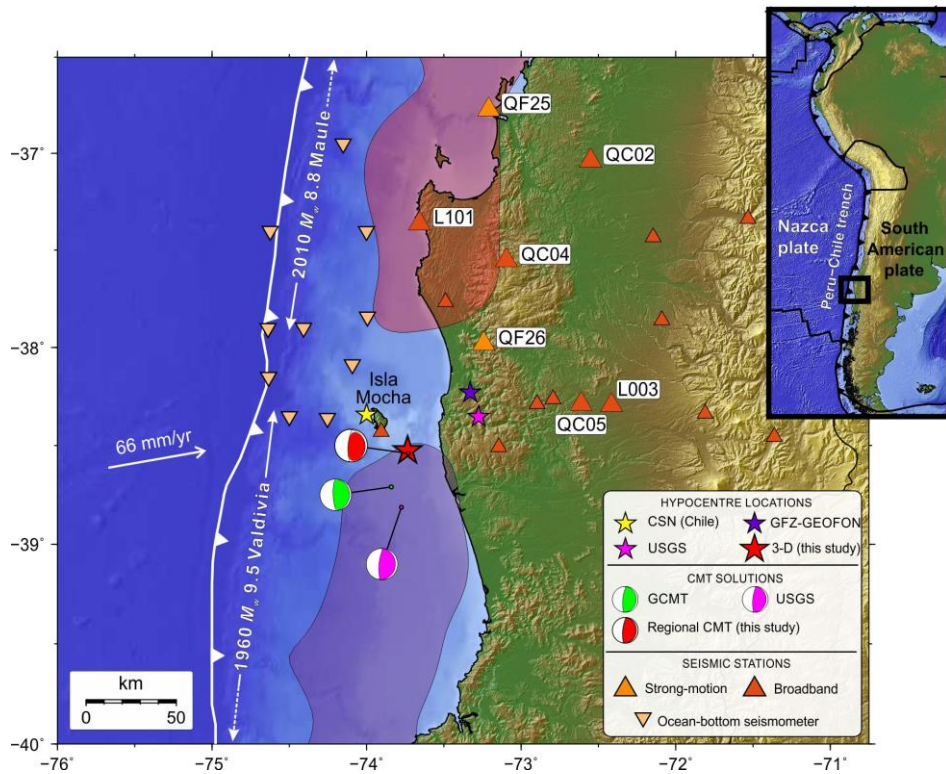


Figure 7.1: Location map of the Araucania earthquake. Stations used for moment tensor inversion are labelled by their corresponding station code. Other stations are used for hypocentre relocation only. Shading indicates rupture areas of great earthquakes in 1960 (Moreno et al., 2009) and 2010 (Moreno et al., 2012). Inset: Regional plate tectonic setting.

In this chapter, we use a multiple point-source inversion of regional seismic data (Sokos and Zahradnik, 2006; Zahradnik et al., 2005). Compared to more conventional slip inversions along pre-defined fault planes (Moreno et al., 2012) and single point-source CMT inversions (Ekström et al., 2012), we can retrieve individual centroid times and allow multiple faulting styles on a grid of trial point-sources. A detailed understanding of 3-D crustal velocity structure (Chapters Four and Five) ensures reliable waveform inversion. Synthetic tests show that we can accurately resolve a range of extended source configurations with offshore rupture using onshore seismic stations. An inversion of observed waveforms reveal that the Araucania earthquake was composed of two ruptures: the first due to thrusting on the plate interface; the second, eleven seconds later, occurred due to slip on an upper plate normal fault.

## 7.2 Mainshock hypocentre relocation

We manually picked P- and S-wave onset times at both onshore and offshore stations at  $< 150$  km distance (Figure 7.1). The onset times were then inverted for the hypocentral location inside our local 3-D velocity model (Chapter Five). Our relocated hypocentre lies approximately halfway between the coastline and Isla Mocha,  $\sim 30$  km to the north of the USGS centroid and gCMT solutions (Figure 7.1, Table 7.1). The hypocentral depth of 23 km is consistent with the location of the subducting plate interface, based on our independent estimate of regional slab geometry (Chapter Five). The large discrepancy in the CSN (Centro Sismológico Nacional) location (30 km relative to our 3-D relocation) is due to 3-D seismic velocity variations that cannot be accounted for using a 1-D velocity model using onshore stations only. This mislocation is also demonstrated by our own location using a 1-D velocity model (Table 7.1).

	Centroid			Moment tensor				Ref.
	Long. (°)	Lat. (°)	Depth (km)	Nodal plane 1	Nodal plane 2	%DC	$M_w$	
<b>Regional CMT</b>	-73.73	-38.54	23	345/18/71	184/73/96	89	7.0	<i>This study</i>
<b>USGS NEIC (w-phase)</b>	-73.35	-38.37	24	16/14/115	171/77/84	96	7.1	USGS NEIC (2011)
<b>Global CMT</b>	-73.84	-38.71	19	005/13/97	178/77/88	97	7.1	Ekström et al. (2012)

Table 7.2: Single point-source CMT solutions for the Araucania earthquake. Nodal planes are described by strike/dip/rake (°).

### 7.2.1 Data selection and processing

For the waveform inversion of the Araucania earthquake, we used broadband and strong-motion stations that were located onshore within an epicentral distance of 200 km from the Araucania earthquake. We used waveforms from stations that have a high

## 7.2 Mainshock hypocentre relocation

signal-to-noise ratio ( $> 10$ ) in the frequency range 0.01–0.10 Hz (Figure 7.2). Due to the close proximity of some stations to the earthquake, we excluded waveform records that were either clipped, had long period disturbances, or instrument tilt effects. These quality-control checks resulted in a set of seven stations (including two strong-motion stations) located north and east of the Araucania earthquake (Figure 7.1).

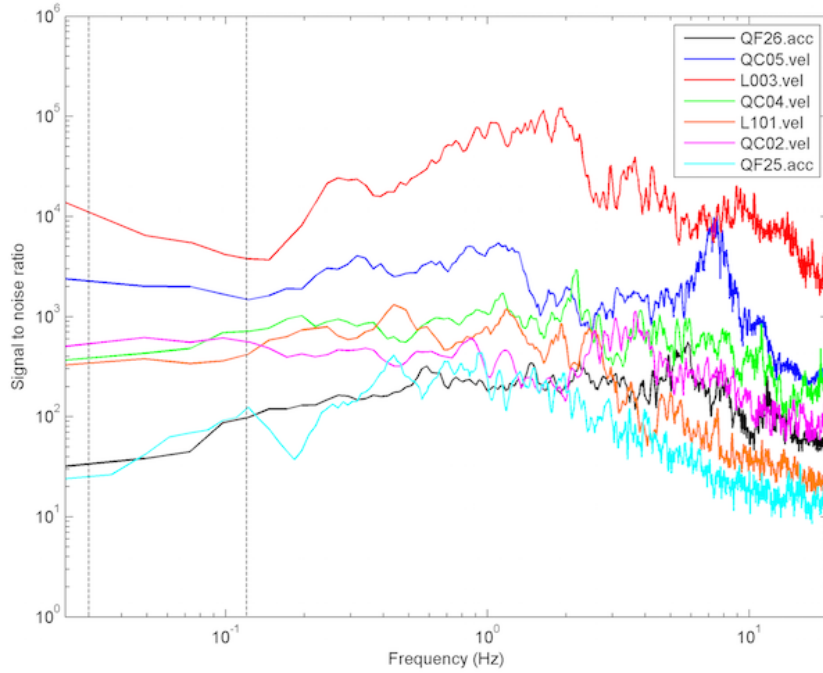


Figure 7.2: Signal-to-noise ratio analysis for stations used in the single and multiple point-source inversions. The dashed vertical lines denote the approximate frequency range used.

### 7.2.2 Inversion algorithm

Iterative deconvolution (ID) (Zahradnik et al., 2005) is used for the multiple point-source inversion of deviatoric moment tensors. ID works by inverting for the best-fitting focal mechanism and timing of sources for a prescribed set of points to minimise the L2 misfit between observed and synthetic waveforms. A grid search is then performed to select the source position that produces the highest correlation between observed and synthetic waveforms. The first inversion explains the full-waveforms using a single source, the synthetics of which are then subtracted from the observed waveforms. The remaining waveforms are then used to invert for subsequent sub-events (Zahradnik et al., 2005). After the retrieval of each sub-event, VR is calculated and manually assessed to ensure that multiple sub-events are required by the data and the waveforms are not solely fitting correlated noise.

For moment tensor inversion, we use the software package, ISOLA (Sokos and Zahradnik, 2006). In the inversion, the moment-rate of the source is prescribed and is found by manually searching for the source length that produces the maximum VR. If the moment-rate of the source is shorter than the minimum inverted period, then the source can be represented by a delta function. To negate artifacts produced by ID, we also test the stability of our multiple point-source solution using non-negative least squares (hereafter, NNLS) inversion (Zahradnik and Sokos, 2014). In the NNLS approach, the double-couple focal mechanism at each source is prescribed. At each trial point-source position, the moment rate is represented by a set of shifted triangles. The weight of each triangle is then inverted for using NNLS. In this chapter, we use one-second triangle shifts. The moment of each source can be constrained, which stabilises the inversion, although the exact value of total moment does not dramatically influence source timings or positions (Quintero et al., 2014).

The inversion is performed on bandpass-filtered displacement waveforms. The effect of different 1-D velocity models was tested; the final solutions were calculated using a velocity model appropriate for the coastline of south-central Chile (Figure 7.3). We analysed the effect of data errors and imperfect Green's functions by systematically removing pieces of data from the inversion (jackknifing). Where subsurface structure is complex, removal of certain stations may have a large effect on the final solution (Sokos and Zahradnik, 2013). Based on the analysis of signal-to-noise ratio (Figure 7.2), we used a lowermost frequency limit of 0.02 Hz throughout this chapter. The upper frequency limit was dependent on the source parameterisation used (single or multiple source).

## 7.3 Synthetic tests

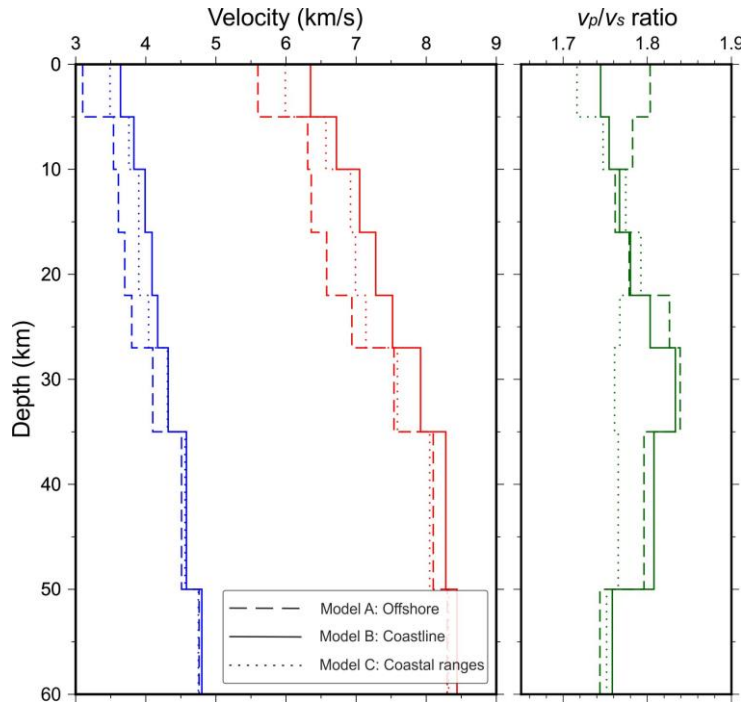


Figure 7.3: 1-D velocity models tested in this study based on our local tomographic model (Chapter Five). Model B (Coastline) was used for the final source solutions.

## 7.3 Synthetic tests

### 7.3.1 Resolving capability of multiple point-sources

Before inverting the real data, we tested the performance of our inversion strategy, and its ability to resolve multiple point-sources by simulating several different source configurations. We then inverted these synthetic waveforms as both single and multiple point-source models. Here, we describe the results using iterative deconvolution (ID). Based on global CMT solutions (Figure 7.1, Table 7.2), we assumed that the causative fault plane was the shallow, eastward dipping subducting plate interface. We designed a 2-D grid of 49 trial point-sources that lie in the same orientation as the megathrust fault (Figure 7.4), according to regional plate interface geometry (Chapter Five). The plane of trial grid positions passes through the hypocentre of the Araucania earthquake.



## Chapter 7: Seismic Slip on an Upper Plate Normal Fault During a Large Subduction Megathrust Rupture

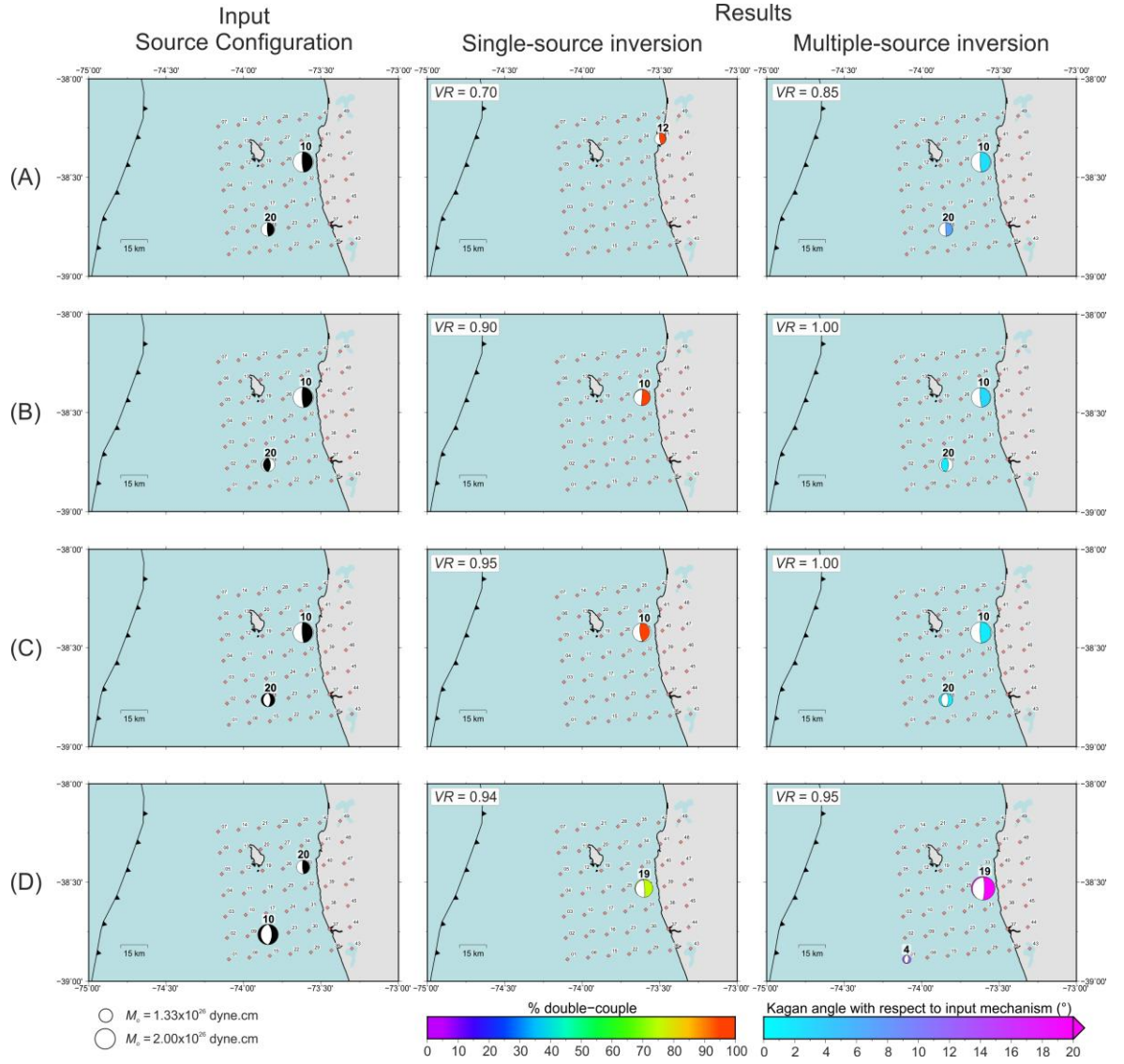


Figure 7.4: Synthetic source recovery tests for different source configurations (A-D). The number above each beach ball represents the input and recovered centroid time of each source. For the single-source inversion, focal mechanisms are coloured by %DC. For the multiple source inversion results, focal mechanisms are coloured by the Kagan angle (minimum rotation angle) with respect to the corresponding input beach ball.

Given the encouraging results from the station coverage test, our next step is to consider whether certain source configurations may bias retrieval of MT parameters. Previous documented examples of using ISOLA to resolve multiple sub-events assumed a fixed focal mechanism (Quintero et al., 2014; Zahradnik and Sokos, 2014). To advance these previous studies, our objective in this chapter is to assess source complexity due to triggering on nearby faults. Therefore, we tested a combination of

### 7.3 Synthetic tests

sub-event faulting types. Our four multiple point-source scenarios and corresponding results are summarised in Figure 7.4 and Table 7.3.

For most of these cases, the inversion resolves the timing of the two sub-events; the relative moment of the sources is also recovered. However, for single point-source inversions, the recovered moment release does not always equal the sum of both input sub-events. This discrepancy is particularly noticeable where both sub-events are reverse faulting (Cases A and B), which also results in a lower variance reduction (VR). Importantly, apart from where the offshore sub-event is larger and ruptures earlier (Case D), the double-couple percentage (%DC) from the single-source inversion is high, potentially masking source complexity (Rivera and Kanamori, 2014). In this case, the retrieved mechanism is most similar to the first sub-event. We speculate that the result may come from the complex superposition of high amplitude long period waves from these two events when they arrive at the stations. This result occurs due to the uneven distribution of stations and means that we may not be able to resolve a doublet involving a larger offshore rupture occurring before a smaller event that is located closer to the stations. Based on VR and sub-event retrieval performance, the best source configuration for our network is the case of a thrust event followed by a smaller extensional rupture further offshore (Case C).

Case	Input sources		Recovered Sources													
			Single-source inversion							Multiple-source inversion						
	Sub-event I (t = 10 s)		Sub-event II (t = 20 s)							Sub-event I						
	Pos.	Mech.	Pos.	Mech.	dt (s)	Mech.	%DC	Pos.	dt (s)	Mech.	Rot. angle	Pos.	dt (s)	Mech.	Rot. angle	
<b>A</b>	33	357/10/90	16	357/10/90	12	29/12/18	90	33	10	4/9/96	3	33	20	5/3/97	1	
<b>B</b>	33	357/10/90	16	0/60/90	10	4/89/-97	97	33	10	351/8/86	3	16	20	1/59/90	1	
<b>C</b>	33	357/10/90	16	0/60/-90	10	15/19/111	99	33	10	0/9/92	2	16	20	1/59/-89	1	
<b>D</b>	16	0/60/-90	33	357/10/90	19	218/9/-49	72	1	4	178/39/-99	12	32	19	210/11/-61	21	

Table 7.3: Results from the synthetic sensitivity tests described in Section 7.3.1 and presented in Figure 7.4. Pos. = source position; Mech. = focal mechanism; Rot. angle = rotation angle with respect to input source mechanism; dt = centroid time shift; Meh = focal mechanism.

## 7.3 Synthetic tests

### 7.3.2 Relative uncertainty estimates

As a second synthetic test, we quantify the relative uncertainty in source mechanism caused by reduced azimuthal coverage on the capability of the inversion to resolve sources located far offshore. Here, we generated 1-D synthetics for a range of single-source faulting types located offshore (Table 7.4). We used a tool in ISOLA to calculate theoretical uncertainty in Green's functions. Such an uncertainty estimate is relative because data variance is unknown. However, relative uncertainties can be calculated between two sets of station configurations. A 5D error ellipsoid is computed and a mean Kagan angle (Kagan, 1991) is given, providing an estimate of the error in focal mechanism parameters, with respect to the best-fitting solution. We computed uncertainties for two scenarios: one using the real station coverage (Figure 7.1), the other using a network with perfect azimuthal distribution. The results from this test are shown in Table 7.4. We found that errors using the actual station coverage are only 12–39% greater than those using a perfect network; uncertainties are smaller when a nodal plane strikes in the same direction as the network (north-west). These results imply that we can trust the focal mechanisms of offshore seismic sources using our station distribution.

The regional CMT solution provides a good fit to the observed waveforms at most stations (Figure 7.5). The centroid lies close to our relocated epicentre; its mechanism is consistent with the teleseismic GCMT and USGS solutions (Figure 7.1, Table 7.2), indicating thrusting along the plate interface. A high double-couple percentage (%DC) indicated by the global (98%) and our regional solutions (85%) suggests a simple faulting style. When we increase the upper frequency limit to  $> 0.06$  Hz, waveform variance reduction (VR) sharply decreases and, at the upper limit of 0.08 Hz, we notice two clear arrivals in the observed waveforms (Figure 7.6, Figure 7.7). We also find that as the upper frequency bandpass cut-off increases, %DC gradually decreases. This trend continues until around 0.057 Hz, above which %DC becomes high. Therefore, the next step is to consider whether a complex source can be resolved using higher frequency waveforms and a multiple point-source parameterisation.










Input focal mechanism at source position 16 (strike/dip/rake)		Focal mechanism uncertainty (mean Kagan angle [°])		% Error due to actual station configuration
		Real station configuration	Ideal station configuration	
010/15/090		4.48	3.91	15%
000/45/090		4.84	3.81	26%
045/45/090		4.25	3.79	12%
090/45/090		5.22	3.78	38%
000/45/-090		4.84	3.81	27%
312/45/-116		5.30	3.97	34%
000/90/180		5.32	3.86	38%
045/90/180		5.38	3.88	39%

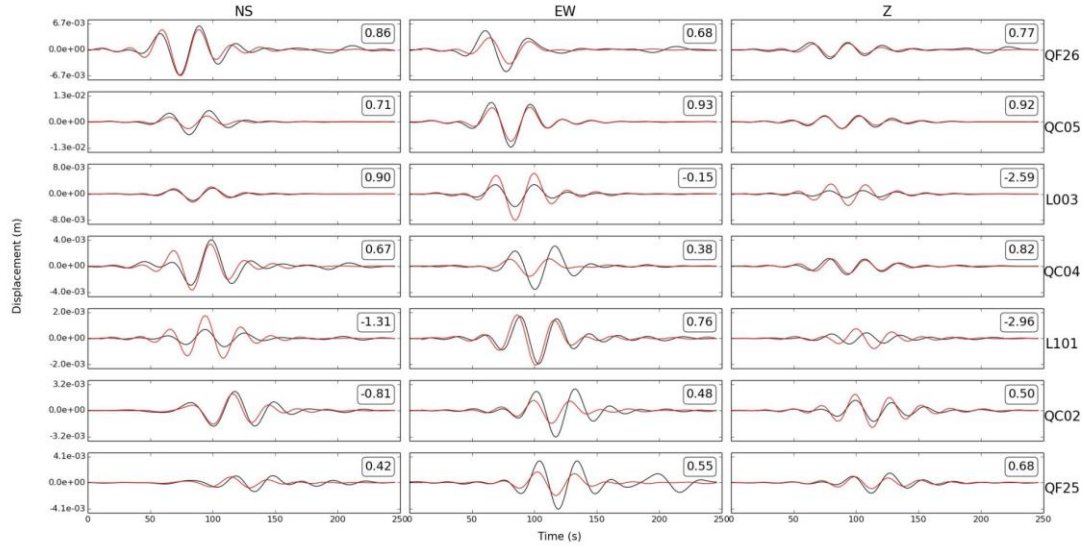
Table 7.4: Relative uncertainty estimates of different faulting styles for a single point-source offshore (source position 16). Uncertainties are calculated for both our actual station distribution (Figure 7.1) and a network of ideally distributed stations.

## 7.4 Multiple point-source solution

We first carried out a multiple point-source inversion using ID, in which the deviatoric moment tensor mechanisms of both sources were allowed to vary. A two-point-source model is a logical progression; an  $M_w \sim 7$  earthquake is likely composed of no more than two to three patches of slip (Zahradnik and Sokos, 2014). The grid of point sources was kept the same as for the single point-source inversion. For the source-time function, we found that with increasing length of the triangle, the total moment gradually increases, whereas VR and %DC of each source reach a maximum at 18 s (Figure 7.8). We therefore fixed the triangle length of each source to 18 s for the ID multiple point-source inversion, although the point-source mechanisms remain consistent for different triangle lengths, suggesting a stable solution.

## 7.4 Multiple point-source solution

**a**



**b**

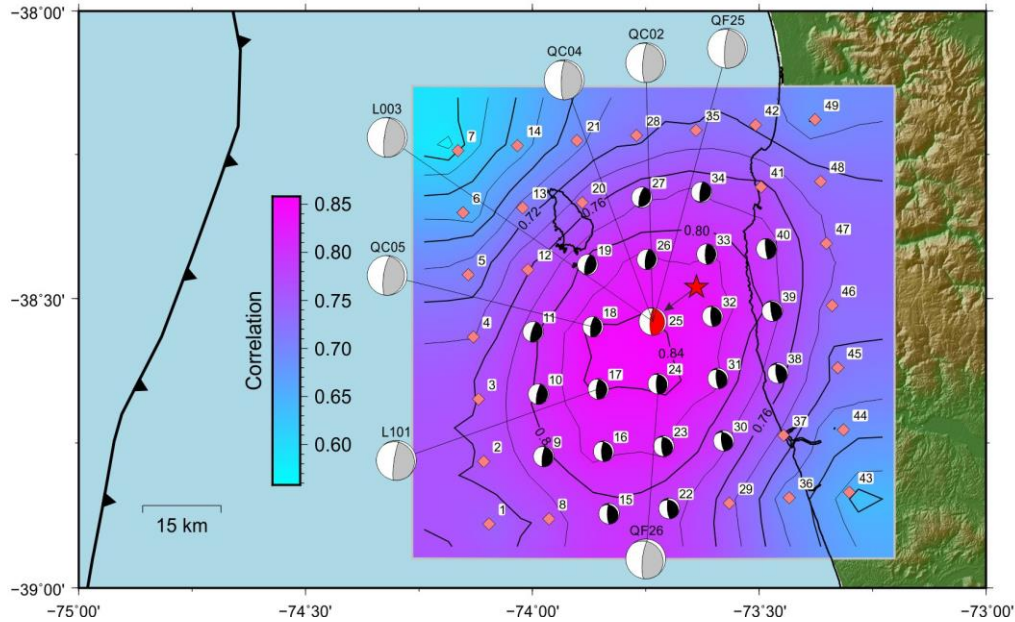


Figure 7.5: Single source inversion results. a) Comparison between the observed (black) and synthetic (red) waveforms. Waveforms are filtered in the frequency range 0.02–0.04 Hz. Station names are shown on the right and the components are labelled at the top. Numbers next to waveforms denote corresponding variance reduction. b) Grey beach balls show solution variability based on jackknifing tests, labelled with the station removed in each inversion. The coloured grid represents the correlation between waveforms for each trial point-source position (numbered). Solutions that lie within 90% of the maximum VR are plotted in black. The highest correlation solution is plotted in red. The red star denotes the epicentre of the Araucania earthquake.

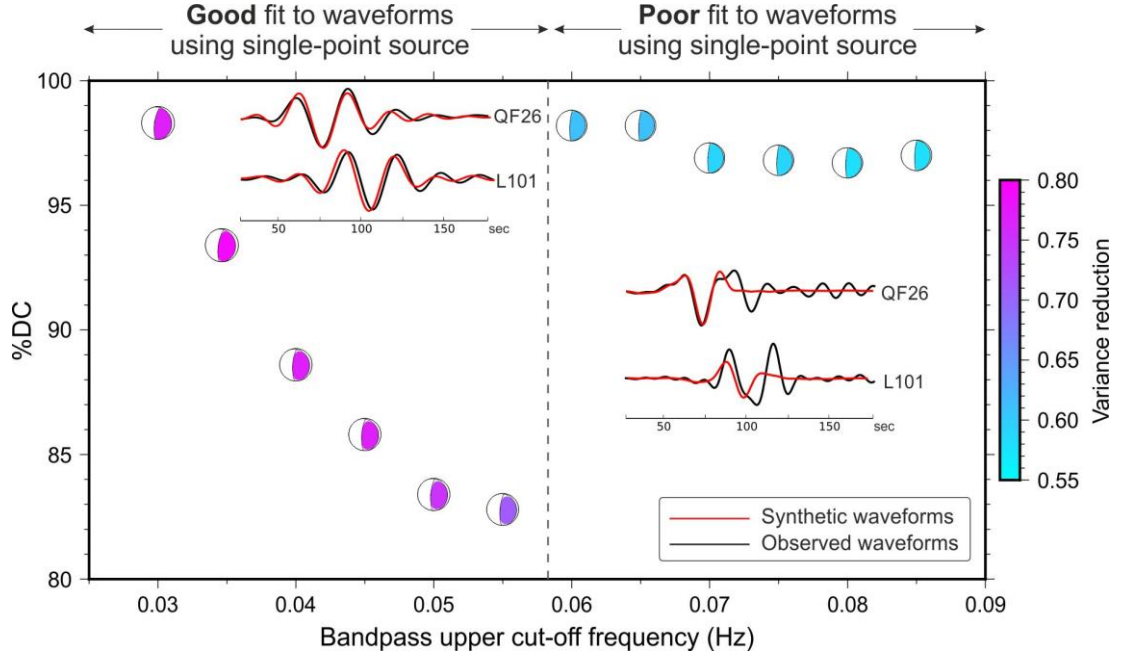


Figure 7.6: Double-couple percentage (%DC) and variance reduction (VR) of the single point-source versus frequency. A transition occurs at 0.057 Hz, where VR suddenly decreases because the waveforms cannot be explained by a single point-source alone. This change is illustrated by representative waveforms at low and high frequencies.

Compared with that of using the first source alone (VR = 0.57), introduction of the second source significantly increases the waveform fit (Figure 7.9a) by 30% (VR = 0.73). In order to test the statistical validity of fitting the waveforms using the second sub-event, we assess the significance of the variance reduction using the  $F$  test. Similar tests have been previously carried out for multiple point-source moment tensor inversions (Adamova et al., 2008; Sipkin, 1986).

Each model is characterised by the variance between synthetic and observed waveforms:

$$E = \sum [O_i - S_i]^2 \quad (7.1)$$

where  $O$  and  $S$  represent the observed and synthetic data, respectively.



## 7.4 Multiple point-source solution

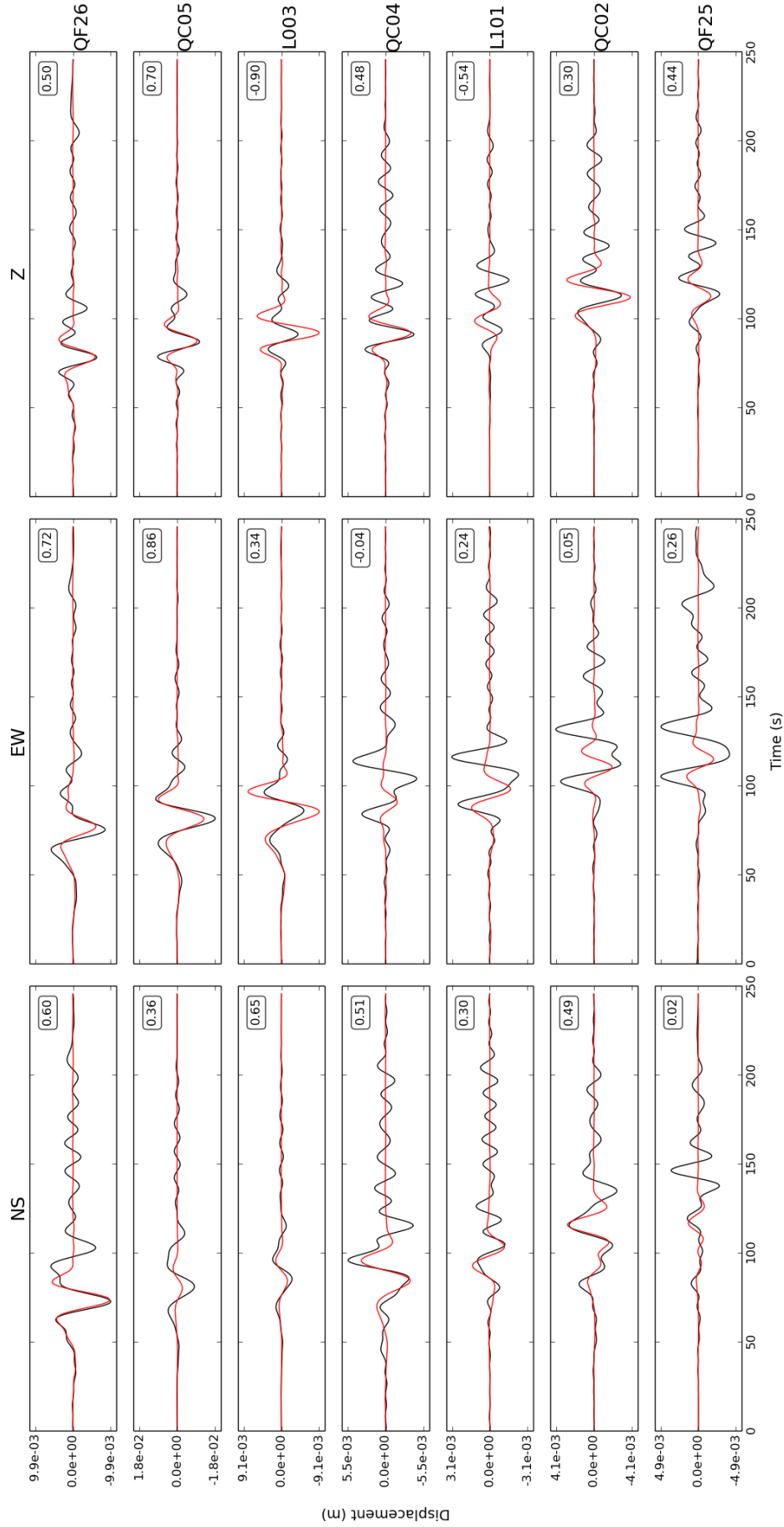


Figure 7.7: Comparison between the observed (black) and synthetic (red) waveforms at high frequencies (0.02–0.08 Hz) solution using a single point-source. Station names are labelled. Numbers alongside each waveform component denote the corresponding VR.



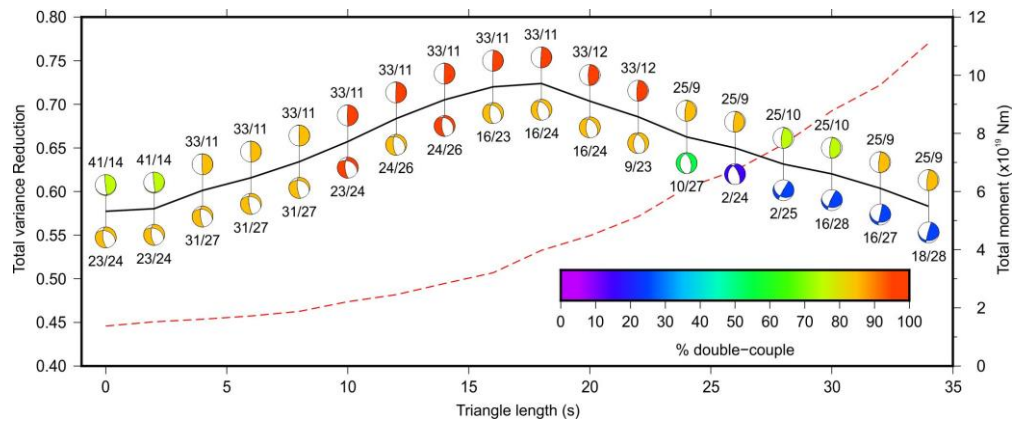


Figure 7.8: Correlation (black line) and total moment (red dashed line) of the multiple point-source solution as a function of triangle length using iterative deconvolution. Beach balls above and below the line give the best-fitting mechanism for Events I and II, respectively.

We therefore define the ratio:

$$F = \frac{E(model\ 2)}{E(model\ 1)} \quad (7.2)$$

which is compared with the  $F$  test values at different confidence levels and for different degrees of freedom,  $dof$ , where  $dof = N - M$ .  $N$  corresponds to the number of data points, and  $M$  is the number of free parameters ( $M = 5$  for a deviatoric inversion). Data at low frequencies are clearly correlated, but we assume that the data are uncorrelated when the waveforms are sampled within the studied period range (Dreger and Woods, 2002) ( $> 12$  s based on our lowpass filter corner). Moment tensors are calculated over a time window that is 245.76 s in length. Based on our low pass filter corner frequency, this time window reduces to 19.7 s, which results in 655 data points for each component. For all three components and seven stations, we thus have a total of 13750 degrees of freedom. The variance ratio,  $F$  between our single and two-point-source moment tensor inversions equals 1.28, which is much greater than the critical  $F$  value of 1.06 at a confidence level of 99.95%. Consequently, we argue that the introduction of a second point-source is statistically significant with a high confidence.

## 7.4 Multiple point-source solution

Faulting styles at each trial point-source position are consistent, with sharp correlation maxima (Figure 7.9b). Based on our results, we can confidently identify the following sequence of events, which can be regarded as a closely-spaced doublet (CSD), both in time and space. Shortly after nucleation, Event I ( $M_w$  6.8) ruptured the megathrust beneath the coast. No more than twelve seconds later, Event II ( $M_w$  6.7) ruptured to the south-west at a shallower depth and with an oblique normal faulting mechanism. As a test of solution stability, we perform jackknifing tests by removing one station at a time from the inversion. The results of these tests are shown in Table 7.5 and demonstrate remarkably consistent centroid positions and focal mechanisms for Events I and II. The jackknifing test therefore indicates that the selected multiple point-source solution is not dependent on one single waveform. Furthermore, a three-point-source approximation did not meaningfully improve the waveform fit (VR = 0.76; 3% increase in VR compared with two point-sources).

Since ID inverts for the first point-source before subsequently calculating the second source, we carried out a test to determine whether Event II is dependent on the chosen location and faulting style of Event I. Normally, we accept the source position that produces the highest waveform correlation. However, for this test, we fixed the position of Event I and chose the corresponding best-fitting mechanism. We carried out the test at all trial point-sources adjacent to Position 33 (the best-fitting position of Event I). The results of this test are shown in Table 7.6. For all but one position of Event I, the position, timing, and mechanism of Event II remain consistent with the chosen solution. When Event I is fixed to Position 25, the MT solution of Event II appears less stable. Position 25 is next to Position 16 (the location of Event II from ID; Figure 7.9), so this discrepancy is expected because the inversion tries to explain both events at Position 25 with a single source. In summary, we find that the Event II solution is stable with respect to the exact position and mechanism of Event I.

We used NNLS to test the certainty of the solution obtained by ID. To search for the best-fitting source configurations, we performed two inversions: one in which total moment was constrained by the ID solution; the other in which moment was allowed to vary. We tested many source positions and faulting styles for Events I and II using NNLS, but we found that the highest VR came from the two-point-source configuration found with ID. Using the mechanisms given by the ID solution, we then

carried out a grid-search over all possible combinations of the two-point-source locations using the NNLS. As expected, the moment-constrained inversion is most similar to the ID solution (Figure 7.10). Nevertheless, both inversions produce results consistent with the ID solution. Importantly, the resulting source-time function obtained by NNLS shows that both events have a similar time function to the 18 s triangle source used in ID (Figure 7.9c). In summary, we find no bias in the results caused by the inversion method.

## 7.5 Comparison with aftershock locations and mechanisms

A thorough analysis of aftershocks is needed because there are no available CMT solutions from global agencies; the largest recorded aftershock had  $M_b$  4.9 (based on the USGS-NEIC catalogue). We searched continuous waveforms from local onshore and OBS stations in the 30 days following the mainshock. To ensure reliable locations, we relocated events that had a minimum of five P-wave and three S-wave observations. The relocation was performed in a similar way to that of the mainshock (Section 7.2). The average standard error in depth of our aftershock relocations is 1.2 km. We also inverted for single point-source moment tensor solutions of aftershocks in the frequency range 0.05–0.11 Hz. The grid search was carried out over a range of depths, centred on each hypocentre location. Centroid depths were generally consistent with hypocentral depths. Solution quality was tested using different combinations of stations and velocity models, as well as crosschecking with first motion polarities.

Locations and mechanisms of aftershocks (Figure 7.11) support our CSD interpretation. From our 44 relocated events, it is clear that there are two distinct groups of aftershocks (Figure 7.11a). One group is located in the coastal region (hereafter, Group A); the other 30–40 km to the south-west (hereafter, Group B). Group B aftershocks have shallower depths, located within the marine forearc, up to 9 km above the plate interface (Figure 7.11b). We obtained 19 CMT solutions from the aftershock sequence (Figure 7.11), all of which have depths in agreement with their hypocentral location. Normal faulting mechanisms dominate aftershock Group B. Group A aftershocks comprise mixed faulting styles, but interplate thrust faulting is most common.

## 7.5 Comparison with aftershock locations and mechanisms

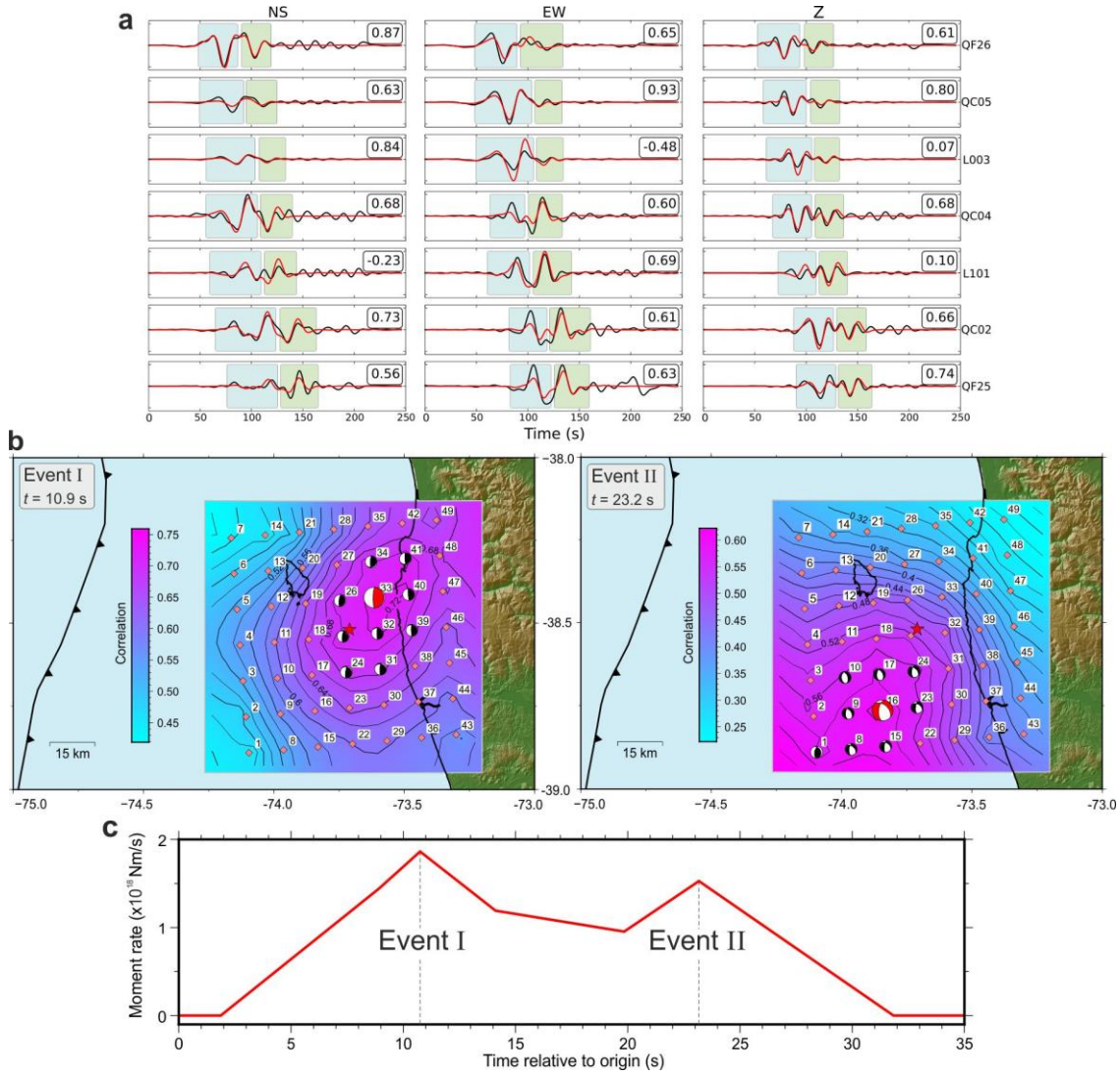


Figure 7.9: a) Observed (black) and synthetic (red) waveforms for the best-fitting high frequency (0.02–0.08 Hz) solution using two point-sources. Station names are labelled. Numbers alongside each waveform component denote VR. Blue and green shading denotes the contribution from each event. b) Waveform correlation for each event as a function of trial point-source position (numbered). The time shifts of Events I and II are shown. Black beach balls are solutions that lie within 90% of the best-fitting solution's (red beach ball) VR. The red star denotes the earthquake's epicentre. c) Resulting moment-rate function obtained using NNLS.

## 7.6 3-D waveform propagation effects

A puzzling location discrepancy between Event II and aftershock Group B (Figure 7.11a) raises the question of possible location bias in the multiple point-source inversion. So far, we have computed synthetic seismograms by calculating Green's functions in a 1-D velocity model. However, in the shallow regions of subduction zones, there are strong lateral velocity gradients, particularly in S-wave velocity (Figure 7.11b, Chapter Five). Therefore, a more realistic velocity model can improve waveform fits and make source inversions more stable.

To account for lateral velocity variations, we simulated waveforms in our 3-D velocity model (Chapter Five) using the spectral element code SPECFEM3D (Komatitsch et al., 2010). For the simulations, we constructed a hexahedral unstructured mesh (Figure 7.12) using the GEOCUBIT software package (Casarotti et al., 2008). The lateral resolution at the surface is 5 km, coarsening at a refinement layer (45 km depth, which is an average Moho depth for the region (Chapters Four and Five). The mesh honours surface relief and bathymetry to ensure that topographic effects on waveform propagation are accurately simulated. Our mesh does not contain dipping geological discontinuities in the subsurface, such as the oceanic Moho, due to the lack of constraints on its geometry. This mesh has been designed for simulations that are accurate up to  $\sim 0.3$  Hz, well above the maximum frequency of our source inversions, ensuring numerically stable simulations.

We generated 3-D synthetics based on our two-point-source solution and used these as input to a multiple point-source inversion using 1-D Green's functions. Whereas the position of Event I remains stable, we find that the inversion shifts Event II 12 km to the south (from position 16 to 15; Figure 7.13). Similarly, when we simulate the waveforms from Event II at the location of aftershock Group B (position 17), we find a similar southward shift, as implied from the real data inversion. Therefore, it is likely that Event II occurred  $\sim 12$  km northward with respect to the formal inversion result of Figure 7.9. This result demonstrates the importance of 3-D structural models to obtain accurate source parameters of offshore subduction earthquakes.

## 7.6 3-D waveform propagation effects

















Station removed	Event I					Event II				
	Time shift (s)	Source location	Nodal plane 1	$M_w$	Focal mech.	Time shift (s)	Source location	Nodal plane 1	$M_w$	Focal mech.
<b>None</b>	10.9	33	356/9/84	6.8		23.7	16	312/45/-116	6.7	
<b>QF26</b>	13.8	39	303/19/29	6.8		23.7	16	317/39/-127	6.7	
<b>QC05</b>	10.9	33	351/3/86	6.8		23.7	16	320/43/-120	6.7	
<b>L003</b>	10.9	33	012/03/96	6.9		22.7	16	321/30/-127	6.8	
<b>QC04</b>	10.9	33	343/3/75	6.8		23.7	16	321/39/-120	6.7	
<b>L101</b>	10.9	33	323/3/47	6.9		23.7	16	316/40/-129	6.8	
<b>QC02</b>	10.9	33	325/3/86	6.8		23.7	16	320/39/-124	6.7	
<b>QF25</b>	10.9	33	334/3/61	6.8		22.7	16	320/32/-127	6.7	

Table 7.5: Source stability of the multiple point-source solution based on the results of removing one station at a time from the inversion (jackknifing). These jackknifing results are compared with the best-fitting solution obtained using all available stations. Source location refers to the grid position illustrated in Figure 7.9b. Stations are ordered in epicentral distance. These results show the remarkably consistent mechanisms for both sub-events, indicating independence from the exact set stations used in the inversion.



















	Event I					Event II				
	Source location	Time shift (s)	Nodal plane 1	$M_w$	Focal mech.	Source location	Time shift (s)	Nodal plane 1	$M_w$	Focal mech.
<b>Best-fitting solution</b>	33	10.9	356/9/084	6.8		16	23.7	312/45/-116	6.7	
<b>Fixed locations for Event I</b>	41	13.6	61/12/152	6.8		16	23.2	314/43/-133	6.7	
	34	11.8	48/16/134	6.8		16	23.2	312/43/-135	6.7	
	27	10.0	41/20/122	6.8		16	23.2	309/44/-137	6.7	
	26	8.8	9/13/092	6.8		16	23.2	310/43/-137	6.7	
	25	7.9	332/14/056	6.9		9	11.2	337/38/070	6.8	
	32	10.3	316/15/045	6.8		16	23.5	313/43/-133	6.7	
	39	12.7	306/14/038	6.8		16	23.2	314/42/-129	6.7	
	40	13.0	336/3/069	6.8		16	23.2	315/42/-133	6.7	

Table 7.6: Dependence of Event II solution on the position and mechanism of Event I.

## 7.7 Discussion and conclusions

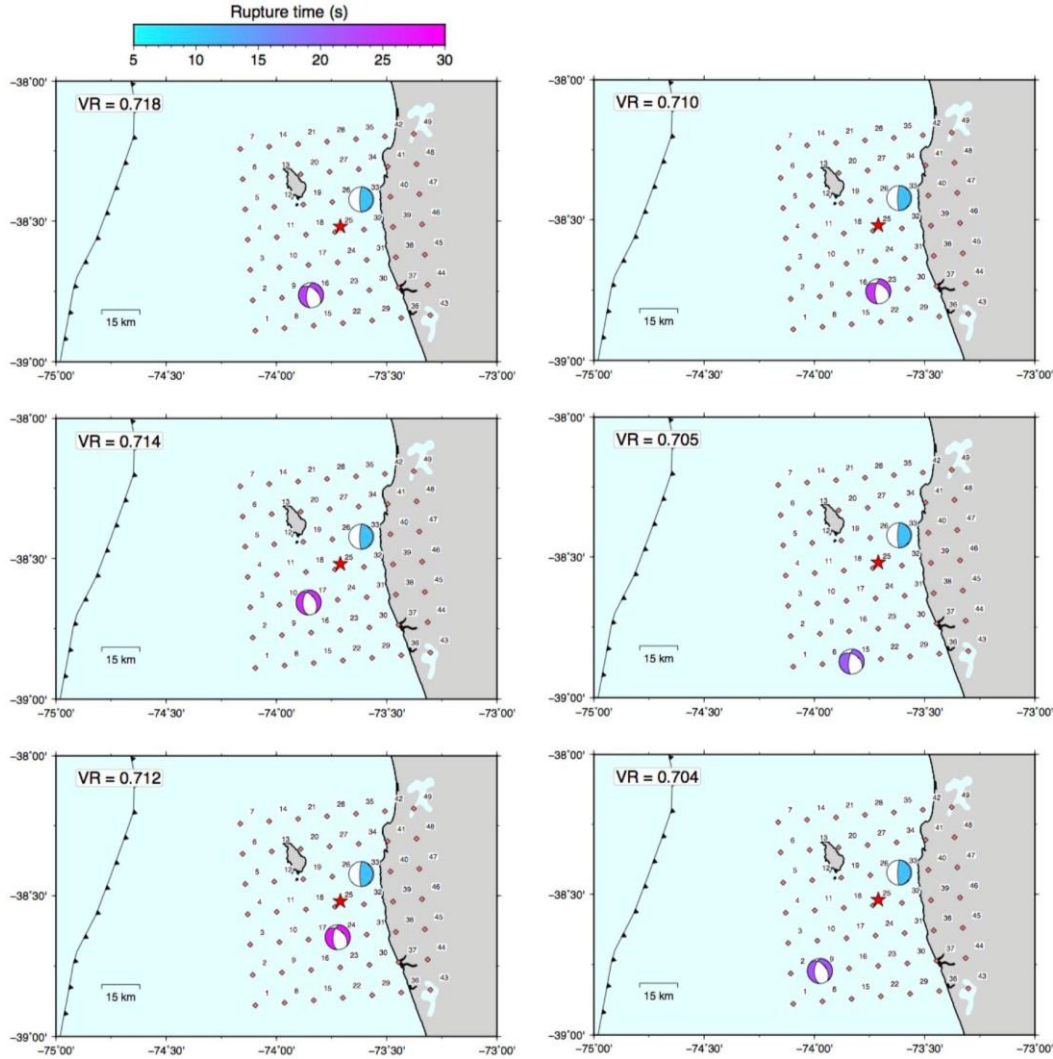


Figure 7.10: Best-fitting solutions (within the 98<sup>th</sup> percentile) for the two-point-source, high frequency solution using the moment-constrained NNLS. The colour of each beach ball indicates the centroid time of each source.

## 7.7 Discussion and conclusions

Based on our aftershock analyses and 3-D waveform simulations it is now clear that Event II ruptured on a normal fault near the base of the overriding crust (Figure 7.11, Figure 7.14). Group B aftershocks are located close to the prominent Mocha-Villarrica fault zone (Figure 7.11). This fault may be related to strong velocity contrasts in the marine forearc beneath Isla Mocha, where Group B aftershocks are located (Figure 7.14). Crustal faulting in the region is pervasive and may extend through the entire crust (see Enclosure 1); (Hicks and Nippres, 2012; Melnick et al., 2009); it is plausible that the geometry of fault networks becomes more complex at the base of the forearc



with possible conjugate faulting (Figure 7.14). Similar faults were found in the rupture area of the 2011 Tohoku earthquake (Tsuji et al., 2013), although in contrast to the Araucania earthquake, these were located closer to the region of greatest coseismic slip. We speculate that these faults are compressional during the interseismic period, but a stress inversion caused by the Maule earthquake (Hardebeck, 2012) may favour postseismic extension. On the basis of approximate fault areas from scaling relations (Blaser et al., 2010), the two fault planes of Events I and II likely do not intersect. There are several possible mechanisms for the triggering of a rupture by a preceding earthquake. Dynamically triggered rupture of the normal fault is likely the dominant failure mechanism given that Event II's centroid time coincides with the passage of high amplitude S-wave arrivals from Event I, as shown by a 3-D waveform simulation (Figure 7.15). However, we cannot completely rule out static stress transfer acting as a partial trigger.

To our knowledge, these results are the first documented case of plate interface thrusting instantaneously activating a large rupture in the overriding plate through dynamic triggering. Past subduction zone doublets have been identified by low %DC in their CMT solutions (Lay et al., 2010b). Conversely, in the case of the Araucania earthquake, the low frequency single point-source solutions of both the global and regional CMT solutions did not yield a low %DC. This discrepancy is also shown by our synthetic tests. It is possible that the short time delay and small distance between Events I and II masks rupture complexity in teleseismic CMT solutions.

Therefore, we investigated whether the double-source configuration of the Araucania earthquake could also be detected in regional waveforms. We compared the Araucania earthquake to other similar-sized aftershocks of the Maule sequence, the March 2012  $M_w$  7.1 Constitución and the March 2010  $M_w$  6.9 Pichilemu earthquakes. gCMT solutions and detailed studies (Ruiz et al., 2013; Ryder et al., 2012) of these earthquakes show that the former is a straightforward plate interface thrusting event, whereas the Pichilemu event occurred on a normal fault in the overriding plate. Therefore, we are able to directly compare a simple plate interface thrust and an upper plate event with a complex doublet involving both faulting styles.

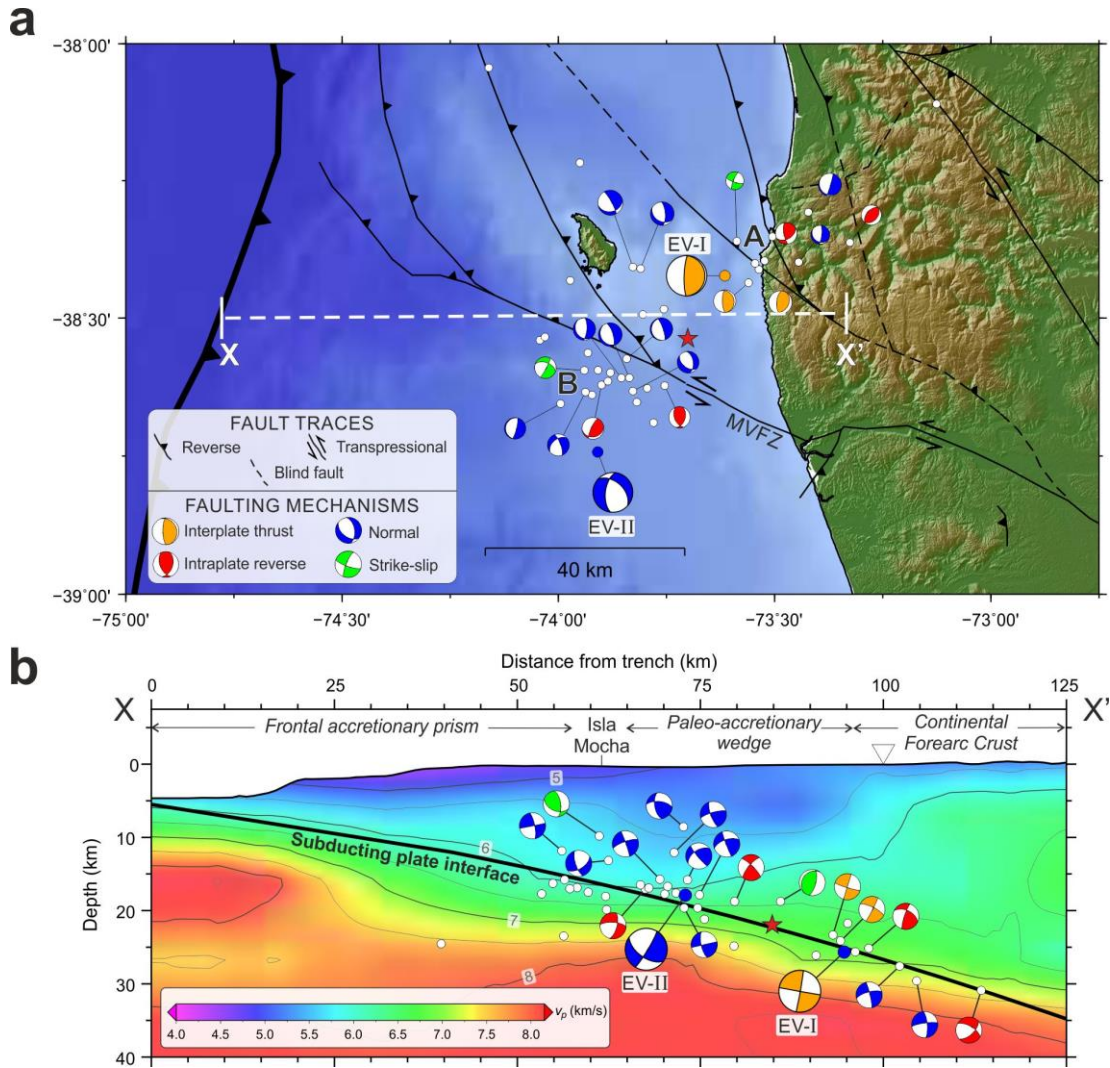


Figure 7.11: a) Map and b) cross-section showing locations and focal mechanisms of aftershocks (Groups A and B) and mainshock events (labelled EV-I and EV-II). Faulting style is classified on principal stress orientations (Frohlich, 1992) and minimum rotation angle with respect to plate interface thrust faulting (Hayes et al., 2013), accounting for plate interface geometry (black line; Chapter Five). We plot the revised location of Event II, based on 3-D waveform modelling. Mapped faults are shown (Melnick et al., 2009; Melnick and Echtler, 2006b); MVFZ = Mocha-Villarrica fault zone. The star denotes the hypocentre of the Araucania earthquake; the triangle shows the coastline.

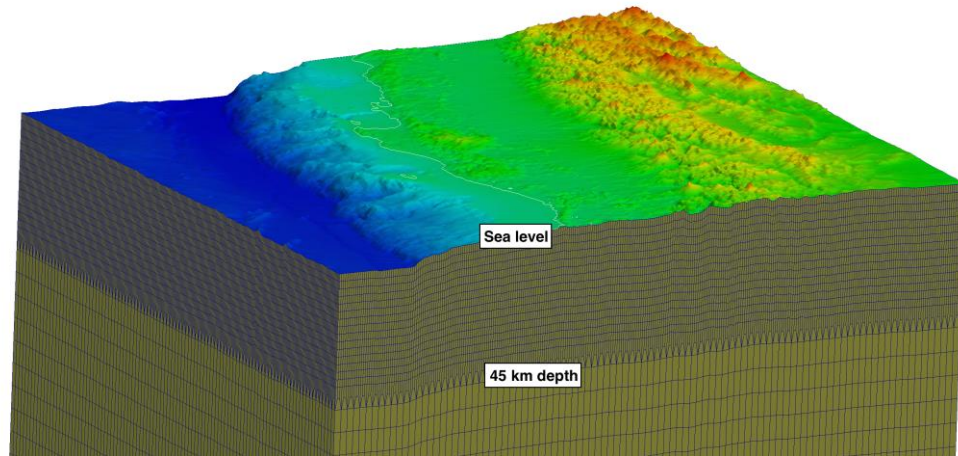


Figure 7.12: 3-D view of the hexahedral mesh used for the 3-D waveform simulations. This mesh honours surface relief and bathymetry, but does not contain dipping geological discontinuities at depth.

We focussed our attention on the closest permanent GSN station that was operating for both earthquakes, TRQA, in Argentina, which is located roughly equidistant ( $8\text{--}9^\circ$ ) from all three earthquakes. Comparison of normalised power spectra for these three events (Figure 7.16) reveals a greater proportion of high frequency energy from the Araucania and Pichilemu earthquakes, particularly in the frequency range  $0.1\text{--}0.2$  Hz. Therefore, we speculate that the partitioning of the Araucania rupture into the upper plate generates more high frequency energy compared to a single-source plate interface rupture. It is possible that higher frequency radiation is due to slip on more immature faults in the upper plate compared to the presumably more mature megathrust fault (Choy et al., 2006). These characteristics may aid with the detection of similar plate interface - upper plate doublets in the future, although frequency content may depend on several other source parameters, such as rupture duration.

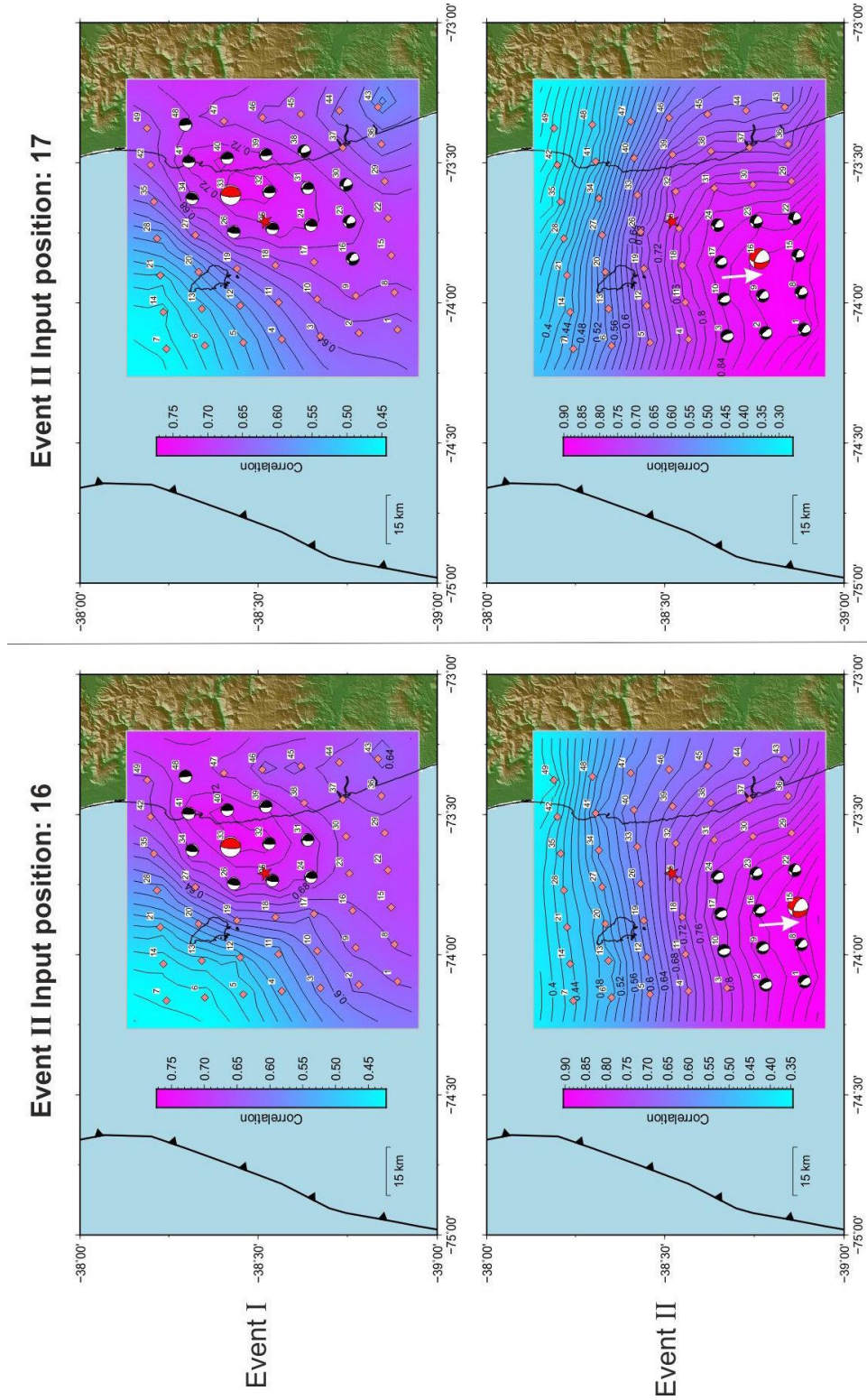


Figure 7.13: Recovery of 3-D synthetic waveforms using the inversion based on 1-D Green's functions. In each case, input sources are based on the result from our real data inversion. On the right, the source position of Event II is placed at source position 17. In each case, the 1-D inversion results in a systematic southward shift, as shown by the arrows.



## Chapter 7: Seismic Slip on an Upper Plate Normal Fault During a Large Subduction Megathrust Rupture

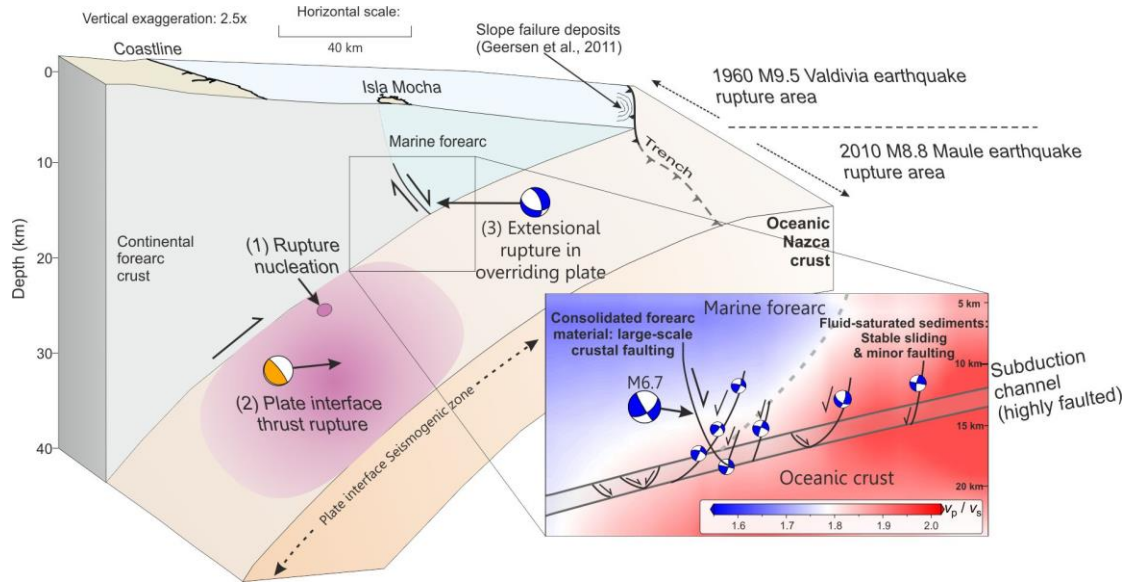


Figure 7.14: Schematic interpretation of the Araucania earthquake rupture. Plate interface thrusting (Event I) triggered a rupture along an extensional fault in the overriding plate (Event II). It is likely that two great earthquakes in 1960 and 2010 brought both faults closer to failure. As shown by ancient submarine landslide deposits in the area (Geersen et al., 2011b), a larger-scale rupture in the overriding plate has the potential to act as a tsunamigenic earthquake. Beach balls represent the focal mechanisms of both mainshock events. The inset shows the interpreted structure of conjugate normal faulting with the background colour representing  $v_p/v_s$  (Chapter Five).

CMT solutions provided by global reporting agencies are accepted by the seismological community and form the basis of slip inversions and examinations of the stress field. CMTs are, therefore, a pillar of earthquake science, yet our results recommend their careful use in the case of slip on multiple fault planes. The precedent set by this study also presents a new perspective for tsunami hazard assessment in subduction zones. Reverse faults as well as normal faults could theoretically be immediately triggered by megathrust slip, causing large seafloor displacement. A wide variety of upper plate faulting has been imaged in subduction zones. For example, steeply-dipping normal faults have been imaged in the upper plate along the northern Chile (von Huene and Ranero, 2003) and southern Peru margins (Audin et al., 2008). Furthermore, a large upper plate reverse faulting event preceded the 2014  $M_w$  8.2 Pisagua, northern Chile earthquake (González et al., 2015) and backthrust faults are widespread in the Sumatra subduction zone (Singh et al., 2010).

## 7.7 Discussion and conclusions

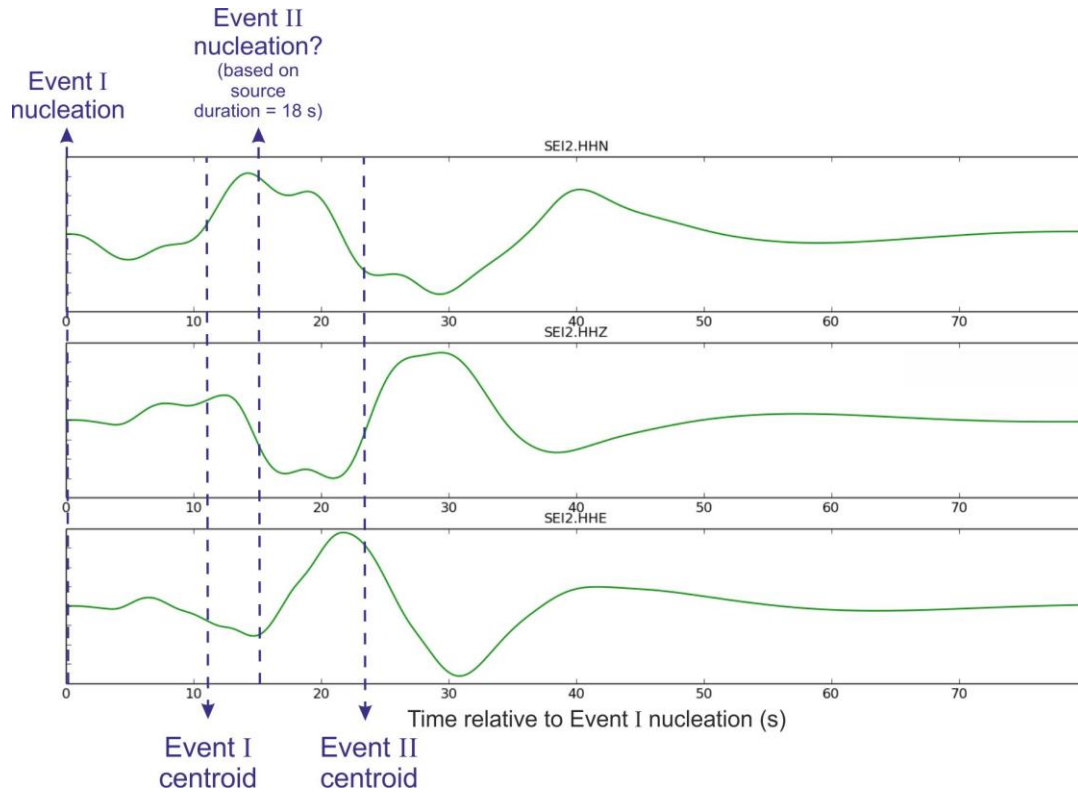


Figure 7.15: Three-component velocity traces of the simulated seismic wavefield of Event I ‘seen’ by Event II. The waveform is bandpass filtered at 0.02–0.15 Hz. The 3-D simulation is generated in the same way as described in Section 7.6; a receiver is placed at the centroid location of Event II. The known centroid times of Events I and II are shown. Although we cannot pinpoint the exact nucleation time of Event II, it is clear that the arrival of high amplitude S-waves from Event I is coincident with the possible nucleation stage of Event II, based on its source duration of 18 s.

Based on our knowledge of seismic velocity structure in the region of the Araucania earthquake (Chapters Four and Five) and scaling relationships of subduction zone earthquake fault dimensions (Blaser et al., 2010), we calculated the expected seafloor static displacement from a rupture in the upper plate. Assumptions were based on an approximation of dislocation faulting in a homogeneous half-space (Y. Okada, 1992). Low  $v_s$  ( $\sim 2.2$  km/s) in the marine forearc (Figure 7.14; Chapter Five) correspond to a lower rigidity, and hence a greater slip for a given fault area and seismic moment. Our calculations show that an  $M_w$  7.0 rupture in the upper plate could result in substantial vertical seafloor displacement of 1.2 m. If this scenario were scaled up to a larger rupture ( $M_w \sim 7.5$ ), slip on the forearc fault could cause a localised tsunami on the continental shelf, although the upper limit of rupture size is controlled by the geometry and frictional properties of these faults (Figure 7.11). A tsunami may

be caused by static vertical displacement or through submarine landslides (Figure 7.14) which have occurred locally in the past (Geersen et al., 2011b).

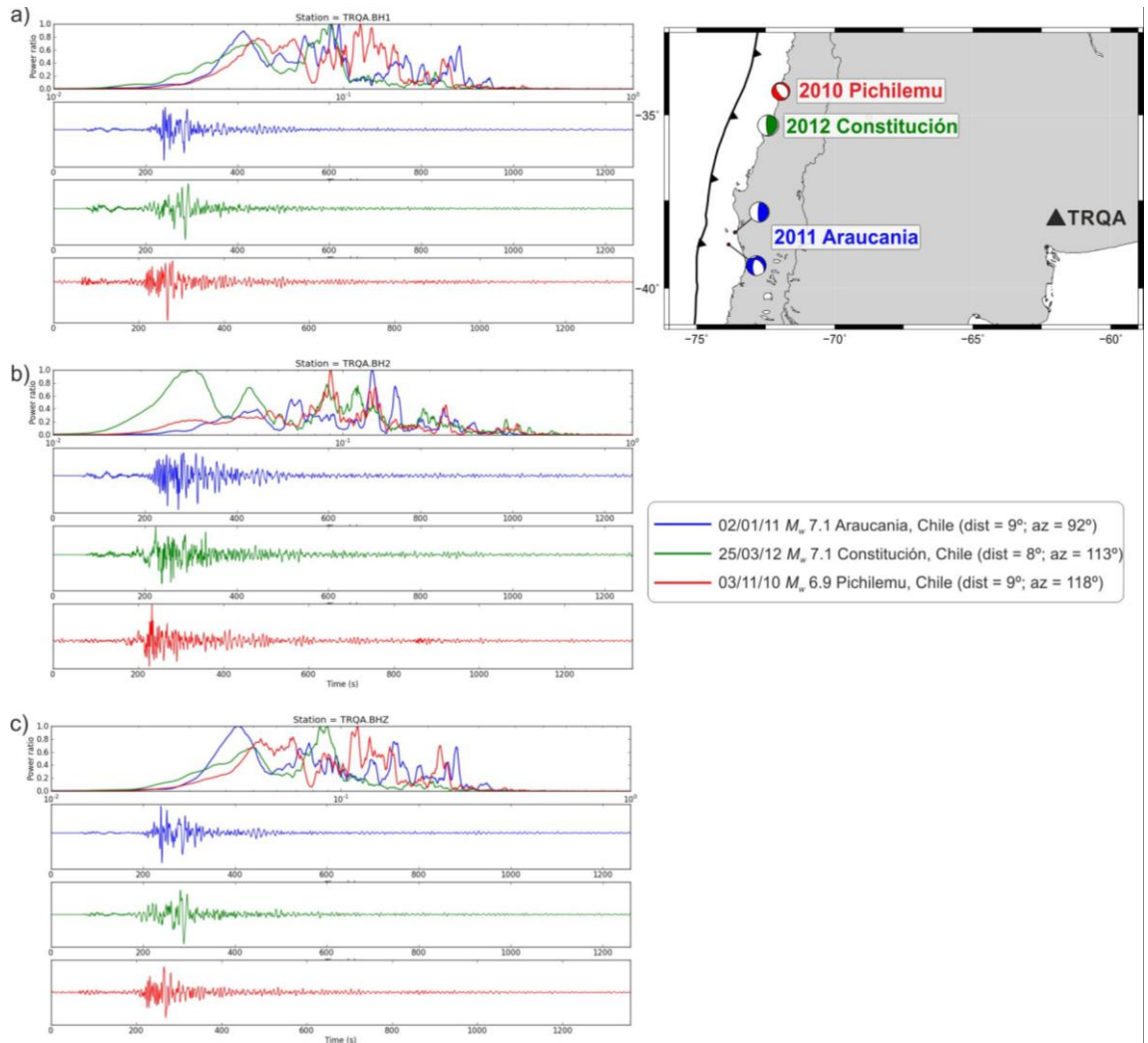


Figure 7.16: Regional recordings of the  $M_w$  7.1 2011 Araucania (plate interface thrusting and upper plate normal faulting), 2012  $M_w$  7.1 Constitución (plate interface thrusting only) and 2010  $M_w$  7.1 Pichilemu (upper plate normal faulting only) earthquakes at the permanent GSN station, TRQA in eastern Argentina. The left-hand panel shows the normalised frequency (top) spectra and traces for each component: a) west; b) east; c) vertical. The map in the right-hand panel shows the location of the three earthquakes, corresponding CMT solutions and the location of station TRQA.

Yet without local strong-motion instruments, GPS networks, or close inspection of regional waveforms, near-field triggered ruptures may be difficult to detect. We speculate that the lack of evidence for Event II in single-source CMT solutions may result in part from the short timing between the two sources. Therefore, we recommend that the ability of teleseismic CMT inversions to resolve different

## 7.7 Discussion and conclusions

doublet configurations is given a full assessment. Furthermore, there is a need to re-evaluate CMT solutions for large earthquakes using local and regional waveforms in subduction zones globally to examine whether CSDs involving the upper plate are ubiquitous



## Chapter 8

# SYNTHESIS: IMPLICATIONS FOR THE INTERPLAY BETWEEN MEGATHRUST PHYSICAL HETEROGENEITY AND SEISMIC SOURCE CHARACTERISTICS

A fundamental question in earthquake seismology is: are spatial distributions of subduction zone earthquakes along faults random, or do specific physical properties in the vicinity of the plate interface encourage or inhibit rupture? In the previous chapters, we identified several sources of compositional and structural heterogeneity in the rupture zone of the Maule earthquake. We now attempt to synthesise these key findings to advance our understanding of the physical factors that govern large earthquakes.

There have been many comprehensive studies published on other large megathrust ruptures, such as the 2011  $M_w$  9.0 Tohoku, Japan earthquake. Therefore, in this thesis, we have the unique opportunity to compare and contrast these earthquakes. For instance, although both earthquakes had similar magnitudes, they are characterised by different slip distributions. The Maule earthquake was a bilateral rupture with most slip occurring along the central part of the seismogenic zone (e.g. Moreno et al., 2012); in contrast, the Tohoku earthquake ruptured a single asperity close to the trench (Ozawa et al., 2011). Understanding the physics that underlies this variability has important implications for subduction zone earthquake hazard on a global scale.

## 8.1 Influence of localised upper plate heterogeneity on seismogenesis

We first consider the role of local heterogeneity in central Chile and its implications for future earthquake hazard along the South American subduction margin. We then turn our attention to the larger-scale pattern of physical properties in the entire seismogenic zone. We put our understanding of 3-D heterogeneity into direct practice by simulating its influence on seismic wave propagation, which can improve subsurface imaging and earthquake source characterisation.

## 8.1 Influence of localised upper plate heterogeneity on seismogenesis

### 8.1.1 Upper plate density anomalies

In Chapter Two, we described the wide range of causes of physical heterogeneity in subduction zones and their varying influence on seismic source processes. From a global assessment of subduction zones in Chapter Two, there is some debate as to whether heterogeneity in the upper or lower plates plays the more dominant role in megathrust seismogenesis. To resolve some of these issues for the South American subduction zone, we generated tomographic models of the central Chile megathrust in Chapters Four and Five. We compared these images with the seismic behaviour of the Maule earthquake rupture zone to reveal some of the structures that govern megathrust segmentation in the region. Our resulting 3-D seismic velocity models highlight two large high velocity bodies that lie beneath the coastline in the rupture area, and just above the plate interface (e.g. Figures 4.1 and 5.10). We confirmed the presence of these imaged structures by the identification of prominent regional gravity anomalies (Figure 5.11).

In our initial seismic velocity model, we interpreted the largest of these high seismic velocity anomalies as a subducted seamount (Chapter Four). We could not resolve whether or not the seamount was still attached to the downgoing plate. However, with the benefit of a more accurate 3-D seismic velocity model (Chapter Five), this structure was seismically faster ( $v_p$  up to 8 km/s) and geometrically larger (up to 40 km wide) than previously thought. Given the lack of evidence for present-day uplift in the overlying forearc (Jara-Muñoz et al., 2015), a seamount still attached to the downgoing plate cannot plausibly exist in the region.

With the lack support of for a subducted seamount, we turned our attention in Chapter Five to identifying the origin of the high seismic velocity structure that we now believe lies within the upper plate. High seismic velocities ( $v_p > 7.5$  km/s) and a positive gravity anomaly are consistent with a composition of peridotite mantle. The contemporary continental mantle lies further to the east (Figure 5.10), so we found it essential to unravel the past history of the forearc by assessing surface geology along the coastline. Based on outcropping mafic intrusives directly above the Cobquecura and Pichilemu velocity anomalies (Figure 5.1), we believe that these blocks of peridotite mantle were emplaced during a mantle upwelling event in the Triassic. There is evidence that similar seismically fast and dense blocks exist in the upper plate in other subduction zones. The Antofagasta region of northern Chile (Husen et al., 2000; Tassara, 2010) and the Kii peninsula in the Nankai subduction zone (Kodaira et al., 2006) provide the clearest examples. Beneath Antofagasta, a high  $v_p$  body of 7.0–7.3 km/s in the upper plate is interpreted as a residual magmatic intrusion (Husen et al., 2000). Beneath the Kii peninsula, high  $v_p$  (up to 6.25 km/s) is inferred to represent plutonic rocks (Kodaira et al., 2006). In contrast, the seismic velocity of the Cobquecura anomaly is much higher (7.6–8.0 km/s), indicating a composition of deeper-sourced mafic material and not intrusive rocks that were emplaced at shallower levels as in the case of the Antofagasta and Nankai structures.

Regardless of the Cobquecura anomaly's exact petrology, a large, dense block of ultramafic material lying above the plate interface dramatically influences dynamic behaviour of the megathrust. This relationship is clearly visible at different stages of the seismic cycle in the Maule segment (Figure 5.13). The proximity of the Maule earthquake's hypocentre to the up-dip edge of the Cobquecura anomaly suggests that rheological discontinuities may contribute to rupture initiation. A similar relationship has been inferred for other large events along the South American subduction zone. One example is the 1995 Antofagasta earthquake that appears to have nucleated at the edge of the forearc batholith (Tassara, 2010). Rheological discontinuities accumulate high shear stresses that are conducive to generating small earthquakes (e.g. Lapusta and Rice, 2003), one of which may have formed the nucleation stage of the Maule earthquake, eventually leading to the full rupture.

## 8.1 Influence of localised upper plate heterogeneity on seismogenesis

Based on the sharp gradient of slip at the coastline during the Maule earthquake (Y. N. Lin et al., 2013; Moreno et al., 2012), we infer that the Cobquecura and Pichilemu anomalies inhibited the down-dip and along-strike rupture extent (Figure 5.13b). However, the smoothing constraints applied in slip inversions cannot answer whether these anomalies acted as a partial or complete barrier. Nevertheless, one important piece of evidence comes from the remarkable pattern of high frequency radiation (Figure 5.13b); (Kiser and Ishii, 2011; Palo et al., 2014). High frequencies are radiated by fast changes in rupture speed or in slip (Meng et al., 2011) due to variations in frictional properties along the plate interface (Palo et al., 2014). We believe this depth dependence of short-period radiation during the Maule earthquake results from stopping phases (Madariaga, 1977) when the rupture front interacts with the base of forearc density anomalies. The decoupling of high frequency radiation from high slip patches and its depth dependence is a common feature of well-recorded large megathrust earthquakes (e.g. Lay, 2015). Although direct evidence for the physical properties that underlie this spatial distribution has so far remained sparse, our results provide strong evidence of physical structures affecting the localisation of high frequency radiation.

In contrast to the Maule rupture, the 1960  $M_w$  9.5 Valdivia, Chile earthquake to the south produced significant slip inland of the coastline (Barrientos and Ward, 1990; Moreno et al., 2009) and as far as the continental Moho – plate interface intersection. The forearc in the Valdivia segment is not characterised by high seismic velocity (Dzierma et al., 2012a; Haberland et al., 2009) and positive gravity anomalies (Álvarez et al., 2014). Furthermore, there is no evidence for mafic intrusives outcropping at the surface (Sernageomin, 2003). Therefore, we speculate that the lack of these dense ultramafic anomalies at the base of the upper plate in the Valdivia region contributed to the large area of the plate interface that was allowed to rupture during the 1960 earthquake.

Given that the plate interface beneath the Cobquecura anomaly experienced minimal coseismic slip during the Maule earthquake ( $< 6$  m), we need to consider the mechanical behaviour of the underlying megathrust fault. The highly-locked nature of this portion of the megathrust (Moreno and Rosenau, 2010) combined with the lack of aftershock activity (Lange et al., 2012; Palo et al., 2014; Rietbrock et al., 2012) and

afterslip (Bedford et al., 2013; Y. N. Lin et al., 2013), indicate that it is behaving aseismically, yet does not creep (Figure 5.13). In line with Tassara (2010), we believe that the high density of the Cobquecura anomaly exerts large normal stress, leading to a strong, highly-coupled plate interface at its base. Elastic energy is rapidly attenuated by portions of faults with high shear strength (Tassara, 2010). Therefore, the rupture front of the Maule earthquake did not have enough energy to fully overcome the portion of the fault with high shear strength at the base of the Cobquecura anomaly.

The highly locked, yet unruptured megathrust beneath the Cobquecura anomaly must remain in slip deficit since the Maule earthquake. Moreno et al. (2012) find that this part of the plate interface corresponds to a deficit of more than 5 m following the 2010 rupture. It is therefore vital to understand the stress conditions of strong mechanical heterogeneities for future seismic hazard in central Chile. We foresee two possible future rupture scenarios. First, the accumulated deficit beneath the Cobquecura anomaly may be released during a moderate–strong earthquake with an approximate magnitude of  $M_w$  7.5–8.0 (as suggested in Chapter Four). Such an earthquake may be similar to the 2007  $M_w$  7.7 Tocopilla event in northern Chile, which slipped along a deeper portion of the plate interface (30–55 km depth) in a region characterised by a high gravity anomaly (Loveless et al., 2010; Tassara, 2010). Alternatively, if the rupture front has enough energy to overcome high shear strength beneath the Cobquecura anomaly, then large slip could occur down to 45 km depth, as well as along the shallower and weaker portion of the megathrust that ruptured in 2010. In this case, a large area of slip could potentially result in an  $M_w$  9.0+ earthquake, but should occur less often compared with a rupture along the weaker portion of the central megathrust alone (Tassara, 2010).

The seismogenic behaviour of forearc density anomalies may therefore vary from one seismic cycle to another, as inferred for the Kii peninsula in the Nankai subduction zone (Kodaira et al., 2006). In order for significant slip to occur along the deeper region of the central Chile megathrust, either the plate interface would have to weaken due to an earlier slow slip event (Kodaira et al., 2006) or the initial rupture would need to be sufficiently large to dynamically weaken the fault (Kanamori and Brodsky, 2004; Scholz, 1998; Tassara, 2010). The time-dependent and bimodal seismogenic response, in which the behaviour of structures alternates between a barrier

## 8.1 Influence of localised upper plate heterogeneity on seismogenesis

and asperity in different seismic cycles, may manifest itself as an earthquake supercycle (e.g. Sieh et al., 2008).

### 8.1.2 Upper plate faulting

As shown above, density anomalies in the upper plate can significantly inhibit rupture of the megathrust plate interface. These structures also affect upper plate seismic activity. At the northern limit of the Maule rupture area, there is a pronounced zone of aftershocks associated with two large normal faulting events ( $M_w$  6.9 and 6.7) in the Pichilemu area. Our tomographic images reveal that a block of relic mantle lies in the upper plate, which acts as a strong rheological discontinuity and is conducive to active faulting at its periphery (Figure 5.16). The Pichilemu anomaly may have acted as an along-strike rupture barrier to the Maule earthquake by partitioning plate interface strain along upper plate faults. Seismic slip along these faults was subsequently triggered due to static stress changes (Ryder et al., 2012). This finding agrees with Aron et al (2013), who suggest that forearc normal faults may be silent during the interseismic period and become active after a large megathrust earthquake. In contrast to the Pichilemu anomaly, upper plate activity did not occur at the edge of the Cobquecura anomaly (Figure 5.16). We speculate that this difference may be due to variations in elastic energy of the rupture as it encountered these two structures.

Extensional faulting after large slip on the megathrust is not unique to Maule. Intense upper plate normal faulting also occurred in the aftermath of the 2011 Tohoku, Japan megathrust earthquake (e.g. Kato et al., 2011); this sequence has several similarities and some differences with the Pichilemu aftershocks. In both cases, the largest upper plate events involved multiple ruptures, with a 15 min gap for the Pichilemu main aftershocks. Furthermore, faulting occurred where active faults were previously assumed to be sparse. In addition, upper plate faulting occurred close to the coseismic rupture limit of the preceding megathrust earthquake and was induced by associated static stress changes (Ryder et al., 2012; Toda and Tsutsumi, 2013). High  $v_p$  anomalies also exist in the vicinity of the upper plate aftershocks in Japan (Kato et al., 2013). However, one important difference exists between these two cases. The Pichilemu normal faults likely extend to the megathrust plate interface at around 30 km depth (Fariás et al., 2011; Ryder et al., 2012); (Figure 5.16), whereas the maximum

depth of upper plate activity in Japan (10 km) is much shallower than the plate interface at around 50 km depth (Toda and Tsutsumi, 2013).

In Chapter Seven, we also demonstrated how forearc faults at the southernmost end of the rupture area influence seismogenesis. We studied the detailed source characteristics of the strongest interplate aftershock of the Maule sequence: the 2011  $M_w$  7.1 Araucania earthquake. Our results show this earthquake was composed of two closely-spaced sub-events: a large plate interface rupture followed by extensional faulting in the upper plate (Figure 7.14). We believe the normal fault rupture was dynamically triggered by S-waves emanating from the first sub-event. Therefore, the Araucania earthquake is the first documented case of dynamic triggering (Figure 7.15) immediately reactivating an upper plate fault due to seismic slip on the plate interface. The characteristics of the Araucania earthquake are rather different to the Pichilemu sequence. Firstly, the Pichilemu sequence occurred in the central part of the forearc beneath the coastline, whereas normal faulting in the Araucania area is located in the lower marine forearc. Furthermore, upper plate faults in the Arauco peninsula region had previously been mapped at the surface (Melnick et al., 2009; Melnick and Echtler, 2006b).

As discussed in Chapter Two, the marine forearc in subduction zones has been shown to host a wide range of faulting structures. For the Araucania earthquake, there is an important question to answer regarding the history of the normal fault. Did the upper plate fault that ruptured exist as a normal fault in the long-term or was it a previously-mapped compressional fault (Melnick et al., 2009); (Figure 7.11a) that became inverted as an extensional structure? Stress inversions have been shown to occur after large megathrust earthquakes (Hardebeck, 2012; Hasegawa et al., 2012). Furthermore, upper plate faults throughout the Chile subduction zone have acted as normal and reverse faults during their long-term history (Allmendinger and González, 2010; Aron et al., 2013; Melnick et al., 2006). The Araucania earthquake is situated in a unique position between the rupture areas of two of the largest megathrust earthquakes ever recorded (Figure 7.1) and weak plate interface coupling of less than 55% (Moreno et al., 2011). Therefore, to understand seismic hazards associated with subduction zone upper plate faulting, important questions to ask are, including: 1) Is upper plate fault reactivation more limited to megathrust segment barriers? 2) Is upper

## 8.1 Influence of localised upper plate heterogeneity on seismogenesis

plate faulting limited to large magnitude earthquakes, or do smaller events also occur? To answer these questions, we have calculated detailed single point-source moment tensor solutions for 55 moderately sized aftershocks ( $M_w$  3.5–5.8) of the Maule earthquake. In addition to our own analysis, we used published moment tensor catalogues of Agurto et al. (2012) and Hayes et al. (2013), as well as those from the GCMT project (Ekström et al., 2012).

These faulting mechanism solutions are shown in Figure 8.1. From our moment tensor solutions, it appears that there are many normal faulting events at the southern end of the rupture and offshore of Concepción, close to Santa Maria Island. Both of these areas are where there was reduced coseismic slip. However, the larger catalogue of Agurto et al. (2012) suggests that several extensional earthquakes also occurred in the region of greatest slip. Moreover, aside from the large group of normal faulting events in the Pichilemu area, Hayes et al. (2013) show normal faulting earthquakes throughout the rupture area. If we remove the interplate thrust faulting events and combine these catalogues, it is clear that extensional events are widespread (Figure 8.2). From the cross-sections, most extensional earthquakes are located in the upper plate (Figure 8.2). Therefore, it is clear that upper plate normal faults are not only limited to regions with lower coupling and do not appear to solely act as rupture barriers as for southern Peru (Audin et al., 2008) and northern Chile (von Huene and Ranero, 2003; Victor et al., 2011). Normal faulting earthquakes located in the shallow marine forearc above the region of high coseismic slip may be analogous to the large extensional structure imaged in the rupture area of the 2011 Tohoku earthquake (Tsuji et al., 2013). Furthermore, when we filter out plate interface thrust events, it becomes apparent that upper plate reverse faults were also activated, particularly in the Arauco peninsula area. These mechanisms imply a complex pattern of conjugate reverse and normal faults in the upper plate (Figure 8.2).



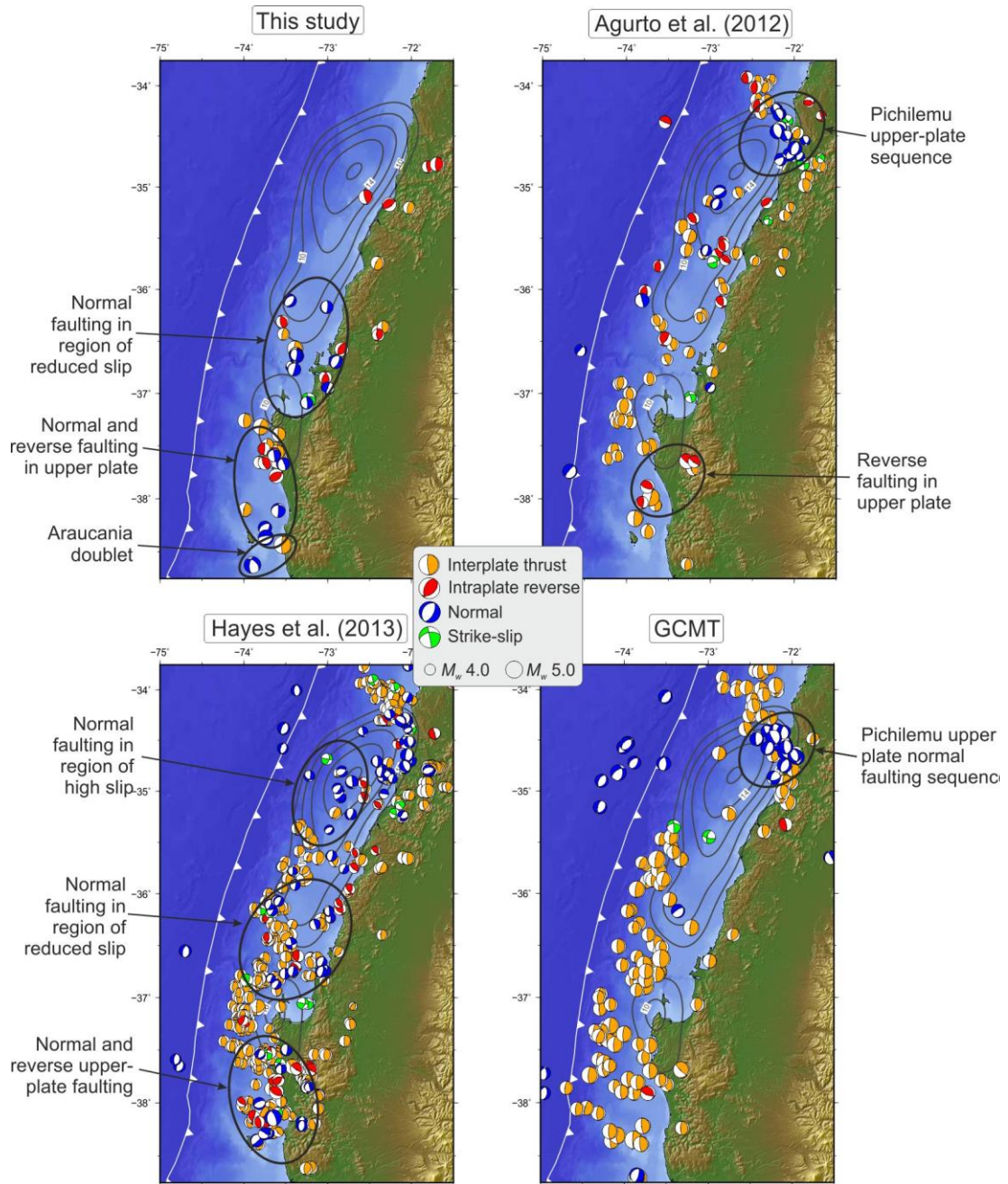


Figure 8.1: Comparison of our preliminary aftershock moment tensor catalogue (top left) with those already published for the period ending December 2010 (Agurto et al., 2012; Hayes et al., 2013). Solutions from the global CMT project (Ekström et al., 2012) are also shown (bottom right). Faulting mechanisms are classified based on the plunge angle of principal stresses (Frohlich, 1992). Reverse faulting style is chosen from the minimum rotation angle with respect to a reference solution representing pure plate interface thrusting based on slab geometry (Chapter Five).

Overall, from passive subsurface imaging of a subduction zone, a detailed study of rupture complexity associated with a large interplate earthquake, and mechanisms of smaller aftershocks, we have shown that seismic source processes in

## 8.2 Physical properties of the seismogenic zone: reconciling global observations

central Chile are strongly influenced by upper plate geological structures. So far, we have only considered localised heterogeneity and its effect on along-strike variations in plate interface velocity. It is worth bringing our understanding of how overall plate interface velocity structure relates to seismic character of the megathrust in a more global context, and how we can begin to interpret such structures.

### 8.2 Physical properties of the seismogenic zone: reconciling global observations

In the previous section, we considered the effect of local structural heterogeneity in the upper plate on subduction zone seismogenic character. Now we consider broader scale velocity structure of the plate interface itself, which we presented for the Maule region in Chapter Five. Although geophysicists have been able to map the depth variation in energy release and seismic slip along the megathrust (Lay et al., 2012), knowledge is lacking on the physical properties controlling this segmentation. Using our detailed velocity model of the plate interface in the central Chile subduction zone, we have been able to constrain the physical factors that govern the depth segmentation of a megathrust rupture. In summary, we found that the region of high coseismic slip is limited to a portion of the plate interface with high  $v_p$  gradient, rising from 6.2–7.0 km/s from 18–26 km depth, and moderately elevated  $v_p/v_s$  of  $\sim 1.83$ . Based on our results, we may be able to constrain rupture potential using seismic velocities. However, to verify this relationship, we need to compare our findings for the Maule earthquake with other well-recorded megathrust ruptures. For this purpose, we study the north-east Japan subduction zone in the region of the 2011 Tohoku earthquake, which is illuminated by the high-resolution 3-D velocity model of Yamamoto et al. (2014).

There are similarities and differences between the plate interface velocity profiles through the region of greatest slip for the Maule and Tohoku earthquakes (Figure 8.3). The  $v_p$  gradient of the Tohoku plate interface is remarkably similar to that of Maule in the depth range 15–35 km. Understanding the mechanism of this velocity gradient is important because it appears to be correlated with the depth of maximum slip in both cases (Figure 8.3), which may help to explain why the largest megathrust ruptures tend to slip in Domain B of the plate interface (Lay et al., 2012).

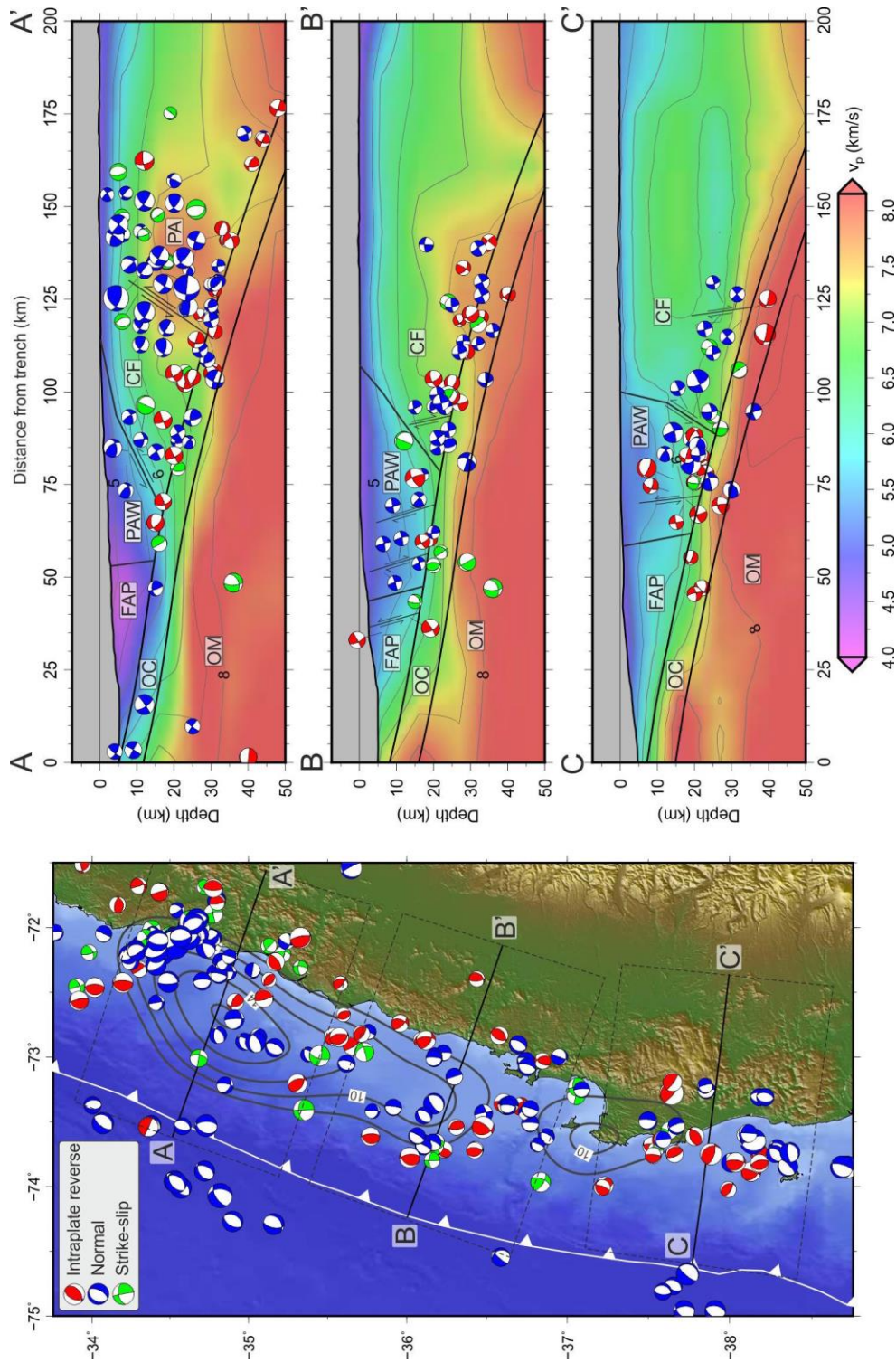


Figure 8.2: Map and cross-sections of intraplate aftershock mechanisms combined from the different catalogues shown in Figure 8.1. Interpretations of possible upper plate fault geometries are illustrated in the cross-sections. FAP = frontal accretionary prism; PAW = palaeo-accretionary wedge; CF = crustal framework; OC = oceanic crust; OM = oceanic mantle.



## 8.2 Physical properties of the seismogenic zone: reconciling global observations

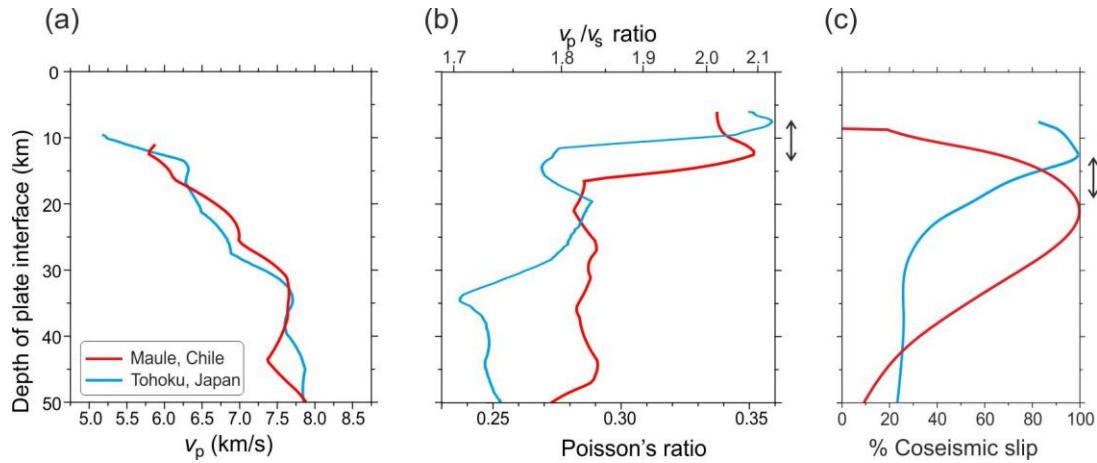


Figure 8.3: Comparison of the relationship between plate interface structure (left:  $v_p$ , centre:  $v_p/v_s$  and megathrust slip for the Maule, Chile and Tohoku, Japan earthquakes. The Maule profiles are drawn in a similar way to Figure 5.12, using the coseismic slip model of Moreno et al. (2012). Seismic velocities for the Tohoku megathrust come from Yamamoto et al. (2014) and coseismic slip is from Gusman et al. (2012). The arrows indicate the depth offset in maximum  $v_p/v_s$  and coseismic slip between both rupture zones.

Given the differences in broad-scale characteristics between the central Chile and north-east Japan subduction margins, we find this similarity in plate interface velocity structure surprising. For instance, the age of the Pacific plate at the Tohoku trench is 130 Ma, whereas the Nazca plate offshore of central Chile is 100 Ma younger (e.g. Müller et al., 2008). Given the age differences, and hence, thermal distinctions of the crust in these two examples, we suggest that the steep  $v_p$  gradient is not thermally controlled. An alternative explanation is increasing confining pressure, which may result in metamorphic phase changes of oceanic crust materials such as basalt and gabbro. However, the oceanic crust is not expected to undergo major metamorphic phase changes until the eclogite transition at around 45 km depth (e.g. Bostock, 2013; Hacker and Abers, 2004). Another mechanism may arise from pore pressure changes in oceanic crust. Previous studies (e.g. Audet et al., 2009; Kato et al., 2010a) infer high fluid pressures within subducting oceanic crust. More evidence of this interpretation is shown by elevated  $v_p/v_s$  of  $\sim 1.83$  at 12–15 km depth (Figure 8.3);  $v_p/v_s$  remains relatively constant, indicating pore pressure is high and close to confining pressure, based on Christensen (1984) and modelling of seismic refraction data by Spudich and Orcutt (1980).

As well as some similarities, the velocity profiles from these two megathrust earthquakes show a remarkable difference. At 18 km depth,  $v_p/v_s$  of the Maule plate interface suddenly decreases from  $\sim 2.1$  to  $\sim 1.83$ . A similar decrease occurs in the Tohoku rupture zone, although at a shallower depth of 10 km (Figure 8.3). We can correlate this discrepancy as to the vastly differing rupture styles for these two earthquakes. Most coseismic slip models for the Maule earthquake show that the rupture did not extend to the trench; most slip stopped at around the same depth of this sharp change in  $v_p/v_s$ . The up-dip limit of rupture is also verified by the lack of plate interface aftershock seismicity at these depths (Figure 5.12). In contrast, significant slip of  $> 30$  m extended to much shallower depths (8–14 km) during the Tohoku earthquake (Lay et al., 2011; Ozawa et al., 2011; Simons et al., 2011).

The above findings indicate a direct relationship between physical properties (as expressed by seismic velocity structure) with seismogenic potential of the subduction megathrust. The sudden decrease in  $v_p/v_s$  is directly related to the amount of fluid saturated sediments at the base of marine forearc and along the subduction channel. These differences likely result from the sedimentation style of each margin. The central Chile subduction zone is an accretionary margin with a thick trench fill of 2.0–2.2 km (Grevemeyer et al., 2003) and a well-defined subduction channel that is up to 1 km thick (Contreras Reyes et al., 2008; Grevemeyer et al., 2003). In contrast, the north-east Japan subduction margin is erosive, with  $\sim 350$  m of sediment at the trench (Kodaira et al., 2012; Nakamura et al., 2013). This difference suggests that a wider volume of overpressured and velocity-strengthening sediment overlies the Maule megathrust. Furthermore, the competent rock framework and backstop of Maule region is at a greater distance from the trench. Therefore, we infer that the physical properties of the Tohoku margin allow shallower brittle failure along the plate interface, increasing its tsunamigenic potential. For the central Chile subduction zone, seafloor geodetic observations (Bürgmann and Chadwell, 2014) are required to confirm the frictional characteristics of the shallowest part of the megathrust.

## 8.3 Future outlook: Application of structural heterogeneity to 3-D seismic wave propagation simulations

As discussed in Section 6.5, the use of waveform simulations in highly heterogeneous media can improve our imaging of both earthquake source mechanisms and subsurface structure. In Chapter Seven, we have already shown the value of these numerical simulations by demonstrating how structural heterogeneity can bias source parameters in multiple point-source moment tensor inversions. The central Chile subduction zone represents an excellent test bed for subduction zone 3-D full-waveform inversion due to the following reasons:

1. There is an excellent coverage of broadband seismic instruments provided by the International Maule Aftershock Deployment.
2. A large database of recorded seismic waveforms from numerous moderate-sized aftershocks exists.
3. A detailed structural model of the subsurface is available from the local earthquake tomography studies documented in this thesis.
4. Reliable moment tensor solutions are available for many aftershocks (Section 8.1.2).

In the context of the work carried out in this project, calculating the sensitivity kernel associated with adjoint sources can help highlight the strengths and possible weaknesses of our 3-D velocity model and moment tensor solutions.

To make a preliminary assessment of the potential for a detailed full-waveform study in central Chile, we generated 3-D waveform simulations for aftershocks of the Maule sequence. Due to extended source effects, we carried out simulations for small to moderate sized events ( $M_w < 5.5$ ) of our moment tensor catalogue (Figure 8.1, top left) to avoid extended source effects. Here, we present results from the simulation of one of these aftershocks; its source parameters are shown in Table 8.1 and its location is shown in Figure 8.4.

Origin time (UTC)	Latitude	Longitude	Centroid depth	$M_w$	Moment tensor						Exponent (dyne.cm)
					$M_{rr}$	$M_{tt}$	$M_{pp}$	$M_{rt}$	$M_{rt}$	$M_{pp}$	
30/03/2010 08:12:56.96	36.95°S	73.00°W	18 km	4.0	-0.17	0.43	-0.27	0.30	1.18	0.26	22

Table 8.1: Source parameters of the test event used for the 3-D waveform simulation described in this section.

The 3-D simulation is calculated on a mesh created using the GEOCUBIT software, as outlined in Section 6.5.2. The mesh is similar to that designed for the Araucania earthquake (Section 7.6); instead, we use a larger volume to incorporate the 500 km long rupture area of the Maule earthquake. Furthermore, we use a finer minimum element spacing of 2000 m (Figure 8.5), allowing stable wave propagation simulations to be carried out up to relatively high frequencies of 0.5 Hz.

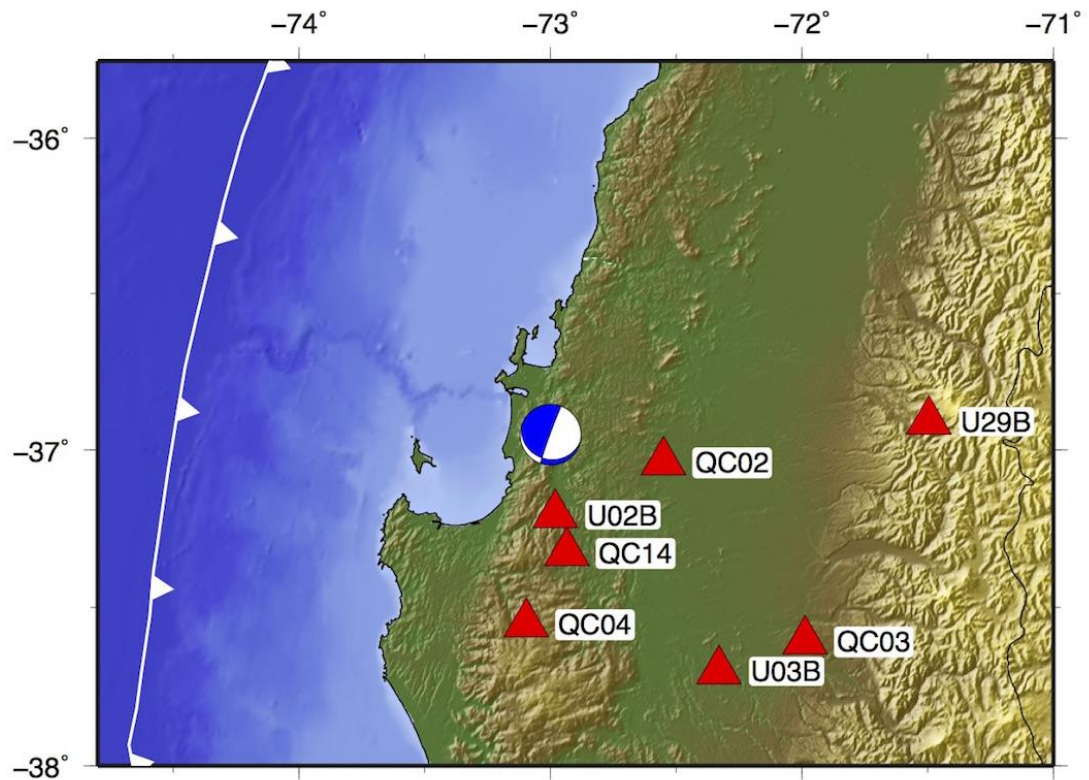


Figure 8.4: Location and faulting mechanism of the event described in Table 8.1 that has been used to simulate seismic wave propagation the central Chile subduction zone. Red triangles denote stations with high-quality broadband recordings of this event (Figure 8.6).

### 8.3 Future outlook: Application of structural heterogeneity to 3-D seismic wave propagation simulations

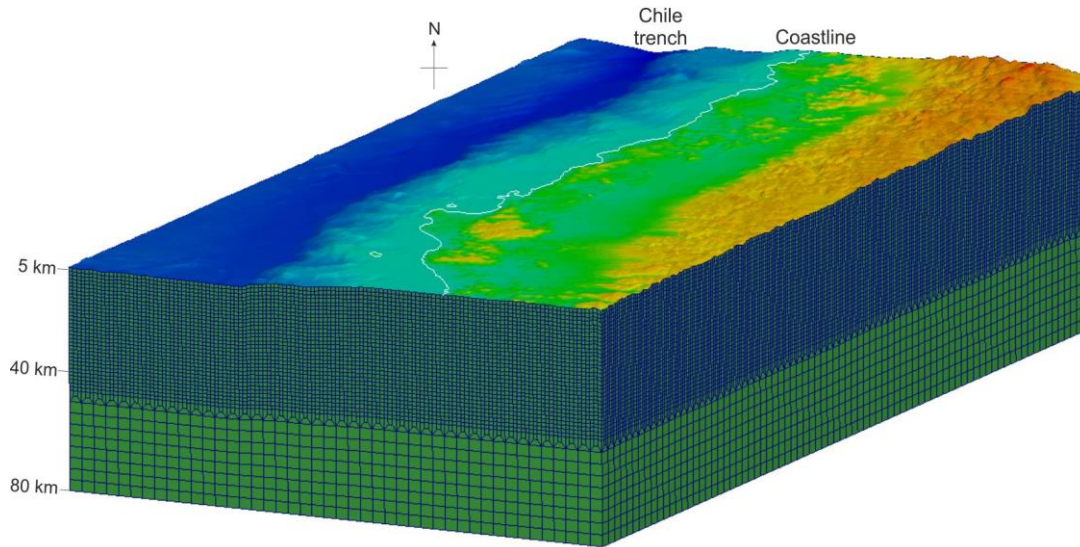


Figure 8.5: 3-D image of the mesh (as viewed from the south) that is used to generate the high frequency 3-D waveform simulations inside the entire rupture zone of the Maule earthquake.

We then compare synthetic traces to the corresponding observed waveforms that have high signal-to-noise ratio ( $> 3$ ); (Figure 8.6). We find excellent fits at many stations up to high frequencies ( $\sim 0.45$  Hz), highlighting the reliability of our 3-D velocity model and moment tensor solution of this earthquake. However, for many traces, there is a phase shift between the S-wave of the predicted and observed waveforms, where the observed S-waves arrive earlier compared to the synthetics. This finding indicates that lower S-wave velocities may be present in the subsurface, which are not described by the original velocity model.

To investigate this discrepancy, we use the adjoint method (e.g. Tromp et al., 2005) to calculate the volumetric sensitivity for specific seismic parameters using finite-frequency kernels. These kernels are a function of the interaction between the earthquake and adjoint wavefields; the latter is generated by considering time-reversed signals at the stations as sources (e.g. Liu and Tromp, 2006; Magnoni et al., 2014). We calculate adjoint traces by using a simple waveform misfit (Tromp et al., 2005), which is the squared difference between the observed and synthetic data (e.g. Krischer et al., 2015), for a window starting at the P-wave onset (Figure 8.6) and ending 25 seconds after the theoretical S-wave arrival time.



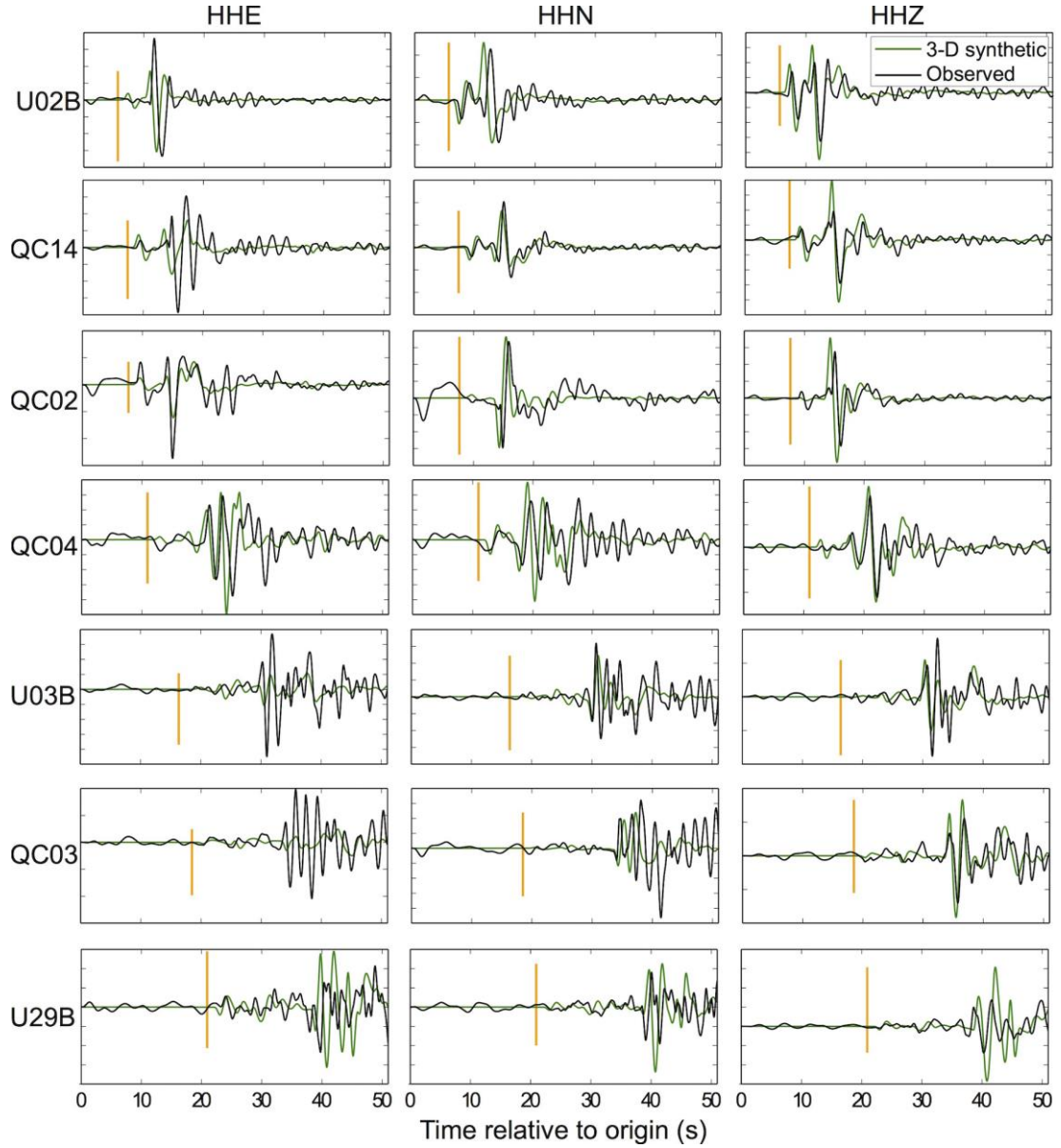


Figure 8.6: Representative velocity waveform fits comparing 3-D synthetics with observed waveforms for the simulated test event. Waveforms are bandpass filtered at 0.05–0.45 Hz. Locations of these stations are shown in Figure 8.4. Orange lines indicate P-wave onset times.

The averaged finite-frequency kernel of shear modulus sensitivity is shown in Figure 8.7. Before describing and interpreting features of the kernel, it is important to state that the volumetric sensitivity shown in Figure 8.7 is not smoothed, so high frequency fluctuations due to numerical noise are present. Nevertheless, one of the main features in the selected frequency band (0.05–0.45 Hz) is high sensitivity close to both the receivers and the earthquake source in the continental forearc. This source-receiver sensitivity pattern is common to finite-frequency kernels (Magnoni et al.,

### 8.3 Future outlook: Application of structural heterogeneity to 3-D seismic wave propagation simulations

2014). High sensitivity to subsurface structure at shallow depths (within the upper 5 km) is likely a consequence of the lack of resolution in our tomographic inversion, due to the lack of shallow seismic sources. Low residual sensitivity in the central continental forearc results from the high resolution in our tomographic inversion (Chapter Five). The other main feature of the kernel is high residual sensitivity within the upper portion of the marine forearc. We speculate that this pattern may be due to limitations in our seismic velocity model due to smearing caused by most sources lying along the plate interface. This high sensitivity may manifest itself as the phase offset between observed and synthetic arrivals in Figure 8.6. Overall, these preliminary results show that the use of full 3-D waveform inversion using multiple aftershocks could help to refine images of subduction zone structure and plate interface properties at an unprecedented scale of imaging.

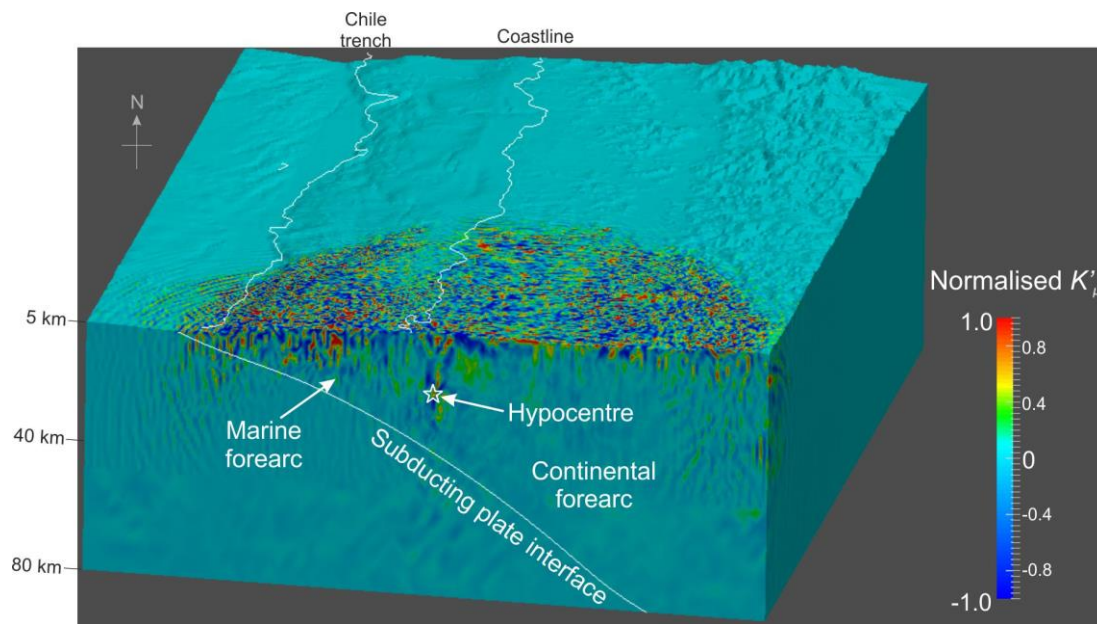


Figure 8.7: Unfiltered isotropic sensitivity kernel of shear modulus (normalised), as viewed from the south, with a vertical slice through the hypocentral region of the studied event. Elevation exaggeration = 2:1.

## Chapter 9

# CONCLUSIONS AND FUTURE WORK

This study set out to understand the physical factors that govern some of the largest earthquake ruptures in the world. To investigate this topic, we focussed on imaging physical properties and complex rupture processes in the area of the 2010  $M_w$  8.8 Maule earthquake in Chile. Here, we respond to the key project aims and research questions posed in Chapter One. We then explain some of the key contributions for the advancement of subduction zone earthquake science, and to assist policymakers in assessing future earthquake hazard. Finally, suggestions are given for future scientific progress in the field.

### 9.1 Response to project aims

The first half of this thesis concerned itself with using local earthquake tomography to determine structural and compositional heterogeneity along and around the subducting plate interface. The results from this part of the project assist the inference of physical properties that influence seismogenic character.

An on-going debate among earthquake scientists is whether physical properties of the upper plate or subducting plate are more dominant in influencing megathrust seismogenic processes. As demonstrated in Chapters Four and Five, one of the main findings of our study was centred on this debate. The Cobquecura anomaly is a large high velocity structure ( $v_p > 7.5$  km/s) beneath the coastline in the centre of the rupture. Although the Cobquecura anomaly appears as a clear seismic velocity anomaly in both

## 9.1 Response to project aims

models, we have shown that automatically determined arrival time datasets may lead to blurred tomographic images, and hence the possible misinterpretation of anomalous structures. In our preliminary tomography study (Chapter Four), we interpreted this feature as a subducted seamount, thereby attributing it to the downgoing plate. Nonetheless, we advocated that, if it was a seamount, it is unlikely to remain attached to the oceanic plate. In Chapter Five, with the benefit of a higher quality seismic dataset, including offshore observations, and additional constraints on surface geology, we interpreted the origin of this structure as an ancient mantle upwelling emplaced at the base of the forearc.

Based on the Maule earthquake, it appears that high velocity structures in the forearc influence the seismic character of the megathrust. In particular, the peripheries of forearc anomalies are conducive to the nucleation of megathrust earthquakes, yet can inhibit overall rupture extent. This barrier mechanism resulted in a distinctive distribution of high frequency radiation during the Maule rupture. To our knowledge, this finding is one of the first documented examples of a physical structure driving depth-dependent high frequency radiation, which is a somewhat ubiquitous feature of large megathrust earthquakes (e.g. Lay, 2015). It is possible that this effect arises from the increase in normal stress exerted on the plate interface by such structures, as suggested by Tassara (2010). However, we cannot rule out other influencing factors such as changes in frictional behaviour, porosity and permeability that may also accompany high velocity structures. Our work therefore demonstrates that high velocity structures of ancient origin in the forearc may influence some present-day subduction earthquakes. Thus, with detailed knowledge of forearc structure and the location of high velocity anomalies, we may be able to assess the seismic character of future large megathrust ruptures.

This conclusion has important implications for earthquake hazard assessment. Specifically, rupture extent is one of the controls on the maximum magnitude of earthquakes, and high frequency seismic radiation can cause strong shaking intensity at the surface. Similar to the Cobquecura anomaly, we infer a mantle-derived origin of the Pichilemu anomaly, which also generates a gap in plate interface aftershock seismicity. This structure may have been a factor causing the abrupt termination of the Maule rupture at its northern end, promoting conditions for strong ( $M_w \sim 6.9$ ) upper

plate normal faulting aftershocks (Ryder et al., 2012). Since large aftershocks in the upper plate can produce high shaking intensities, this finding adds further credibility to our conclusion that locating upper plate density anomalies may help to constrain subduction zone seismic hazard.

It is possible, though, that the relationship between physical properties and seismogenic character may not remain fixed over time. To illustrate this point, the preseismically locked Cobquecura anomaly did not significantly rupture during the Maule earthquake and underwent minimal postseismic deformation. This interpretation begs an important question as to the rupture potential of high velocity anomalies in the forearc: do these structures act as asperities or barriers? As discussed in the preceding chapter, it is entirely possible that the behaviour of physical structures may change from one seismic cycle to another. For example, during the Maule earthquake, the Cobquecura anomaly acted as a barrier, yet it may behave as an asperity in a future rupture. Consequently, there remains potential for an  $M_w$  7.5+ earthquake beneath the coastal ranges of central Chile. However, the precise seismic behaviour depends critically on the amount of strain accumulated by, and stress transferred to, the Cobquecura anomaly.

Aside from the more localised effects of forearc high velocity anomalies, low seismic velocities ( $v_p < 6.25$  km/s;  $v_p/v_s > 1.85$ ) correlate with minimal slip at the up-dip end of the plate interface during the Maule rupture. Therefore, we conclude that a wide down-dip extent ( $\sim 80$  km) of fluid-saturated sediments at the base of the upper plate may inhibit large slip at the trench. These sediments presumably display velocity-strengthening frictional behaviour. Seismic velocities in the north-east Japan subduction zone and the characteristics of the 2011 Tohoku earthquake support this relationship. Here, fluid-saturated sediments do not extend as far landward as for the Maule rupture zone. This difference has implications for the tsunami potential of some subduction zones, adding further value to the use of seismic velocity structure in determining rupture attributes.

## 9.1 Response to project aims

The second part of this thesis focussed on imaging source complexity of megathrust earthquakes. Stress transfer between nearby faults is responsible for several earthquake phenomena, but it is not known how slip on the plate interface interacts with faults in the upper plate at short timescales. In particular, the dominant stress triggering mechanisms are difficult to resolve, and is a subject of much debate (e.g. Freed, 2004). By carrying out a multiple point-source inversion of local waveform recordings from the 2011  $M_w$  7.1 Araucania earthquake, we found that this event was composed of rupture on the plate interface ( $M_w$  6.8) followed by almost instantaneous reactivation ( $\sim 11$  s) of a normal fault in the overriding plate ( $M_w$  6.7). To our knowledge, this finding is the first direct evidence for rapidly triggered slip on an upper plate fault due to plate interface slip. The use of 3-D waveform simulations provides evidence that the second event resulted from dynamic triggering by S-waves from the initial thrusting rupture. By relating the source configuration to seismic velocity structure, we find that normal faults may preferentially occur along structural discontinuities in the marine forearc, such as the backstop. Shallow dip-slip ruptures could generate a localised tsunami. Furthermore, given that the upper plate earthquake does not appear to have had a signature in teleseismic waveforms, it is possible that some triggered events may not be detectable by real-time tsunami warning systems.

In seismic imaging, our strategy of combining offshore with onshore data in local earthquake tomography was key to seismically imaging the Chilean subduction zone. We have shown that incorporating observations from extensive ocean-bottom seismometer networks can illuminate the entire seismogenic zone of the subducting plate interface. In Chapter Four, we demonstrated that using onshore data alone leads to blurred images of the subsurface, particularly in  $v_s$ , and poorly constrained hypocentral locations of offshore earthquakes. Hence, we recommend the use of future OBS deployments and permanent cabled observatories to illuminate physical properties in subduction zones. The synthetic tests on waveform inversion in Chapter Seven are a demonstration of how certain locations of sub-events will not be resolved under circumstances of poor station coverage. Furthermore, we show that structural heterogeneity can bias source parameters of offshore earthquakes. The simulation of 3-D waveforms, therefore, is a valuable tool that can accurately resolve moment tensor parameters using onshore stations alone for many subduction zone ruptures.

Overall, the main conclusions of this thesis are that for central Chile, upper plate structures exert a strong control on the rupture characteristics of large subduction earthquakes. In particular, we have identified vital interplays of the subducting plate interface with forearc anomalies and upper plate faults. Based on our preliminary analysis of small–moderate earthquake mechanisms (Section 8.1.2), upper plate faults may occur throughout megathrust segments. Furthermore, given that these structures are present in other parts of the South American subduction zone (e.g. Audin et al., 2008; Tassara, 2010) and other convergent margins (e.g. Kodaira et al., 2006; Tsuji et al., 2011), they must be regarded as having important influences on many large earthquakes.

## 9.2 Limitations of this study and ideas for future research

As explained above, this thesis has highlighted some significant implications for the science of subduction zone earthquakes, and understanding of their hazards. Still, due to limitations of this study and the analyses chosen, there are many possible further lines of investigation, as detailed below.

First, we have speculated that based on our knowledge of the Maule rupture zone and the comparisons made with the Tohoku earthquake, seismic velocity structure may help to characterise future earthquake ruptures. However, in order to generate a unified model of this relationship, more studies of subduction margins with high-resolution velocity models and detailed recordings of megathrust behaviour should be considered. For example, one could include the combination detailed velocity models of the Hikurangi subduction zone (e.g. Eberhart-Phillips and Reyners, 2012) with knowledge gleaned on the distribution of interseismic locking and the characteristics of slow slip events (e.g. Wallace and Beavan, 2010). For the Maule earthquake, we have not considered transient subduction phenomena, such as slow slip events and seismic tremor, so the inclusion of the Hikurangi case study could help to widen the applicability of a unified model.

A similar limitation is attached to our conclusion of closely-spaced doublets and dynamic triggering of slip in the upper plate. Although our single study of the Araucania earthquake is a unique observation, we have alluded to reduced imaging capability of complex sources by using traditional teleseismic source inversions.

## 9.2 Limitations of this study and ideas for future research

Consequently, we cannot rule out that the Araucania earthquake is an isolated example. In our opinion, it is possible that similar closely-spaced doublets have occurred in other regions. Hence, we suggest that a full assessment is given to moderately large ( $M_w$  6.8–7.5) offshore subduction earthquakes where local and regional strong-motion waveform data is available. For example, in the South American subduction zone, the 25/09/2013  $M_w$  7.1 Acari, Peru earthquake may fulfil these criteria. For this size of earthquake, it is possible that there are not enough large aftershocks to resolve rupture on multiple faults using teleseismic CMT solutions. It must be noted, though, that based on our synthetic tests on the resolvability of multiple point-source inversions using onshore stations only, such results should be carefully interpreted. If available, geodetic observations, for example GPS and InSAR, may help to constrain multiple point-source faulting solutions. Identifying the Araucania doublet from teleseismic waveforms was not within the scope of our study. Nevertheless, we suggest that detailed synthetic tests on the ability of teleseismic moment tensor inversions to identify closely-spaced doublets in subduction zones.

Although we have shown the value of passive seismic imaging with the inclusion of ocean-bottom data, there are inherent limitations with this approach. For example, by making interpretations on the relationship between seismic velocities and megathrust behaviour, we implicitly assume that seismic velocities remain fixed over time. In fact, it is possible that time-dependent velocity changes may be prevalent, particularly in the aftermath of a large megathrust earthquake. Husen and Kissling (2001) used a 4-D tomographic inversion to show a significant increase in  $v_p/v_s$  due to increase in crack density and changes in pore fluid pressure following the 1995 Antofagasta earthquake. For the Maule earthquake, it would be theoretically possible to calculate several tomography models for different periods of the aftershock sequence. However, variability in station coverage over time, particularly with OBS networks, and the choice of damping value for each model could make such a procedure complex. There is one further inherent limitation to the applicability of LET imaging in other subduction zones, namely the lack of evenly-distributed sources in a seismic gap. For example, the Cascadia subduction zone has little measureable offshore background seismicity, making LET difficult. Therefore, we recommend the continued investment into offshore active-source seismic experiments, and



development of passive seismic imaging, such as ambient noise tomography using OBS stations.

Throughout our interpretation of velocity models, we have neglected the possible presence of a subduction channel at greater depths (i.e.  $> 25$  km), due to the limitations on nodal spacing in the inversion scheme. Grevemeyer et al. (2003) and Contreras-Reyes et al. (2008) suggest that the subduction channel in the Maule region may be up to 1 km thick. Adjoint full-waveform tomography may help to resolve  $v_s$  of such thin layers. Our preliminary work on finite-frequency sensitivity kernels (Figure 8.7) shows the seismic wavefield is dependent on velocity structure close to the seismic source (i.e. the subducting plate interface for many aftershocks). Also, since we have shown in Chapter Seven that structural heterogeneity might bias source parameters, 3-D full-waveform inversion could improve the precision of seismic source inversions by using more accurate Green's functions. Such 3-D full-waveform tomography has been carried out on a regional scale for continental faults zones, such as the southern California region (Tape et al., 2009), yet no such study has yet been published for a subduction margin. Full-waveform simulations can also be valuable for seismic hazard assessment. These models can predict peak ground velocities and accelerations for different rupture scenarios in central Chile, particularly where topographic effects are important to consider (Section 6.5).

Although we have qualitatively interpreted visual correlations between physical properties and megathrust processes, we lack knowledge on the physics that control fault behaviour. Furthermore, our simple relationship between slip and seismic velocity does not account for dynamic processes that can cause brittle failure, such as weakening due to rapid thermal pressurisation (Faulkner et al., 2011). A unified model of seismic velocities as a proxy for megathrust rupture characteristics would require constraints on frictional laws (e.g. Scholz, 1998). Laboratory deformation experiments on rock samples at high stress could help to provide additional constraints on frictional behaviour. Moreover, there is a growing need to develop time-dependent numerical simulations of megathrust behaviour (e.g. Dinther et al., 2013) over many periods of the seismic cycle. These models would need to use realistic 3-D subduction zone structure, such as that presented in this thesis, which could prove valuable to these simulations. Whilst we lack knowledge of long-term slip histories in subduction zones,

## 9.2 Limitations of this study and ideas for future research

simulations could quantify stress accumulation and release over many seismic cycles, as well as deciphering the stress state of high velocity structures, such as the Cobquecura anomaly.

Although we have imaged complex structural heterogeneity along a subduction megathrust, geodetic inversions for interseismic locking and coseismic slip tend to use rather simplistic parameterisations of subsurface properties (such as Young's modulus and Poisson's ratio; Section 1.1.2). For instance, the plate interface beneath the outer marine forearc in central Chile is characterised by a high Poisson's ratio of  $\sim 0.35$  (Figure 5.12); however, no published slip inversion for the Maule earthquake incorporates such high values. Therefore, we recommend that these inversions account for realistic structural properties in order to assess the effect on locking and slip distributions close to the trench.

# REFERENCES

- Abercrombie, R.E., Antolik, M., Felzer, K., Ekström, G., 2001. The 1994 Java tsunami earthquake: Slip over a subducting seamount. *J. Geophys. Res.* 106, 6595–6607. doi:10.1029/2000JB900403
- Adamova, P., Sileny, J., 2010. Non-Double-Couple Earthquake Mechanism as an Artifact of the Point-Source Approach Applied to a Finite-Extent Focus. *B. Seismol. Soc. Am.* 100, 447–457. doi:10.1785/0120090097
- Adamova, P., Sokos, E.N., Zahradnik, J., 2008. Problematic non-double-couple mechanism of the 2002 Amfilochia Mw5 earthquake, Western Greece. *J. Seismol.* 13, 1–12. doi:10.1007/s10950-008-9112-4
- Agurto, H., Rietbrock, A., Ryder, I.M.A., Miller, M., 2012. Seismic-afterslip characterization of the 2010 MW 8.8 Maule, Chile, earthquake based on moment tensor inversion. *Geophys. Res. Lett.* 39, L20303. doi:10.1029/2012GL053434
- Aki, K., Christoffersson, A., Husebye, E.S., 1977. Determination of the three-dimensional seismic structure of the lithosphere. *J. Geophys. Res.* 82, 277–296. doi:10.1029/JB082i002p00277
- Aki, K., Lee, W.H.K., 1976. Determination of three-dimensional velocity anomalies under a seismic array using first P arrival times from local earthquakes: 1. A homogeneous initial model. *J. Geophys. Res.* 81, 4381–4399. doi:10.1029/JB081i023p04381
- Aki, K., Richards, P.G., 1980. *Quantitative Seismology*, Second. ed. W.H. Freeman, San Francisco.
- Allmendinger, R.W., González, G., 2010. Invited review paper: Neogene to Quaternary tectonics of the coastal Cordillera, northern Chile. *Tectonophysics* 495, 93–110. doi:10.1016/j.tecto.2009.04.019
- Ammon, C.J., Kanamori, H., Lay, T., 2008. A great earthquake doublet and seismic stress transfer cycle in the central Kuril islands. *Nature* 451, 561–565. doi:10.1038/nature06521
- Ando, M., 1975. Source mechanisms and tectonic significance of historical earthquakes along the nankai trough, Japan. *Tectonophysics* 27, 119–140. doi:10.1016/0040-1951(75)90102-X
- Armijo, R., Thiele, R., 1990. Active faulting in northern Chile: ramp stacking and lateral decoupling along a subduction plate boundary? *Earth Planet. Sci. Lett.* 98, 40–61. doi:10.1016/0012-821X(90)90087-E
- Aron, F., Allmendinger, R.W., Cembrano, J., González, G., Yáñez, G., 2013. Permanent fore-arc extension and seismic segmentation: Insights from the 2010 Maule earthquake, Chile. *J. Geophys. Res.* doi:10.1029/2012JB009339
- Audet, P., Bostock, M.G., Christensen, N.I., Peacock, S.M., 2009. Seismic evidence for overpressured subducted oceanic crust and megathrust fault sealing. *Nature* 457, 76–78. doi:10.1038/nature07650
- Audin, L., Lacan, P., Tavera, H., Bondoux, F., 2008. Upper plate deformation and

## References

- seismic barrier in front of Nazca subduction zone: The Chololo Fault System and active tectonics along the Coastal Cordillera, southern Peru. *Tectonophysics* 459, 174–185. doi:10.1016/j.tecto.2007.11.070
- Avouac, J.-P., 2011. Earthquakes: The lessons of Tohoku-Oki. *Nature* 475, 300–300. doi:10.1038/nature10265
- Álvarez, O., Nacif, S., Gimenez, M., Folguera, A., Braitenberg, C., 2014. GOCE derived vertical gravity gradient delineates great earthquake rupture zones along the Chilean margin. *Tectonophysics*. doi:10.1016/j.tecto.2014.03.011
- Backus, G., Gilbert, F., 1968. The Resolving Power of Gross Earth Data. *Geophys. J. Int.* 16, 169–205. doi:10.1111/j.1365-246X.1968.tb00216.x
- Bangs, N.L.B., Moore, G.F., Gulick, S.P.S., Pangborn, E.M., Tobin, H.J., Kuramoto, S., Taira, A., 2009. Broad, weak regions of the Nankai Megathrust and implications for shallow coseismic slip. *Earth Planet. Sci. Lett.* 284, 44–49. doi:10.1016/j.epsl.2009.04.026
- Barrientos, S.E., 1987. Is the Pichilemu-Talcahuano (Chile) a seismic gap. *Seismol. Res. Lett.* 61, 43–48.
- Barrientos, S.E., Ward, S.N., 1990. The 1960 Chile earthquake: inversion for slip distribution from surface deformation. *Geophys. J. Int.* 103, 589–598. doi:10.1111/j.1365-246X.1990.tb05673.x
- Bassett, D., Sutherland, R., Henrys, S., Stern, T.A., Scherwath, M., Benson, A., Toulmin, S., Henderson, M., 2010. Three-dimensional velocity structure of the northern Hikurangi margin, Raukumara, New Zealand: Implications for the growth of continental crust by subduction erosion and tectonic underplating. *Geochem., Geophys., Geosyst.* 11, Q10013. doi:10.1029/2010GC003137
- Beck, S., Barrientos, S.E., Kausel, E., Reyes, M., 1998. Source characteristics of historic earthquakes along the central Chile subduction zone. *J. S. Am. Earth Sci.* 11, 115–129. doi:10.1016/S0895-9811(98)00005-4
- Beck, S.L., Rietbrock, A., Tilmann, F., Barrientos, S.E., Meltzer, A.S., Oppenheimer, D.H., Bataille, K., Roecker, S.W., Vilotte, J.-P., Russo, R.M., 2014. Advancing Subduction Zone Science After a Big Quake. *Eos Trans. Am. Geophys. Union* 95, 193–194. doi:10.1002/2014EO230001
- Bedford, J., Moreno, M., Baez, J.C., Lange, D., Tilmann, F., Rosenau, M., Heidbach, O., Bartsch, M., Tassara, A., Bevis, M., Vigny, C., 2013. A high-resolution, time-variable afterslip model for the 2010 Maule Mw = 8.8, Chile megathrust earthquake. *Earth Planet. Sci. Lett.* 383, 26–36. doi:10.1016/j.epsl.2013.09.020
- Bell, R., Holden, C., Power, W., Wang, X., Downes, G., 2014. Hikurangi margin tsunami earthquake generated by slow seismic rupture over a subducted seamount. *Earth Planet. Sci. Lett.* 397, 1–9. doi:10.1016/j.epsl.2014.04.005
- Beroza, G.C., Ide, S., 2011. Slow Earthquakes and Nonvolcanic Tremor. *Annu. Rev. Earth Planet. Sci.* 39, 271–296. doi:10.1146/annurev-earth-040809-152531
- Bilek, S.L., 2010. The role of subduction erosion on seismicity. *Geology* 38, 479–480. doi:10.1130/focus052010.1
- Bilek, S.L., Lay, T., 2002. Tsunami earthquakes possibly widespread manifestations of frictional conditional stability. *Geophys. Res. Lett.* 29, 18–1–18–4.

doi:10.1029/2002GL015215

- Bilek, S.L., Lay, T., 1999. Rigidity variations with depth along interplate megathrust faults in subduction zones. *Nature* 400, 443–446. doi:10.1038/22739
- Bilek, S.L., Schwartz, S.Y., DeShon, H.R., 2003. Control of seafloor roughness on earthquake rupture behavior. *Geology* 31, 455–458. doi:10.1130/0091-7613(2003)031<0455:COSROE>2.0.CO;2
- Blanpied, M.L., Lockner, D.A., Byerlee, J.D., 1995. Frictional slip of granite at hydrothermal conditions. *J. Geophys. Res.* 100, 13045. doi:10.1029/95JB00862
- Blaser, L., Krüger, F., Ohrnberger, M., Scherbaum, F., 2010. Scaling Relations of Earthquake Source Parameter Estimates with Special Focus on Subduction Environment. *B. Seismol. Soc. Am.* 100, 2914–2926. doi:10.1785/0120100111
- Bohm, M., 2004. 3-D Lokalbebentomographie der sudlichen Anden zwischen 36° und 40°S. Freie Universitat Berlin, Germany.
- Bostock, M.G., 2013. The Moho in subduction zones. *Tectonophysics* 609, 547–557. doi:10.1016/j.tecto.2012.07.007
- Bostock, M.G., Hyndman, R.D., Rondenay, S., Peacock, S.M., 2002. An inverted continental Moho and serpentinization of the forearc mantle. *Nature* 417, 536–538. doi:10.1038/417536a
- Bouchon, M., 1981. A simple method to calculate Green's functions for elastic layered media. *B. Seismol. Soc. Am.* 71, 959–971.
- Bürgmann, R., Chadwell, D., 2014. Seafloor Geodesy. *Annu. Rev. Earth Planet. Sci.* 42, 509–534. doi:10.1146/annurev-earth-060313-054953
- Bürgmann, R., Kogan, M.G., Steblov, G.M., Hilley, G., Levin, V.E., Apel, E., 2005. Interseismic coupling and asperity distribution along the Kamchatka subduction zone. *J. Geophys. Res.* 110, B07405. doi:10.1029/2005JB003648
- Calvert, A., Sandvol, E., Seber, D., Barazangi, M., Roecker, S.W., Mourabit, T., Vidal, F., Alguacil, G., Jabour, N., 2000. Geodynamic evolution of the lithosphere and upper mantle beneath the Alboran region of the western Mediterranean: Constraints from travel time tomography. *J. Geophys. Res.* 105, 10871–10898. doi:10.1029/2000JB900024
- Campos, J., Hatzfeld, D., Madariaga, R., Lopez, G., Kausel, E., Zollo, A., Iannacone, G., Fromm, R., Barrientos, S.E., Lyon-Caen, H., 2002. A seismological study of the 1835 seismic gap in south-central Chile. *Phys. Earth. Planet. Inter.* 132, 177–195. doi:10.1016/S0031-9201(02)00051-1
- Campus, P., Suhadolc, P., Panza, G.F., Sileny, J., 1996. Complete moment tensor retrieval for weak events: application to orogenic and volcanic areas. *Tectonophysics* 261, 147–163. doi:10.1016/0040-1951(96)00063-7
- Carlson, R.L., Miller, D.J., 2003. Mantle wedge water contents estimated from seismic velocities in partially serpentinized peridotites. *Geophys. Res. Lett.* 30, 1250. doi:10.1029/2002GL016600
- Casarotti, E., Stupazzini, M., Lee, S.J., Komatitsch, D., Piersanti, A., Tromp, J., 2008. CUBIT and Seismic Wave Propagation Based Upon the Spectral-Element Method: An Advanced Unstructured Mesher for Complex 3D Geological Media, in: *Proceedings of the 16th International Meshing Roundtable*. Springer Berlin

## References

- Heidelberg, Berlin, Heidelberg, pp. 579–597. doi:10.1007/978-3-540-75103-8\_32
- Centro Sismológico Nacional, 2011. Centro Sismológico Nacional, Universidad de Chile [WWW Document]. URL <http://www.sismologia.cl> (accessed 5.24.15).
- Cerveny, V., Molotkov, I. A., Psencik, I., 1977. Ray method in seismology. University of Karlova Press, Czechoslovakia.
- Chauhan, A.P.S., Singh, S.C., Hananto, N.D., Carton, H., Klingelhoefer, F., Dessa, J.X., Permana, H., White, N.J., Graindorge, D., Team, S.S., 2009. Seismic imaging of forearc backthrusts at northern Sumatra subduction zone. *Geophys. J. Int.* 179, 1772–1780. doi:10.1111/j.1365-246X.2009.04378.x
- Chen, A.T., Frohlich, C., Latham, G.V., 1982. Seismicity of the forearc marginal wedge (accretionary prism). *J. Geophys. Res.* 87, 3679–3690. doi:10.1029/JB087iB05p03679
- Chester, F.M., Rowe, C., Ujiie, K., Kirkpatrick, J., Regalla, C., Remitti, F., Moore, J.C., Toy, V., Wolfson-Schwehr, M., Bose, S., Kameda, J., Mori, J.J., Brodsky, E.E., Eguchi, N., Toczko, S., Expedition 343 and 343T Scientists, 2013. Structure and composition of the plate-boundary slip zone for the 2011 Tohoku-Oki earthquake. *Science* 342, 1208–1211. doi:10.1126/science.1243719
- Chlieh, M., Perfettini, H., Tavera, H., Avouac, J.-P., Remy, D., Nocquet, J.M., Rolandone, F., Bondoux, F., Gabalda, G., Bonvalot, S., 2011. Interseismic coupling and seismic potential along the Central Andes subduction zone. *J. Geophys. Res.* 116, B12405. doi:10.1029/2010JB008166
- Choy, G.L., McGarr, A., Kirby, S.H., Boatwright, J., 2006. An Overview of the Global Variability in Radiated Energy and Apparent Stress, in: Abercrombie, R.E., McGarr, A., Di Toro, G., Kanamori, H. (Eds.), *Earthquakes: Radiated Energy and the Physics of Faulting*. American Geophysical Union, pp. 43–57. doi:10.1029/170GM06
- Christensen, N.I., 2004. Serpentinites, Peridotites, and Seismology. *Int. Geol. Rev.* 46, 795–816. doi:10.2747/0020-6814.46.9.795
- Christensen, N.I., 1996. Poisson's ratio and crustal seismology. *J. Geophys. Res.* 101, 3139–3156. doi:10.1029/95JB03446
- Christensen, N.I., 1984. Pore pressure and oceanic crustal seismic structure. *Geophys. J. Int.* 79, 411–423.
- Cifuentes, I.L., 1989. The 1960 Chilean earthquakes. *J. Geophys. Res.* 94, 665. doi:10.1029/JB094iB01p00665
- Clift, P., Vannucchi, P., 2004. Controls on tectonic accretion versus erosion in subduction zones: Implications for the origin and recycling of the continental crust. *Rev. Geophys.* 42, RG2001. doi:10.1029/2003RG000127
- Cloos, M., 1992. Thrust-type subduction-zone earthquakes and seamount asperities: A physical model for seismic rupture. *Geology* 20, 601–604. doi:10.1130/0091-7613(1992)020<0601:TTSZEA>2.3.CO;2
- Cloos, M., Shreve, R.L., 1996. Shear-zone thickness and the seismicity of Chilean- and Marianas-type subduction zones. *Geology* 24, 107–110. doi:10.1130/0091-7613(1996)024<0107:SZTATS>2.3.CO;2
- Cloos, M., Shreve, R.L., 1988. Subduction-channel model of prism accretion, melange

- formation, sediment subduction, and subduction erosion at convergent plate margins: 1. Background and description. *Pure. Appl. Geophys.* 128, 455–500. doi:10.1007/BF00874548
- Collings, R., Lange, D., Rietbrock, A., Tilmann, F., Natawidjaja, D.H., Suwargadi, B.W., Miller, M., Saul, J., 2012. Structure and seismogenic properties of the Mentawai segment of the Sumatra subduction zone revealed by local earthquake traveltimes tomography. *J. Geophys. Res.* 117, B01312. doi:10.1029/2011JB008469
- Collot, J.Y., Agudelo, W., Ribodetti, A., Marcaillou, B., 2008. Origin of a crustal splay fault and its relation to the seismogenic zone and underplating at the erosional north Ecuador–south Colombia oceanic margin. *J. Geophys. Res.* 113, B12102. doi:10.1029/2008JB005691
- Collot, J.Y., Marcaillou, B., Sage, F., Michaud, F., Agudelo, W., Charvis, P., Graindorge, D., Gutscher, M.A., Spence, G., 2004. Are rupture zone limits of great subduction earthquakes controlled by upper plate structures? Evidence from multichannel seismic reflection data acquired across the northern Ecuador–southwest Colombia margin. *J. Geophys. Res.* 109, B11103. doi:10.1029/2004JB003060
- Contreras Reyes, E., Becerra, J., Kopp, H., Reichert, C., Díaz Naveas, J., 2014. Seismic structure of the north-central Chilean convergent margin: Subduction erosion of a paleomagmatic arc. *Geophys. Res. Lett.* 41, 1523–1529.
- Contreras Reyes, E., Grevemeyer, I., Flueh, E.R., Reichert, C., 2008. Upper lithospheric structure of the subduction zone offshore of southern Arauco peninsula, Chile, at ~38°S. *J. Geophys. Res.* 113, B07303. doi:10.1029/2007JB005569
- Contreras-Reyes, E., Flueh, E.R., Grevemeyer, I., 2010. Tectonic control on sediment accretion and subduction off south central Chile: Implications for coseismic rupture processes of the 1960 and 2010 megathrust earthquakes. *Tectonics* 29.
- Contreras-Reyes, E., Jara, J., Grevemeyer, I., Ruiz, S., Carrizo, D., 2012. Abrupt change in the dip of the subducting plate beneath north Chile. *Nature Geosci.* 5, 342–345. doi:10.1038/ngeo1447
- Contreras-Reyes, E., Jara, J., Maksymowicz, A., Weinrebe, W., 2013. Sediment loading at the southern Chilean trench and its tectonic implications. *J. Geodyn.* 66, 134–145. doi:10.1016/j.jog.2013.02.009
- Dahlen, F.A., Suppe, J., Davis, D., 1984. Mechanics of fold-and-thrust belts and accretionary wedges: Cohesive Coulomb Theory. *J. Geophys. Res.* 89, 10087–10101. doi:10.1029/JB089iB12p10087
- Dannowski, A., Grevemeyer, I., Kraft, H., Arroyo, I., 2013. Crustal thickness and mantle wedge structure from receiver functions in the Chilean Maule region at 35° S. *Tectonophysics*. doi:10.1016/j.tecto.2013.02.015
- Darwin, C., 1851. Geological observations on coral reefs, volcanic islands, and on South America: Being the geology of the voyage of the Beagle, under the command of Captain Fitzroy, RN, during the years 1832 to 1836, *Geology*. Smith, Elder. doi:10.1130/G20178.2
- Davis, D., Suppe, J., Dahlen, F.A., 1983. Mechanics of fold-and-thrust belts and

## References

- accretionary wedges. *J. Geophys. Res.* 88, 1153–1172. doi:10.1029/JB088iB02p01153
- Dean, S.M., McNeill, L.C., Henstock, T.J., Bull, J.M., Gulick, S.P.S., Austin, J.A., Bangs, N.L.B., Djajadihardja, Y.S., Permana, H., 2010. Contrasting décollement and prism properties over the Sumatra 2004-2005 earthquake rupture boundary. *Science* 329, 207–210. doi:10.1126/science.1189373
- DeMets, C., Gordon, R.G., Argus, D.F., 2010. Geologically current plate motions. *Geophys. J. Int.* 181, 1–80. doi:10.1111/j.1365-246X.2009.04491.x
- DeShon, H.R., Schwartz, S.Y., 2004. Evidence for serpentinization of the forearc mantle wedge along the Nicoya Peninsula, Costa Rica. *Geophys. Res. Lett.* 31, L21611. doi:10.1029/2004GL021179
- DeShon, H.R., Schwartz, S.Y., Newman, A.V., González, V., Protti, M., Dorman, L.M., Dixon, T.H., Sampson, D.E., Flueh, E.R., 2006. Seismogenic zone structure beneath the Nicoya Peninsula, Costa Rica, from three-dimensional local earthquake P- and S-wave tomography. *Geophys. J. Int.* 164, 109–124. doi:10.1111/j.1365-246X.2005.02809.x
- Dessa, J.X., Klingelhoefer, F., Graindorge, D., Andre, C., Permana, H., Gutscher, M.A., Chauhan, A., Singh, S.C., the SUMATRA-OBS Scientific Team, 2009. Megathrust earthquakes can nucleate in the forearc mantle: Evidence from the 2004 Sumatra event. *Geology* 37, 659–662. doi:10.1130/G25653A.1
- Dinther, Y., Gerya, T.V., Dalguer, L.A., Mai, P.M., Morra, G., Giardini, D., 2013. The seismic cycle at subduction thrusts: Insights from seismo-thermo-mechanical models. *J. Geophys. Res. Solid Earth* 118, 6183–6202. doi:10.1002/2013JB010380
- Dominguez, S., Malavieille, J., Lallemand, S.E., 2000. Deformation of accretionary wedges in response to seamount subduction: Insights from sandbox experiments. *Tectonics* 19, 182–196.
- Dreger, D., Savage, B., 1999. Aftershocks of the 1952 Kern County, California, earthquake sequence. *B. Seismol. Soc. Am.* 89, 1094–1108.
- Dreger, D., Woods, B., 2002. Regional distance seismic moment tensors of nuclear explosions. *Tectonophysics* 356, 139–156. doi:10.1016/S0040-1951(02)00381-5
- Dreger, D.S., Helmberger, D.V., 1993. Determination of source parameters at regional distances with three-component sparse network data. *J. Geophys. Res.* 98, 8107. doi:10.1029/93JB00023
- Dzierma, Y., Rabbel, W., Thorwart, M., Koulakov, I., Wehrmann, H., Hoernle, K., Comte, D., 2012a. Seismic velocity structure of the slab and continental plate in the region of the 1960 Valdivia (Chile) slip maximum — Insights into fluid release and plate coupling. *Earth Planet. Sci. Lett.* 331–332, 164–176. doi:10.1016/j.epsl.2012.02.006
- Dzierma, Y., Thorwart, M., Rabbel, W., 2012b. Moho topography and subducting oceanic slab of the Chilean continental margin in the maximum slip segment of the 1960 Mw 9.5 Valdivia (Chile) earthquake from P-receiver functions. *Tectonophysics* 530–531, 180–192. doi:10.1016/j.tecto.2011.12.016
- Dziewonski, A.M., Hager, B.H., O'Connell, R.J., 1977. Large-scale heterogeneities in



- the lower mantle. *J. Geophys. Res.* 82, 239–255. doi:10.1029/JB082i002p00239
- Dziewoński, A.M., Chou, T.A., Woodhouse, J.H., 1981. Determination of earthquake source parameters from waveform data for studies of global and regional seismicity. *J. Geophys. Res.* 86, 2825–2852. doi:10.1029/JB086iB04p02825
- Dziewoński, A.M., Woodhouse, J.H., 1983. Studies of the seismic source using normal-mode theory, in: Kanamori, H., Boschi, E. (Eds.), *Earthquakes: Observations, Theory and Interpretation*. Earthquakes: Observations, theory and interpretation, Amsterdam, pp. 45–137.
- Eberhart-Phillips, D., 1993. Local earthquake tomography: earthquake source regions, in: Iyer, H.M., Hirahara, K. (Eds.), *Seismic Tomography - Theory and Practice*. London, pp. 613–643.
- Eberhart-Phillips, D., 1990. Three-dimensional P and S velocity structure in the Coalinga Region, California. *J. Geophys. Res.* 95, 15343–15363. doi:10.1029/JB095iB10p15343
- Eberhart-Phillips, D., 1989. Active faulting and deformation of the Coalinga Anticline as interpreted from three-dimensional velocity structure and seismicity. *J. Geophys. Res.* 94, 15565–15586. doi:10.1029/JB094iB11p15565
- Eberhart-Phillips, D., 1986. Three-dimensional velocity structure in northern California Coast Ranges from inversion of local earthquake arrival times. *B. Seismol. Soc. Am.* 76, 1025–1052.
- Eberhart-Phillips, D., Michael, A.J., 1998. Seismotectonics of the Loma Prieta, California, region determined from three-dimensional  $V_p$ ,  $V_p/V_s$ , and seismicity. *J. Geophys. Res.* 103, 21099. doi:10.1029/98JB01984
- Eberhart-Phillips, D., Reyners, M., 2012. Imaging the Hikurangi Plate interface region, with improved local-earthquake tomography. *Geophys. J. Int.* 190, 1221–1242.
- Eberhart-Phillips, D., Reyners, M., 1999. Plate interface properties in the Northeast Hikurangi Subduction Zone, New Zealand, from converted seismic waves. *Geophys. Res. Lett.* 26, 2565–2568. doi:10.1029/1999GL900567
- Eberhart-Phillips, D., Reyners, M., Chadwick, M., Chiu, J.M., 2005. Crustal heterogeneity and subduction processes: 3-D  $V_p$ ,  $V_p/V_s$  and  $Q$  in the southern North Island, New Zealand. *Geophys. J. Int.* 162, 270–288. doi:10.1111/j.1365-246X.2005.02530.x
- Ekström, G., Nettles, M., Dziewoński, A.M., 2012. The global CMT project 2004–2010: Centroid-moment tensors for 13,017 earthquakes. *Phys. Earth. Planet. Inter.* 200–201, 1–9. doi:10.1016/j.pepi.2012.04.002
- Ellsworth, W.L., 1977. Three-dimensional structure of the crust and mantle beneath the island of Hawaii. Massachusetts Institute of Technology, Cambridge.
- Fariás, M., Comte, D., Roecker, S.W., Carrizo, D., Pardo, M., 2011. Crustal extensional faulting triggered by the 2010 Chilean earthquake: The Pichilemu Seismic Sequence. *Tectonics* 30. doi:10.1029/2011TC002888
- Faulkner, D.R., Mitchell, T.M., Behn, J., Hirose, T., Shimamoto, T., 2011. Stuck in the mud? Earthquake nucleation and propagation through accretionary forearcs. *Geophys. Res. Lett.* 38. doi:10.1029/2011GL048552

## References

- Fojtíková, L., Vavryčuk, V., Cipciar, A., Madarás, J., 2010. Focal mechanisms of micro-earthquakes in the Dobrá Voda seismoactive area in the Malé Karpaty Mts. (Little Carpathians), Slovakia. *Tectonophysics* 492, 213–229. doi:10.1016/j.tecto.2010.06.007
- Folguera, A., Ramos, V.A., 2009. Collision of the Mocha fracture zone and a < 4 Ma old wave of orogenic uplift in the Andes (36–38 S). *Lithosphere* 1, 364–369.
- Franzese, J.R., Spalletti, L.A., 2001. Late Triassic–early Jurassic continental extension in southwestern Gondwana: tectonic segmentation and pre-break-up rifting. *J. S. Am. Earth Sci.* 14, 257–270. doi:10.1016/S0895-9811(01)00029-3
- Freed, A.M., 2004. Earthquake triggering by static, dynamic, and postseismic stress transfer. *Annu. Rev. Earth Planet. Sci.* 33, 335–367. doi:10.1146/annurev.earth.33.092203.122505
- Frohlich, C., 2006. Deep earthquakes. Cambridge University Press, Cambridge.
- Frohlich, C., 1994. Earthquakes with Non—Double-Couple Mechanisms. *Science* 264, 804–809. doi:10.1126/science.264.5160.804
- Frohlich, C., 1992. Triangle diagrams: ternary graphs to display similarity and diversity of earthquake focal mechanisms. *Phys. Earth. Planet. Inter.* 75, 193–198. doi:10.1016/0031-9201(92)90130-N
- Frohlich, C., Billington, S., Engdahl, E.R., Malahoff, A., 1982. Detection and location of earthquakes in the Central Aleutian Subduction Zone using island and ocean bottom seismograph stations. *J. Geophys. Res.* 87, 6853–6864. doi:10.1029/JB087iB08p06853
- Fuis, G., 1998. West margin of North America — a synthesis of recent seismic transects, *Tectonophysics* 288, 265–269. doi:10.1016/S0040-1951(97)00300-4.
- Fuller, C.W., Willett, S.D., Brandon, M.T., 2006. Formation of forearc basins and their influence on subduction zone earthquakes. *Geology* 34, 65–68. doi:10.1130/g21828.1
- Furlong, K.P., Lay, T., Ammon, C.J., 2009. A great earthquake rupture across a rapidly evolving three-plate boundary. *Science* 324, 226–229. doi:10.1126/science.1167476
- Gagnon, K., Chadwell, C.D., Norabuena, E., 2005. Measuring the onset of locking in the Peru–Chile trench with GPS and acoustic measurements. *Nature* 434, 205–208. doi:10.1038/nature03412
- Gallovic, F., Zahradnik, J., 2012. Complexity of the Mw 6.3 2009 L'Aquila (central Italy) earthquake: 1. Multiple finite-extent source inversion. *J. Geophys. Res.* 117, B04307. doi:10.1029/2011JB008709
- Garth, T., Rietbrock, A., 2014. Order of magnitude increase in subducted H<sub>2</sub>O due to hydrated normal faults within the Wadati-Benioff zone. *Geology* 42, 207–210. doi:10.1130/G34730.1
- Geersen, J., Behrmann, J.H., Völker, D., Krastel, S., Ranero, C.R., Diaz Naveas, J., Weinrebe, W., 2011a. Active tectonics of the South Chilean marine fore arc (35 S–40 S). *Tectonics* 30.
- Geersen, J., Völker, D., Behrmann, J.H., Reichert, C., Krastel, S., 2011b. Pleistocene giant slope failures offshore Arauco Peninsula, Southern Chile. *J. Geol. Soc.*

- London 168, 1237–1248. doi:10.1144/0016-76492011-027
- Geersen, J., McNeill, L., Henstock, T.J., Gaedicke, C., 2013. The 2004 Aceh-Andaman Earthquake: Early clay dehydration controls shallow seismic rupture, *Geochem. Geophys. Geosyst.*, 14, 3315–3323. doi:10.1002/ggge.20193
- Geller, R.J., 2011. Shake-up time for Japanese seismology. *Nature* 472, 407–409. doi:10.1038/nature10105
- Gilbert, F., 1973. Derivation of Source Parameters from Low-Frequency Spectra. *Phil. Trans. R. Soc. Lond. A* 274, 369–371. doi:10.1098/rsta.1973.0065
- Glodny, J., Echtler, H., Collao, S., Ardiles, M., Burón, P., Figueroa, O., 2008. Differential Late Paleozoic active margin evolution in South-Central Chile (37°S–40°S) – the Lanahue Fault Zone. *J. S. Am. Earth Sci.* 26, 397–411. doi:10.1016/j.jsames.2008.06.001
- Glodny, J., Gräfe, K., Echtler, H., Rosenau, M., 2007. Mesozoic to Quaternary continental margin dynamics in South-Central Chile (36–42°S): the apatite and zircon fission track perspective. *Int. J. Earth Sci.* 97, 1271–1291. doi:10.1007/s00531-007-0203-1
- Goldfinger, C., Kulm, L.D., Yeats, R.S., McNeill, L.C., Hummon, C., 1997. Oblique strike-slip faulting of the central Cascadia submarine forearc. *J. Geophys. Res.* 102, 8217–8243. doi:10.1029/96JB02655
- González, G., Salazar, P., Loveless, J.P., Allmendinger, R.W., Aron, F., Shrivastava, M., 2015. Upper plate reverse fault reactivation and the unclamping of the megathrust during the 2014 northern Chile earthquake sequence. *Geology* 43, 671–674. doi:10.1130/G36703.1
- Graeber, F.M., Asch, G., 1999. Three-dimensional models of Pwave velocity and P-to-S-velocity ratio in the southern central Andes by simultaneous inversion of local earthquake data. *J. Geophys. Res.* 104, 20237. doi:10.1029/1999JB900037
- Grevemeyer, I., Diaz-Naveas, J.L., Ranero, C.R., Villinger, H.W., 2003. Heat flow over the descending Nazca plate in central Chile, 32°S to 41°S: observations from ODP Leg 202 and the occurrence of natural gas hydrates. *Earth Planet. Sci. Lett.* 213, 285–298. doi:10.1016/S0012-821X(03)00303-0
- Groß, K., Micksch, U., TIPTEQ Research Group, Seismics Team, 2008. The reflection seismic survey of project TIPTEQ—the inventory of the Chilean subduction zone at 38.2° S. *Geophys. J. Int.* 172, 565–571. doi:10.1111/j.1365-246X.2007.03680.x
- Gusman, A.R., Tanioka, Y., Sakai, S., Tsushima, H., 2012. Source model of the great 2011 Tohoku earthquake estimated from tsunami waveforms and crustal deformation data. *Earth Planet. Sci. Lett.* 341–344, 234–242. doi:10.1016/j.epsl.2012.06.006
- Haberland, C., Rietbrock, A., Lange, D., Bataille, K., Dahm, T., 2009. Structure of the seismogenic zone of the southcentral Chilean margin revealed by local earthquake traveltimes tomography. *J. Geophys. Res.* 114, B01317. doi:10.1029/2008jb005802
- Haberland, C., Rietbrock, A., Lange, D., Bataille, K., Hofmann, S., 2006. Interaction between forearc and oceanic plate at the south-central Chilean margin as seen in local seismic data. *Geophys. Res. Lett.* 33. doi:10.1029/2006GL028189

## References

- Hacker, B.R., Abers, G.A., 2004. Subduction Factory 3: An Excel worksheet and macro for calculating the densities, seismic wave speeds, and H<sub>2</sub>O contents of minerals and rocks at pressure and temperature. *Geochem., Geophys., Geosyst.* 5, Q01005. doi:10.1029/2003GC000614
- Hardebeck, J.L., 2012. Coseismic and postseismic stress rotations due to great subduction zone earthquakes. *Geophys. Res. Lett.* 39, L21313. doi:10.1029/2012GL053438
- Hardebeck, J.L., Shearer, P.M., 2002. A New Method for Determining First-Motion Focal Mechanisms. *B. Seismol. Soc. Am.* 92, 2264–2276. doi:10.1785/0120010200
- Hariri, El, M., Bilek, S.L., DeShon, H.R., Engdahl, E.R., Bisrat, S., 2013. Along-strike variability of rupture duration in subduction zone earthquakes. *J. Geophys. Res. Solid Earth* 118, 646–664. doi:10.1029/2012JB009548
- Harris, R.N., Conder, J.A., Heuret, A., 2014. The thermal structure of the subduction thrust within accretionary and erosive margins. *Tectonophysics* 633, 221–231. doi:10.1016/j.tecto.2014.07.009
- Hasegawa, A., Yoshida, K., Asano, Y., Okada, T., Iinuma, T., Ito, Y., 2012. Change in stress field after the 2011 great Tohoku-Oki earthquake. *Earth Planet. Sci. Lett.* 355–356, 231–243. doi:10.1016/j.epsl.2012.08.042
- Hayes, G.P., Bergman, E., Johnson, K.L., Benz, H.M., Brown, L., Meltzer, A.S., 2013. Seismotectonic framework of the 2010 February 27 Mw 8.8 Maule, Chile earthquake sequence. *Geophys. J. Int.* 195, 1034–1051. doi:10.1093/gji/ggt238
- Hayes, G.P., Wald, D.J., 2009. Developing framework to constrain the geometry of the seismic rupture plane on subduction interfaces a priori—a probabilistic approach. *Geophys. J. Int.* 176, 951–964.
- Hayes, G.P., Wald, D.J., Johnson, R.L., 2012. Slab1.0: A three-dimensional model of global subduction zone geometries. *J. Geophys. Res.* 117. doi:10.1029/2011JB008524
- Helmholtz-Zentrum - Potsdam Deutsches GeoForschungsZentrum (GFZ), 2011. GEOFON Program GFZ Potsdam :: gzf2011adjs [WWW Document]. URL <http://geofon.gfz-potsdam.de/eqinfo/event.php?id=gzf2011adjs> (accessed 5.24.15).
- Henstock, T.J., McNeill, L.C., Tappin, D.R., 2006. Seafloor morphology of the Sumatran subduction zone: Surface rupture during megathrust earthquakes? *Geology* 34, 485–488. doi:10.1130/22426.1
- Herrmann, R.B., Benz, H.M., Ammon, C.J., 2011. Monitoring the Earthquake Source Process in North America. *B. Seismol. Soc. Am.* 101, 2609–2625. doi:10.1785/0120110095
- Heuret, A., Conrad, C.P., Funiciello, F., Lallemand, S., Sandri, L., 2012. Relation between subduction megathrust earthquakes, trench sediment thickness and upper plate strain. *Geophys. Res. Lett.* 39, L05304.
- Heuret, A., Lallemand, S., Funiciello, F., Piromallo, C., Faccenna, C., 2011. Physical characteristics of subduction interface type seismogenic zones revisited. *Geochem., Geophys., Geosyst.* 12, Q01004. doi:10.1029/2010GC003230

- Hicks, S.P., Nippress, S.E.J., 2012. Sub-slab mantle anisotropy beneath south-central Chile. *Earth Planet. Sci. Lett.* 357, 203–213. doi:10.1016/j.epsl.2012.09.017
- Hsu, Y.-J., Simons, M., Avouac, J.-P., Galetzka, J., Sieh, K., Chlieh, M., Natawidjaja, D.H., Prawirodirdjo, L., Bock, Y., 2006. Frictional afterslip following the 2005 Nias-Simeulue earthquake, Sumatra. *Science* 312, 1921–1926.
- Huene, Von, R., Klaeschen, D., Cropp, B., Miller, J., 1994. Tectonic structure across the accretionary and erosional parts of the Japan Trench margin. *J. Geophys. Res.* 99, 22349–22361. doi:10.1029/94JB01198
- Huene, Von, R., Ranero, C.R., 2003. Subduction erosion and basal friction along the sediment-starved convergent margin off Antofagasta, Chile. *J. Geophys. Res.* 108, 2079. doi:10.1029/2001JB001569
- Huene, Von, R., Ranero, C.R., Scholl, D.W., 2009. Convergent Margin Structure in High-Quality Geophysical Images and Current Kinematic and Dynamic Models, in: Lallemand, S., Funiciello, F. (Eds.), *Subduction Zone Geodynamics*, *Frontiers in Earth Sciences*. Springer Berlin Heidelberg, Berlin, pp. 137–157. doi:10.1007/978-3-540-87974-9\_8
- Huene, Von, R., Ranero, C.R., Vannucchi, P., 2004. Generic model of subduction erosion. *Geology* 32, 913–916. doi:10.1130/G20563.1
- Huene, Von, R., Scholl, D.W., 1991. Observations at convergent margins concerning sediment subduction, subduction erosion, and the growth of continental crust. *Rev. Geophys.* 29, 279. doi:10.1029/91RG00969
- Husen, S., Kissling, E., 2001. Postseismic fluid flow after the large subduction earthquake of Antofagasta, Chile. *Geology* 29, 847–850. doi:10.1130/0091-7613(2001)029<0847:PFFATL>2.0.CO;2
- Husen, S., Kissling, E., Flueh, E., Asch, G., 1999. Accurate hypocentre determination in the seismogenic zone of the subducting Nazca Plate in northern Chile using a combined on-/offshore network. *Geophys. J. Int.* 138, 687–701. doi:10.1046/j.1365-246x.1999.00893.x
- Husen, S., Kissling, E., Flueh, E.R., 2000. Local earthquake tomography of shallow subduction in north Chile: A combined onshore and offshore study. *J. Geophys. Res.* 105, 28183–28198. doi:10.1029/2000JB900229
- Husen, S., Kissling, E., Quintero, R., 2002. Tomographic evidence for a subducted seamount beneath the Gulf of Nicoya, Costa Rica: The cause of the 1990 Mw = 7.0 Gulf of Nicoya earthquake. *Geophys. Res. Lett.* 29, 79–1 – 79–4.
- Husen, S., Quintero, R., Kissling, E., Hacker, B., 2003. Subduction-zone structure and magmatic processes beneath Costa Rica constrained by local earthquake tomography and petrological modelling. *Geophys. J. Int.* 155, 11–32. doi:10.1046/j.1365-246X.2003.01984.x
- Hyndman, R.D., Peacock, S.M., 2003. Serpentinization of the forearc mantle. *Earth Planet. Sci. Lett.* 212, 417–432. doi:10.1016/S0012-821X(03)00263-2
- Hyndman, R.D., Wang, K., Yamano, M., 1995. Thermal constraints on the seismogenic portion of the southwestern Japan subduction thrust. *J. Geophys. Res.* 100, 15373–15392. doi:10.1029/95JB00153
- Hyndman, R.D., Yamano, M., Oleskevich, D.A., 1997. The seismogenic zone of

## References

- subduction thrust faults. *Island Arc* 6, 244–260. doi:10.1111/j.1440-1738.1997.tb00175.x
- Ishii, M., Shearer, P.M., Houston, H., Vidale, J.E., 2005. Extent, duration and speed of the 2004 Sumatra–Andaman earthquake imaged by the Hi-Net array. *Nature*. doi:10.1038/nature03675
- Ito, A., Fujie, G., Miura, S., Kodaira, S., Kaneda, Y., Hino, R., 2005. Bending of the subducting oceanic plate and its implication for rupture propagation of large interplate earthquakes off Miyagi, Japan, in the Japan Trench subduction zone. *Geophys. Res. Lett.* 32, L05310. doi:10.1029/2004GL022307
- Jara-Muñoz, J., Melnick, D., Brill, D., Strecker, M.R., 2015. Segmentation of the 2010 Maule Chile earthquake rupture from a joint analysis of uplifted marine terraces and seismic-cycle deformation patterns. *Quat. Sci. Rev.* 113, 171–192. doi:10.1016/j.quascirev.2015.01.005
- Jechumtálová, Z., Bulant, P., 2014. Effects of 1-D versus 3-D velocity models on moment tensor inversion in the Dobrá Voda area in the Little Carpathians region, Slovakia. *J. Seismol.* 18, 511–531. doi:10.1007/s10950-014-9423-6
- Jechumtálová, Z., Šílený, J., 2005. Amplitude ratios for complete moment tensor retrieval. *Geophys. Res. Lett.* 32, L22303. doi:10.1029/2005GL023967
- Jost, M.L., Herrmann, R.B., 1989. A Student's Guide to and Review of Moment Tensors. *Seismol. Res. Lett.* 60, 37–57. doi:10.1785/gssrl.60.2.37
- Julian, B.R., Gubbins, D., 1977. Three-dimensional seismic ray tracing. *J. Geophys* 43, 95–114.
- Julian, B.R., Miller, A.D., Foulger, G.R., 1998. Non-double-couple earthquakes 1. Theory. *Rev. Geophys.* 36, 525–549. doi:10.1029/98RG00716
- Kagan, Y.Y., 1991. 3-D rotation of double-couple earthquake sources. *Geophys. J. Int.* 106, 709–716. doi:10.1111/j.1365-246X.1991.tb06343.x
- Kagan, Y.Y., Jackson, D.D., 1995. New seismic gap hypothesis: Five years after. *J. Geophys. Res.* 100, 3943–3959. doi:10.1029/94JB03014
- Kagan, Y.Y., Jackson, D.D., Geller, R.J., 2012. Characteristic Earthquake Model, 1884–2011, R.I.P. *Seismol. Res. Lett.* 83, 951–953. doi:10.1785/0220120107
- Kanamori, H., 1972. Mechanism of tsunami earthquakes. *Phys. Earth. Planet. Inter.* 6, 346–359. doi:10.1016/0031-9201(72)90058-1
- Kanamori, H., Brodsky, E.E., 2004. The physics of earthquakes. *Rep. Prog. Phys.* 67, 1429–1496. doi:10.1088/0034-4885/67/8/R03
- Kanamori, H., Thio, H.-K., Dreger, D., Hauksson, E., Heaton, T., 1992. Initial investigation of the Landers, California, Earthquake of 28 June 1992 using TERRAScope. *Geophys. Res. Lett.* 19, 2267–2270. doi:10.1029/92GL02320
- Kato, A., Igarashi, T., Obara, K., Sakai, S., Takeda, T., Saiga, A., Iidaka, T., Iwasaki, T., Hirata, N., Goto, K., Miyamachi, H., Matsushima, T., Kubo, A., Katao, H., Yamanaka, Y., Terakawa, T., Nakamichi, H., Okuda, T., Horikawa, S., Tsumura, N., Umino, N., Okada, T., Kosuga, M., Takahashi, H., Yamada, T., 2013. Imaging the source regions of normal faulting sequences induced by the 2011 M9.0 Tohoku–Oki earthquake. *Geophys. Res. Lett.* 40, 273–278. doi:10.1002/grl.50104

- Kato, A., Iidaka, T., Ikuta, R., Yoshida, Y., Katsumata, K., Iwasaki, T., Sakai, S., Thurber, C.H., Tsumura, N., Yamaoka, K., Watanabe, T., Kunitomo, T., Yamazaki, F., Okubo, M., Suzuki, S., Hirata, N., 2010a. Variations of fluid pressure within the subducting oceanic crust and slow earthquakes. *Geophys. Res. Lett.* 37, L14310. doi:10.1029/2010GL043723
- Kato, A., Miyatake, T., Hirata, N., 2010b. Asperity and Barriers of the 2004 Mid-Niigata Prefecture Earthquake Revealed by Highly Dense Seismic Observations. *B. Seismol. Soc. Am.* 100, 298–306. doi:10.1785/0120090218
- Kato, A., Sakai, S., Obara, K., 2011. A normal-faulting seismic sequence triggered by the 2011 off the Pacific coast of Tohoku Earthquake: Wholesale stress regime changes in the upper plate. *Earth Planets Space*.
- Kelleher, J., McCann, W., 1976. Buoyant zones, great earthquakes, and unstable boundaries of subduction. *J. Geophys. Res.* 81, 4885–4896. doi:10.1029/JB081i026p04885
- Kelleher, J.A., 1972. Rupture zones of large South American earthquakes and some predictions. *J. Geophys. Res.* 77, 2087–2103. doi:10.1029/JB077i011p02087
- Kikuchi, M., Kanamori, H., 1991. Inversion of complex body waves—III. *B. Seismol. Soc. Am.* 81, 2335–2350.
- Kimura, G., Kitamura, Y., Hashimoto, Y., Yamaguchi, A., Shibata, T., Ujiie, K., Okamoto, S., 2007. Transition of accretionary wedge structures around the up-dip limit of the seismogenic subduction zone. *Earth Planet. Sci. Lett.* 255, 471–484. doi:10.1016/j.epsl.2007.01.005
- Kiser, E., Ishii, M., 2013. The 2010 Maule, Chile, Coseismic Gap and Its Relationship to the 25 March 2012 Mw 7.1 Earthquake. *B. Seismol. Soc. Am.* 103, 1148–1153. doi:10.1785/0120120209
- Kiser, E., Ishii, M., 2011. The 2010 Mw 8.8 Chile earthquake: Triggering on multiple segments and frequency-dependent rupture behavior. *Geophys. Res. Lett.* 38, L07301. doi:10.1029/2011GL047140
- Kissling, E., 1988. Geotomography with local earthquake data. *Rev. Geophys.* 26, 659. doi:10.1029/RG026i004p00659
- Kissling, E., Ellsworth, W.L., Eberhart-Phillips, D., Kradolfer, U., 1994. Initial reference models in local earthquake tomography. *J. Geophys. Res.* 99, 19635–19646. doi:10.1029/93JB03138
- Kissling, E., Kradolfer, U., Maurer, H., 1995. Program VELEST USERS GUIDE - Short Introduction.
- Kisslinger, C., 1980. Evaluation of S to P amplitude ratios for determining focal mechanisms from regional network observations. *B. Seismol. Soc. Am.* 70, 999–1014.
- Klingelhoefer, F., Gutscher, M.-A., Ladage, S., Dessa, J.-X., Graindorge, D., Franke, D., André, C., Permana, H., Yudistira, T., Chauhan, A., 2010. Limits of the seismogenic zone in the epicentral region of the 26 December 2004 great Sumatra-Andaman earthquake: Results from seismic refraction and wide-angle reflection surveys and thermal modeling. *J. Geophys. Res.*, 115, B01304, doi:10.1029/2009JB006569.

## References

- Knopoff, L., Randall, M.J., 1970. The compensated linear-vector dipole: A possible mechanism for deep earthquakes. *J. Geophys. Res.* 75, 4957–4963. doi:10.1029/JB075i026p04957
- Kodaira, S., Hori, T., Ito, A., Miura, S., Fujie, G., Park, J.-O., Baba, T., Sakaguchi, H., Kaneda, Y., 2006. A cause of rupture segmentation and synchronization in the Nankai trough revealed by seismic imaging and numerical simulation. *J. Geophys. Res.* 111, B09301. doi:10.1029/2005JB004030
- Kodaira, S., Iidaka, T., Kato, A., Park, J.-O., Iwasaki, T., Kaneda, Y., 2004. High pore fluid pressure may cause silent slip in the Nankai Trough. *Science* 304, 1295–1298. doi:10.1126/science.1096535
- Kodaira, S., No, T., Nakamura, Y., Fujiwara, T., Kaiho, Y., Miura, S., Takahashi, N., Kaneda, Y., Taira, A., 2012. Coseismic fault rupture at the trench axis during the 2011 Tohoku-oki earthquake. *Nature Geosci.* 5, 646–650. doi:10.1038/ngeo1547
- Kodaira, S., Takahashi, N., Nakanishi, A., Miura, S., Kaneda, Y., 2000. Subducted Seamount Imaged in the Rupture Zone of the 1946 Nankaido Earthquake. *Science*. doi:10.1126/science.289.5476.104
- Komatitsch, D., Erlebacher, G., Göldeke, D., Michéa, D., 2010. High-order finite-element seismic wave propagation modeling with MPI on a large GPU cluster. *Journal of Computational Physics* 229, 7692–7714. doi:10.1016/j.jcp.2010.06.024
- Komatitsch, D., Liu, Q., Tromp, J., Süß, P., Stidham, C., Shaw, J.H., 2004. Simulations of Ground Motion in the Los Angeles Basin Based upon the Spectral-Element Method. *B. Seismol. Soc. Am.* 94, 187–206. doi:10.1785/0120030077
- Koper, K.D., Hutko, A.R., Lay, T., Sufri, O., 2012. Imaging short-period seismic radiation from the 27 February 2010 Chile ( $M_w$  8.8) earthquake by back-projection of P, PP, and PKIKP waves. *J. Geophys. Res.* 117. doi:10.1029/2011JB008576
- Kopp, H., 2013. Invited review paper: The control of subduction zone structural complexity and geometry on margin segmentation and seismicity. *Tectonophysics* 589, 1–16. doi:10.1016/j.tecto.2012.12.037
- Kopp, H., Flueh, E.R., Petersen, C.J., Weinrebe, W., Wittwer, A., Meramex Scientists, 2006. The Java margin revisited: Evidence for subduction erosion off Java. *Earth Planet. Sci. Lett.* 242, 130–142. doi:10.1016/j.epsl.2005.11.036
- Krawczyk, C.M., Mechie, J., Lüth, S., Tašárová, Z., Wigger, P.J., Stiller, M., Brasse, H., Echtler, H.P., Araneda, M., Bataille, K., 2006. Geophysical Signatures and Active Tectonics at the South-Central Chilean Margin, in: *The Andes, Frontiers in Earth Sciences*. Springer Berlin Heidelberg, pp. 171–192. doi:10.1007/978-3-540-48684-8\_8
- Krischer, L., Fichtner, A., Zukauskaitė, S., Igel, H., 2015. Large-Scale Seismic Inversion Framework. *Seismol. Res. Lett.* doi:10.1785/0220140248
- Kubo, A., Fukuyama, E., Kawai, H., Nonomura, K., 2002. NIED seismic moment tensor catalogue for regional earthquakes around Japan: quality test and application. *Tectonophysics* 356, 23–48.
- Kumar, R., Gupta, S.C., Kumar, A., 2014. Effect of azimuthal coverage of an earthquake on moment tensor solutions estimated by waveform inversion. *Arab. J. Geosci.* 1–14. doi:10.1007/s12517-014-1666-6



- Lange, D., Bedford, J., Moreno, M., Tilmann, F., Baez, J.C., Bevis, M., Krüger, F., 2014. Comparison of postseismic afterslip models with aftershock seismicity for three subduction-zone earthquakes: Nias 2005, Maule 2010 and Tohoku 2011. *Geophys. J. Int.* 199, 784–799. doi:10.1093/gji/ggu292
- Lange, D., Tilmann, F., Barrientos, S.E., Contreras-Reyes, E., Methe, P., Moreno, M., Heit, B., Agurto, H., Bernard, P., Vilotte, J.-P., 2012. Aftershock seismicity of the 27 February 2010 Mw 8.8 Maule earthquake rupture zone. *Earth Planet. Sci. Lett.* 317–318, 413–425. doi:10.1016/j.epsl.2011.11.034
- Lange, D., Tilmann, F., Rietbrock, A., Collings, R., Natawidjaja, D.H., Suwargadi, B.W., Barton, P., Henstock, T., Ryberg, T., 2010. The Fine Structure of the Subducted Investigator Fracture Zone in Western Sumatra as Seen by Local Seismicity. *Earth Planet. Sci. Lett.* 298, 47–56.
- Lapusta, N., Rice, J.R., 2003. Nucleation and early seismic propagation of small and large events in a crustal earthquake model. *J. Geophys. Res.* 108, 2205. doi:10.1029/2001JB000793
- Lawson, C.L., Hanson, R.J., 1995. *Solving Least Squares Problems*. Society for Industrial and Applied Mathematics, Philadelphia. doi:10.1137/1.9781611971217
- Lay, T., 2015. The surge of great earthquakes from 2004 to 2014. *Earth Planet. Sci. Lett.* 409, 133–146. doi:10.1016/j.epsl.2014.10.047
- Lay, T., Ammon, C.J., Kanamori, H., Koper, K.D., Sufri, O., Hutko, A.R., 2010a. Teleseismic inversion for rupture process of the 27 February 2010 Chile ( $M_w$  8.8) earthquake. *Geophys. Res. Lett.* 37, L13301. doi:10.1029/2010GL043379
- Lay, T., Ammon, C.J., Kanamori, H., Rivera, L., Koper, K.D., Hutko, A.R., 2010b. The 2009 Samoa-Tonga great earthquake triggered doublet. *Nature* 466, 964–968. doi:10.1038/nature09214
- Lay, T., Ammon, C.J., Kanamori, H., Xue, L., Kim, M.J., 2011. Possible large near-trench slip during the 2011  $M_w$  9.0 off the Pacific coast of Tohoku Earthquake. *Earth Planets Space* 63, 687–692. doi:10.5047/eps.2011.05.033
- Lay, T., Duputel, Z., Ye, L., Kanamori, H., 2013. The December 7, 2012 Japan Trench intraplate doublet ( $M_w$  7.2, 7.1) and interactions between near-trench intraplate thrust and normal faulting. *Phys. Earth. Planet. Inter.* 220, 73–78. doi:10.1016/j.pepi.2013.04.009
- Lay, T., Kanamori, H., 1981. An asperity model of large earthquake sequences. *Earthquake Prediction*. doi:10.1029/ME004p0579
- Lay, T., Kanamori, H., Ammon, C.J., Koper, K.D., Hutko, A.R., Ye, L., Yue, H., Rushing, T.M., 2012. Depth-varying rupture properties of subduction zone megathrust faults. *J. Geophys. Res.* 117, B04311. doi:10.1029/2011JB009133
- Lee, S.J., Chan, Y.C., Komatitsch, D., Huang, B.S., Tromp, J., 2009. Effects of Realistic Surface Topography on Seismic Ground Motion in the Yangminshan Region of Taiwan Based Upon the Spectral-Element Method and LiDAR DTM. *B. Seismol. Soc. Am.* 99, 681–693. doi:10.1785/0120080264
- Lee, W.H.K., Valdes, C.M., 1985. HYPO71PC: A personal computer version of the HYPO71 earthquake location program. US Geological Survey Open-file Report 85.

## References

- Lees, J.M., Crosson, R.S., 1989. Tomographic inversion for three-dimensional velocity structure at Mount St. Helens using earthquake data. *J. Geophys. Res.* 94, 5716–5728. doi:10.1029/JB094iB05p05716
- Li, S., Moreno, M., Rosenau, M., Melnick, D., Oppenheimer, D.H., 2014. Splay fault triggering by great subduction earthquakes inferred from finite element models. *Geophys. Res. Lett.* 41, 385–391. doi:10.1002/2013GL058598
- Lieser, K., Grevemeyer, I., Lange, D., Flueh, E., Tilmann, F., Contreras Reyes, E., 2014. Splay fault activity revealed by aftershocks of the 2010 Mw 8.8 Maule earthquake, central Chile. *Geology* 42, 823–826.
- Lin, G., Shearer, P.M., Matoza, R.S., Okubo, P.G., Amelung, F., 2014. Three-dimensional seismic velocity structure of Mauna Loa and Kilauea volcanoes in Hawaii from local seismic tomography. *J. Geophys. Res. Solid Earth* 119, 4377–4392. doi:10.1002/2013JB010820
- Lin, Y.N., Sladen, A., Ortega-Culaciati, F., Simons, M., Avouac, J.-P., Fielding, E.J., Brooks, B.A., Bevis, M., Genrich, J., 2013. Coseismic and postseismic slip associated with the 2010 Maule Earthquake, Chile: Characterizing the Arauco Peninsula barrier effect. *J. Geophys. Res.* doi:10.1002/jgrb.50207
- Liu, Q., Tromp, J., 2006. Finite-Frequency Kernels Based on Adjoint Methods. *B. Seismol. Soc. Am.* 96, 2383–2397. doi:10.1785/0120060041
- Llenos, A.L., McGuire, J.J., 2007. Influence of fore-arc structure on the extent of great subduction zone earthquakes. *J. Geophys. Res.* 112, B09301. doi:10.1029/2007JB004944
- Lorito, S., Romano, F., Atzori, S., Tong, X., Avallone, A., McCloskey, J., Cocco, M., Piersanti, A., 2011. Limited overlap between the seismic gap and coseismic slip of the great 2010 Chile earthquake. *Nature Geosci.* 4, 173–177. doi:10.1038/NGEO1073
- Loveless, J.P., Pritchard, M.E., Kukowski, N., 2010. Testing mechanisms of subduction zone segmentation and seismogenesis with slip distributions from recent Andean earthquakes. *Tectonophysics* 495, 15–33. doi:10.1016/j.tecto.2009.05.008
- Lucassen, F., Trumbull, R., Franz, G., Creixell, C., Vásquez, P., Romer, R.L., Figueroa, O., 2004. Distinguishing crustal recycling and juvenile additions at active continental margins: the Paleozoic to recent compositional evolution of the Chilean Pacific margin (36–41°S). *J. S. Am. Earth Sci.* 17, 103–119. doi:10.1016/j.jsames.2004.04.002
- Madariaga, R., 1977. High-frequency radiation from crack (stress drop) models of earthquake faulting. *Geophys. J. Int.* 51, 625–651. doi:10.1111/j.1365-246X.1977.tb04211.x
- Maercklin, N., Zollo, A., Orefice, A., Festa, G., Emolo, A., De Matteis, R., Delouis, B., Bobbio, A., 2011. The Effectiveness of a Distant Accelerometer Array to Compute Seismic Source Parameters: The April 2009 L'Aquila Earthquake Case History. *B. Seismol. Soc. Am.* 101, 354–365. doi:10.1785/0120100124
- Magnoni, F., Casarotti, E., Michelini, A., 2014. Spectral-Element Simulations of Seismic Waves Generated by the 2009 L'Aquila Earthquake. *B. Seismol. Soc. Am.* 104, 73–94.

- Marone, C., 1998. Laboratory-derived friction laws and their application to seismic faulting. *Annu. Rev. Earth Planet. Sci.* 26, 643–696. doi:10.1146/annurev.earth.26.1.643
- Martin, M.W., Kato, T.T., Rodriguez, C., Godoy, E., Duhart, P., McDonough, M., Campos, A., 1999. Evolution of the late Paleozoic accretionary complex and overlying forearc-magmatic arc, south central Chile (38°–41°S): Constraints for the tectonic setting along the southwestern margin of Gondwana. *Tectonics* 18, 582–605. doi:10.1029/1999TC900021
- Matsumoto, Y., Ishikawa, T., Fujita, M., Sato, M., Saito, H., Mochizuki, M., Yabuki, T., Asada, A., 2008. Weak interplate coupling beneath the subduction zone off Fukushima, NE Japan, inferred from GPS/acoustic seafloor geodetic observation. *Earth Planets Space* 60, e9–e12. doi:10.1186/BF03353114
- McCaffrey, R., 1993. On the role of the upper plate in great subduction zone earthquakes. *J. Geophys. Res.* 98, 11953–11966. doi:10.1029/93JB00445
- McCaffrey, R., Goldfinger, C., 1995. Forearc Deformation and Great Subduction Earthquakes: Implications for Cascadia Offshore Earthquake Potential. *Science* 267, 856–859. doi:10.1126/science.267.5199.856
- Melnick, D., Bookhagen, B., Echtler, H., Strecker, M.R., 2006. Coastal deformation and great subduction earthquakes, Isla Santa Maria, Chile (37°S). *Geological Society of America Bulletin*. doi:10.1130/B25865
- Melnick, D., Bookhagen, B., Strecker, M.R., Echtler, H.P., 2009. Segmentation of megathrust rupture zones from fore-arc deformation patterns over hundreds to millions of years, Arauco peninsula, Chile. *J. Geophys. Res. Solid Earth* 114, B01407. doi:10.1029/2008JB005788
- Melnick, D., Echtler, H.P., 2006a. Inversion of forearc basins in south-central Chile caused by rapid glacial age trench fill. *Geology* 34, 709–712. doi:10.1130/G22440.1
- Melnick, D., Echtler, H.P., 2006b. Morphotectonic and Geologic Digital Map Compilations of the South-Central Andes (36°–42°S), in: *The Andes, Frontiers in Earth Sciences*. Springer Berlin Heidelberg, pp. 565–568. doi:10.1007/978-3-540-48684-8\_30
- Melnick, D., Moreno, M., Motagh, M., Cisternas, M., Wesson, R.L., 2012. Splay fault slip during the Mw 8.8 2010 Maule Chile earthquake. *Geology* 40, 251–254. doi:10.1130/G32712.1
- Meltzner, A.J., Sieh, K., Chiang, H.-W., Wu, C.-C., Tsang, L.L.H., Shen, C.-C., Hill, E.M., Suwargadi, B.W., Natawidjaja, D.H., Philipposian, B., Briggs, R.W., 2015. Time-varying interseismic strain rates and similar seismic ruptures on the Nias–Simeulue patch of the Sunda megathrust. *Quat. Sci. Rev.* 122, 258–281.
- Meng, L., Inbal, A., Ampuero, J.-P., 2011. A window into the complexity of the dynamic rupture of the 2011 Mw 9 Tohoku-Oki earthquake. *Geophys. Res. Lett.* 38, L00G07. doi:10.1029/2011GL048118
- Métois, M., Socquet, A., Vigny, C., 2012. Interseismic coupling, segmentation and mechanical behavior of the central Chile subduction zone. *J. Geophys. Res.* 117, B03406. doi:10.1029/2011JB008736
- Métois, M., Socquet, A., Vigny, C., Carrizo, D., Peyrat, S., Delorme, A., Maureira, E.,

## References

- Valderas-Bermejo, M.C., Ortega, I., 2013. Revisiting the North Chile seismic gap segmentation using GPS-derived interseismic coupling. *Geophys. J. Int.* 194, 1283–1294. doi:10.1093/gji/ggt183
- Michael, A.J., Eberhart-Phillips, D., 1991. Relations among fault behavior, subsurface geology, and three-dimensional velocity models. *Science* 253, 651–654.
- Mochizuki, K., Yamada, T., Shinohara, M., Yamanaka, Y., Kanazawa, T., 2008. Weak Interplate Coupling by Seamounts and Repeating  $M \sim 7$  Earthquakes. *Science* 321, 1194–1197. doi:10.1126/science.1160250
- Mogi, K., 1969. Relationship between the Occurrence of Great Earthquakes and Tectonic Structures. *Bull. Earthquake Res. Inst.* 47, 429–451.
- Moore, J.C., Saffer, D.M., 2001. Updip limit of the seismogenic zone beneath the accretionary prism of southwest Japan: An effect of diagenetic to low-grade metamorphic processes and increasing effective stress. *Geology* 29, 183–186. doi:10.1130/0091-7613(2001)029<0183:ULOTSZ>2.0.CO;2
- Moreno, M., Bolte, J., Klotz, J., Melnick, D., 2009. Impact of megathrust geometry on inversion of coseismic slip from geodetic data: Application to the 1960 Chile earthquake. *Geophys. Res. Lett.* 36, L16310. doi:10.1029/2009GL039276
- Moreno, M., Haberland, C., Oppenheimer, D.H., Rietbrock, A., Angiboust, S., Heidbach, O., 2014. Locking of the Chile subduction zone controlled by fluid pressure before the 2010 earthquake. *Nature Geosci.* 7, 292–296. doi:10.1038/ngeo2102
- Moreno, M., Melnick, D., Rosenau, M., Baez, J.C., Klotz, J., Oppenheimer, D.H., Tassara, A., Chen, J., Bataille, K., Bevis, M., Socquet, A., Bolte, J., Vigny, C., Brooks, B., Ryder, I.M.A., Grund, V., Smalley, R., Carrizo, D., Bartsch, M., Hase, H., 2012. Toward understanding tectonic control on the Mw 8.8 2010 Maule Chile earthquake. *Earth Planet. Sci. Lett.* 321–322, 152–165. doi:10.1016/j.epsl.2012.01.006
- Moreno, M., Melnick, D., Rosenau, M., Bolte, J., Klotz, J., Echtler, H., Baez, J.C., Bataille, K., Chen, J., Bevis, M., Hase, H., Oppenheimer, D.H., 2011. Heterogeneous plate locking in the South–Central Chile subduction zone: Building up the next great earthquake. *Earth Planet. Sci. Lett.* 305, 413–424. doi:10.1016/j.epsl.2011.03.025
- Moreno, M., Rosenau, M., 2010. 2010 Maule earthquake slip correlates with pre-seismic locking of Andean subduction zone. *Nature* 467, 198–202. doi:10.1038/nature09349
- Morrow, C.A., Shi, L.Q., Byerlee, J.D., 1982. Strain hardening and strength of clay-rich fault gouges. *J. Geophys. Res.* 87, 6771. doi:10.1029/JB087iB08p06771
- MoscOSO, E., Grevemeyer, I., Contreras-Reyes, E., Flueh, E.R., Dzierma, Y., Rabbel, W., Thorwart, M., 2011. Revealing the deep structure and rupture plane of the 2010 Maule, Chile earthquake (Mw = 8.8) using wide angle seismic data. *Earth Planet. Sci. Lett.* 307, 147–155. doi:10.1016/j.epsl.2011.04.025
- Müller, R.D., Landgrebe, T.C.W., 2012. The link between great earthquakes and the subduction of oceanic fracture zones. *Solid Earth* 3, 447–465. doi:10.5194/se-3-447-2012
- Müller, R.D., Sdrolias, M., Gaina, C., Roest, W.R., 2008. Age, spreading rates, and

- spreading asymmetry of the world's ocean crust. *Geochem., Geophys., Geosyst.* 9, Q04006. doi:10.1029/2007GC001743
- Nakajima, J., Matsuzawa, T., Hasegawa, A., 2002. Moho depth variation in the central part of northeastern Japan estimated from reflected and converted waves. *Phys. Earth. Planet. Inter.* 130, 31–47. doi:10.1016/S0031-9201(01)00307-7
- Nakamura, Y., Kodaira, S., Miura, S., Regalla, C., Takahashi, N., 2013. High-resolution seismic imaging in the Japan Trench axis area off Miyagi, northeastern Japan. *Geophys. Res. Lett.* 49, 1713–1718. doi:doi:10.1002/grl.50364
- Nippress, S.E.J., Rietbrock, A., Heath, A.E., 2010. Optimized automatic pickers: Application to the ANCORP data set. *Geophys. J. Int.* 181, 911–925.
- Nishimura, T., Hirasawa, T., Miyazaki, S., Sagiya, T., Tada, T., Miura, S., Tanaka, K., 2004. Temporal change of interplate coupling in northeastern Japan during 1995–2002 estimated from continuous GPS observations. *Geophys. J. Int.* 157, 901–916. doi:10.1111/j.1365-246X.2004.02159.x
- Okada, T., Hasegawa, A., Suganomata, J., Zhao, D., Zhang, H., Thurber, C.H., 2007. Imaging the source area of the 1995 southern Hyogo (Kobe) earthquake (M7.3) using double-difference tomography. *Earth Planet. Sci. Lett.* 253, 143–150.
- Okada, Y., 1992. Internal deformation due to shear and tensile faults in a half-space. *B. Seismol. Soc. Am.* 82, 1018–1040.
- Okamura, Y., Tsujino, T., Arai, K., Sasaki, T., Satake, K., Joshima, M., 2008. Fore arc structure and plate boundary earthquake sources along the southwestern Kuril subduction zone. *J. Geophys. Res.* 113, B06305. doi:10.1029/2007JB005246
- Oleskevich, D.A., Hyndman, R.D., Wang, K., 1999. The updip and downdip limits to great subduction earthquakes: Thermal and structural models of Cascadia, south Alaska, SW Japan, and Chile. *J. Geophys. Res.* 104, 14965–14991.
- Olsen, K.B., Day, S.M., Minster, J.B., Cui, Y., Chourasia, A., Faerman, M., Moore, R., Maechling, P., Jordan, T., 2006. Strong shaking in Los Angeles expected from southern San Andreas earthquake. *Geophys. Res. Lett.* 33, L07305. doi:10.1029/2005GL025472
- Ozawa, S., Nishimura, T., Suito, H., Kobayashi, T., Tobita, M., Imakiire, T., 2011. Coseismic and postseismic slip of the 2011 magnitude-9 Tohoku-Oki earthquake. *Nature* 475, 373–376. doi:10.1038/nature10227
- Pacheco, J.F., Sykes, L.R., 1992. Seismic moment catalog of large shallow earthquakes, 1900 to 1989. *B. Seismol. Soc. Am.* 82, 1306–1349.
- Palo, M., Tilmann, F., Krüger, F., Ehlert, L., Lange, D., 2014. High-frequency seismic radiation from Maule earthquake (Mw 8.8, 2010 February 27) inferred from high-resolution backprojection analysis. *Geophys. J. Int.* 199, 1058–1077. doi:10.1093/gji/ggu311
- Parada, M.A., Nyström, J.O., Levi, B., 1999. Multiple sources for the Coastal Batholith of central Chile (31–34°S): geochemical and Sr–Nd isotopic evidence and tectonic implications. *Lithos* 46, 505–521. doi:10.1016/S0024-4937(98)00080-2
- Park, J.-O., Fujie, G., Wijerathne, L., Hori, T., Kodaira, S., Fukao, Y., Moore, G.F., Bangs, N.L.B., Kuramoto, S., Taira, A., 2010. A low-velocity zone with weak

## References

- reflectivity along the Nankai subduction zone. *Geology* 38, 283–286. doi:10.1130/G30205.1
- Park, J.-O., Moore, G.F., Tsuru, T., Kodaira, S., Kaneda, Y., 2004. A subducted oceanic ridge influencing the Nankai megathrust earthquake rupture. *Earth Planet. Sci. Lett.* 217, 77–84. doi:10.1016/S0012-821X(03)00553-3
- Park, J.-O., Tsuru, T., Kodaira, S., Cummins, P.R., Kaneda, Y., 2002. Splay Fault Branching Along the Nankai Subduction Zone. *Science* 297, 1157–1160. doi:10.1126/science.1074111
- Pavlis, G.L., Booker, J.R., 1980. The mixed discrete-continuous inverse problem: Application to the simultaneous determination of earthquake hypocenters and velocity structure. *J. Geophys. Res.* 85, 4801–4810. doi:10.1029/JB085iB09p04801
- Pavlis, N.K., Holmes, S.A., Kenyon, S.C., Factor, J.K., 2008. An earth gravitational model to degree 2160: EGM2008. *Geophys. Res. Abstr.* 10.
- Peacock, S.M., 2001. Are the lower planes of double seismic zones caused by serpentine dehydration in subducting oceanic mantle? *Geology* 29, 299–302. doi:10.1130/0091-7613(2001)029<0299:ATLPOD>2.0.CO;2
- Pereyra, V., Lee, W.H.K., Keller, H.B., 1980. Solving two-point seismic-ray tracing problems in a heterogeneous medium Part 1. A general adaptive finite difference method. *B. Seismol. Soc. Am.* 70, 79–99.
- Perfettini, H., Avouac, J.-P., Tavera, H., Kositsky, A., Nocquet, J.M., Bondoux, F., Chlieh, M., Sladen, A., Audin, L., Farber, D.L., Soler, P., 2010. Seismic and aseismic slip on the Central Peru megathrust. *Nature* 465, 78–81. doi:10.1038/nature09062
- Peter, D., Komatitsch, D., Luo, Y., Martin, R., Le Goff, N., Casarotti, E., Le Loher, P., Magnoni, F., Liu, Q., Blitz, C., Nissen-Meyer, T., Basini, P., Tromp, J., 2011. Forward and adjoint simulations of seismic wave propagation on fully unstructured hexahedral meshes. *Geophys. J. Int.* 186, 721–739. doi:10.1111/j.1365-246X.2011.05044.x
- Pollitz, F.F., Brooks, B., Tong, X., Bevis, M.G., Foster, J.H., Bürgmann, R., Smalley, R., Vigny, C., Socquet, A., Ruegg, J.C., Campos, J., Barrientos, S.E., Parra, H., Soto, J.C.B., Cimbaro, S., Blanco, M., 2011. Coseismic slip distribution of the February 27, 2010 Mw 8.8 Maule, Chile earthquake. *Geophys. Res. Lett.* 38, L09309. doi:10.1029/2011GL047065
- Protti, M., González, V., Newman, A.V., Dixon, T.H., Schwartz, S.Y., Marshall, J.S., Feng, L., Walter, J.I., Malservisi, R., Owen, S.E., 2014. Nicoya earthquake rupture anticipated by geodetic measurement of the locked plate interface. *Nature Geosci.* 7, 117–121. doi:10.1038/ngeo2038
- Quintero, R., Zahradnik, J., Sokos, E.N., 2014. Near-regional CMT and multiple-point source solution of the September 5, 2012, Nicoya, Costa Rica Mw 7.6 (GCMT) earthquake. *J. S. Am. Earth Sci.* 55, 155–165. doi:10.1016/j.jsames.2014.07.009
- Ramachandran, K., Hyndman, R.D., Brocher, T.M., 2006. Regional P wave velocity structure of the Northern Cascadia Subduction Zone. *J. Geophys. Res.* 111, B12301. doi:10.1029/2005JB004108
- Ramos-Martínez, J., McMechan, G.A., 2001. Source-Parameter Estimation by Full

- Waveform Inversion in 3D Heterogeneous, Viscoelastic, Anisotropic Media. *B. Seismol. Soc. Am.* 91, 276–291. doi:10.1785/0120000017
- Ranero, C.R., Grevemeyer, I., Sahling, H., Barckhausen, U., Hensen, C., Wallmann, K., Weinrebe, W., Vannucchi, P., Huene, Von, R., McIntosh, K., 2008. Hydrogeological system of erosional convergent margins and its influence on tectonics and interplate seismogenesis. *Geochem., Geophys., Geosyst.* 9, Q03S04. doi:10.1029/2007GC001679
- Ranero, C.R., Huene, Von, R., 2000. *Nature* 404, 748–752. doi:10.1038/35008046
- Rawlinson, N., Pozgay, S., Fishwick, S., 2010. Seismic tomography: A window into deep Earth. *Phys. Earth. Planet. Inter.* 178, 101–135. doi:10.1016/j.pepi.2009.10.002
- Rea, D.K., Ruff, L.J., 1996. Composition and mass flux of sediment entering the world's subduction zones: Implications for global sediment budgets, great earthquakes, and volcanism. *Earth Planet. Sci. Lett.* 140, 1–12. doi:10.1016/0012-821X(96)00036-2
- Reyners, M., Eberhart-Phillips, D., Stuart, G., Nishimura, Y., 2006. Imaging subduction from the trench to 300 km depth beneath the central North Island, New Zealand, with Vp and Vp/Vs. *Geophys. J. Int.* 165, 565–583. doi:10.1111/j.1365-246X.2006.02897.x
- Rietbrock, A., Ryder, I.M.A., Hayes, G., Haberland, C., Comte, D., Roecker, S.W., Lyon-Caen, H., 2012. Aftershock seismicity of the 2010 Maule Mw= 8.8, Chile, earthquake: Correlation between co-seismic slip models and aftershock distribution? *Geophys. Res. Lett.* 39, L08310. doi:10.1029/2012GL051308
- Rivera, L., Kanamori, H., 2014. Diagnosing Source Geometrical Complexity of Large Earthquakes. *Pure. Appl. Geophys.* 171, 2819–2840. doi:10.1007/s00024-013-0769-4
- Robinson, D.P., Das, S., Watts, A.B., 2006. Earthquake rupture stalled by a subducting fracture zone. *Science* 312, 1203–1205. doi:10.1126/science.1125771
- Roecker, S.W., 1981. Seismicity and tectonics of the Pamir-Hindu Kush region of central Asia. Cambridge.
- Romanowicz, B.A., 1982. Moment tensor inversion of long period Rayleigh waves: A new approach. *J. Geophys. Res.* 87, 5395. doi:10.1029/JB087iB07p05395
- Ruegg, J.C., Rudloff, A., Vigny, C., Madariaga, R., De Chabaliér, J.B., Campos, J., Kausel, E., Barrientos, S.E., Dimitrov, D., 2009. Interseismic strain accumulation measured by GPS in the seismic gap between Constitución and Concepción in Chile. *Phys. Earth. Planet. Inter.* 175, 78–85. doi:10.1016/j.pepi.2008.02.015
- Ruff, L.J., 1989. Do Trench Sediments Affect Great Earthquake Occurrence in Subduction Zones?, in: Ruff, L.J., Kanamori, H. (Eds.), *Pageoph Topical Volumes*. Birkhäuser Basel, Basel, pp. 263–282–282. doi:10.1007/978-3-0348-9140-0\_9
- Ruff, L.J., Kanamori, H., 1983. Seismic coupling and uncoupling at subduction zones. *Tectonophysics* 99, 99–117. doi:10.1016/0040-1951(83)90097-5
- Ruff, L.J., Kanamori, H., 1980. Seismicity and the subduction process. *Phys. Earth. Planet. Inter.* 23, 240–252. doi:10.1016/0031-9201(80)90117-X

## References

- Ruff, L.J., Tichelaar, B.W., 1996. What Controls the Seismogenic Plate Interface in Subduction Zones?, Subduction Top to Bottom, Geophysical Monograph Series. American Geophysical Union, Washington, D. C. doi:10.1029/GM096p0105
- Ruiz, S., Grandin, R., Dionicio, V., Satriano, C., Fuenzalida, A., Vigny, C., Kiraly, E., Meyer, C., Baez, J.C., Riquelme, S., Madariaga, R., Campos, J., 2013. The Constitución earthquake of 25 March 2012: A large aftershock of the Maule earthquake near the bottom of the seismogenic zone. *Earth Planet. Sci. Lett.* doi:10.1016/j.epsl.2013.07.017
- Ryder, I.M.A., Kelson, K., Bürgmann, R., Floyd, M., Socquet, A., Vigny, C., Carrizo, D., 2012. Large extensional aftershocks in the continental forearc triggered by the 2010 Maule earthquake, Chile. *Geophys. J. Int.* 188, 879–890. doi:10.1111/j.1365-246X.2011.05321.x
- Saffer, D.M., Marone, C., 2003. Comparison of smectite- and illite-rich gouge frictional properties: application to the updip limit of the seismogenic zone along subduction megathrusts. *Earth Planet. Sci. Lett.* 215, 219–235. doi:10.1016/S0012-821X(03)00424-2
- Saffer, D.M., Tobin, H.J., 2011. Hydrogeology and Mechanics of Subduction Zone Forearcs: Fluid Flow and Pore Pressure. *Annu. Rev. Earth Planet. Sci.* 39, 157–186. doi:10.1146/annurev-earth-040610-133408
- Sage, F., Collot, J.Y., Ranero, C.R., 2006. Interplate patchiness and subduction-erosion mechanisms: Evidence from depth-migrated seismic images at the central Ecuador convergent margin. *Geology* 34, 997. doi:10.1130/G22790A.1
- Sallarès, V., 2005. Structure and tectonics of the erosional convergent margin off Antofagasta, north Chile (23°30'S). *J. Geophys. Res.* 110, B06101. doi:10.1029/2004JB003418
- Satake, K., 1985. Effects of station coverage on moment tensor inversion. *B. Seismol. Soc. Am.* 75, 1657–1667.
- Savage, J.C., 1995. Interseismic uplift at the Nankai subduction zone, southwest Japan, 1951–1990. *J. Geophys. Res.* 100, 6339–6350. doi:10.1029/95JB00242
- Scholl, D.W., Huene, Von, R., Vallier, T.L., Howell, D.G., 1980. Sedimentary masses and concepts about tectonic processes at underthrust ocean margins. *Geology* 8, 564–568. doi:10.1130/0091-7613(1980)8<564:SMACAT>2.0.CO;2
- Scholz, C.H., 1998. Earthquakes and friction laws. *Nature* 391, 37–42. doi:10.1038/34097
- Scholz, C.H., Small, C., 1997. The effect of seamount subduction on seismic coupling. *Geology* 25, 487–490. doi:10.1130/0091-7613(1997)025<0487:TEOSSO>2.3.CO;2
- Schwartz, S.Y., Rokosky, J.M., 2007. Slow slip events and seismic tremor at circum-Pacific subduction zones. *Rev. Geophys.* 45, RG3004. doi:10.1029/2006RG000208
- Seriani, G., Carcione, J.M., Priolo, E., 1992. Numerical simulation of interface waves by high-order spectral modeling techniques. *J. Acoust. Soc. Am.* 92, 2456. doi:10.1121/1.404528
- Sernageomin, 2003. Mapa Geológico de Chile: versión digital. Servicio Nacional de



- Geología y Minería, Santiago, Chile.
- Sieh, K., Natawidjaja, D.H., 2000. Neotectonics of the Sumatran fault, Indonesia. *J. Geophys. Res.* 105, 28295–28326. doi:10.1029/2000JB900120
- Sieh, K., Natawidjaja, D.H., Meltzner, A.J., Shen, C.C., Cheng, H., Li, K.S., Suwargadi, B.W., Galetzka, J., Philiposian, B., Edwards, R.L., 2008. Earthquake Supercycles Inferred from Sea-Level Changes Recorded in the Corals of West Sumatra. *Science* 322, 1674–1678. doi:10.1126/science.1163589
- Simoes, M., Avouac, J.-P., Cattin, R., Henry, P., 2004. The Sumatra subduction zone: A case for a locked fault zone extending into the mantle. *J. Geophys. Res.* 109, B10402. doi:10.1029/2003JB002958
- Simons, M., Minson, S.E., Sladen, A., Ortega-Culaciati, F., Jiang, J., Owen, S.E., Meng, L., Ampuero, J.-P., Wei, S., Chu, R., Helmberger, D.V., Kanamori, H., Hetland, E., Moore, A.W., Webb, F.H., 2011. The 2011 magnitude 9.0 Tohoku-Oki earthquake: mosaicking the megathrust from seconds to centuries. *Science* 332, 1421–1425. doi:10.1126/science.1206731
- Singh, S.C., Hananto, N., Mukti, M., Robinson, D.P., Das, S., Chauhan, A., Carton, H., Gratacos, B., Midnet, S., Djajadihardja, Y., Harjono, H., 2011a. Aseismic zone and earthquake segmentation associated with a deep subducted seamount in Sumatra. *Nature Geosci.* 4, 308–311. doi:10.1038/ngeo1119
- Singh, S.C., Hananto, N.D., Chauhan, A.P.S., 2011b. Enhanced reflectivity of backthrusts in the recent great Sumatran earthquake rupture zones. *Geophys. Res. Lett.* 38, L04302. doi:10.1029/2010GL046227
- Singh, S.C., Hananto, N.D., Chauhan, A.P.S., Permana, H., Denolle, M., Hendriyana, A., Natawidjaja, D.H., 2010. Evidence of active backthrusting at the NE Margin of Mentawai Islands, SW Sumatra. *Geophys. J. Int.* 180, 703–714. doi:10.1111/j.1365-246X.2009.04458.x
- Sipkin, S.A., 1986. Interpretation of non-double-couple earthquake mechanisms derived from moment tensor inversion. *J. Geophys. Res.* 91, 531–547. doi:10.1029/JB091iB01p00531
- Smith, G. L., McNeill, L. C., Wang, K., He, J., Henstock, T.J., 2013. Thermal structure and megathrust seismogenic potential of the Makran subduction zone, *Geophys. Res. Lett.*, 40, 1528–1533. doi:10.1002/grl.50374
- Snoke, J.A., 2003. FOCMEC: focal mechanism determinations, in: Lee, W.H.K., Kanamori, H., Jennings, P., Kisslinger, C. (Eds.), *International Handbook of Earthquake Engineering Seismology, Part B*. Academic Press, San Diego, San Diego, pp. 1629–1630.
- Sobiesiak, M., Meyer, U., Schmidt, S., Götze, H.J., Krawczyk, C.M., 2007. Asperity generating upper crustal sources revealed by b value and isostatic residual anomaly grids in the area of Antofagasta, Chile. *J. Geophys. Res.* 112, B12308. doi:10.1029/2006JB004796
- Sokos, E.N., Zahradnik, J., 2013. Evaluating Centroid-Moment-Tensor Uncertainty in the New Version of ISOLA Software. *Seismol. Res. Lett.* 84, 656–665. doi:10.1785/0220130002
- Sokos, E.N., Zahradnik, J., 2007. ISOLA a Fortran code and a Matlab GUI to perform

- multiple-point source inversion of seismic data. *Comput. Geosci.* 34, 967–977.
- Sokos, E.N., Zahradnik, J., 2006. A Matlab GUI for use with ISOLA Fortran codes. Users' guide.
- Sokos, E.N., Zahradnik, J., Kiratzi, A., Janský, J., Gallovic, F., Novotny, O., Kostelecký, J., Serpetsidaki, A., Tselentis, G.-A., 2012. The January 2010 Efpalio earthquake sequence in the western Corinth Gulf (Greece). *Tectonophysics* 530–531, 299–309. doi:10.1016/j.tecto.2012.01.005
- Song, T.-R.A., Simons, M., 2003. Large trench-parallel gravity variations predict seismogenic behavior in subduction zones. *Science* 301, 630. doi:10.1126/science.1085557
- Sparkes, R., Tilmann, F., Hovius, N., Hillier, J., 2010. Subducted seafloor relief stops rupture in South American great earthquakes: Implications for rupture behaviour in the 2010 Maule, Chile earthquake. *Earth Planet. Sci. Lett.* 298, 89–94. doi:10.1016/j.epsl.2010.07.029
- Spencer, C., Gubbins, D., 1980. Travel-time inversion for simultaneous earthquake location and velocity structure determination in laterally varying media. *Geophys. J. Int.* 63, 95–116. doi:10.1111/j.1365-246X.1980.tb02612.x
- Spinelli, G.A., Saffer, D.M., Underwood, M.B., 2006. Hydrogeologic responses to three-dimensional temperature variability, Costa Rica subduction margin. *J. Geophys. Res.* 111, B04403. doi:10.1029/2004JB003436
- Spudich, P., Orcutt, J., 1980. Petrology and porosity of an oceanic crustal site: Results from wave form modeling of seismic refraction data. *J. Geophys. Res.* 85, 1409–1433. doi:10.1029/JB085iB03p01409
- Stern, T.A., Davey, F.J., 1990. Deep seismic expression of a foreland basin: Taranaki basin, New Zealand. *Geology* 18, 979–982. doi:10.1130/0091-7613(1990)018<0979:DSEOAF>2.3.CO;2
- Strasser, M., Moore, G.F., Kimura, G., Kitamura, Y., Kopf, A.J., Lallemand, S., Park, J.-O., Screaton, E.J., Su, X., Underwood, M.B., Zhao, X., 2009. Origin and evolution of a splay fault in the Nankai accretionary wedge. *Nature Geosci.* 2, 648–652. doi:10.1038/ngeo609
- Sykes, L.R., 1971. Aftershock zones of great earthquakes, seismicity gaps, and earthquake prediction for Alaska and the Aleutians. *J. Geophys. Res.* 76, 8021–8041. doi:10.1029/JB076i032p08021
- Šílený, J., Milev, A., 2008. Source mechanism of mining induced seismic events — Resolution of double couple and non double couple models. *Tectonophysics* 456, 3–15. doi:10.1016/j.tecto.2006.09.021
- Tape, C., Liu, Q., Maggi, A., Tromp, J., 2010. Seismic tomography of the southern California crust based on spectral-element and adjoint methods. *Geophys. J. Int.* 180, 433–462.
- Tape, C., Liu, Q., Maggi, A., Tromp, J., 2009. Adjoint tomography of the southern California crust. *Science* 325, 988–992. doi:10.1126/science.1175298
- Tassara, A., 2010. Control of forearc density structure on megathrust shear strength along the Chilean subduction zone. *Tectonophysics* 495, 34–47. doi:10.1016/j.tecto.2010.06.004

- Tassara, A., Echaurren, A., 2012. Anatomy of the Andean subduction zone: Three-dimensional density model upgraded and compared against global-scale models. *Geophys. J. Int.* 189, 161–168.
- Thurber, C.H., 1993. Local earthquake tomography: velocities and  $V_p/V_s$ -theory, in: Iyer, H.M., Hirahara, K. (Eds.), *Seismic Tomography - Theory and Practice*. Chapman and Hall, London, pp. 563–583.
- Thurber, C.H., 1992. Hypocenter-velocity structure coupling in local earthquake tomography. *Phys. Earth. Planet. Inter.* 75, 55–62. doi:10.1016/0031-9201(92)90117-E
- Thurber, C.H., 1986. Analysis methods for kinematic data from local earthquakes. *Rev. Geophys.* 24, 793. doi:10.1029/RG024i004p00793
- Thurber, C.H., 1983. Earthquake locations and three-dimensional crustal structure in the Coyote Lake area, central California. *J. Geophys. Res.* 88, 8226–8236. doi:10.1029/JB088iB10p08226
- Thurber, C.H., Eberhart-Phillips, D., 1999. Local earthquake tomography with flexible gridding. *Comput. Geosci.* 25, 809–818. doi:10.1016/S0098-3004(99)00007-2
- Toda, S., Stein, R.S., Richards-Dinger, K., Bozkurt, S.B., 2005. Forecasting the evolution of seismicity in southern California: Animations built on earthquake stress transfer. *J. Geophys. Res.* 110, B05S16. doi:10.1029/2004JB003415
- Toda, S., Tsutsumi, H., 2013. Simultaneous Reactivation of Two, Subparallel, Inland Normal Faults during the Mw 6.6 11 April 2011 Iwaki Earthquake Triggered by the Mw 9.0 Tohoku-oki, Japan, Earthquake. *B. Seismol. Soc. Am.* 103, 1584–1602. doi:10.1785/0120120281
- Tong, X., Sandwell, D., Luttrell, K., Brooks, B., Bevis, M., Shimada, M., Foster, J., Smalley, R., Parra, H., Báez Soto, J.C., Blanco, M., Kendrick, E., Genrich, J., Caccamise, D.J., 2010. The 2010 Maule, Chile earthquake: Downdip rupture limit revealed by space geodesy. *Geophys. Res. Lett.* 37, L24311. doi:10.1029/2010GL045805
- Toomey, D.R., Foulger, G.R., 1989. Tomographic inversion of local earthquake data from the Hengill-Grensdalur Central Volcano Complex, Iceland. *J. Geophys. Res.* 94, 17497–17510. doi:10.1029/JB094iB12p17497
- Trehu, A.M., Blakely, R.J., Williams, M.C., 2012. Subducted seamounts and recent earthquakes beneath the central Cascadia forearc. *Geology* 40, 103–106. doi:10.1130/G32460.1
- Tromp, J., Tape, C., Liu, Q., 2005. Seismic tomography, adjoint methods, time reversal and banana-doughnut kernels. *Geophys. J. Int.* 160, 195–216. doi:10.1111/j.1365-246X.2004.02453.x
- Tsai, V.C., Nettles, M., Ekström, G., Dziewonski, A.M., 2005. Multiple CMT source analysis of the 2004 Sumatra earthquake. *Geophys. Res. Lett.* 32, L17304. doi:10.1029/2005GL023813
- Tsuji, T., Ito, Y., Kido, M., Osada, Y., Fujimoto, H., Ashi, J., Kinoshita, M., Matsuoka, T., 2011. Potential tsunamigenic faults of the 2011 off the Pacific coast of Tohoku Earthquake. *Earth Planets Space* 63, 831–834. doi:10.5047/eps.2011.05.028
- Tsuji, T., Kawamura, K., Kanamatsu, T., Kasaya, T., Fujikura, K., Ito, Y., Tsuru, T.,

## References

- Kinoshita, M., 2013. Extension of continental crust by anelastic deformation during the 2011 Tohoku-oki earthquake: The role of extensional faulting in the generation of a great tsunami. *Earth Planet. Sci. Lett.* 364, 44–58. doi:10.1016/j.epsl.2012.12.038
- Tsuji, T., Tokuyama, H., Costa Pisani, P., Moore, G.F., 2008. Effective stress and pore pressure in the Nankai accretionary prism off the Muroto Peninsula, southwestern Japan. *J. Geophys. Res.* 113, B11401. doi:10.1029/2007JB005002
- Udías, A., Madariaga, R., Bufo, E., 2014. Source mechanisms of earthquakes. Cambridge University Press, Cambridge.
- Ueno, T., Shibutani, T., Ito, K., 2008. Configuration of the Continental Moho and Philippine Sea Slab in Southwest Japan Derived from Receiver Function Analysis: Relation to Subcrustal Earthquakes. *B. Seismol. Soc. Am.* 98, 2416–2427. doi:10.1785/0120080016
- Um, J., Thurber, C.H., 1987. A fast algorithm for two-point seismic ray tracing. *B. Seismol. Soc. Am.* 77, 972–986.
- United States Geological Survey National Earthquake Information Center, 2011. M7.2 - Araucania, Chile [WWW Document]. URL [http://earthquake.usgs.gov/earthquakes/eventpage/usp000hsfq#scientific\\_tensor](http://earthquake.usgs.gov/earthquakes/eventpage/usp000hsfq#scientific_tensor) (accessed 5.24.15).
- United States Geological Survey National Earthquake Information Center, 2014. Earthquakes with 1,000 or More Deaths 1900-2014 [WWW Document]. URL [http://earthquake.usgs.gov/earthquakes/world/world\\_deaths.php](http://earthquake.usgs.gov/earthquakes/world/world_deaths.php) (accessed 8.1e.15).
- Vallée, M., Bouchon, M., 2004. Imaging coseismic rupture in far field by slip patches. *Geophys. J. Int.* 156, 615–630. doi:10.1111/j.1365-246X.2004.02158.x
- Vannucchi, P., Remitti, F., Bettelli, G., 2008. Geological record of fluid flow and seismogenesis along an erosive subducting plate boundary. *Nature* 451, 699–703. doi:10.1038/nature06486
- Vásquez, P., Franz, G., 2008. The Triassic Cobquecura Pluton (Central Chile): An example of a fayalite-bearing A-type intrusive massif at a continental margin. *Tectonophysics* 459, 66–84. doi:10.1016/j.tecto.2007.11.067
- Vásquez, P., Glodny, J., Franz, G., Frei, D., Romer, R.L., 2011. Early Mesozoic Plutonism of the Cordillera de la Costa (34°–37°S), Chile: Constraints on the Onset of the Andean Orogeny. *J. Geol.* 119, 159–184. doi:10.1086/658296
- Victor, P., Sobiesiak, M., Glodny, J., Nielsen, S.N., Oppenheimer, D.H., 2011. Long-term persistence of subduction earthquake segment boundaries: Evidence from Mejillones Peninsula, northern Chile. *J. Geophys. Res.* 116, B02402. doi:10.1029/2010JB007771
- Vigny, C., Socquet, A., Peyrat, S., Ruegg, J.C., Métois, M., Madariaga, R., Morvan, S., Lancieri, M., Lacassin, R., Campos, J., Carrizo, D., Bejar-Pizarro, M., Barrientos, S.E., Armijo, R., Aranda, C., Valderas-Bermejo, M.C., Ortega, I., Bondoux, F., Baize, S., Lyon-Caen, H., Pavez, A., Vilotte, J.-P., Bevis, M., Brooks, B., Smalley, R., Parra, H., Baez, J.C., Blanco, M., Cimbaro, S., Kendrick, E., 2011. The 2010 Mw 8.8 Maule megathrust earthquake of Central Chile, monitored by GPS. *Science* 332, 1417–1421. doi:10.1126/science.1204132

- Völker, D., Grevemeyer, I., Stipp, M., Wang, K., He, J., 2011. Thermal control of the seismogenic zone of southern central Chile. *J. Geophys. Res.* 116, B10305. doi:10.1029/2011JB008247
- Vrolijk, P., 1990. On the mechanical role of smectite in subduction zones. *Geology* 18, 703–707. doi:10.1130/0091-7613(1990)018<0703:OTMROS>2.3.CO;2
- Wallace, L.M., 2004. Subduction zone coupling and tectonic block rotations in the North Island, New Zealand. *J. Geophys. Res.* 109, B12406. doi:10.1029/2004JB003241
- Wallace, L.M., Beavan, J., 2010. Diverse slow slip behavior at the Hikurangi subduction margin, New Zealand. *J. Geophys. Res.* 115, B12402. doi:10.1029/2010JB007717
- Wallace, L.M., Reyners, M., Cochran, U., Bannister, S., Barnes, P.M., Berryman, K., Downes, G., Eberhart-Phillips, D., Fagereng, A., Ellis, S., Nicol, A., McCaffrey, R., Beavan, R.J., Henrys, S., Sutherland, R., Barker, D.H.N., Litchfield, N., Townend, J., Robinson, R., Bell, R., Wilson, K., Power, W., 2009. Characterizing the seismogenic zone of a major plate boundary subduction thrust: Hikurangi Margin, New Zealand. *Geochem., Geophys., Geosyst.* 10, Q10006. doi:10.1029/2009GC002610
- Wang, D., Mori, J., 2011. Frequency-dependent energy radiation and fault coupling for the 2010 Mw8.8 Maule, Chile, and 2011 Mw9.0 Tohoku, Japan, earthquakes. *Geophys. Res. Lett.* 38, L22308. doi:10.1029/2011GL049652,
- Wang, K., 2010. Geophysics. Finding fault in fault zones. *Science* 329, 152–153. doi:10.1126/science.1192223
- Wang, K., Bilek, S.L., 2014. Invited review paper: Fault creep caused by subduction of rough seafloor relief. *Tectonophysics* 610, 1–24. doi:10.1016/j.tecto.2013.11.024
- Wang, K., Bilek, S.L., 2011. Do subducting seamounts generate or stop large earthquakes? *Geology* 39, 819–822. doi:10.1130/G31856.1
- Wang, K., Hu, Y., 2006. Accretionary prisms in subduction earthquake cycles: The theory of dynamic Coulomb wedge. *J. Geophys. Res.* 111, B06410. doi:10.1029/2005JB004094
- Watts, A.B., Koppers, A.A., Robinson, D.P., 2010. Seamount subduction and earthquakes.
- Wells, R.E., Blakely, R.J., Sugiyama, Y., Scholl, D.W., Dinterman, P.A., 2003. Basin-centered asperities in great subduction zone earthquakes: A link between slip, subsidence, and subduction erosion? *J. Geophys. Res.* 108, 2507. doi:10.1029/2002JB002072
- White, D.J., 1989. Two-Dimensional Seismic Refraction Tomography. *Geophys. J. Int.* 97, 223–245. doi:10.1111/j.1365-246X.1989.tb00498.x
- Wigger, P.J., Schmitz, M., Araneda, M., Asch, G., Baldzuhn, S., Giese, P., Heinsohn, W.-D., Martínez, E., Ricaldi, E., Röwer, P., 1994. Variation in the crustal structure of the southern Central Andes deduced from seismic refraction investigations, in: *Tectonics of the Southern Central Andes*. Springer, pp. 23–48.
- Wyss, M., Wiemer, S., 1999. How Can One Test the Seismic Gap Hypothesis? The

## References

- Case of Repeated Ruptures in the Aleutians. *Pure. Appl. Geophys.* 155, 259–278–278. doi:10.1007/s000240050265
- Yamamoto, Y., Obana, K., Kodaira, S., Hino, R., Shinohara, M., 2014. Structural heterogeneities around the megathrust zone of the 2011 Tohoku earthquake from tomographic inversion of onshore and offshore seismic observations. *J. Geophys. Res. Solid Earth*. doi:10.1002/2013JB010582
- Yuan, X., Sobolev, S.V., Kind, R., Oppenheimer, D.H., Bock, G., Asch, G., Schurr, B., Graeber, F., Rudloff, A., Hanka, W., Wylegalla, K., Tibi, R., Haberland, C., Rietbrock, A., Giese, P., Wigger, P.J., Röwer, P., Zandt, G., Beck, S., Wallace, T., Pardo, M., Comte, D., 2000. Subduction and collision processes in the Central Andes constrained by converted seismic phases. *Nature* 408, 958–961. doi:10.1038/35050073
- Zahradnik, J., Custódio, S., 2012a. Moment Tensor Resolvability: Application to Southwest Iberia. *B. Seismol. Soc. Am.* 102, 1235–1254. doi:10.1785/0120110216
- Zahradnik, J., Custódio, S., 2012b. Moment Tensor Resolvability: Application to Southwest Iberia. *B. Seismol. Soc. Am.* 102, 1235–1254. doi:10.1785/0120110216
- Zahradnik, J., Gallovic, F., Sokos, E.N., Serpetsidaki, A., Tselentis, G.-A., 2008a. Quick Fault-Plane Identification by a Geometrical Method: Application to the MW 6.2 Leonidio Earthquake, 6 January 2008, Greece. *Seismol. Res. Lett.* 79, 653–662. doi:10.1785/gssrl.79.5.653
- Zahradnik, J., Gallovic, F., Sokos, E.N., Tselentis, G.-A., 2011. Preliminary slip model of M9 Tohoku earthquake from strong-motion stations in Japan - an extreme application of ISOLA code. Report to European Mediterranean Seismological Center.
- Zahradnik, J., Jansky, J., Plicka, V., 2008b. Detailed Waveform Inversion for Moment Tensors of M~4 Events: Examples from the Corinth Gulf, Greece. *B. Seismol. Soc. Am.* 98, 2756–2771.
- Zahradnik, J., Plešinger, A., 2010. Toward Understanding Subtle Instrumentation Effects Associated with Weak Seismic Events in the Near Field. *B. Seismol. Soc. Am.* 100, 59–73. doi:10.1785/0120090087
- Zahradnik, J., Serpetsidaki, A., Sokos, E.N., Tselentis, G.-A., 2005. Iterative Deconvolution of Regional Waveforms and a Double-Event Interpretation of the 2003 Lefkada Earthquake, Greece. *B. Seismol. Soc. Am.* 95, 159–172. doi:10.1785/0120040035
- Zahradnik, J., Sokos, E.N., 2014. The Mw 7.1 Van, Eastern Turkey, earthquake 2011: two-point source modelling by iterative deconvolution and non-negative least squares. *Geophys. J. Int.* 196, 522–538. doi:10.1093/gji/ggt386
- Zahradnik, J., Sokos, E.N., Tselentis, G.-A., Martakis, N., 2008c. Non-double-couple mechanism of moderate earthquakes near Zakynthos, Greece, April 2006; explanation in terms of complexity. *Geophys. Prospect.* 56, 341–356. doi:10.1111/j.1365-2478.2007.00671.x
- Zhang, H., Thurber, C.H., 2006. Development and Applications of Double-difference Seismic Tomography. *Pure. Appl. Geophys.* 163, 373–403. doi:10.1007/s00024-

005-0021-y

- Zhang, H., Thurber, C.H., Bedrosian, P., 2009. Joint inversion for  $V_p$ ,  $V_s$ , and  $V_p/V_s$  at SAFOD, Parkfield, California. *Geochem., Geophys., Geosyst.* 10, Q11002. doi:10.1029/2009GC002709
- Zhao, D., 2015. *Multiscale Seismic Tomography*. Springer Japan, Tokyo.
- Zhao, D., Hasegawa, A., Horiuchi, S., 1992. Tomographic imaging of P and S wave velocity structure beneath northeastern Japan. *J. Geophys. Res.* 97, 19909–19928. doi:10.1029/92JB00603





# ENCLOSURES